UNIVERSITÉ DE MONTRÉAL

APPRECIATION OF SYNVOLCANIC VERSUS SYNTECTONIC FEATURES AT THE MOBRUN VOLCANOGENIC MASSIVE SULPHIDE DEPOSIT, ROUYN-NORANDA DISTRICT, QUEBEC.

par

Sassan LIAGHAT

DÉPARTEMENT DE GÉNIE MINÉRAL

ÉCOLE POLYTECHNIQUE

THÈSE PRÉSENTÉE EN VUE DE L'OBTENTION

DU GRADE DE PHILOSOPHIAE DOCTOR (Ph.D.)

(GÉNIE MINÉRAL)

Mars, 1994

ISBN 0-315-93390-9

UNIVERSITÉ DE MONTRÉAL

ÉCOLE POLYTECHNIQUE

Cette thèse intitulée:

APPRECIATION OF SYNVOLCANIC VERSUS SYNTECTONIC FEATURES AT THE MOBRUN VOLCANOGENIC MASSIVE SULPHIDE DEPOSIT, ROUYN-NORANDA DISTRICT, QUEBEC.

Présentée par: **Sassan LIAGHAT**

en vue de l'obtention du grade de: Philosophiae Doctor (Ph.D.)

a été dûment acceptée par le jury d'examen constitué de:

M. **TANGUAY, Marc**, Ph.D., Président

M. **BROWN, Alex**, Ph.D., membre et directeur de recherche

M. **HUBERT, Claude**, Ph.D., membre et co-directeur

M. **DARLING, Richard**, Ph.D., membre

M. **MACLEAN, Wallace**, Ph.D., membre.

DEDICATION

This thesis is dedicated to my wife. Without her support throughout our married life, I would never be where I am today. I will forever be indebted to her. All that I am is worth nothing without her love.

SOMMAIRE

Les corps de sulfures massifs volcanogènes et les roches volcaniques qui leur sont associées sont fréquemment affectés par une déformation et un métamorphisme reliés à des événements tectoniques majeurs. Une quantité importante d'information sur l'évolution post-minéralisation de ces dépôts peut être obtenue à partir d'analyses pétrographiques et géochimiques détaillées de la minéralogie et des textures finales. Afin d'évaluer ces différents paramètres, nous avons étudié le gisement de sulfures massifs archéen de la mine Mobrun, qui représente un bon exemple d'un gisement intensément déformé et métamorphisé. La nature, la texture et la quantité de matériel échangé lors previèment de l'altération hydrothermale synvolcanique et deuxièment, du métamorphisme et de la déformation, ont été examinées dans les sulfures et dans les roches hôtes afin de déterminer le rôle respectif de chacun de ces processus.

La présente étude démontre que les techniques impliquant les éléments immobiles tels le Ti le Y et le Zr, peuvent être utilisés pour identifier les affinités chimiques et les identités lithologiques des roches volcaniques même si celles-ci ont été affectées par une succession d'événements d'altération et de métamorphisme. Les calculs de changement de masse montrent que le transfert de masse est important dans plusieurs échantillons et plus particulièrement dans les échantillons déformés. Les roches qui ont subi l'altération hydrothermale sont caractérisées

par des changements de masse globaux de -20 % jusqu'à +25 %. Les roches altérées qui, en plus ont été déformées, montrent des changements de masse de -65 % jusqu'à +55 % en réponse aux effets combinés du métamorphisme et de la déformation. Les changements de volume, pour leur part, sont calculés en comparant le volume des roches hôtes à celui du précurseur correspondant pour les roches altérées seulement et les roches altérées et déformées. Le calcul du volume pour les roches hôtes utilise les compositions globales de celles-ci, leurs minéralogies normatives et les densités standard des minéraux normatifs. Les changements de volume ayant eu lieu lors de l'altération hydrothermale sont de l'ordre de -21% jusqu'à +24% alors que ceux reliés au métamorphisme et à la déformation sont de -66% jusqu'à +51%.

La relation entre la déformation à l'échelle microscopique et la distribution (et les caractères chimiques) des minéraux dans les roches encaissantes altérées ont été étudiées par pétrographie, par microsonde électronique, par diffraction aux rayons X et par spectrométrie à la fluorescence X. Les résultats indiquent que la diffusion par solution a joué un rôle majeur dans le transfert de masse des divers éléments à l'échelle microscopique lors de la déformation. Les variations dans la distribution des minéraux sont causées en partie par leur dissolution préférentielle et leur reprécipitation dans les divers sites microstructuraux.

Les textures de croissance minérale primaires ainsi que celles résultant de la déformation peuvent être identifiés dans les différentes générations de sulfures

dans la lentille principale du gisement de Mobrun. La déformation cataclastique de la pyrite s'est accompagnée par une remobilisation des autres sulfures, plus ductiles ainsi que des autres minéraux résultant en diffusion de solution et en cataclase dans la pyrite. La remobilisation des minéraux qui remplissent les fractures cataclastiques indique l'importance du transfert de masse dans les sulfures. De plus, la remobilisation des constituants de la minéralisation à plus grande échelle (à l'échelle du gisement) est une caractéristique étendue, comme le montre la présence des veines syntectoniques.

Nous avons reconnu une dissolution et un transfert de matériel à petite échelle (micrométrique jusqu'à métrique) ainsi qu'à grande échelle (à l'échelle du gisement), aussi bien dans les sulfures que dans les minéraux silicatés. Ces mouvements de matériel ont eu lieu entre les différentes parties des clivages et entre les roches encaissantes et les veinules syntectoniques, ce qui implique un échange de masse important en présence d'une grande quantité de fluide syntectonique.

Les conditions de pression et de température effectives durant le métamorphisme et la déformation à la mine Mobrun ont été déterminées. Les compositions moléculaires des surcroissances de séricite ont été utilisées comme géobaromètre (la méthode "b_0") et les surcroissances de chlorite ont servi de géothermomètre. Ces méthodes ont permis d'évaluer la température et la pression

qui prévalaient lors du paroxysme de la déformation et du métamorphisme à environ 300°C et 2 à 3 kilobars, respectivement.

ABSTRACT

Volcanic-hosted massive sulphide bodies and their hydrothermally altered host rocks may be affected by overprinted metamorphism and deformation associated with major tectonic events, and much information about the post-ore history of these deposits can be obtained from detailed petrographic and chemical analyses of the resulting textures and mineralogies. In this study of a regionally metamorphosed and intensely deformed Archean massive sulphide deposit (Main Lens) of the Mobrun mine, the nature, texture and magnitude of material exchanged at the microscopic scale of both sulphide and silicate rocks have been investigated for the synvolcanic hydrothermal alteration and the syntectonic metamorphism-deformation events.

This study demonstrates that immobile element techniques (involving Ti, Y, Zr, etc.) may be used to identify the chemical affinity and precursor lithologies of volcanic rocks even though they have undergone multiple alteration and metamorphism. Mass change calculations show that mass transport is significant in many samples, particulary in deformed samples. Hydrothermally altered rocks are characterized by overall mass changes of -20% to +25%, whereas deformed hydrothermally altered samples present changes of -65% to +55% resulting from the additional metamorphism-deformation effects. Volume changes are calculated using the bulk compositions of the host rocks, their normative mineralogies, and

standard normative mineral densities, and compared to the volume of the corresponding precursors of both altered only and deformed altered rocks. The volume changes during hydrothermal alteration and metamorphism-deformation are calculated to have been on the order of -21% to +24% and -66% to +51%, respectively.

The relationship between microstructural deformation patterns and the distribution (and chemical characteristics) of minerals in the altered wall rocks has been investigated by petrographic, scanning electron microprobe, X-ray diffraction and X-ray fluorescence spectrometry analyses. These analyses indicate that solution-precipitation creep played a major role in the mass transfer of remobilized constituents at the microscopic scale during deformation. Variations in the distribution of minerals has resulted in part from their preferential dissolution and reprecipitation in various microstructural sites.

Both primary growth textures and deformation features are recognized among the various generations of the sulphides in the Main Lens of the Mobrun deposit. Brittle cataclastic deformation of pyrite was accompanied by remobilization of more ductile sulphides and other minerals, giving rise to both solution-precipitation creep and cataclasis in pyrite. The extent of mass transfer among sulphides accounts for the remobilization of minerals filling cataclastic fractures. In addition, long-range (deposit-scale) remobilization of ore constituents, evident in syntectonic veins, is a widespread feature.

Among sulphide and silicate minerals, we recognize short-range (micrometre- to metre-scale) and long-range dissolution and transfer of material within the cleavage domains and between wall rocks and syntectonic veinlets, implying significant mass exchange in the presence of large volumes of syntectonic fluid.

Pressure-temperature conditions during metamorphism-deformation at Mobrun have been determined using the molecular compositions of overgrowth sericite as a geobarometer (the "b_0" method) and overgrowth chlorite as a geothermometer. These methods give a temperature of ~300°C and a pressure of ~2 to 3 kbars for peak metamorphism-deformation.

RÉSUMÉ

Dans plusieurs cas, les lentilles de sulfures massifs et leurs roches hôtes altérées ont subi une évolution tectonique et métamorphique postérieure à leur mise en place. Dans ces cas, de nombreuses évidences de déformation, de recristallisation et de transfert de masse peuvent être observées. Des études qui permettent d'évaluer les effets reliés à la déformation et au métamorphisme, ainsi que ceux reliés aux processus synvolcaniques dans les dépôts de sulfures massifs, permettent une meilleure compréhension du rôle de chacun des processus dans la genèse du gîte. Le gisement de Mobrun, situé dans le camp minier de Rouyn-Noranda, a été choisi en raison de l'intense déformation qui l'a affecté afin d'examiner les effets de la déformation à l'échelle microscopique ainsi que ceux du métamorphisme, pour les contraster avec les caractéristiques volcanologiques primaires.

La lentille principale à la mine Mobrun est contenue dans des laves et des roches pyroclastiques felsiques qui sont maintenant en position subverticale. Le gisement présente plusieurs caractéristiques qui se comparent avec les dépôts de sulfures volcanogènes de type Noranda. Les évidences géologiques indiquent que les lentilles de sulfures massifs à la mine Mobrun sont essentiellement stratiformes et donc qu'elles représentent une partie intégrante de l'empilement volcanique.

Le corps minéralisé principal est zoné avec une zone riche en cuivre et une autre riche en zinc. Aucune évidence d'une zone de veinules importante n'est

présente sous le gisement. De plus, une altération importante en séricite se retrouve aussi bien dans le mur que le toit du gisement sans toutefois qu'il n'y ait de cheminée d'altération apparente ou de zone chloritisée. Lors de la déformation et du métamorphisme, les sulfures de la lentille principale et les roches hôtes ont été modifiées de façon chimique et texturale. Les roches hôtes ont développé une foliation qui est subparallèle au corps minéralisé.

En se basant sur les modèles courants pour la formation des sulfures massifs volcanogènes et sur les effets évidents de la déformation syntectonique à Mobrun, on peut assumer que le gisement a subi les effets cumulatifs de l'altération hydrothermale synvolcanique ainsi que de la déformation et du métamorphisme régional. La présente étude a été entreprise dans le but d'identifier la nature et l'origine des caractéristiques de la déformation et les effets du métamorphisme tant dans les sulfures que dans les roches hôtes silicatées. À cet effet, des études pétrographiques détaillées et des analyses chimiques ont été entreprises afin de vérifier la minéralogie et les textures qui résultent de ces processus.

Les études microstructurales décrivent les caractéristiques majeures des effets du métamorphisme et de la déformation des roches hôtes, telles la schistosité, le clivage de pression-dissolution, le clivage de crénulation, les ombres de pression, le "crack-seal", les "pull-aparts" et les boudins. La géométrie de ces microstructures permet de comprendre les mécanismes de déformation et l'importance des transferts de masse et de volume syntectoniques au gisement de Mobrun. La relation entre les

structures de déformation à l'échelle microscopique et la distribution des minéraux et leurs caractéristiques chimiques a été étudiée à l'aide de la microsonde électronique, du diffractomètre à rayons X et du spectromètre à fluorescence X. Les analyses démontrent que la schistosité et les clivages sont le résultat du développement de minces zones où la différenciation chimique et minéralogique est importante.

La chimie et la minéralogie des lamelles de la schistosité sont différentes de celles des microlithons. Les plans de schistosité présentent un appauvrissement en SiO_2 en raison d'une déficience en quartz et un enrichissement en Al_2O_3 et K_2O dû à l'augmentation de la séricite dans ces plans par rapport aux microlithons. Des grains fins de rutile sont concentrés dans les lamelles de la schistosité en raison de leur insolubilité.

Il existe des changements dans les compositions chimiques totales entre les roches non déformées et celles déformées. Il y a un appauvrissement en SiO_2 et une augmentation en Al_2O_3, en K_2O et en éléments immobiles (Ti, Zr, Y et Nb) dans les roches déformées. Les analyses à la microsonde des séricites dans les ombres de pression ont montré des compositions différentes de celles des séricites dans les plans de clivage. Les séricites des ombres de pression sont caractérisées par une concentration plus élevée en Si, K, Fe, et Mg et plus basse en Al, Na et Ti.

Les variations chimiques associées avec la schistosité et le clivage montrent que la distribution des minéraux résulte de leur dissolution préférentielle dans

différents sites microstructuraux. La croissance de grains de phyllosilicate a été contrôlée par le comportement des éléments chimiques qui ont interagit avec l'eau lors du métamorphisme.

Le rôle du transfert de masse lors du développement des microstructures indique que la diffusion de solution a contribué de façon majeure au transport de masse. Les éléments ont été remobilisés par une dissolution locale dans les zones de haute déformation pour être déposés à nouveau dans les zones de plus faible déformation dans les couches adjacentes. La présence marquée de veines d'extension syntectoniques remplies de quartz, de calcite et de pyrite sont une manifestation d'un transfert de masse sur de plus grandes distances que celles impliquées dans le remplissage des sites de pression-dissolution.

Malgré la superposition de l'altération, du métamorphisme et de la déformation sur les roches à la mine Mobrun, l'utilisation des éléments chimiques immobiles tels Zr, Y, Nb, HREE et Ti s'est avérée concluante pour identifier l'affinité chimique ainsi que les lithologies originales des roches volcaniques. Des roches présentant une affinité tholéiitique (Zr/Y = 4.5) se retrouvent dans le mur alors que des rhyolites calco-alcalines (Zr/Y = 8) caractérisent le toit du gisement. La corrélation entre les concentrations en éléments immobiles et l'intensité de la foliation dans les roches est marquée. Les roches fortement foliées sont fortement enrichies ou appauvries en Zr, Y, Ti et HREE par rapport aux roches peu foliées. Cette différence est attribuée aux transferts de masse durant l'événement du

métamorphisme et de la déformation.

Les transferts de masse dus à l'altération hydrothermale ainsi qu'au métamorphisme et à la déformation dans les roches hôtes possèdent une grande variation de concentration en éléments immobiles. Les différences absolues du contenu en Zr, pour les compositions reconstituées ainsi que pour les roches altérées par rapport aux précurseurs correspondants, ont été utilisées pour détecter les changements de masse qui résultent de l'altération hydrothermale ainsi que du métamorphisme et de la déformation. Les changements de volume ont été calculés à partir de la composition globale en utilisant la combinaison de la minéralogie normative et la densité des minéraux par rapport au volume du précurseur correspondant et ce pour les roches altérées et déformées. Les calculs de changement de masse démontrent que le transport de masse est important dans plusieurs échantillons altérés par hydrothermalisme. Toutefois, ces changements de masse sont plus importants dans les roches déformées. Les échantillons ayant été affectés par les effets de l'altération hydrothermale seulement sont caractérisés par des changements de masse globaux de -20 % jusqu'à +25 %. Les roches déformées présentent des changements de masse de -65 % jusqu'à +55 % qui sont reliés à l'effet combiné de la déformation et du métamorphisme. La magnitude des changements de volume dans les deux cas est semblable à celle des changements de masse.

La lentille principale de Mobrun contient des sulfures laminés, massifs et

bréchiques ainsi que des sulfures à grains fins qui sont parfois sous la forme colloïdale. Une partie de la minéralisation est aussi présente sous forme de veines. La forme générale des corps minéralisés de même que leur distribution sont dues à une déposition des sulfures sous forme exhalative. La déformation et la recristallisation des minéraux de sulfure sont le résultat de la déformation et du métamorphisme. Ces processus ont eu pour effet de détruire partiellement les structures primaires formées durant les événements exhalatifs. Toutefois, certaines caractéristiques primaires tel le rubanement de sphalérite-pyrite ainsi que les textures framboidales et colloformes de la pyrite, sont conservées. Les microstructures développées dans les sulfures lors du métamorphisme et de la déformation montrent que la pyrite s'est comportée principalement de façon fragile malgré quelques évidences d'une certaine ductilité. La pyrite à grain fin présente des dislocations, de la pression-dissolution et du fluage cataclastique. Le comportement des autres sulfures est principalement ductile. Des mâcles de déformation et de recristallisation dynamique sont observées dans la sphalérite. Dans certains cas, la sphalérite apparaît comme relativement insoluble dans les films de pression-dissolution. La chalcopyrite présente une texture de "chalcopyrite disease" ainsi qu'une recristallisation dans les micro-fractures de la pyrite. La galène montre des caractéristiques de recristallisation à l'intérieur des microstructures.

En plus des caractéristiques de microstructures primaires, plusieurs roches

sulfurées ont subi une recristallisation. Ces effets apparaissent à l'échelle microscopique comme de la diffusion de solution, de la recristallisation dynamique, des surcroissances ainsi que des remplissages de fractures. Les phases plus ductiles (la galène, la chalcopyrite et la sphalérite) ont tendance à migrer vers les zones abritées des ombres de pression et les micro-fractures dans les cristaux de pyrite. Les veines de pyrite de type "crack-seal" qui se sont formées par des processus métamorphiques sont
communs à la mine Mobrun. De telles textures supportent l'idée d'une remobilisation de la minéralisation sur de plus grandes distances que celles observées dans les structures de pression-dissolution.

La température du paroxysme de la déformation et du métamorphisme à Mobrun a été déterminé en utilisant les compositions moléculaires des surcroissances des grains de chlorite. Cette méthode a permis d'obtenir des températures d'environ 300°C pour la formation de ces chlorites métamorphiques. La pression atteinte durant le même événement a été déterminée à partir de la composition moléculaire de la séricite. Ce géobaromètre, qui se base sur le contenu en céladonite dans la muscovite, résulte de la corrélation positive entre le paramètre b_0 et la pression. Selon la carte géobarique de Guidotti et Sassi (1986), une pression absolue de 2 à 3 kilobars peut être estimée pour les pressions maximales à Mobrun.

Les études d'inclusions fluides ont été effectuées sur quelques surcroissances de grains de quartz et dans des veines de quartz en extension. Les inclusions fluides

contiennent une phase liquide saline, probablement un fluide métamorphique faible en chlorure. Des résultats sur quelques inclusions fluides suggèrent que le CO_2 est aussi un composé important dans le fluide métamorphique.

Les microstructures des sulfures à Mobrun sont similaires à celles qui se retrouvent dans les roches hôtes silicatées. Le transfert de masse par pression-dissolution a été un important type de déformation dans les roches hôtes silicatées ainsi que dans les sulfures, particulièrement pour la pyrite. Dans les roches silicatés, les transferts de matériel de courte distance (du micromètre jusqu'à l'échelle de l'échantillon) sont reconnus. Cependant, plus de 50 % des changements de masse et de volume dans les roches peuvent être attribués à des transferts de matériel (principalement le quartz) à l'échelle du gisement durant la déformation et le métamorphisme.

Plusieurs évidences suggèrent qu'une minéralisation sulfurée préexistante à Mobrun a été remobilisée de façon importante sous des conditions de déformation et de métamorphisme. La remobilisation de la minéralisation à des faibles échelles est une caractéristique bien développée de la minéralisation pour des distances de l'ordre du micromètre jusqu'à une dizaine de centimètres. La remobilisation syntectonique de grande échelle (à l'échelle du gisement) de la minéralisation a aussi été reconnue dans les veines en extension, particulièrement dans la zone de "stringer" où la minéralisation hydrothermale est typiquement associée avec un système de veines en extension ou de remplacement.

La méthode analytique utilisée dans cette étude, qui consiste en une combinaison d'études microscopique et géochimique, peut être employée afin de générer de l'information sur l'histoire post-minéralisation des dépôts de sulfures massifs métamorphisés en général.

ACKNOWLEDGMENTS

It is my great privilege to have had Professor Alex. C. Brown as my supervisor throughout my Ph.D. program at Ecole Polytechnique. I thank him most sincerely for his dedication, guidance, kindness, support and patience over the past four years. His example has been an inspiration to me in demonstrating those philosophies which are crucial to successful research. He deserves my particular gratitude for his indulgence and dedication during the numerous reviews of this thesis to transform it into its present state.

I also wish to express my sincerest gratitude to my thesis co-supervisor, Professor Claude Hubert, for his dedication, kindness, invaluable guidance and very helpful comments.

I would like to thank Professor Gaston Pouliot for his very generous assistance in geochemical and X-ray analyses and his many pertinent comments and suggestions.

I am greatly indebted to my M.Sc. thesis supervisor, Professor W. H. MacLean, McGill University. I will always be grateful to him for what I have learned from him, not only concerning science and research but also with regard to dedication and perseverance.

Special thanks are given to Drs. L. Hoy, C. Ji and D. Sangster for their scientific and editorial assistance; to Mr. G. Gélinas for the preparation of thin

and polished sections; to Mr. P. Samson for help with microprobe analyses; to Mr. G. Gauthier and Mr. J. L. Bastien for geochemical analyses; to Mr. J. Riopel for his permission to use his rock samples and documents; to J.P. Desrochers for translating the Abstract and Summary into proper French; and to my graduate collegues, N. Teasdale, M. Richard, A. Belkabir, M. Bouabdellah and others, for their constant help and friendship.

I am eternally grateful to my dear wife, Afsaneh, for her love, patience, and encouragement throughout this study. She has sacrificed her education so that I could pursue my studies and instead has dedicated herself to the care and upbringing of our dear children, Soroush and Samin. Her actions exemplify the meaning of the word "mother".

Finally, I thank God for his mercies and countless blessings throughout the years.

The research was authorized by Michel Bouchard and P.J. LaFleur of Audrey Resources Inc., and was supported by a Natural Sciences and Engineering Research Council of Canada (NSERC) Strategic Grant to my supervisors.

TABLE OF CONTENTS

LIST OF FIGURES

* * *

* * *

* * *

* * *

* * *

LIST OF TABLES

* * *

LIST OF APPENDICES

CHAPTER 1

INTRODUCTION

1.1 FOREWORD

Volcanogenic massive sulphide (VMS) deposits of the Noranda camp have been the topic of many genetic studies. In the late 1950s, a volcanic-exhalative model emerged for this type of deposit (Oftedahl, 1958 and Hawley, 1959) and with the discovery of active exhalative vents on the seafloor (e.g., Edmond et al., 1979), geologists have acquired a great deal of insight into the formation of ancient volcanogenic massive sulphide deposits.

During the last two decades, the importance of post-ore metamorphic and deformation processes have been considered in many studies (e.g., Sangster, 1972, 1979; Marshall and Gilligan, 1987, 1993) and genetic models for some deposits whose geological settings differ significantly from those predicted by the volcanic-exhalative model alone have been re-examined (e.g., the Bousquet deposits: Tourigny et al, 1988; Marquis et al., 1990). Most of these studies describe the detailed nature and origin of deformational features and metamorphic effects resulting from intense shearing and greenschist facies metamorphism. For example, centimetre-scale banding associated with massive sulphide deposits in the Bousquet mining camp was initially perceived to be synsedimentary in origin

(Vaillant and Hutchinson, 1982; Stone, 1988), whereas this layering has been re-interpreted subsequently as tectonic banding (Tourigny et al., 1988).

In many cases, massive sulphide orebodies and their altered host rocks have undergone post-ore tectonism and metamorphism and show evidence of deformation, recrystallization and mass transfer. The results address the continuing debate (e.g., Brill, 1989; Lianxing and McClay, 1992) over the origins of many microscopic features of these deposits, some of which have been attributed to original synsedimentation-synvolcanic textures, others to syntectonic overprinting. Clearly, there is a need for further studies to distinguish such metamorphic-deformational effects from synvolcanic features in massive sulphide deposits, and hence we welcomed the opportunity to examine the microstructural-scale effects of deformation and metamorphism on the Mobrun massive sulphide deposits and their host rocks in the Noranda mining camp.

VMS deposits of the Noranda camp are now referred to as Noranda-type (Morton and Franklin, 1987). These deposits are commonly stratabound and contain footwall alteration pipes which are related to syngenetic feeder systems and are composed of chlorite, quartz ± sericite in their inner zones and sericite, quartz ± chlorite in their outer zones. In the case of Noranda-type deposits, the massive sulphide zones consist of elliptical bodies proximal to the exhalative vents which are characterized by extensive alteration pipes in their footwalls (Large 1977, 1981; Franklin et al., 1981)(Fig. 1.1).

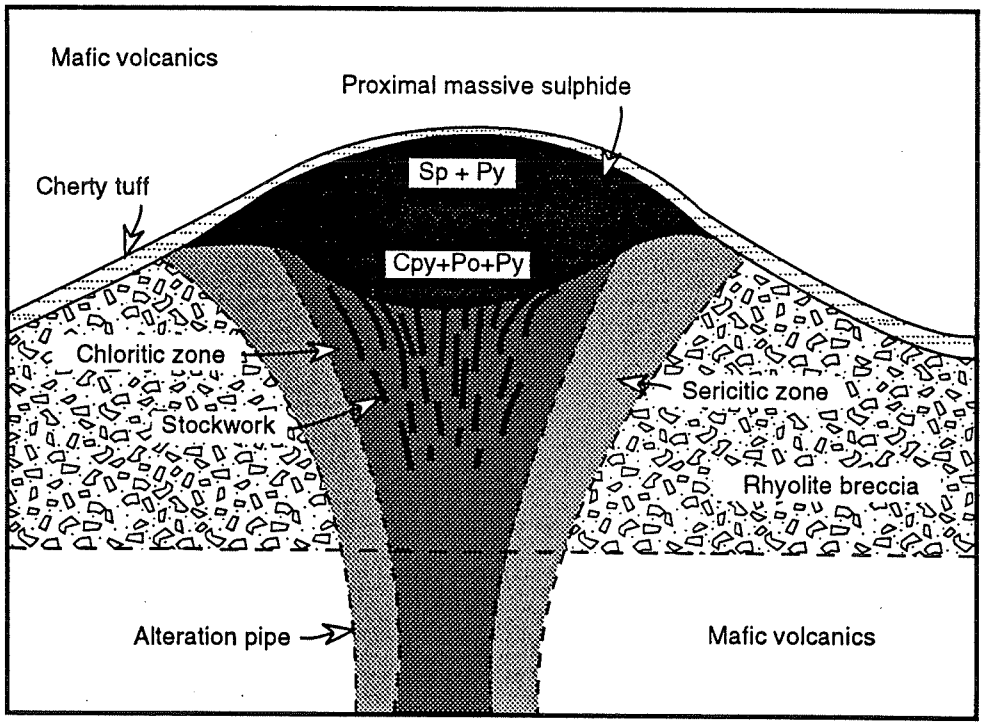

Fig. 1.1 Typical cross-section of a Noranda-type massive sulphide deposit.

VMS deposits generally form from hot metalliferous fluids emerging from exhalative vents on the seafloor. Rapid (effectively instantaneous) cooling forces sulphides to precipitate in and around the hydrothermal vent. A major portion of the sulphides is deposited within the sulphide mound by diagenetic interaction between the fluid and previously deposited sulphides. Commonly, a metal zonation is observed in the resulting massive sulphide orebody: chalcopyrite is generally concentrated with pyrrhotite, pyrite and magnetite in the footwall vent complex and in the basal portion of the sulphide mound, whereas the outer portions of the body are characterized by concentrations of sphalerite ± galena with pyrite. Figure 1.1 shows the typical features of Noranda-type VMS deposits.

1.2 TERMINOLOGY

Marshall and Gilligan (1987, 1993), Gilligan and Marshall (1987) show that considerable variation exists in the usage of terms dealing with the mobilization of ores during synvolcanic and syntectonic events. This variation is apparent in many papers dealing with metamorphosed deposits (e.g., Mookherjee, 1976; Pederson, 1980; McClay, 1984). In order to evaluate the effects of metamorphism on the Mobrun deposits in a consistent fashion, the following definitions (not necessarily following those of the Glossary of the American Geological Institute, for example) are used in this study:

Deformation describes processes in which structural changes (e.g., attitude, configuration, volume) occurred in rocks. Also, this term is used to cover faulting, the development of schistosity, and the redistribution of minerals.

Hydrothermal alteration refers to the metasomatism resulting from the initial synvolcanic hydrothermal activity.

Internal and external remobilization refers to as remobilization of ores within and out of the orebody, respectively.

Metamorphism describes processes by which chemical and mineralogical changes occurred in rock under elevated pressures and temperatures.

Note: the term metamorphism-deformation, even though it is clearly a multistage event, is used here as a single event to describe chemical and mechanical modification of rocks during post-hydrothermal mineralization event.

Mobilization refers to the initial synvolcanic emplacement of VMS ores and related silicate constituents.

Remobilization refers to redistributions of pre-existing sulphide concentrations and silicate host-rock components, e.g., parts of the pre-existing rock constituents have been moved from their primary position and have been redeposited at microscopic to megascopic distances from their sources as a result of deformational forces associated with a metamorphic-tectonic event.

Short- and long-range remobilizations are minor and major-scale transpositions of pre-existing ore material and associated host rocks. The transport distance is

considered "short-range" for remobilizations of micrometre to hand-specimen scales, and "long-range" for deposit-scale remobilizations or larger.

1.3 METHODOLOGY

This study concentrates on the lithogeochemistry and textures of the sulphide ores and associated felsic host rocks of the Mobrun massive sulphide deposit, placing emphasis on recrystallization and mass transfers that occurred during deformation of the deposit. To understand these phenomena, the following specific studies were undertaken on the massive sulphide orebodies and their host rocks: a) descriptions of metamorphic and remobilization features and analyses of the relative micro-scale mobility of chemical components, especially in microstructural deformation sites (Chapter 3), b) a geochemical study of altered Mobrun wall rocks, with particular consideration for the relationship to the intensity of deformation (Chapter 4), c) calculations of mass and volume changes of the Mobrun host rocks during deformation (Chapter 5), d) descriptions of remobilization features of the sulphide ores (Chapter 6), and e) identification of the pressure and temperature of deformation (Chapter 7).

1.4 LOCATION AND ACCESS

The Mobrun massive sulphide deposits are located in Dufresnoy township approximately 35 km northeast of the town of Rouyn-Noranda (600 km northwest of Montreal). The area is accessible from Rouyn-Noranda by highway 101 north to Dalembert, with an exit eastward toward Cléricy, and then, before reaching the village of Cléricy, a turn northward on a gravel mine property road.

1.5 HISTORY AND PRODUCTION

The Mobrun Main Lens massive sulphide deposit was detected in 1954 by Rio Canadian Exploration Ltd. while exploring electromagnetic anomalies with the aid of a "mobile road unit" (from which the name "Mobrun" is derived). One year later the location of the Main Lens orebody was confirmed with the first hole drilled in the area. In the following years, until 1985, numerous companies conducted various investigations including additional drilling, geophysical surveys and metallurgical tests. During this period, the 3 million tonne Main Lens deposit of low-grade massive sulphide was considered uneconomic. In 1985, with increasing metal and gold prices, Resources Audrey Inc. prepared a portion of the deposit for open-pit mining, which led in turn to the initiation of mining and the development of underground levels in 1987. In 1987, exploration holes also

intersected massive sulphide mineralization in what became known as the satellite 930 zone. Three other satellite lenses (850, 870, and the North-East) were subsequently found in the vicinity of the Main Lens.

The 1100 Lens, a major sulphide body discovered south of the Main Lens in 1988, was not accessible at the time of this study. This deposit is currently in preparation for mining, with reserves estimated to be sufficient up to the year 2003 (Audrey Resources Inc., 1990).

Before closure of the Main Lens complex in late 1992, the Main, 850, 870 and 930 lenses produced over 700,000 tonnes of ore over a six year period. The Main Lens complex contained 3.37 Mt, of which about 1 Mt were economic with grades of 0.8% Cu, 2.4% Zn, 30.2 g/t Ag and 2.2 g/t Au (Table 1.1). The 1100 Lens contains at least 17 Mt of ore, with economic reserves of about 10 Mt grading 0.8% Cu, 5.4% Zn, 37.4 g/t Ag and 1.3 g/t Au to a depth of 700 m (Caumartin and Caillé 1990)(see Table 1.1). The total reserves in the 1100 complex were estimated at least at 24 Mt; of this 10.5 Mt were considered economic as of 1990 (Audrey Resources Inc. 1990). The Mobrun mine has been the second largest base-metal resource in the Noranda camp, next in size to the Horne deposit (see Table 1.2).

Table 1.1 Tonnages and grades of the Mobrun Main Lens and 1100 Lens complexes.

	Lens	Mineral inventory (t)	Ore reserves (t)	Grade Cu (%)	Zn (%)	Ag (g/t)	Au (g/t)
Main Lens Complex	Main	3374045	955017	0.81	2.44	30.32	2.20
	850	38417	38417	0.77	2.97	41.48	3.66
	870	38349	38349	0.86	3.18	46.20	5.05
	930	103204	103204	1.49	1.92	41.05	5.44
Total			1134987	0.87	2.44	32.21	2.64
1100 Lens Complex		24920000	10400000	0.76	5.43	37.40	1.35
Total			11534987	0.77	5.14	36.89	1.48

Data from Caumartin and Caille (1990) and Resourses Audrey Inc. (1990).

Table 1.2 Tonnages and grades of massive sulphide deposits in the Noranda camp.

Deposits	Mineral Inventory	Cu %	Zn %	Ag g/t	Au g/t
Mobrun (M. L)	3.3	0.8	2.4	30.3	2.2
Mobrun (1100	25.0	0.7	5.4	39.4	1.5
MacDonald	3.2	0.0	4.7	19.0	0.6
Delbridge	0.4	0.6	8.7	62.0	2.1
Horne	54.0	2.2	?	13.0	6.1
Horne (No. 5)	24.0	0.1	1.2	?	1.4
Quemont	15.0	1.2	1.9	19.0	4.9
Millenbach	3.5	3.5	4.5	48.0	0.9
Norbec	4.3	2.8	4.7	43.0	0.9
Vauze	0.4	2.9	1.4	25.0	0.8
Corbet	2.7	2.9	2.0	20.0	0.9
Ansil	1.5	7.2	0.8	26.0	1.7
Aldermac	3.2	1.6	4.0	34.0	0.3
New Insco	1.0	2.5	?	15.0	0.9

Data from Chartrand and Cattalani (1990), Riopel et al. (1992).

1.6 PREVIOUS STUDIES

General outlines of the geology of the Mobrun area may be found in Ambrose (1941) and Trudel (1979) from mapping of the Cléricy region, and in Duquette (1977), McConnell (1976), Labelle (1985), Beaumier (1984), Tassé (1978) and Gélinas et al. (1977, 1984) which deal with the petrography, petrochemistry and geochemistry of rocks in the Mobrun region.

The geology of the Mobrun mine has been described by O'Dowd (1984, 1985), Gilbert (1985), MacRobbie and Watkinson (1986), and Caumartin and Caillé (1990). They defined the lithological units, general structures, alteration features and geochemistry of the host rocks. Studies by Riopel et al. (1992), in reports to the Ministère de l'Énergie et des Ressources, describe the mineralogy, bulk-rock geochemistry and stable-isotope geochemistry of the deposits of the Main Lens complex, with emphasis on their structural context. The M.Sc. thesis of Riopel (1991) emphasized descriptions of micro- to macro-scale deformational features, both brittle and ductile, of the sulphide bodies and associated silicate rocks.

Barrett et al. (1992) emphasized the lithogeochemistry of the volcanic host rocks of the Mobrun mine and described the chemostratigraphy of the original volcanic sequence enclosing the orebodies, using techniques based on immobile and incompatible trace elements. They identified primary variations in rhyolite

compositions near footwall-hangingwall contacts of both the Main Lens and 1100 Lens complexes, and they defined different compositions of rhyolite near the Main Lens complex. Mass changes during hydrothermal alteration of silicate host rocks of the Main Lens complex were also calculated. According to their work, alteration zones associated with mineralization have mass gains in FeO and MgO and K_2O, and a mass loss in silica. Calculations of mass change indicate that the footwall generally lost silica relative to the hangingwall.

LaRocque and Hodgson (1993) argue that the Mobrun deposits exhibit characteristics typical of Mattabi-type deposits. Their samples were taken partly from a new ramp into the 1100 Lens, which was not available at the time of this or previous studies. The key observations supporting LaRocque and Hodgson's Mattabi model consist of occurrences of (1) a fragmental volcanic rock indicative of shallow-water explosive volcanism following hydrothermal alteration in a footwall stockwork system, (2) ferro-dolomite minerals in the upper stratigraphic footwall of the 1100 Lens complex, (3) extensive carbonate alteration in the footwall of the 1100 Lens, and (4) a broad, semi-conformable alteration zone around the stockwork vent. However, LaRocque and Hodgson (1993) note the absence of aluminous alteration minerals (e.g., chloritoid) and argillic alteration which are typical of Mattabi-type deposit. They also note that the carbonitization observed in 1100 footwall rocks is absent in the Main Lens host rocks.

The distribution of gold in the Mobrun Main Lens has been examined and

discussed in detail by LaRocque and Hodgson (1993). From ion microprobe analyses, they relate gold contents to particular facies of pyrite and other sulphide minerals. According to this work, gold was deposited syngenetically along with other components of the massive sulphide bodies and was initially hosted in pyrite as a solid-solution or as submicroscopic inclusions. Gold is interpreted to have been remobilized into veins of quartz, calcite, chalcopyrite and/or sphalerite during metamorphism and recrystallization of pyrite.

Parts of the present study have been presented at the annual meetings of the Geological Association of Canada - Mineralogical Association of Canada (GAC-MAC) (Liaghat, et al., 1992, 1993, 1994).

CHAPTER 2

GEOLOGY

2.1 REGIONAL GEOLOGY

The volcanic strata hosting the base-metal deposits of the Noranda camp belong to the Blake River Group (BRG), one of the youngest volcanic units of the Abitibi Greenstone Belt. Some 760 km long by 200 km wide, this is the largest continuous Archean greenstone belt in the Canadian Shield (Fig. 2.1). The east/west-trending belt is located in the southeastern part of the Superior Province and is truncated by rocks of Grenville Province to the east and by the Kapuskasing Structural Zone to the west.

The geology of the Abitibi Greenstone Belt has been the subject of numerous regional studies (Dimroth et al., 1982a, b; Dimroth et al., 1983; Gélinas et al., 1984; Hubert et al., 1984; Lajoie and Ludden, 1985; Ludden et al., 1986; Ludden and Hubert, 1986). These reports describe the general petrographic, petrologic, structural and geochemical features of the area, and provide a modern interpretation of the tectonic history of the Abitibi Greenstone Belt. The structural elements of the Abitibi belt are assigned to three generations (Hubert et al., 1984). The principal deformations, D_1 and D_2, produced Z-shaped interference patterns. Major faults are interpreted as strike-slip and, together with their subsidiary

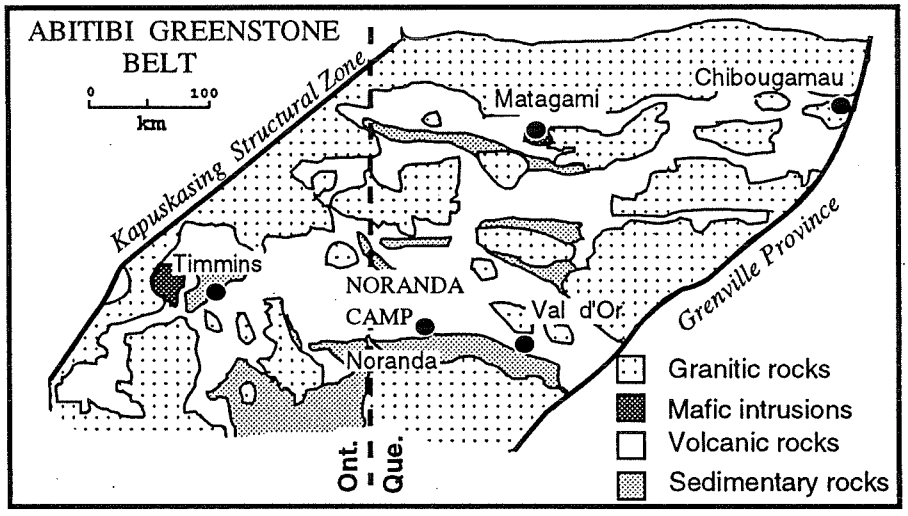

Fig. 2.1 Generalized geological map of the Abitibi Greenstone Belt.

systems, they are compatible with wrench fault tectonics (Hubert et al., 1984). Numerous faults also cut the volcanic strata.

The Blake River Group strata typically occurs in lozenge-shaped domains and those of the Noranda district are bounded to the north by the Destor-Porcupine Fault and to the south by the Larder Lake-Cadillac Fault (Dimroth et al., 1982; Dimroth et al., 1983; Hubert et al., 1984)(Fig. 2.2, see insert). The BRG was folded during the Kenoran Orogeny to produce an overall configuration of an east trending syncline to the northeast and east of the Noranda camp (Goodwin, 1977). The rocks have been regionally metamorphosed to the prehnite-pumpellyite and greenschist facies (Jolly, 1978). Where late-stage felsic plutons (e.g., the Lake Dufault granodiorite) intrude the volcanic stratigraphy, lower amphibolite facies hornfels metamorphism has formed biotite, garnet, cordierite, hornblende, actinolite, and anthophyllite. Extensive diorite sills and dikes have also intruded the BRG, filling faults which may have large vertical displacements (e.g., the Dufresnoy sill).

The BRG was divided according to age and chemical variations by Goodwin (1977). The Noranda sub-group, which hosts the majority of the base-metal mines in the central Noranda district (Fig. 2.2), is composed mainly of sheet-like and tabular flows of basalts, andesite and rhyolite. These volcanic rocks consist of both tholeiitic and calc-alkaline series (Spence, 1975; Goodwin, 1977, 1982; Gélinas et al., 1977, 1984; Ujike and Goodwin, 1987; Cattalani et al., 1988). The sub-group

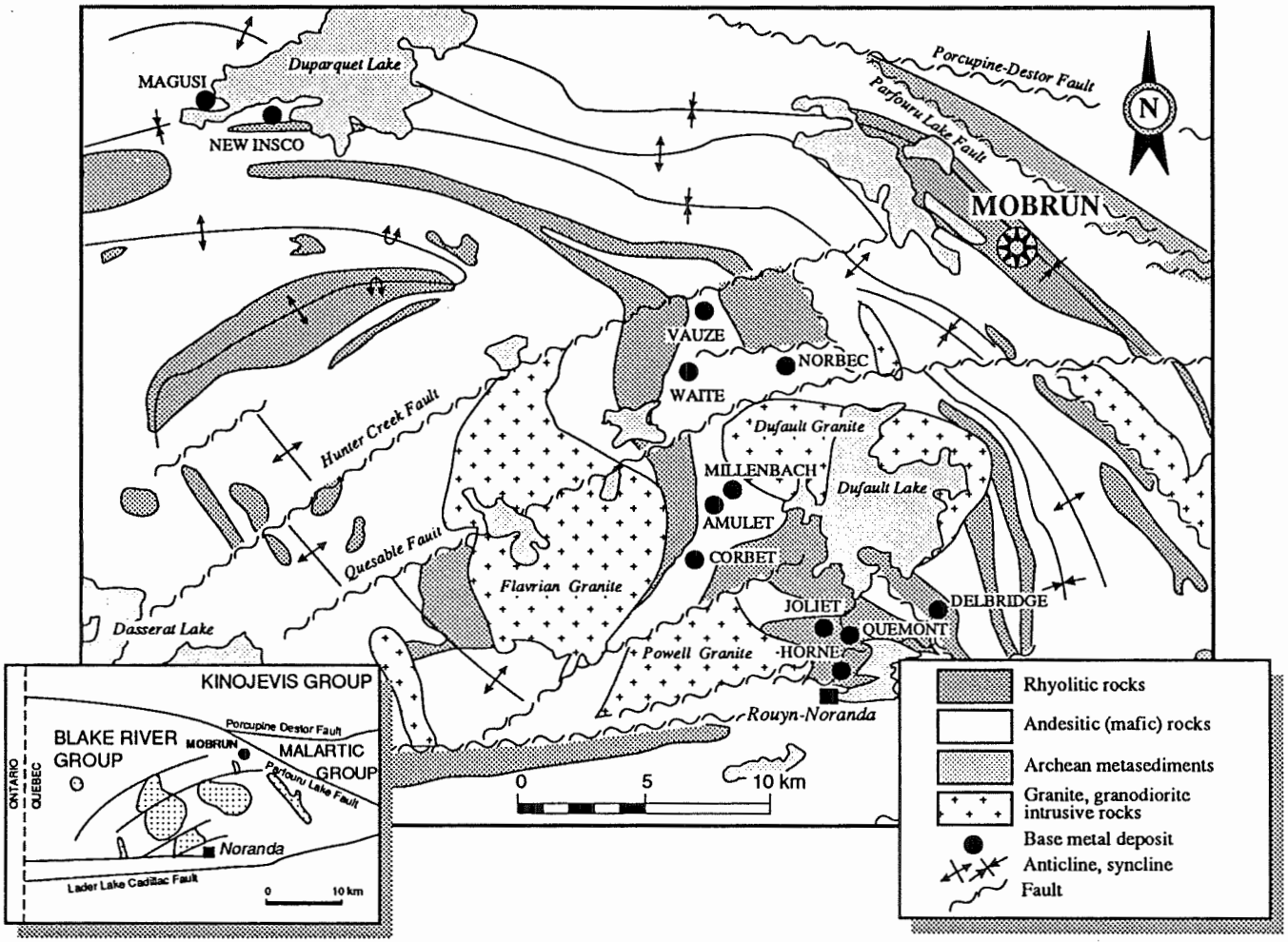

Fig. 2.2 Regional geology of the Noranda mining camp, and location of its major massive sulphide deposits, including Mobrun. Insert: generalized geological map of the Blake River Group; the thin lines represent major faults.

has been further subdivided by Spence and de Rosen-Spence (1975) to highlight the occurrence of five major rhyolitic units (Fig. 2.3).

Massive sulphide deposits in the Noranda area are generally clustered at the top of the third and fourth rhyolite units (Spence and de Rosen-Spence, 1975). The host rocks of the Mobrun mine area are considered to be part of the fifth (uppermost) volcanic zone (Fig. 2.3)(Spence, 1967; Goodwin and Ridler, 1970), although a strict correlation of Mobrun volcanics with the BRG remains unconfirmed. The distribution, tonnage and grades of the principal massive sulphide deposits in the Noranda area are given in Figure 2.2 and Table 1.2, respectively.

The mafic volcanic rocks of the Noranda sub-group are pillowed to massive and occur as extensive sheets traceable for several kilometres and up to 800 metres thick. The mafic rocks range in composition from basalt to dacite with a mean composition in the andesite field. The rhyolites are generally tabular and up to 200 metres thick, but may also occur as domes several hundreds of metres thick. The lava flows are massive to brecciated. Pyroclastic rocks account for less than 1% of the volcanism in the metal-rich Noranda sub-group of the BRG (Spence, 1975).

Geological ages for the Noranda volcanic rocks are in the 2703-2698 Ma range (Mortensen, 1987, 1993). The metamorphic grade is generally greenschist to sub-greenschist facies (Baragar, 1968; Goodwin and Ridler 1970; Jolly, 1978;

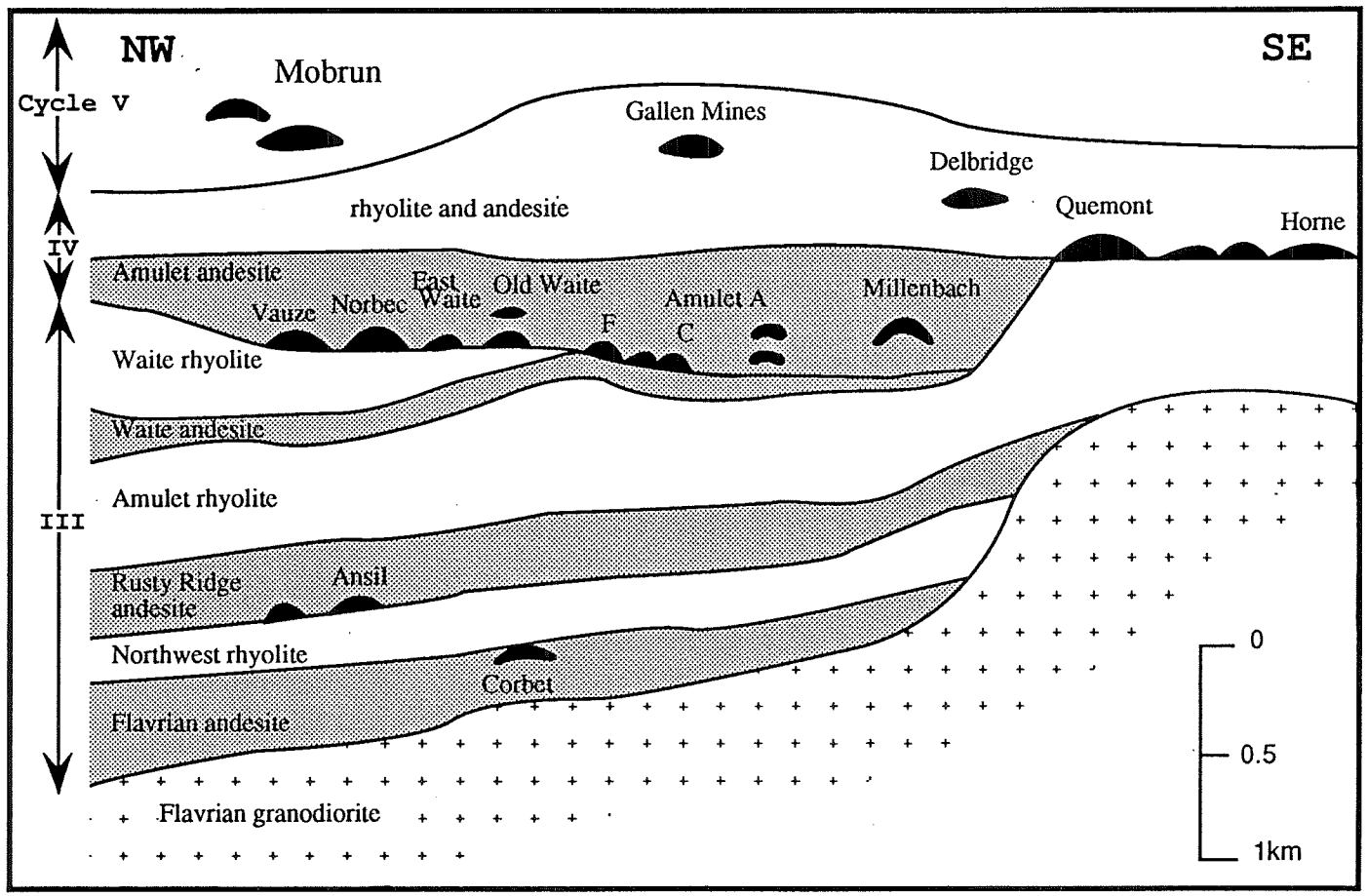

Fig. 2.3 Schematic N-S section showing the stratigraphic position of the Noranda volcanic complex and the stratigraphic locations of its massive sulphide deposits, including Mobrun (modified after Spence and de Rosen-Spence, 1975).

Powell et al., 1993).

2.2 LOCAL GEOLOGY

The Mobrun Cu-Zn-Au massive sulphide deposits are located along the northeast margin of the Noranda area, within felsic volcanic strata of the BRG (Spence, 1967; Spence and de Rosen-Spence, 1975). The BRG in this area consists of pillowed to massive basaltic-andesitic flows together with mafic to felsic volcanoclastic rocks and associated felsic intrusives and sedimentary rocks.

The Mobrun orebodies are hosted by the Reneault and Destor formations (Trudel, 1979)(Fig. 2.4). The Reneault Formation consists of bimodal mafic and felsic calc-alkaline volcanic rocks, and the Destor Formation is composed of mafic to intermediate tholeiitic lavas. Granitoid, pyroxenitic and syenitic intrusive rocks are present in the region, and the Dalembert andesitic tuff is located at the centre of the area. The orebodies are situated approximately 4 km west of the Kewagama metasediments (Figs. 2.2, 2.4).

Two other ore deposits are also reported in the Mobrun region (Trudel, 1979): the North Briar deposit, which is composed of disseminated, mainly pyritic sulphides and located about 1 km southeast of the Mobrun Main Lens; and the Copper Hill deposit which consists of pyrite-chalcopyrite veins associated with quartz veins and located about 2 km southeast of Mobrun.

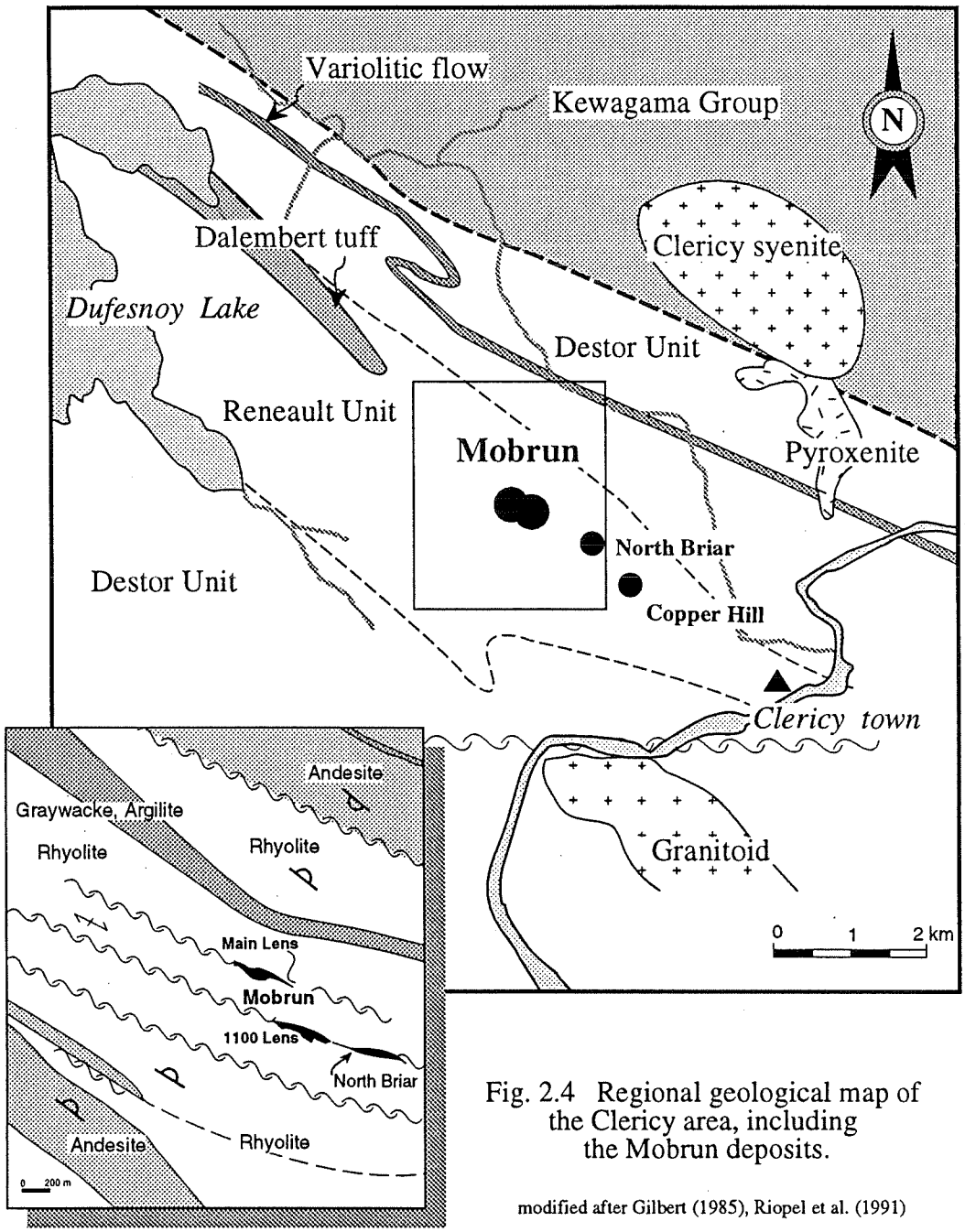

Fig. 2.4 Regional geological map of the Clericy area, including the Mobrun deposits.

modified after Gilbert (1985), Riopel et al. (1991)

Five tectonic zones, all part of the Dufresnoy shear zone, have been recognized in the Mobrun mine district (Riopel et al., 1991) (Fig. 2.4, see insert). They trend northeast and parallel the Main and 1100 Lenses as well as the host rhyolite breccia in the southern portion of the property. Two of these faults transect the Main and 1100 Lenses. The northernmost shear zones coincide with the axial trace of the Clericy syncline (Ambrose, 1941; Trudel, 1979) which is in contact with andesites of the Destor Formation on the south and rhyolites of the Reneault Formation on the north. The fourth shear zone to the south hosts the Copper Hill sulphide zone (Trudel, 1979). The southernmost shear zone crosses a unit of unmineralized rhyolite breccia (Gilbert, 1985).

Close to the mineralized shear zones, the regional schistosity, S_1, of the Mobrun property is oriented parallel to stratigraphy (110°-120°) and is cut by a second schistosity, S_2, striking east-west and dipping steeply to the south (70°). Trudel (1979) reported two late cross-cutting schistosities, S_3 and S_4, oriented 020°-88° and 353°-87°, respectively. They deformed earlier foliations and form small-scale S and Z chevron folds. At the eastern end of the Main Lens, two north/south-trending faults cut the satellite sulphide lenses and merge into a single fault extending south to the western edge of the 1100 Lens, with a dextral offset of at least 100 m. Another north/south-trending fault, probably with the same structural characteristics, cuts the eastern edge of the 1100 Lens (Fig. 2.5).

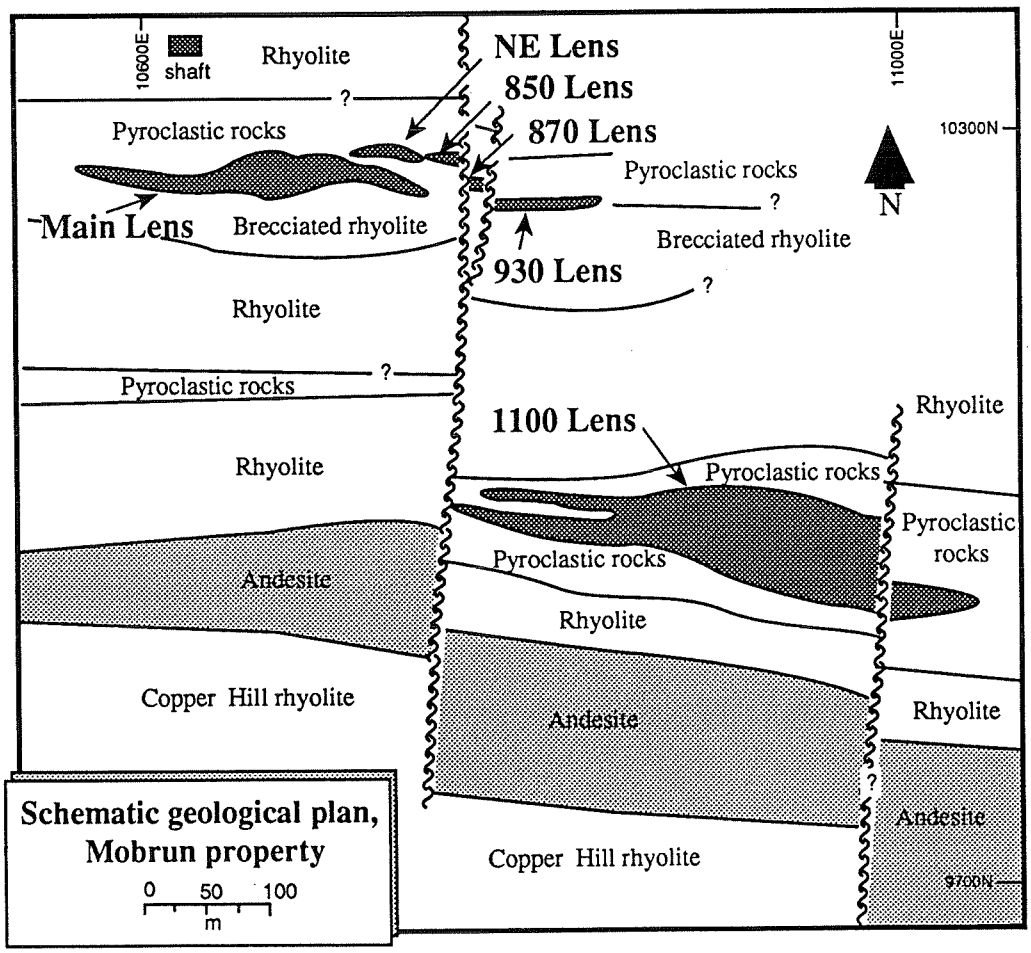

Fig. 2.5 The Mobrun property, with surface projections of the Main Lens, satellite Lenses, and the 1100 Lens. Modified after Caumartin and Caillé (1990).

2.3 STRATIGRAPHY

The stratigraphy of the Mobrun property has been investigated by Gilbert (1985) and Caumartin and Caillé (1990). The strata have a westerly strike and subvertical dip with the tops facing north. The polarity has been determined from graded bedding and from the occurrence of footwall stringer zones on the southern margins of the orebodies (Caumartin and Caillé, 1990). From south to north (i.e., from stratigraphically older to younger), the following sequence is observed (Figs. 2.5 and 2.6).

1) Copper Hill rhyolite: On the Mobrun property, the stratigraphic sequence begins with the Copper Hill rhyolite unit which is strongly altered and sheared, and consists of a series of massive aphyric rhyolite flows interbedded with minor lapilli tuff. The unit hosts the cupriferous Copper Hill stringer-type mineralization (Trudel, 1979; O'Dowd, 1985).

2) Andesitic flows: The Copper Hill rhyolite is overlain by about 90 metres of andesitic flow units which are commonly massive, fine-grained and amygdaloidal. The andesites are chloritized and silicified and contain up to 5% pyrite mineralization.

3) Rhyolitic flows: The andesites are overlain by moderately altered rhyolite flows containing a few quartz and albite phenocrysts and exhibiting a distinctive spherulitic structure.

4) Pyroclastic rocks: This unit is composed of numerous pyroclastic flows and rhyolitic units, with compositions generally ranging from intermediate to felsic. According to LaRocque and Hodgson (1993), the 1100 Lens is underlain by an intermediate lappili tuff, and the lower part of the complex is hosted by flows and tuff.

5) Massive rhyolite: The pyroclastic host rocks of the 1100 Lens are overlain by a 250 m-thick massive rhyolite. The rhyolite is moderately sericitized and consists of a homogeneous aphanitic quartz+feldspar-rich matrix.

6) Brecciated rhyolite: A 10 to 30 m-thick brecciated and hydrothermally altered rhyolite lies directly beneath the Main Lens. It extends more than 600 m east-west along the ore unit.

7) Felsic tuff: Up to 30 metres of felsic ash tuff overlies the massive sulphide bodies of the Main Lens complex. The tuff is variably altered and contains pyrite fragments, especially next to the ore body. The upper contact is marked by a thin graphitic schist.

8) Rhyolite breccia and pyroclastic rocks: Hangingwall tuffs are overlain by up to 15 m of brecciated rhyolite and pyroclastic rocks. This unit exhibits a well-developed schistosity and disseminated sulphides.

9) Second pyritic tuff: This thin (up to 4.5 m thick) tuff is strongly schistose and contains 5 to 10% pyrite in a very fine-grained quartz-sericite-chlorite matrix.

10) Felsic ash tuff: This is a very fine-grained, finely laminated, highly schistose

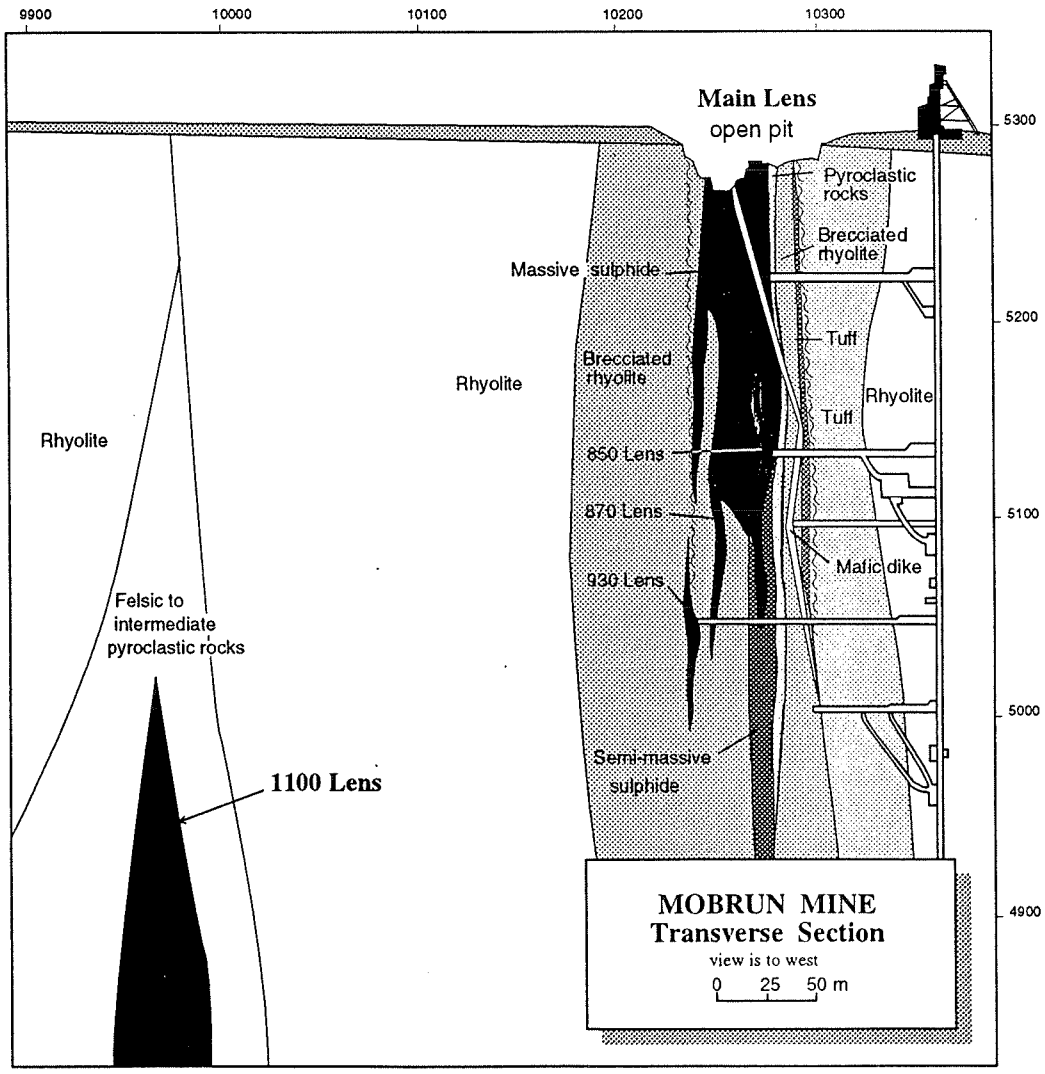

Fig. 2.6 N-S section through the Main Lens and its satellite lenses of massive sulphide mineralization, as well as a projection of the upper portion of the 1100 Lens onto this section. Modified after Caumartin and Caillé (1990).

tuff measuring up to 40 m in thickness.

11) Rhyolitic flows and intercalated tuff: This rhyolite consists mainly of aphanitic quartz and feldspar containing quartz phenocrysts. Interlayered tuffs are relatively coarser grained and chloritized compared to the rhyolitic flows.

12) Dalembert pyroclastics: The felsic flow-tuff unit is overlain by the andesitic Dalembert pyroclastic unit which can be traced laterally for at least 20 km (Tassé et al., 1987).

2.4 MINE GEOLOGY

As stated above, the 1100 deposit is not yet fully accessible and the following description of the mine geology at Mobrun is consequently restricted mainly to the Main Lens and its satellites. Only a cursory description is given of the 1100 Lens.

2.4.1 Main Lens

The Main Lens is subvertical, with a strike of 250 metres and an overall width of about 15 metres (Fig. 2.6). The enclosing volcanic strata strike N290°-300° and dip subvertically with tops facing north. The numerous volcanic rock units of the mine area consist mainly of felsic pyroclastic rocks and lavas, together with lesser amounts of intermediate volcanic rocks and minor mafic lavas (Caumartin and Caillé, 1990)(Fig. 2.6).

The rocks have been metamorphosed to the greenschist facies, and are characterized in the southern (footwall) wallrocks by pervasive sericitization, silicification and weak chloritization. Widespread chloritic alteration zones or pipes, typical of many Noranda-type volcanogenic massive sulphide deposits (Morton and Franklin, 1987), are not present at Mobrun. Alteration in the hangingwall is characterized by moderate sericitization and chloritization, and is generally less pervasive and intense than footwall alteration.

The mine stratigraphy is cut by three intrusive units: (1) an altered massive mafic dike, emplaced subparallel to the volcanic lithologies, cuts the wallrocks and massive sulphide orebodies and shows evidence of deformation at the thin-section scale; (2) a quartz-feldspar porphyry dike which follows the foliation of the sericite schist; and (3) NS-trending porphyry dikes of intermediate composition. Three sets of shear zones have affected the mine stratigraphy (Riopel et al., 1991). The first is a N280°-trending reverse shear zone (northern block thrusted up) with dips varying between 50 to 75° in the hangingwall next to the Main Lens. The second consists of dextral shearing in the footwall rocks south of the mine; the strike is between N90° and N110° and the dip is subvertical. The third system of shearing consists of a combination of two networks: one has a strike of N275°-N95° and is associated with a second network striking N330°-N340°. The sigmoidal-shaped massive sulphide body of the Main Lens is located between these two shear zones. Two NS-trending subvertical splay-fault systems show dextral

displacements of the 870 satellite lens by about 20 m (Riopel et al., 1991)(Fig. 2.5). The tuff overlying the Main Lens has a strong foliation, S_1, oriented between N110° and N229°, parallel to lithological contacts. The crenulation cleavage, S_2, is oriented N40° and N70° in strongly deformed tuffs.

Mineralization in the Main Lens consists chiefly of pyrite (~90%), sphalerite (~5-6%), chalcopyrite (~2%) and minor amounts of magnetite and galena. The sulphide ores are massive to semi-massive, and vary from fine-grained massive, to nodular, to brecciated and fragmental. Colloform and cataclastic textures are observed in many pyrite grains. The highest copper concentrations occur at the base and near the central portion of the Main Lens, and the highest zinc and gold concentrations tend to occur in the eastern and western fringes, on the northern (hangingwall) side of the lens. Silver is more or less correlated with gold in the orebody. The sulphide lens has very sharp vertical contacts with the host rocks.

2.4.2 Satellite Lenses

The Main Lens complex contains four satellite lenses: the North-East, 850, 870, 930 zones. These lenses are described by Caumartin and Caillé (1990) as having originally consisted of a single thin sheet of ore located stratigraphically above and to the east of the Main Lens. The *en echelon* satellite lenses resulted from dextral offsets of about 20 metres each along two north-striking faults (Caumartin and Caillé, 1990)(Fig. 2.5). The satellite lenses have average gold

contents 2 to 3 times higher than those of the Main Lens.

2.4.3 Footwall

About 30 metres of brecciated rhyolite are intercalated with pyroclastic rocks directly beneath the Main Lens. Locally, this footwall unit has sharp contacts with the massive ore zone. The rhyolite is sericitized and includes coarse silicified fragments ranging from 0.1 to 1.0 mm in size and composed of aphanitic quartz and feldspar (Fig. 2.7). Foliation is moderate and grades stratigraphically deeper into the footwall rocks to the south into relatively undeformed and unaltered rhyolite. Fractures and veinlets in the breccia are filled with quartz, calcite, and pyrite. The pyrite is partially recrystallized and occurs as granulated rims and open-space fillings of fractures.

In many cases, pyrite fills conjugate veinlets and joints which have been partially flattened into lozenge-shaped arrays by northeast-southwest compression. In the stringer zone close to the massive sulphide body, where deformation was most intense, these pyrite veinlets are commonly well-organized into orientations subparallel or parallel to the apparent bedding (i.e., subparallel to foliation) of the massive sulphide orebody.

In addition to this syntectonic deformation, the stringer zone underwent intense hydrothermal alteration. Despite the apparent small size of the stringer zone at Mobrun, it is interpreted to have been part of the channelway for exhaling

ore-forming solutions (Caumartin and Caillé, 1990). The feeder zone is intersected by a steeply dipping EW-trending fault plane with accompanying shearing movement.

The ambiguity between footwall sulphides initially deposited parallel to initial exhalative bedding and sulphides possibly brought into orientations subparallel to bedding by pervasive compressive deformation is a major question addressed in this study. Do these sulphide veinlets represent hydrothermal stockwork-type mineralization which has been deformed into subparallel attitudes, or were the veinlets created only during post-ore deformation and thus represent syntectonic sulphide mineralization which was also brought into subparallel positions during progressive deformation?

2.4.4 Hangingwall

A large interval of felsic pyroclastic rocks lies stratigraphically above (to the north of) most of the massive sulphides. The hangingwall/massive sulphide contact is marked by a thin graphitic schist. Massive graphite encloses nodules of pyrite and chalcopyrite in very thin laminae oriented subparallel to planes of foliation. Films of graphite fill grain boundaries within the sericite schist, as well as in the massive sulphide bodies.

Fig. 2.7 Photomicrograph of quartz-plagioclase porphyritic rhyolite. Plagioclase (albite) is mildly sericitized; matrix is quartz, sericite, carbonate and plagioclase. Crossed polars, field of view 2 mm across.

Fig. 2.8 Photomicrograph of discrete crenulation cleavages in the hangingwall rhyolite. Cleavage lamella and rock matrix are composed mainly of sericite and quartz. Crossed polars, field of view 2 mm across.

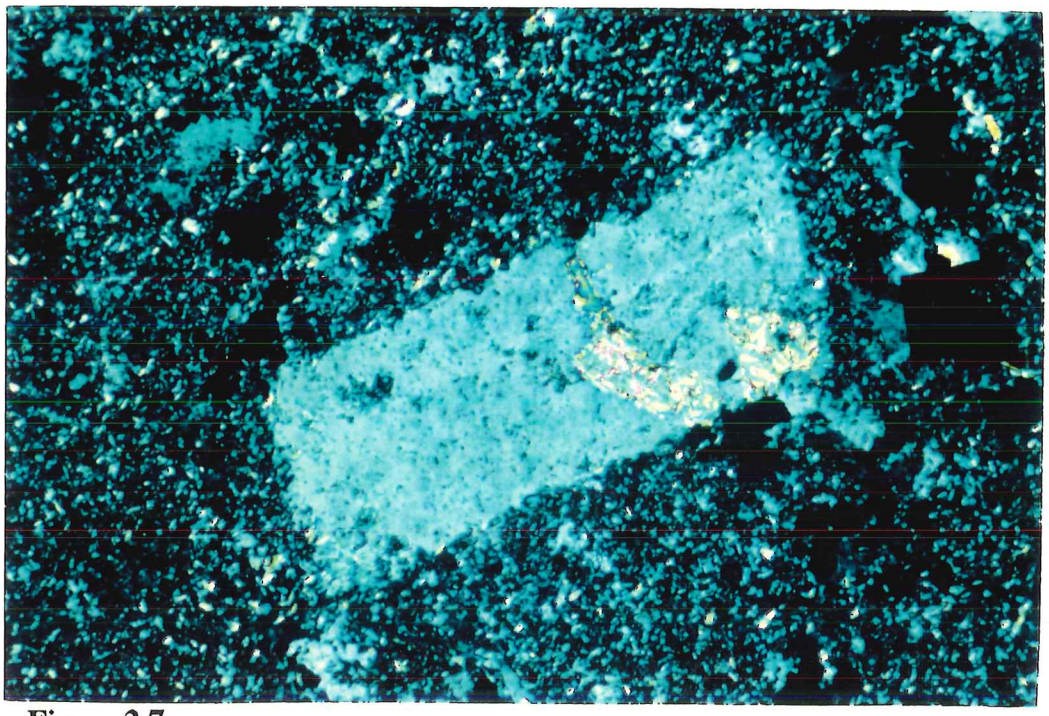

Fig. 2.7

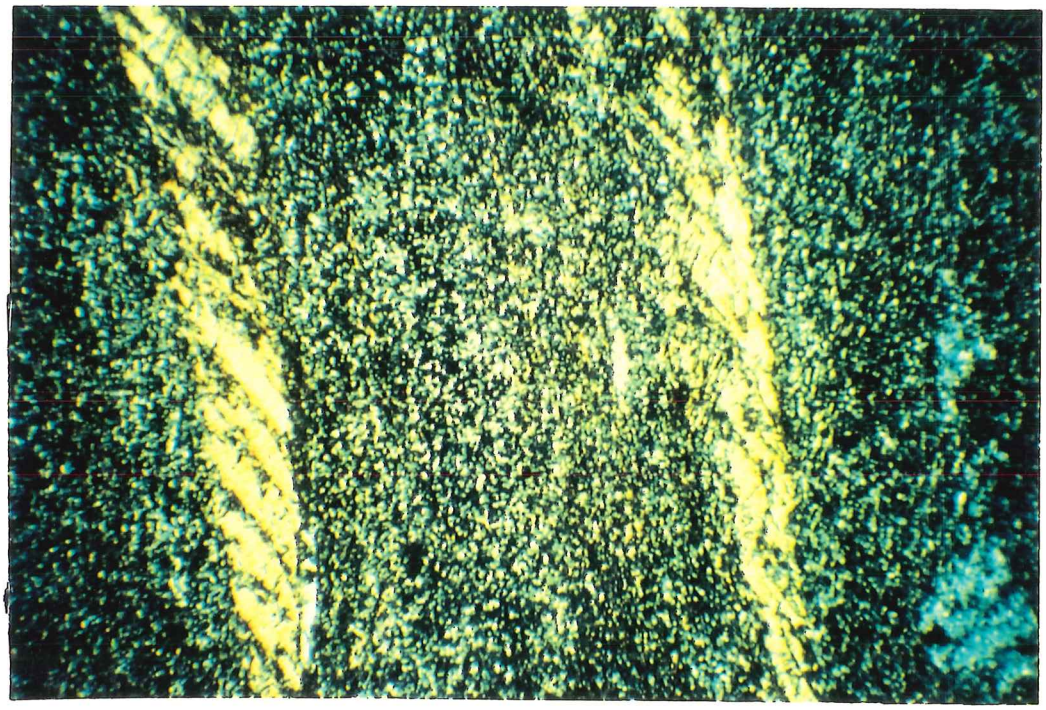

Fig. 2.8

The hangingwall rocks consists of thinly laminated, microcrystalline sericite, quartz and chlorite, together with feldspar and quartz phenocrysts. It is characterized by a discrete crenulation cleavage (Fig. 2.8), and by the occurrence of boudinaged lamellae and/or highly flattened nodules of pyrite along the schistosity. Spherulitic textures consisting of finely fibrous quartz and sericite have been observed within the rocks of the hangingwall (Fig. 2.9).

2.4.5 1100 Lens

The geology of the 1100 Lens complex is known mainly from limited studies of diamond drill core data and a ramp into the upper portions of the ore lens (Barrett et al., 1993; LaRocque and Hodgson, 1993). The 1100 Lens complex, located approximately 250 m southeast of the Main Lens complex, consists of four separate, closely spaced zones: the A, B (1100), C and D Lenses. The orebody extends approximately 300 metres laterally, more than 380 metres vertically and has a maximum thickness of 50 metres. The zinc grades are approximately twice those of the Main Lens, but gold contents are lower (Barrett et al., 1993).

2.5 HYDROTHERMAL ALTERATION

The volcanic host rocks of the Mobrun deposit were strongly altered during synvolcanic hydrothermal activities. Footwall brecciated rhyolite as well as felsic

lapilli tuff in the hangingwall were sericitized, silicified and weakly chloritized.

Although, the Mobrun host rocks have been extensively altered, a strongly chloritized alteration pipe is apparently absent. However, there are areas of intense chloritization (Fig. 10) along parts of the footwall orebody contact and in some areas adjacent to mafic dikes. The apparent absence of an alteration pipe suggests either that the alteration zone was destroyed by distortion during deformation (Caumartin and Caillé, 1990) or that overall hydrothermal discharge generally was broad and relatively unfocused. The latter case has been postulated for Mobrun by LaRocque and Hodgson (1993), calling upon venting into shallow water environments as proposed for Mattabi-type VMS deposits (Morton and Franklin, 1987). Another exceptional alteration feature at Mobrun, comparable to Noranda-type deposits, is the major extent of such alteration in the hangingwall, which may reflect the existence of an unusually large hydrothermal system during post ore formation.

2.6 DEFORMATION-METAMORPHISM

The hydrothermally altered host rocks of the Mobrun mine are invariably schistose along directions subparallel to the orebody. As shown below, these schistose rocks underwent further recrystallization and mass changes during regional metamorphism and tectonism.

Fig. 2.9 Photomicrograph of quartz-sericite spherulites within the hangingwall rhyolite. Crossed polars, field of view 2 mm across.

Fig. 2.10 Photomicrograph of locally intense chloritization in part of the footwall rhyolite. At the bottom, the rock sericitized and carbonitized. Crossed polars, field of view 2 mm across.

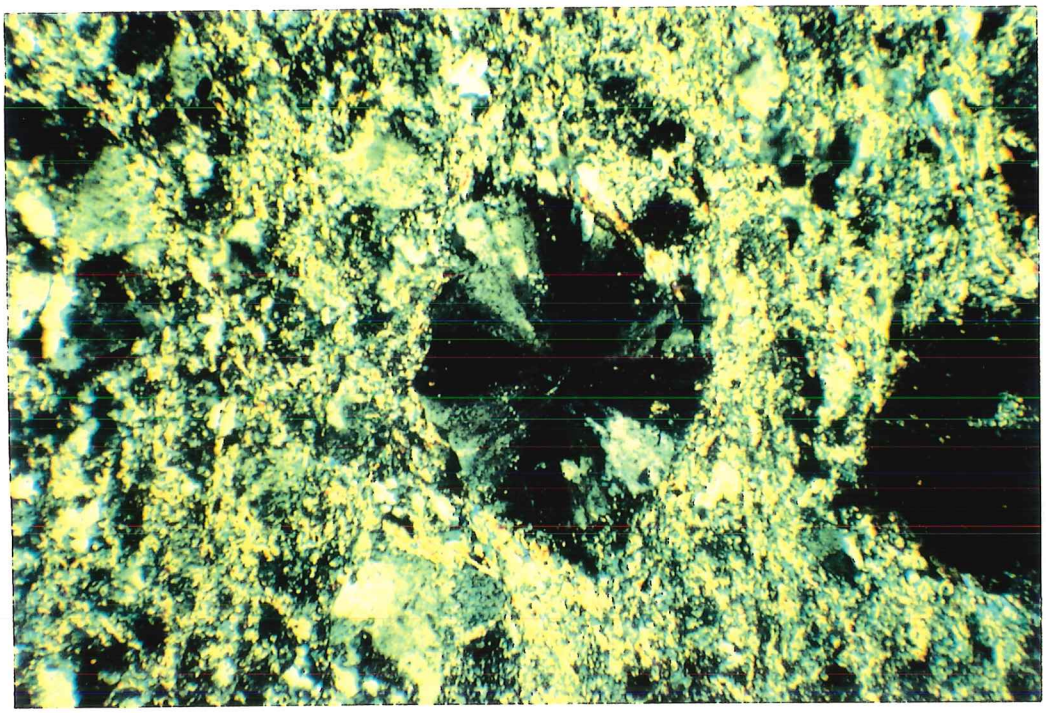

Fig. 2.9

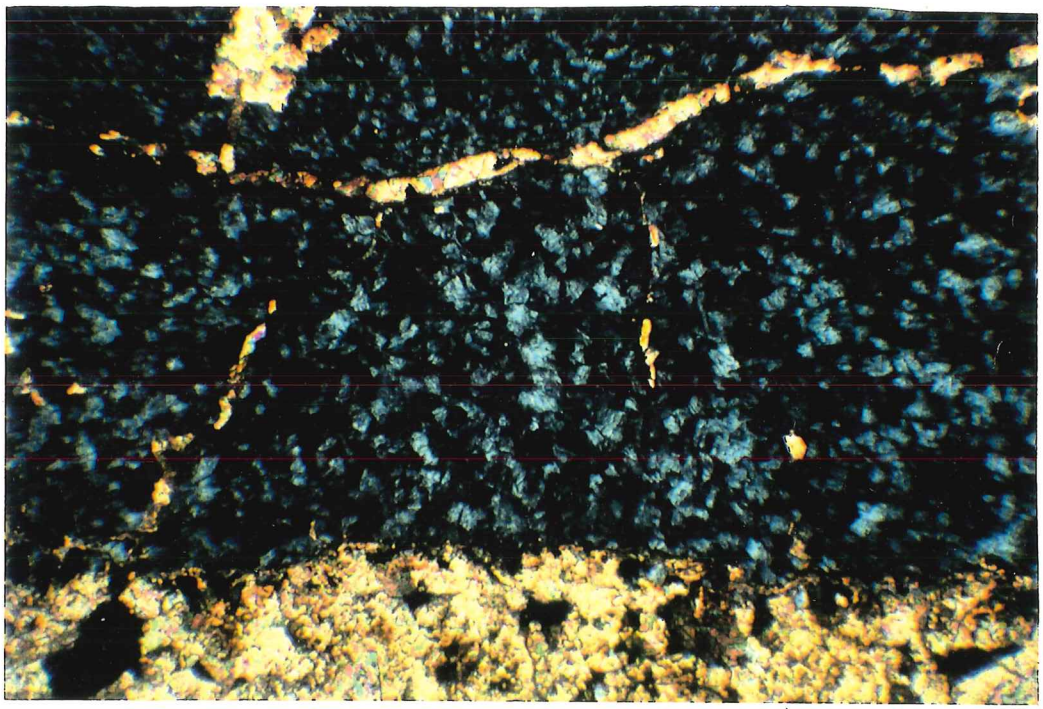

Fig. 2.10

CHAPTER 3

MICROSTRUCTURAL STUDIES

3.1 INTRODUCTION

Based on current models for the formation of volcanic-associated massive sulphide deposits and on the obvious overprint of syntectonic deformation at Mobrun, it can be assumed that the Mobrun deposit underwent episodes of both synvolcanic hydrothermal alteration and syntectonic regional metamorphism-deformation. This chapter focuses on microstructural features and associated mass transfers that occurred in the siliceous host rocks during metamorphism and deformation.

Footwall and hangingwall samples clearly showing microstructural features were chosen for detailed microchemical analyses to establish whether specific chemical changes can be related to these syntectonic processes. Petrographic studies of thin-sections and numerous chemical analyses (X-ray diffraction, X-ray fluorescence spectrometry, electron microprobe and the scanning electron microprobe) were used (1) to identify the microstructural features and the compositions of associated minerals, and (2) to characterize the mineralogical and chemical differentiations associated with the development of schistosity in the wallrocks at Mobrun. To clarify the materials of this chapter and avoid any

misunderstanding of microstructural terms used in this study, Figures 3.1, 3.2, illustrate the terminology used by the author.

3.2 MICROSTRUCTURAL FEATURES

Microstructural observations and chemical analyses of foliation within the Mobrun samples (see below) indicate preferential dissolution of material during syntectonic metamorphism-deformation. These effects were superimposed on rocks which had previously undergone mass transfers during synvolcanic hydrothermal alteration (Fig. 3.1). The preferential dissolution and precipitation of material during metamorphism-deformation are described in the following sections.

3.2.1 Schistosity

Schistosity fabrics in the Mobrun host rocks are thin, sharply defined, planar discontinuities and are somewhat irregularly and heterogeneously distributed. The regional schistosity (S_1) is oriented parallel to stratigraphy and is cut by a second schistosity (S_2) striking east-west and dipping steeply to the south. Where deformation has been intense near the Main Lens, the two schistosities (S_1 and S_2) seem to converge into parallel attitudes. They are oriented in subvertical directions subparallel to the long axes of the orebodies.

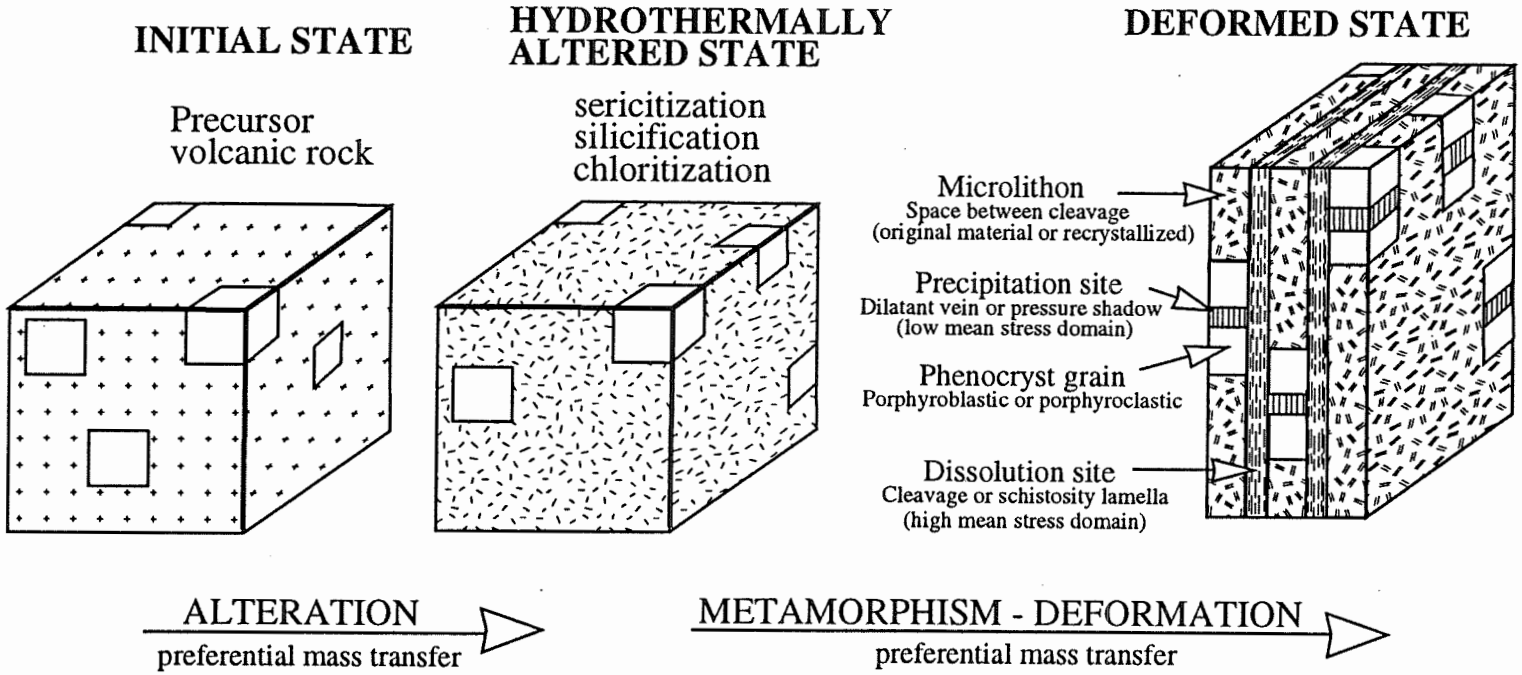

Fig. 3.1 Schematic diagram illustrating the sequence of alteration and deformation events and typical development of microstructural features in the deformed rocks. Note the expression of microstructural terms used in this study. Boxes represent features seen at the thin-section scale.

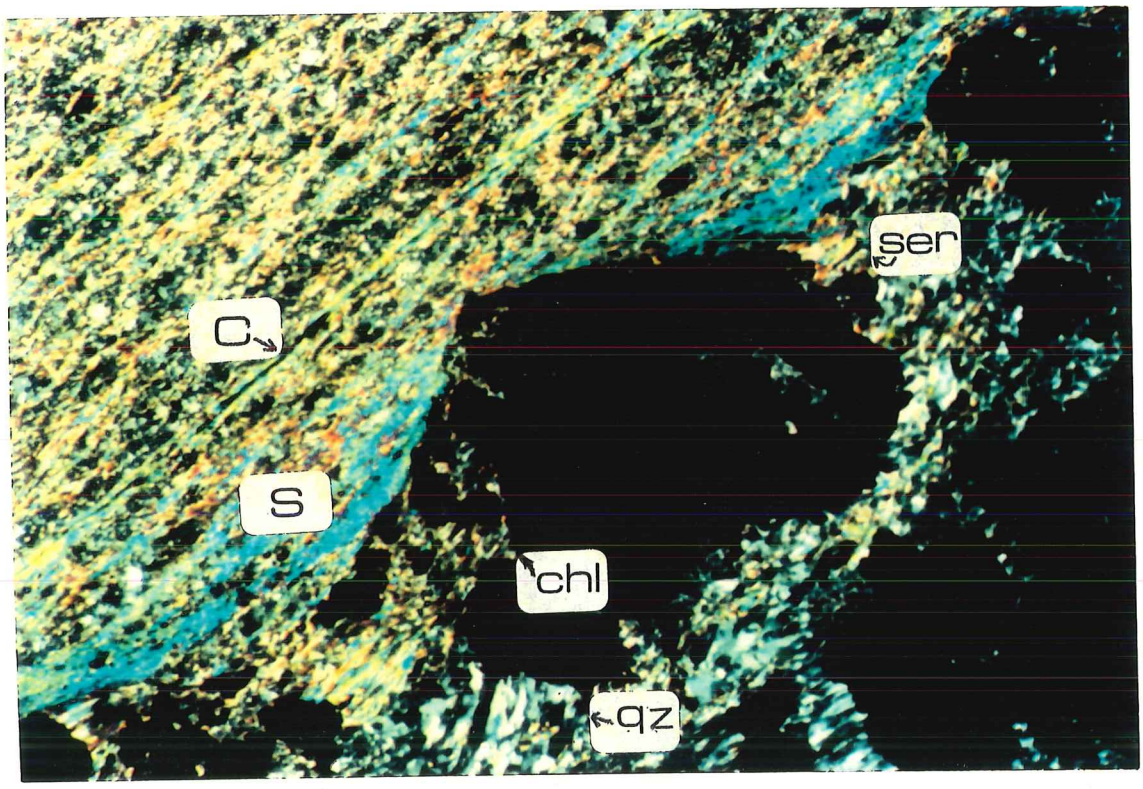

Fig. 3.2 Photomicrograph illustrating a typical schistosity fabric (S) in the silicate hostrocks of the Mobrun deposit following a dissolution process. The photograph also shows a dark through-going cleavage seam (C), oriented subparallel to the schistosity, where an accumulation of insoluble residues suggests a pressure-solution origin. Precipitation domains occurring as pressure shadows adjacent to pyrite grains contain sericite (Ser), chlorite (Chl) and quartz (qz). Crossed polars, field of view 2 mm across.

Close to the orebodies, the rocks are highly schistose, whereas stratigraphically deeper within the footwall units, the wallrocks are relatively undeformed and grade into less altered rhyolite. In the least deformed samples, mica is not organized into laminae sufficiently to produce a good continuous schistosity (Fig. 3.3); the mica laminae may nevertheless show a slight tendency to be clustered. Highly deformed (i.e., schistose) samples consist of sericite schists (Fig. 3.4). The schistosity is represented by a parallel array of sericite and chlorite grains with a very high degree of preferred orientation. Interstitial lenticular quartz grains have a preferred shape orientation, with their long axes parallel to schistosity.

Detailed microstructural studies of schistosity surfaces indicate partial resorption of primary mineral grains, indicating that material has been locally remobilized and concentrated in certain new common minerals such as sericite, and in some cases chlorite, with preferred orientations (Fig. 3.4). Laminae lying parallel to schistosity contain abundant sericite grains up to a few millimetres long, whereas, in the space between these microlithons, the original grain-size is much smaller (<1 mm) and sericite there occurs only as relict shreds within quartz grains (Fig. 3.4; See also Figure 3.1 for an explanation of terms such as "microlithon").

Fig. 3.3 Photomicrograph of typical least-deformed rock at Mobrun, hydrothermally altered with partially altered albite phenocryst. Little layer silicate preferred orientation is apparent. Crossed polars, field of view 2 mm across.

Fig. 3.4 Photomicrograph of typical deformed rock at Mobrun, showing sinus to anastomosing sericite schistosity lamellae. Note the stronger silicate layers and grain-shape preferred orientation of quartz (qz) in spaces between schistosity surfaces. Crossed polars, field of view 1 mm across.

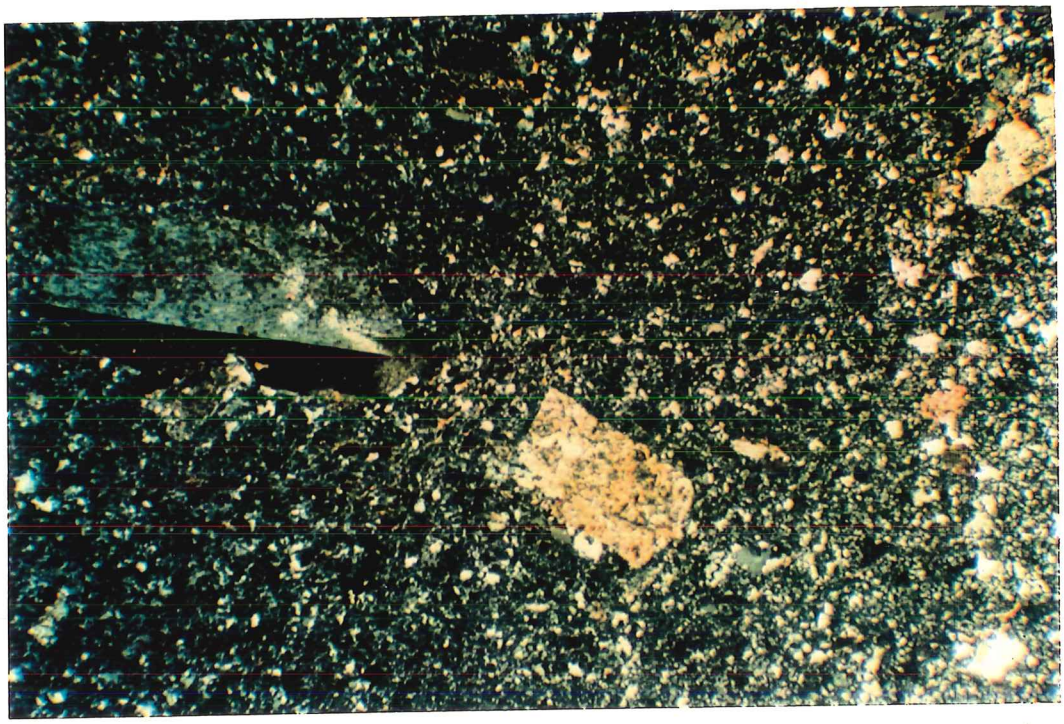

Fig. 3.3

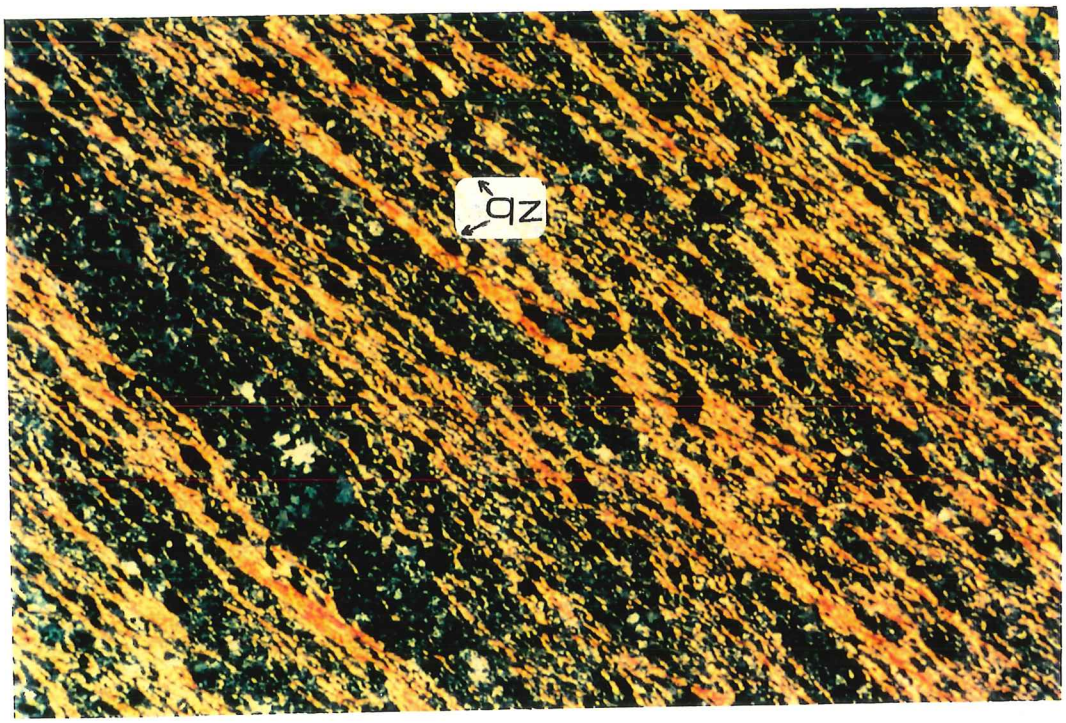

Fig. 3.4

3.2.2 Pressure-solution cleavage

Pressure solution cleavage at Mobrun applies mainly to the solution and removal of quartz; these processes result in the passive concentration of residual phyllosilicates and is largely responsible for the development of solution cleavage. The residual quartz grains are also commonly elongate along the direction of the cleavage, although some quartz grains have more rounded, equant sections, possibility reflecting inherited detrital grain shapes. The microlithon material commonly displays different forms compared to the cleavage surfaces, and has been described as an unfractionated microlithon (Williams, 1972).

Pressure-solution is commonly revealed by such features as insoluble minerals seams, truncated grains, and overgrowth grains (Rutter, 1983). The presence of syntectonic veins also suggests a directed-pressure environment in which pressure-solution must have occurred. Pressure-solution at Mobrun developed where quartz was dissolved along the cleavage surfaces, forming dark seams of insoluble material (e.g., rutile, zircon, sericite and chlorite)(Fig. 3.5a, b and Fig. 3.2).

Silica has migrated by solution and redeposition of quartz in precipitation sites (low-strain domains) such as pressure shadows and in other extensional areas (e.g., in pull-apart spaces between boudins and in crack-seal veins; these structures are explained below in sections 3.2.6, 7; also, see Figure 3.1 for further explanations of the terms used here). Phenocrysts of quartz grains (Fig. 3.6) are

Fig. 3.5a, b Photomicrographs of typical microfabric of pressure-solution cleavages (see arrows). The cleavages have discontinuous, anastomosing traces characterized by thin layers of subparallel dimensionally oriented sericite associated with resistant minerals. Crossed polars, field of view 1 mm across.

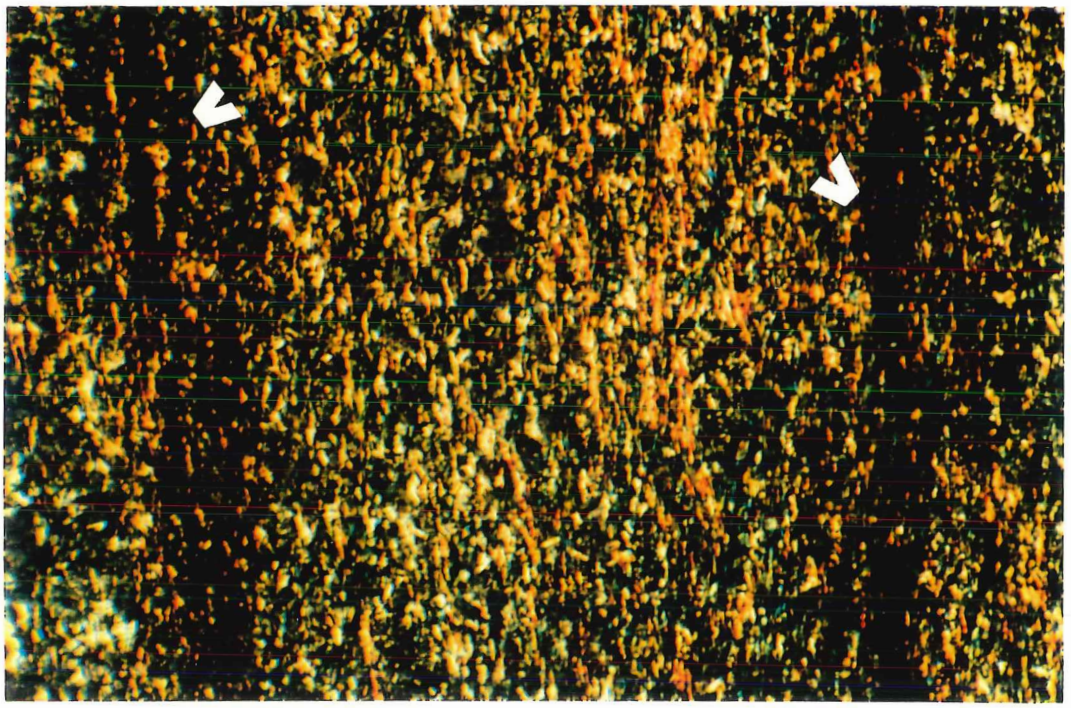

Fig. 3.5a

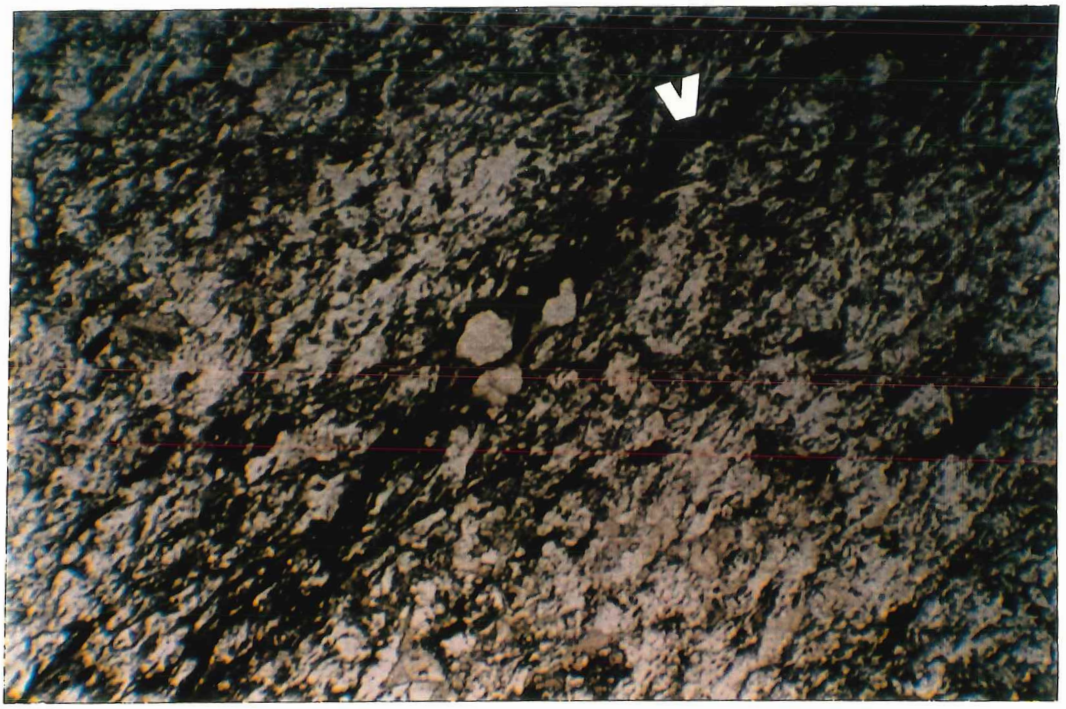

Fig. 3.5b

commonly truncated along the cleavage, providing direct evidence for pressure-solution activity. Pressure-solution cleavage may truncate albite grains (Fig. 3.7) and it may cut through pre-existing quartz veins (Fig. 3.8). The veins are truncated by sutured cleavage surfaces along which insoluble residues are concentrated, also indicating that solution was responsible for the formation of the cleavage.

3.2.3 Differentiation-crenulation cleavage

Some rocks close to the orebody, especially hangingwall units, are characterized by crenulation cleavages. The mica grains in these crenulations were originally oriented parallel to an early (S_1) schistosity, and have been subsequently rotated toward parallelism with the later (S_2) schistosity (Fig. 3.9). Williams (1972b) has suggested that crenulated cleavage formed in this manner is caused by shortening normal to the older cleavage.

The crenulation cleavage at Mobrun is defined by alternating quartz-rich and mica-rich domains (Fig. 3.9). The quartz-rich domains are up to four times wider than their adjacent mica-rich domains which occupy the shorter limbs of asymmetrical microfolds. Insoluble residues (see chemical analyses below), concentrated along dark surfaces oriented subparallel to the axial surfaces of these crenulations, suggest a pressure-solution origin.

Fig. 3.6 Photomicrograph showing pressure-solution cleavage which truncates quartz grains along the cleavage surface. Pressure solution is the process whereby silica diffuses around grain margins from highly stressed areas to less stressed portions (pressure shadow) of adjacent grains. Crossed polars, field of view 1 mm across.

Fig. 3.7 Photomicrograph showing part of an albite crystal (lower right) modified by pressure-solution truncations. Seam of pressure-solution appears as thin and slightly wavy adjacent to truncated albite grain. Crossed polars, field of view is 2 mm across.

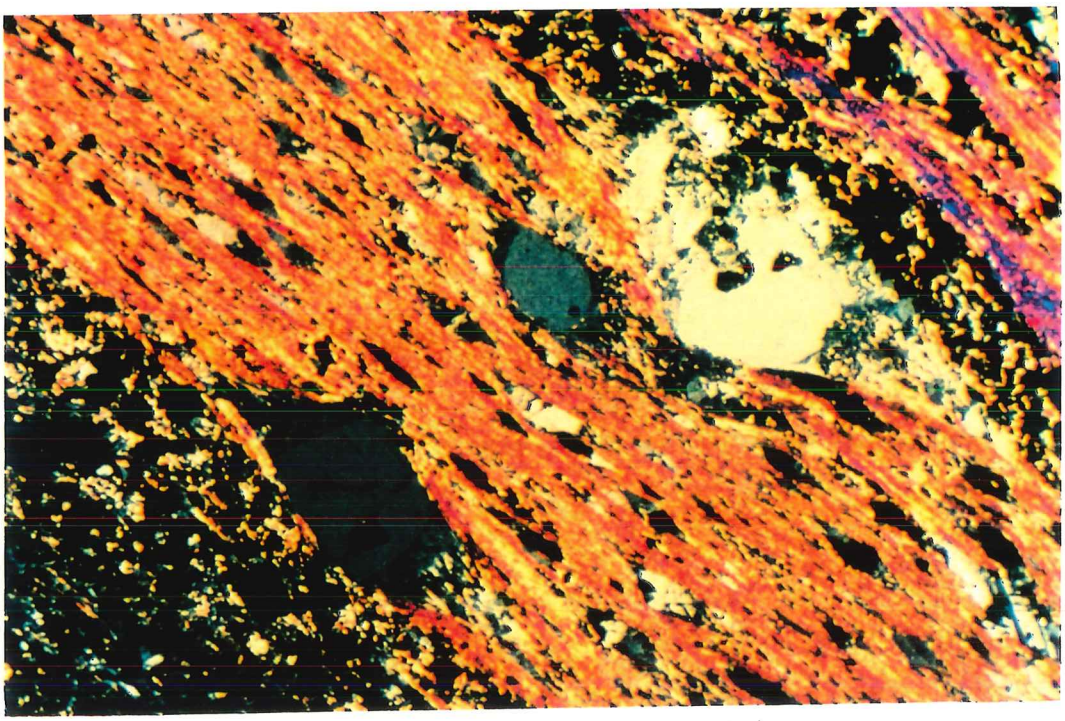

Fig. 3.6

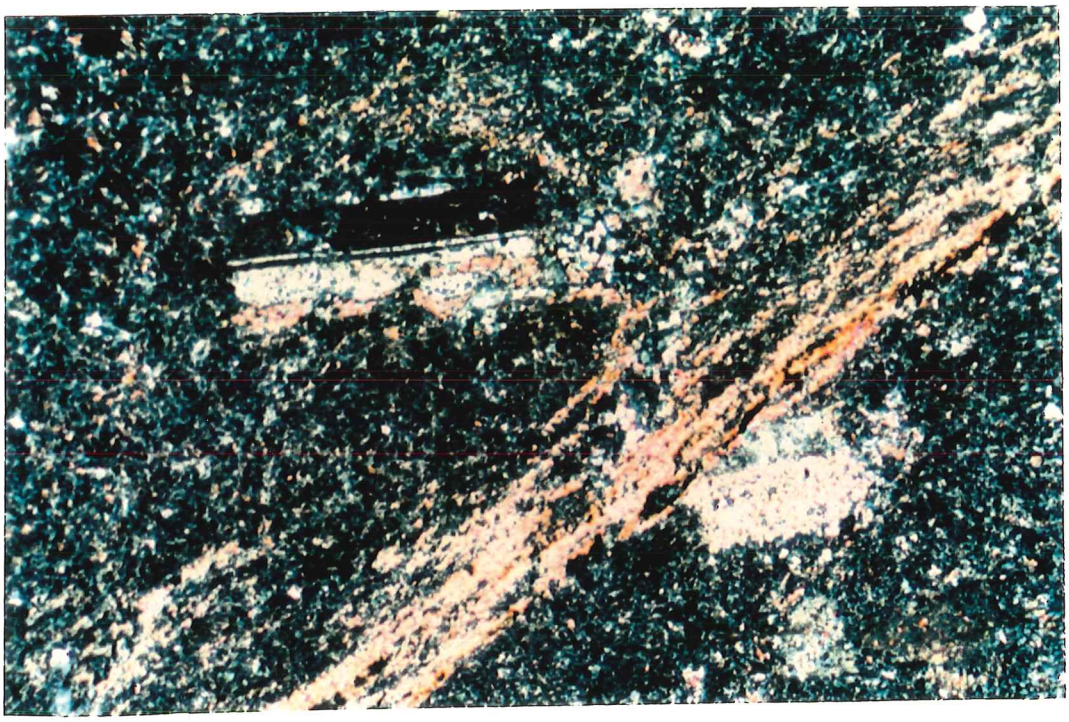

Fig. 3.7

Fig. 3.8 Photomicrograph showing a quartz veinlet (see arrow) truncated by a discrete crenulation cleavage. The vein was probably initially continuous, and deformation was followed by solution removal of parts of the rocks along the discrete crenulation surface in a direction normal to the cleavage. Crossed polars, field of view 2 mm across.

Fig. 3.9 Photomicrograph of schistosity and differentiated crenulation cleavage. The crenulation cleavage contains fine-grained microcrystalline sericite and quartz. Note early (S_1) and later (S_2) schistosity, as well as mica-rich (M) and quartz-rich (Q) domains. Crossed polars, field of view 1 mm across.

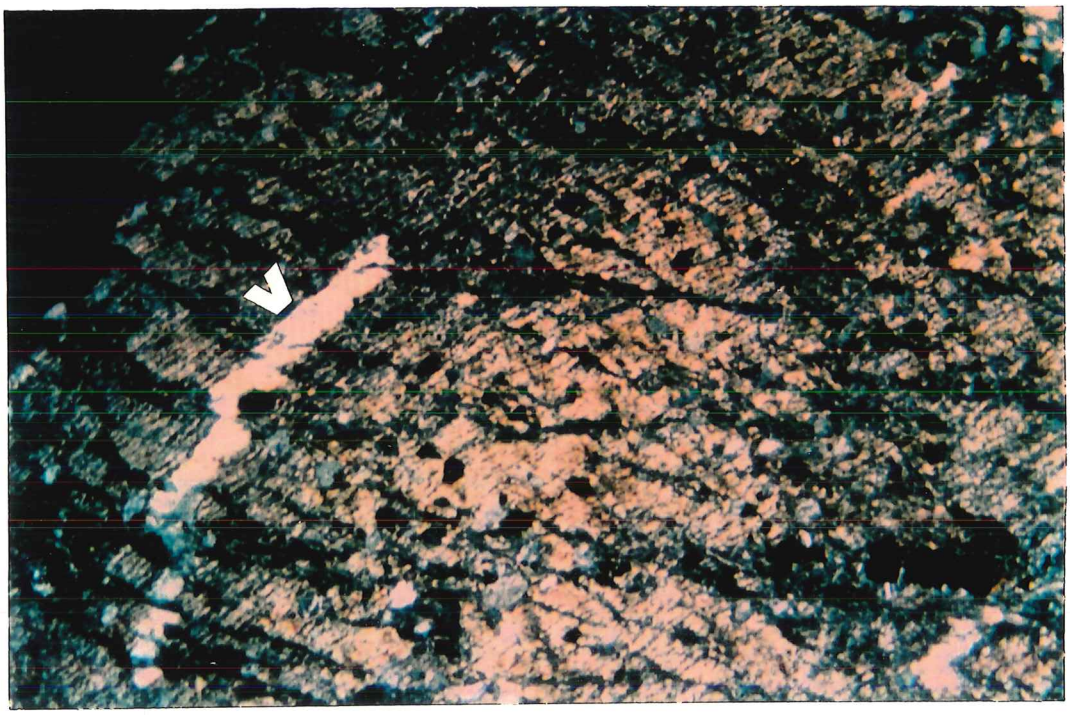

Fig. 3.8

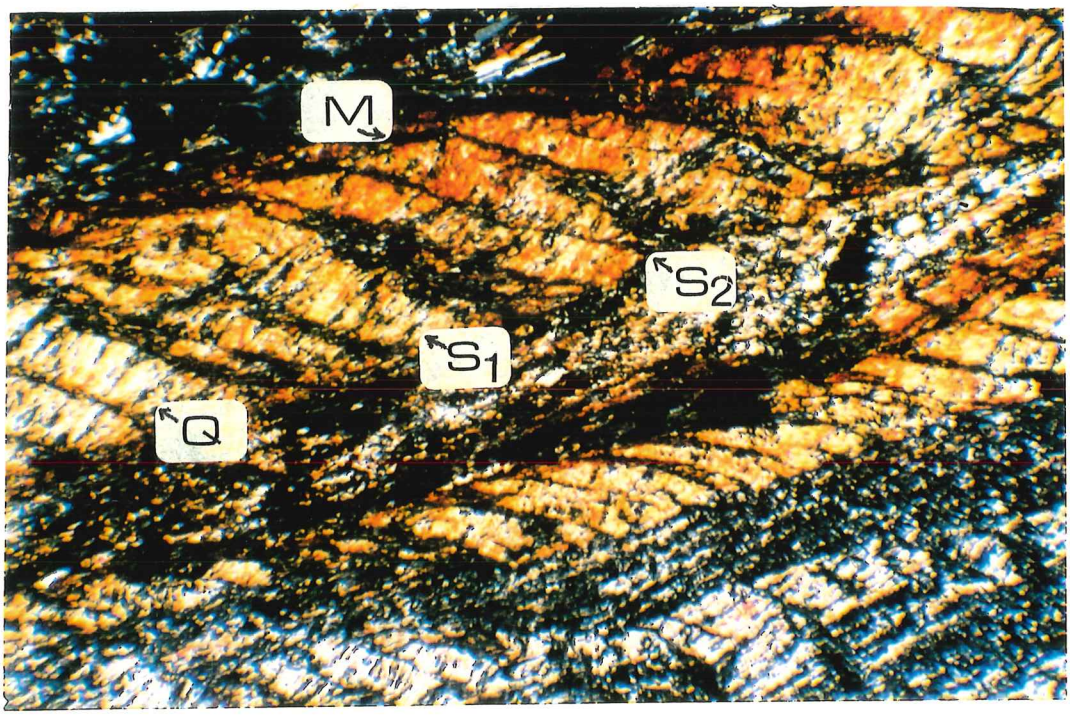

Fig. 3.9

Figure 3.9 shows a highly prominent crenulation cleavage from a sulphide-rich rhyolite in the hangingwall at Mobrun.

3.2.4 Porphyroblastic and porphyroclastic grains

Phenocrysts of minerals such as quartz and feldspar are widespread throughout the rhyolitic host rocks of the Main Lens. Studies of these minerals within their schistose matrices establish the local relative timing between the formation of these minerals and the deformation event. Crystals formed prior or contemporaneous to deformation may be recognized from evidence of mechanical strain, such as extensional fractures and grain disruptions; the absence of strain identifies them as post-tectonic porphyroclasts (Spary, 1969). In addition, porphyroblasts formed prior or contemporaneous to deformation show foliations that are deflected around the crystals without any connections with pre-existing grains (Ferguson and Harte, 1975). Such features are observed in some quartz (Fig. 3.10) and feldspar phenocrysts in the Mobrun wallrocks, and thus, they are considered to be pre- to syntectonic relative to the schistosity formed during the S_1 deformation.

The sharp truncation of schistosity by phenocrysts and the absence of an internal schistosity in those phenocrysts have been accepted by many authors (e.g., Ferguson and Harte, 1975) as evidence for a post-foliation age for such porphyroblasts. Many disseminated euhedral pyrite grains in the footwall and

hangingwall rocks at Mobrun show this lack of internal deformation and deflected foliations. Instead, fibrous grains in the matrix retain their orientations parallel to the main schistosity within the matrix right up to the margins of the pyrite porphyroblasts (Fig. 3.11). However, most of these pyrite grains also have pressure shadows and locally abraded margins produced by deformation. Overall, this evidence indicates syn- to post-tectonic growth of the pyrite porphyroblasts (Ferguson and Harte, 1975).

Some quartz phenocrysts have embayment textures. Embayed phenocrysts suggest rapid growth prior to lava extrusion. The presence of undeformed sericite and fine-grained quartz within these embayments suggest that hydrothermal alteration probably preceded deformation in the surrounding matrix (Fig. 3.12). In deformed rocks, the quartz grains have elliptical shapes elongated along the schistosity and show evidence of dissolution in high-strain areas (Fig. 3.10). Riopel et al., (1991) recognized sigmoidal and S-shaped features in some pyrite and quartz porphyroblasts, suggesting syntectonic growth in these cases (Wilson, 1972).

Albite forms large grains with simple and multiple twinning textures, the whole enclosed by fine-grained mica. In some cases, the albite grains are wrapped around and truncated by a later foliation (Fig. 3.7). Some syn- to post-tectonic albite truncates foliation sharply and shows helicitic structures preserving the first set of foliation as curved lines of tiny opaque grains and quartz (Riopel et al., 1992).

Fig. 3.10 Photomicrograph showing a phenocryst of quartz (porphyroclastic) with foliations deflected around it. Fibrous mica-quartz intergrowth on the end of the quartz phenocryst, where the phenocryst surface is at a high angle to schistosity. Note irregularly development of overgrowth quartz in parts of the syntaxial pressure shadow rim. Crossed polars, field of view 1 mm across.

Fig. 3.11 undeflected schistosity sharply truncated against a pyrite grain, indicating that the pyrite grain overgrew the cleaved matrix. After overgrowth, sericite filled pressure shadows developed on part of the pyrite, indicating syntectonic growth. Crossed polars, field of view 1 mm across.

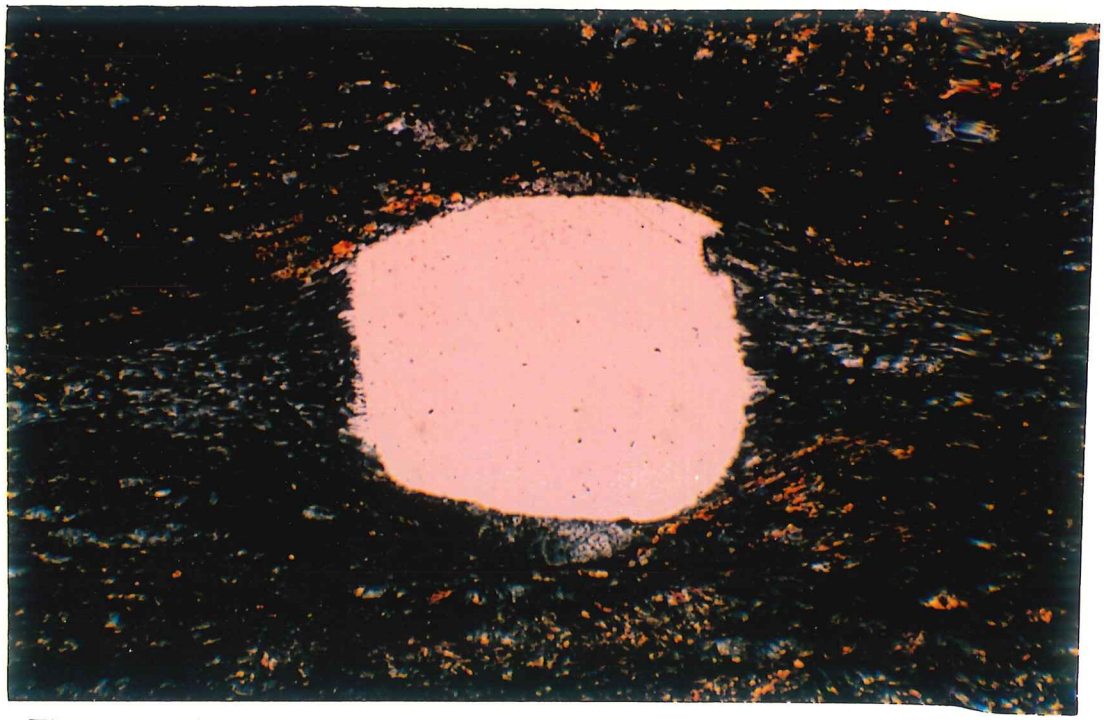

Fig. 3.10

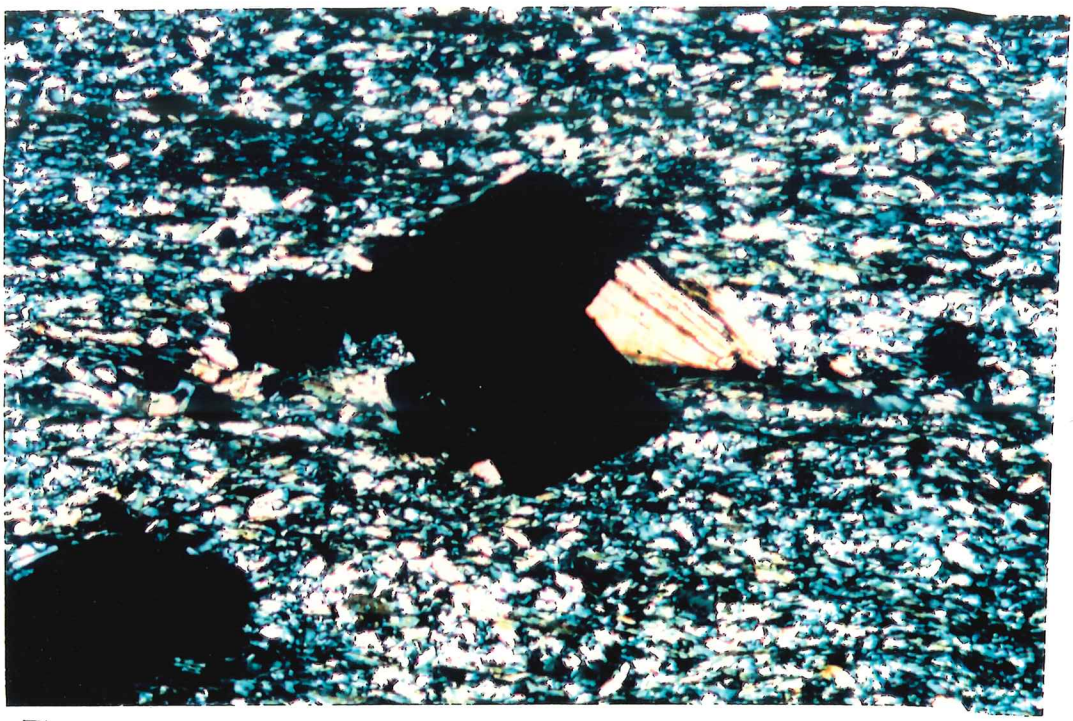

Fig. 3.11

3.2.5 Pressure shadows and pressure fringes

The incremental deformation of heterogeneous rocks containing large crystals more rigid than the matrix may result in the formation of minor textural heterogeneities adjacent to the rigid crystals. These structures are referred to as pressure shadow or pressure fringe effects (Spary, 1969; Williams, 1972).

Pressure shadows typically occur where the foliation wraps around rigid porphyroblasts or porphyroclasts. Their elliptical shapes indicate symmetrical coaxial growth on either side of rigid grains. In pressure fringe, minerals grow preferentially adjacent to a central rigid crystal. The orientation of crystals within the fringe is related to the orientations of the boundaries of the rigid crystal and the foliation in the host rock. Pressure fringes are distinguished from pressure shadows in that the former contain symmetrically oriented mineral growths completely distinct from the rock texture away from the fringes.

Structures of the pressure-shadow type are a common feature of deformed rock at Mobrun, especially around pyrite, quartz and albite grains in foliated rocks. The shadows are composed of quartz, sericite, calcite and minor amounts of chlorite forming distinct entities from those of the adjacent matrix foliation. Figure 3.12 shows a fine-grained unfoliated matrix within the shadow of a quartz phenocryst. Secondary overgrowths of quartz commonly start adjacent to the central quartz grain.

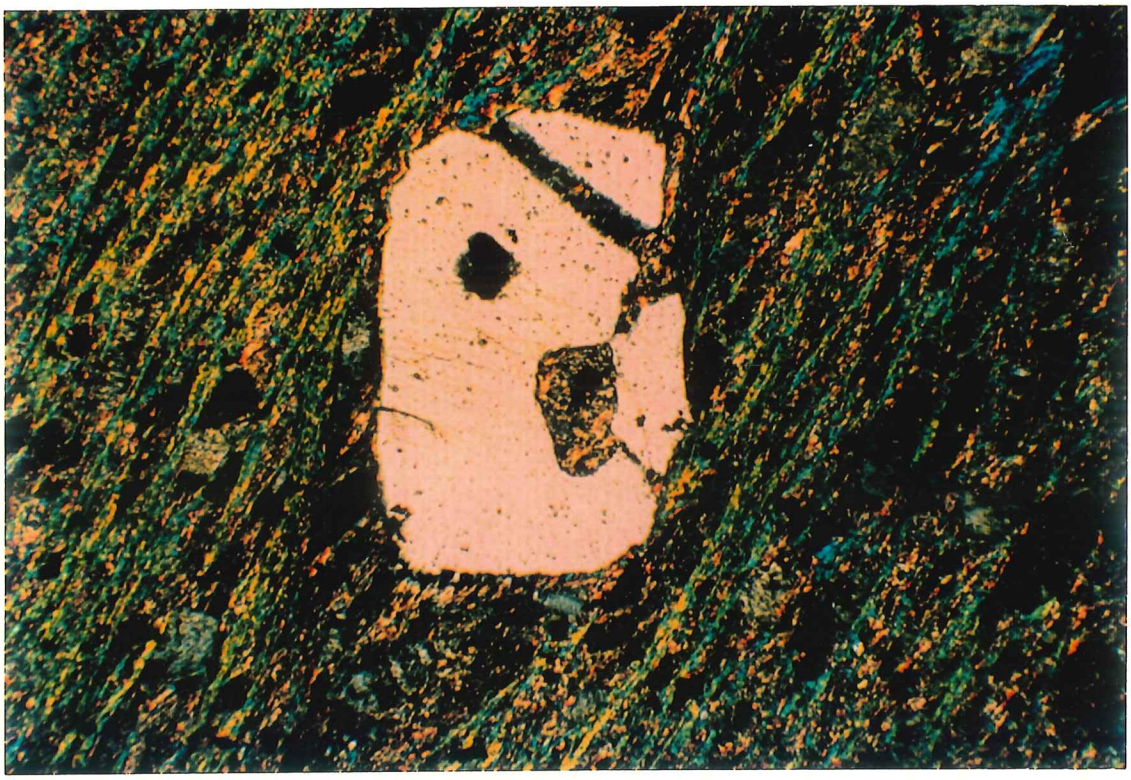

Fig. 3.12 Photomicrograph of an embayed quartz phenocryst. Unfoliated sericite alteration is observed in the embayment. Crossed polars, field of view 1 mm across.

The pressure fringes at the Mobrun mine are generally composed of fibrous quartz, calcite, sericite and chlorite in approximately ellipsoidal regions. The central rigid crystal is generally pyrite, quartz or albite; Figure 3.13 shows euhedral pyrite with quartz and sericite-filled pressure fringes. Disseminated pyrite with elongate overgrowths of quartz are also widespread at Mobrun. In this study, no further significance is attached to the above-mentioned distinctions between pressure shadows and pressure fringes, and hence pressure-fringe features are referred to by the general name "pressure shadows" for the remainder of this report. Both simple and complex internal structures have been observed and many fringes are composed of a number of mineral fibres. Disseminated euhedral pyrite porphyroblasts and porphyroclasts are generally overgrown by or are intergrown with fibrous quartz and phyllosilicates (Figs. 3.13a, b).

The material filling the pressure shadows is necessarily derived from a solution which infiltrated the overgrowth sites and became supersaturated. Contrasting components of solubility and prolonged sealing may have promoted the formation of complex polymineralic shadows with zones of different mineral compositions (Fig. 3.13a). Conversely, the pressure shadow may represent complex intergrowths of minerals without apparent zoning (Fig. 3.13b).

The geometrical forms of fibrous crystals in shadows can be used to determine the orientation of the principal incremental strain and the progressive history of the deformation event. Most of the pressure shadows at the Mobrun

Fig. 3.13 Disseminated euhedral pyrite crystals generally overgrown by pressure fringes of quartz-sericite and minor chlorite. (a) The material filling pressure shadow sites may have promoted the formation of polymetallic fringes with different layers of minerals or (b) may be a complex intergrowth of minerals without apparent zoning. Crossed polars, field of view 1 mm across.

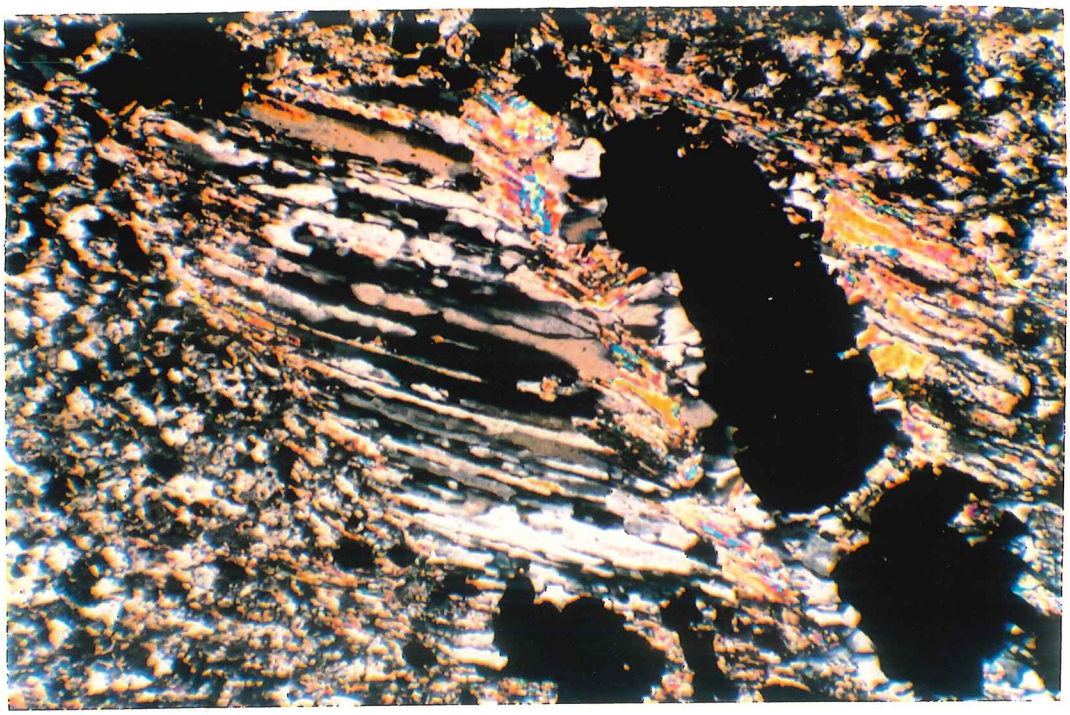

Fig. 3.13a

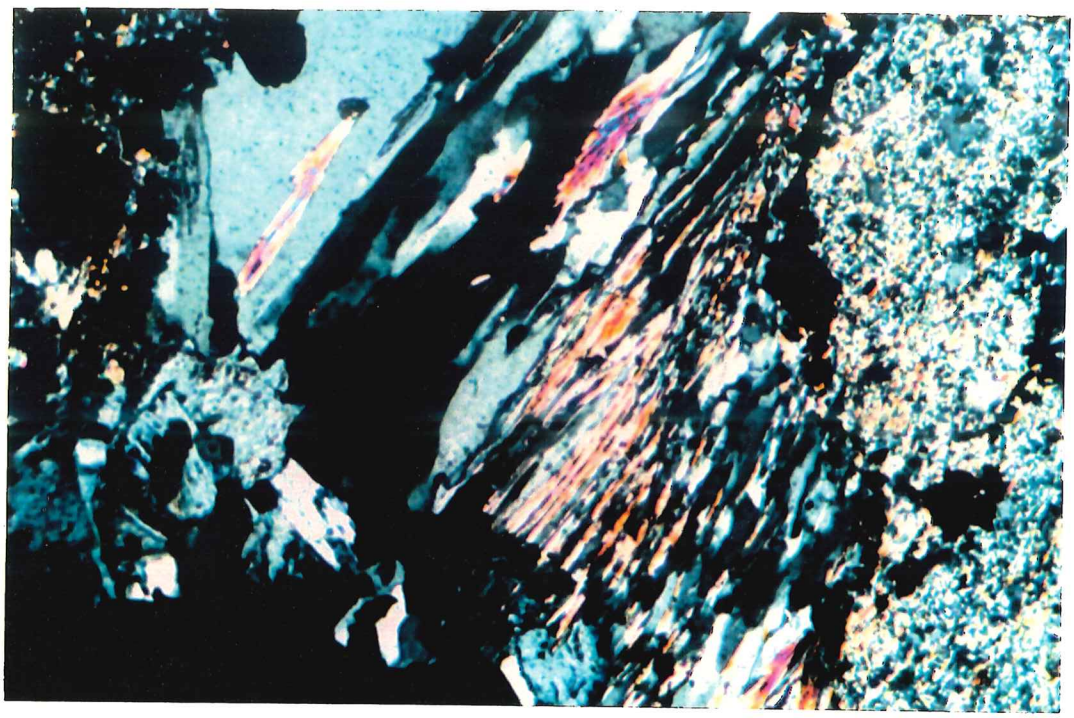

Fig. 3.13b

mine are symmetrical and grew parallel to the foliation direction. This direction is represented by the maximum elongation of fringing minerals and generally lies parallel to the least principal stress (Williams, 1972; Ferguson and Harte, 1975). Both straight and curved axes of fibre growth in pressure shadows are observed in the Mobrun samples. Straight fibres result from non-rotational movements and can be correlated with flattening movements, whereas the formation of curved shadows (Fig. 3.14) shows that the host porphyroblast was rotated as the crystal fibres grew on its surface.

These features at Mobrun may have been caused by the rotation of grains during microshear movements. However, not all curved fibres formed by post-depositional rotation; Spary (1969) argued that the quartz fibres are curved, not because they have been bent, but because the orientations of the older outer portions reflects and retains the early orientation of the porphyroblast whereas the material of later portions next to the porphyroblast reflect growth preferentially perpendicular to the crystal faces of the porphyroblast near the end of its rotation. Some profiles of pressure fringes and shadows are extremely irregular in shape, possibly due to complex strains or to strains repeatedly applied in various directions.

Fig. 3.14 Photomicrograph showing quartz curved-fibres developed in a pressure shadow around pyrite grains. Crossed polars, field of view 1 mm across.

Fig. 3.15 Photomicrograph showing a syntectonic crack-seal pyrite vein. Vein filling developed by repeated increments of microcrack opening followed by deposition of pyrite from a syntectonic solution. Crossed polars, field of view 2 mm across.

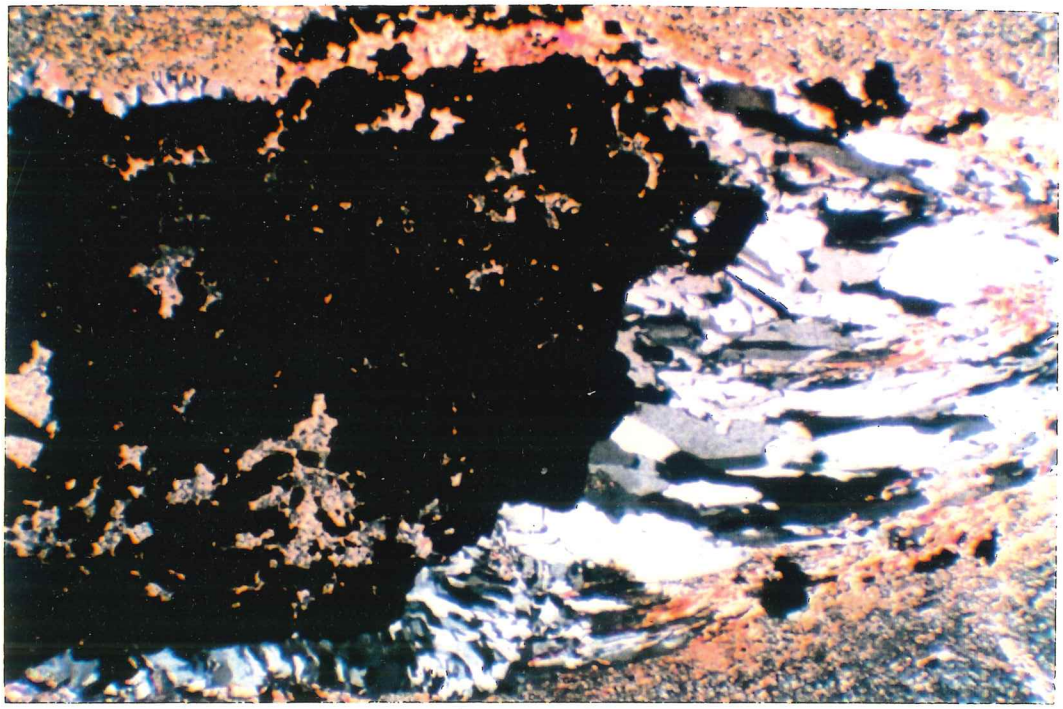

Fig. 3.14

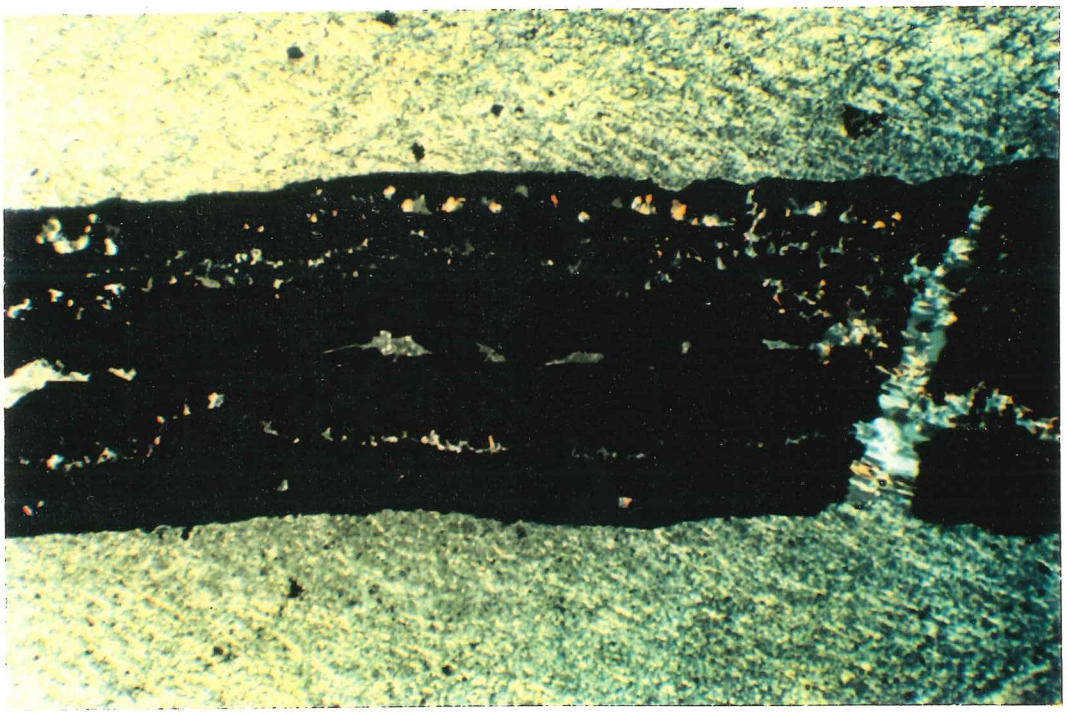

Fig. 3.15

3.2.6 Crack-seal extensional veins

Ramsay (1980) demonstrates that some fibrous vein fillings develop by repeated increments of microfracturing followed by repeated depositions of material from solution. This "crack-seal" deformation (Ramsay, 1980) occurs where the accumulated elastic strain is followed by brittle failure and results in a fibrous syntectonic vein filling (Cox and Etheridge, 1983). The geometry of crack-seal features has been described as a result of stress-induced rock seams and the chemical transfer (pressure-solution) of material into the veins (Ramsay, 1980; De Roo, 1989).

The Mobrun host rocks show evidence of crack-seal features that involved repeated microcracking and sealing by syntaxial overgrowth during deformation-metamorphism events. Fibrous filling minerals are oriented perpendicular to vein walls. Pyrite-filled crack-seal veins are observed in the stringer zone of the Mobrun footwall, particularly between breccia blocks of the footwall rocks (see Fig. 6.35, Chapter 6), as well as in portions of the hangingwall rocks. In acid-etched polished thin sections of these pyrite-filled veinlets, the repeatedly sealed veinlets exhibit open-space filling textures (see the colloform texture of Fig. 6.15, Chapter 6). Some pyritic crack-seal veins are accompanied by thin layers of quartz during the sealing period.

In Figure 3.15 in which a veinlet (0.5 mm wide) of pyrite passes through a quartz-sericite matrix, the two sides of the fracture have sharp contacts with the

silicate wallrock material and the veinlet was built up by repetitions of the crack-seal process. Cracks occur repeatedly along previous vein-wallrock contacts because overall this is the mechanically weakest surface in the rock (Ramsay, 1980). Small amounts of wallrock material are commonly detached and incorporated in the vein fillings during each crack-seal event.

The quartz-calcite type of crack-seal veins are observed in least deformed rocks (Figs. 3.16a,b). Some of these vein fillings are monomineralic, containing only calcite or quartz (Fig. 16a). Multiphase crack-seal veins consist of fibrous layers of quartz and calcite. Although, successive fillings of new quartz or calcite are generally in optical continuity with former grains, in some cases, a misfit of new grains, fragment of broken wall, or minute inclusions within minerals highlight the crack-seal boundaries (Fig. 3.16b). The mineral components in these crack-seal veins are generally similar to the composition of the vein walls, but they are probably also influenced by the compositions of the fluids circulating into the cracks.

Various generations of simple extensional veins filled mainly with quartz and/or calcite are observed at Mobrun. A particularly striking aspect of this vein material is its fibrous crystal morphology. The geometry of these veins may have changed with the displacement that took place across the fractures. For example, at the thin-section scale (see Figure 3.17), the latest vein of the two intersecting veins, runs horizontally across the section and shows well-developed fibrous

Fig. 3.16 (a) Multiphase crack-seal veins containing quartz and calcite. (b) successive filling by calcite within crack seal veins. Note different sealing periods. Centre of veins is filled with quartz. Crossed polars, field of view 1 mm across.

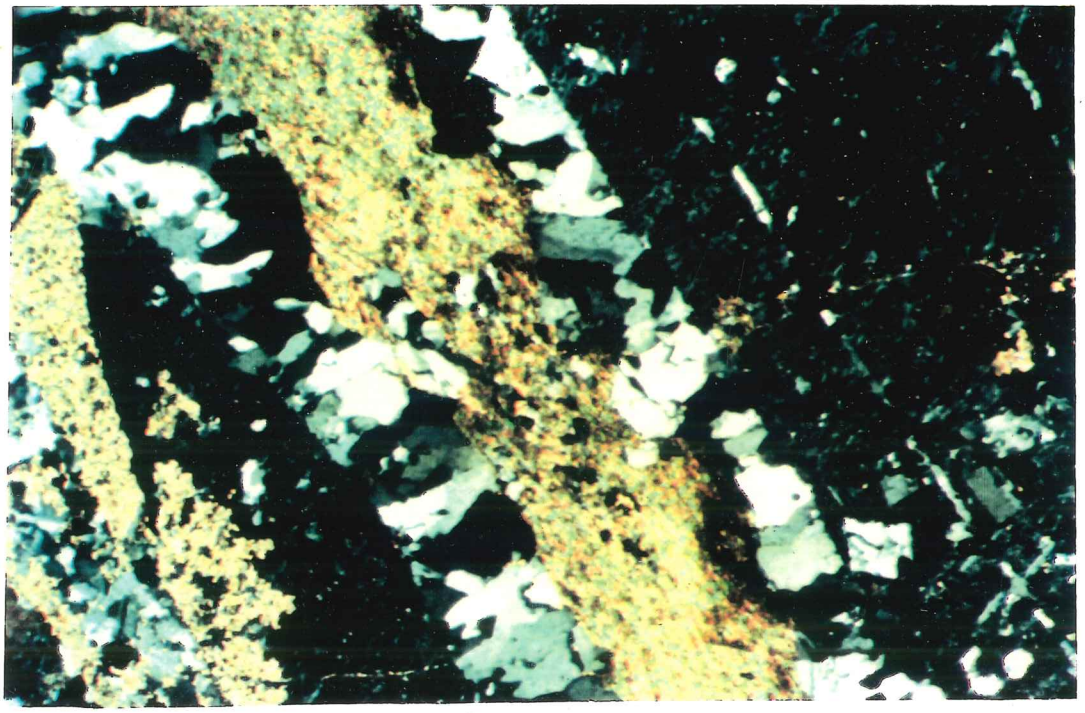

Fig. 3.16a

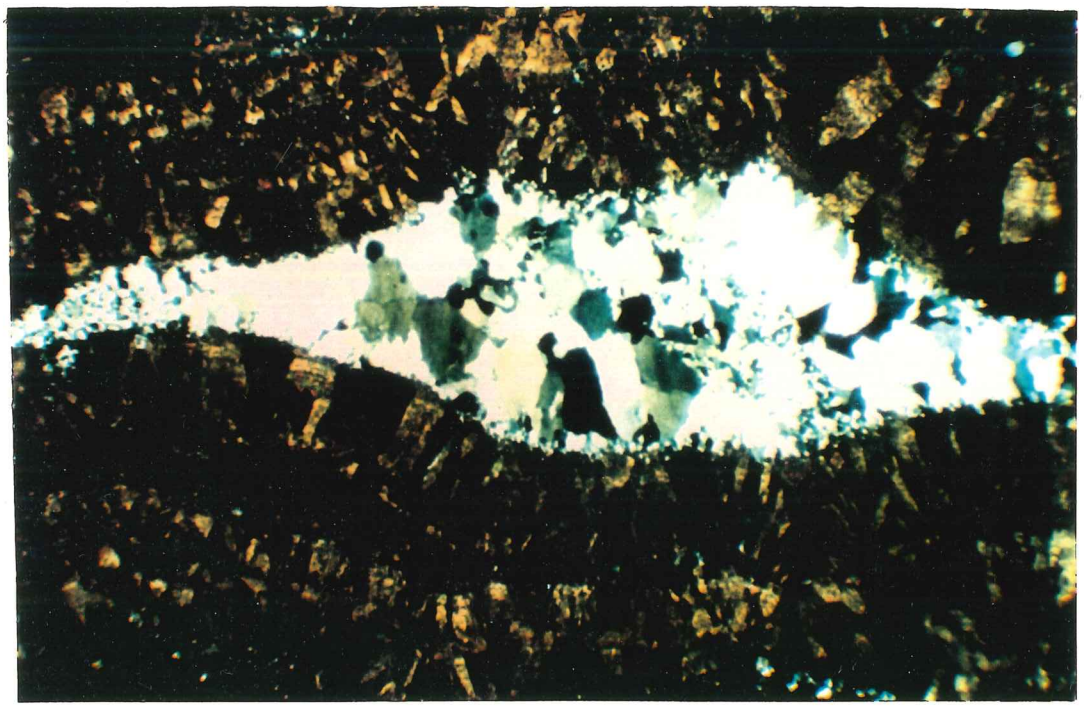

Fig. 3.16b

crystals of quartz. The dilation that took place during the formation of this late vein can be inferred from the mismatched relationships of the early formed veins. In this case, the late veins give the displacement vector across the earlier vein.

3.2.7 Pull-aparts and Boudins

Tensional microfracture features, pull-aparts and micro-boudins are observed in some quartz, feldspar and pyrite grains. The opening of these microfractures resulted in local elongations subparallel to the direction of extension (approximately vertical at the Mobrun mine). Boudins apparently forms by differential extension along foliation. The foliation around a microfracture is pinched in toward the resulting void such that structures resembling boudins are formed. The microfractures are filled later by fibrous syntaxial overgrowths composed of layered silicates, quartz and carbonate on the host grains. Figure 3.18 shows a pull-apart fracture in a quartz phenocryst, with a filling of secondary quartz overgrowths. Boudinage structures consisting of a pulled-apart albite grain filled with quartz and carbonate are shown in Figure 3.19. In general. these microstructures are filled by a syntaxial overgrowth of fibrous layered silicates, quartz and/or carbonate.

Fig. 3.17 Photomicrograph showing various generations of extensional veins. The late quartz vein runs horizontally across the section and gives the displacement vector across the earlier vein (running horizontally). Crossed polars, field of view 2 mm across.

Fig. 3.18 Tension microfracture (pull-apart) in a quartz phenocryst. The opening of these microfractures has resulted in local elongation subparallel to the extension direction which is roughly vertical. The microcrack opening has been followed by the sealing by fibrous quartz. Crossed polars, field of view 1 mm across.

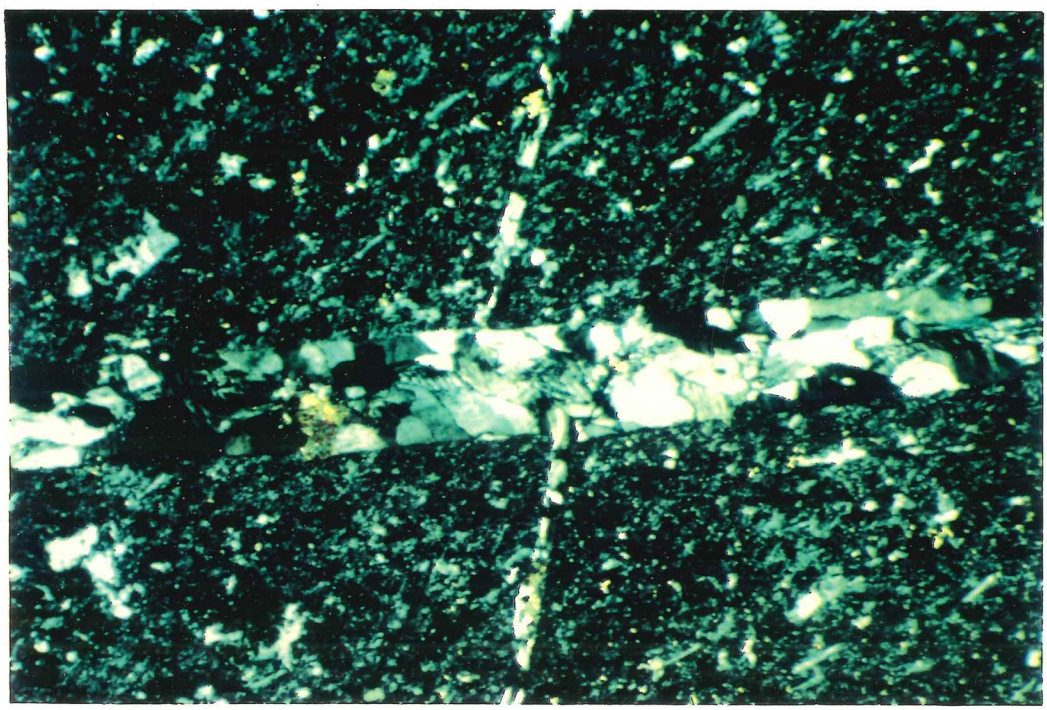

Fig. 3.17

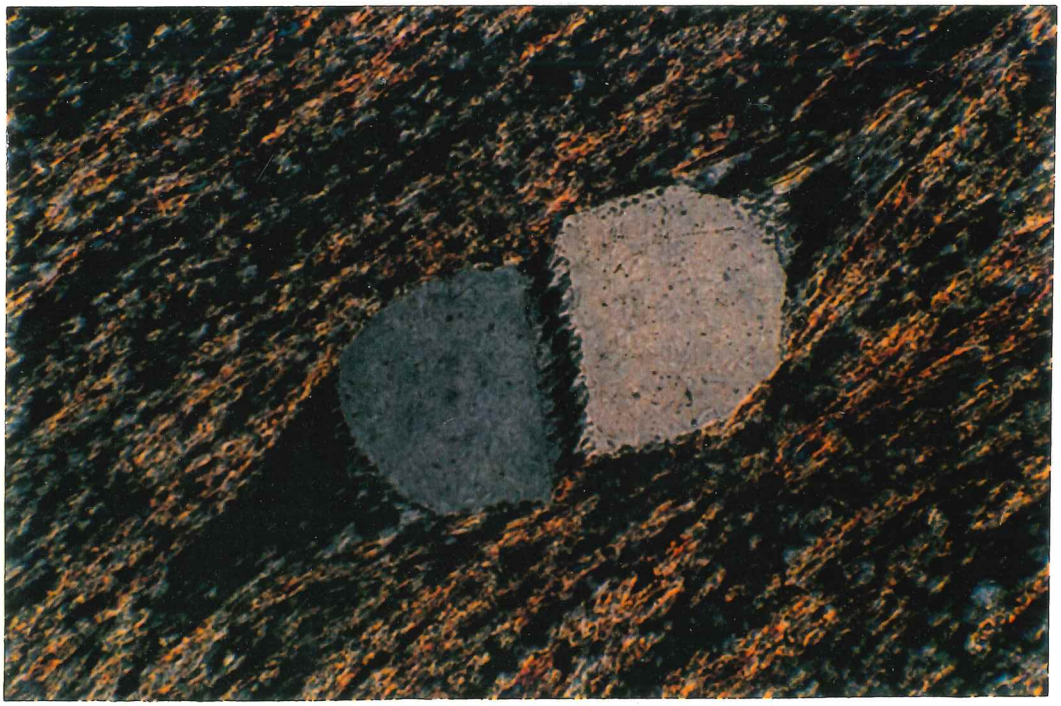

Fig. 3.18

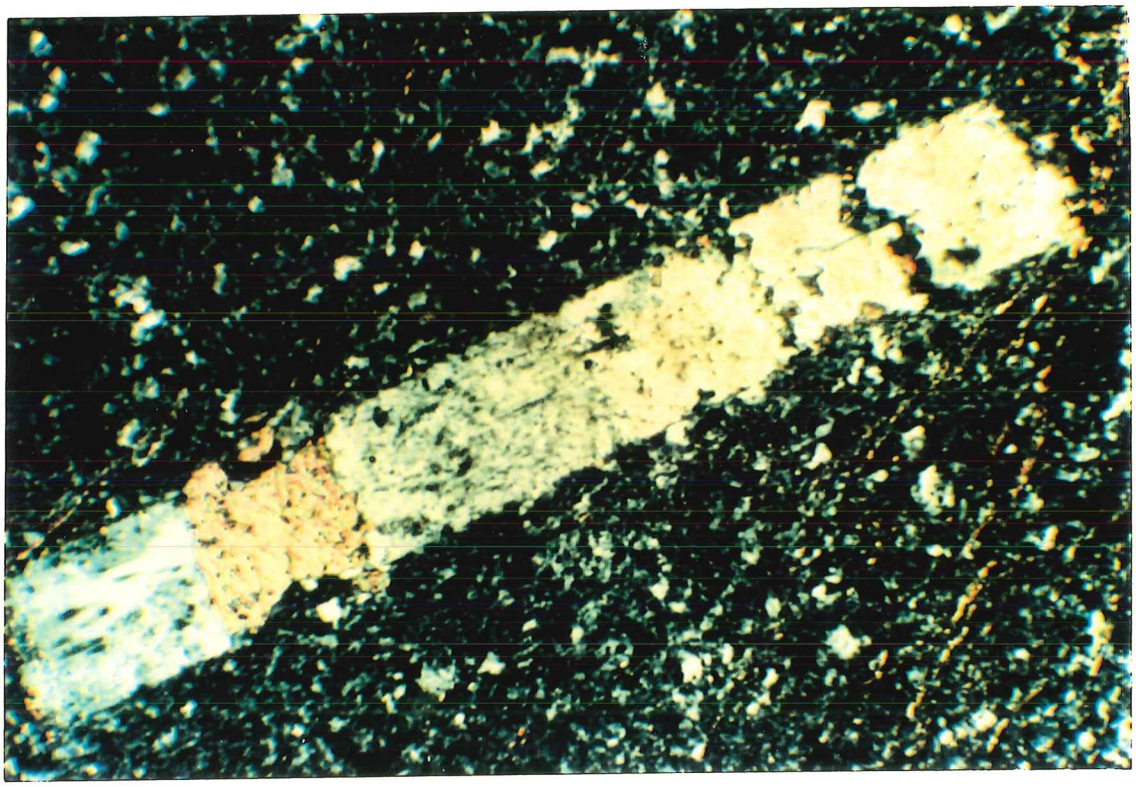

Fig. 3.19 Boudinage structure in albite filled by carbonate and quartz. Crossed polars, field of view 1 mm across.

3.2.8 Significance of microstructural features

The remarkable geometry of all of the above microstructural features provides a number of keys to the understanding of deformation at Mobrun. In general, during metamorphism-deformation, minerals dissolve from dissolution sites in schistosity surfaces (high-strain domains) and precipitate in dilatant veins and pressure shadows sites (low-strain domains), (Fig. 3.1).

Mass transfers during metamorphism-deformation have been detected during different stages, as evidenced: (1) by crack-seal pyrite-quartz vein microstructures, indicating repetitions of host-rock failure and vein-filling, (2) by zones of quartz and mica in pressure shadows, indicating mineralogical dissolution at various stages of deformation, and (3) by remobilization, essentially around pyritic aggregates and silicate phenocrysts, where mass transfers led to addition to pressure shadows around pyrite and in tension veins.

Successive structural veins indicate that progressive incremental cracking in the rock matrix was followed by sealing of the crack walls by crystalline material precipitated from a fluid phase. Microcracks were filled with fluids containing components which were closely related chemically to the components forming the main body of the rock, and which were probably derived by local chemical solution and transfer of materials. Therefore, the abundance of minerals and the analyses of specific composition of minerals in different microstructural sites (see Knipe, 1979; Gray, 1978) of Mobrun may provide information on the

chemical development of the deposit during the metamorphism-deformation event.

Note: In the next sections, the mineralogical and chemical comparisons have been made as follows:

1) Bulk chemical analyses between undeformed (least-schistosed) and deformed (highly schistose) rocks (Section 3.3),

2) Microstructural chemical analyses of different microstructural sites of cleavage (pressure-solution cleavage) and associated features, such as pressure shadow, pull-aparts, etc., (Section 3.4).

3.3 CHEMISTRY OF SCHISTOSITY - EVIDENCE FOR THE PREFERENTIAL DISSOLUTION OF MATERIALS

3.3.1 Mineralogical differentiation

X-ray diffractometry was used in an attempt to describe the mineralogical differentiation associated with schistosity at Mobrun. Portions of highly schistose domains (giving schistosity-lamellae compositions) and non-schistose domains (giving microlithon compositions) of rock were selected for analysis. Peak heights on diffractometer traces provide a semi-quantitative estimate of the relative proportions of mineral components present. The diffractometry shows that schistose domains have a distinctive mineralogy similar to the microlithon mineralogy (Fig. 3.20). The mineralogy consists essentially of quartz and sericite.

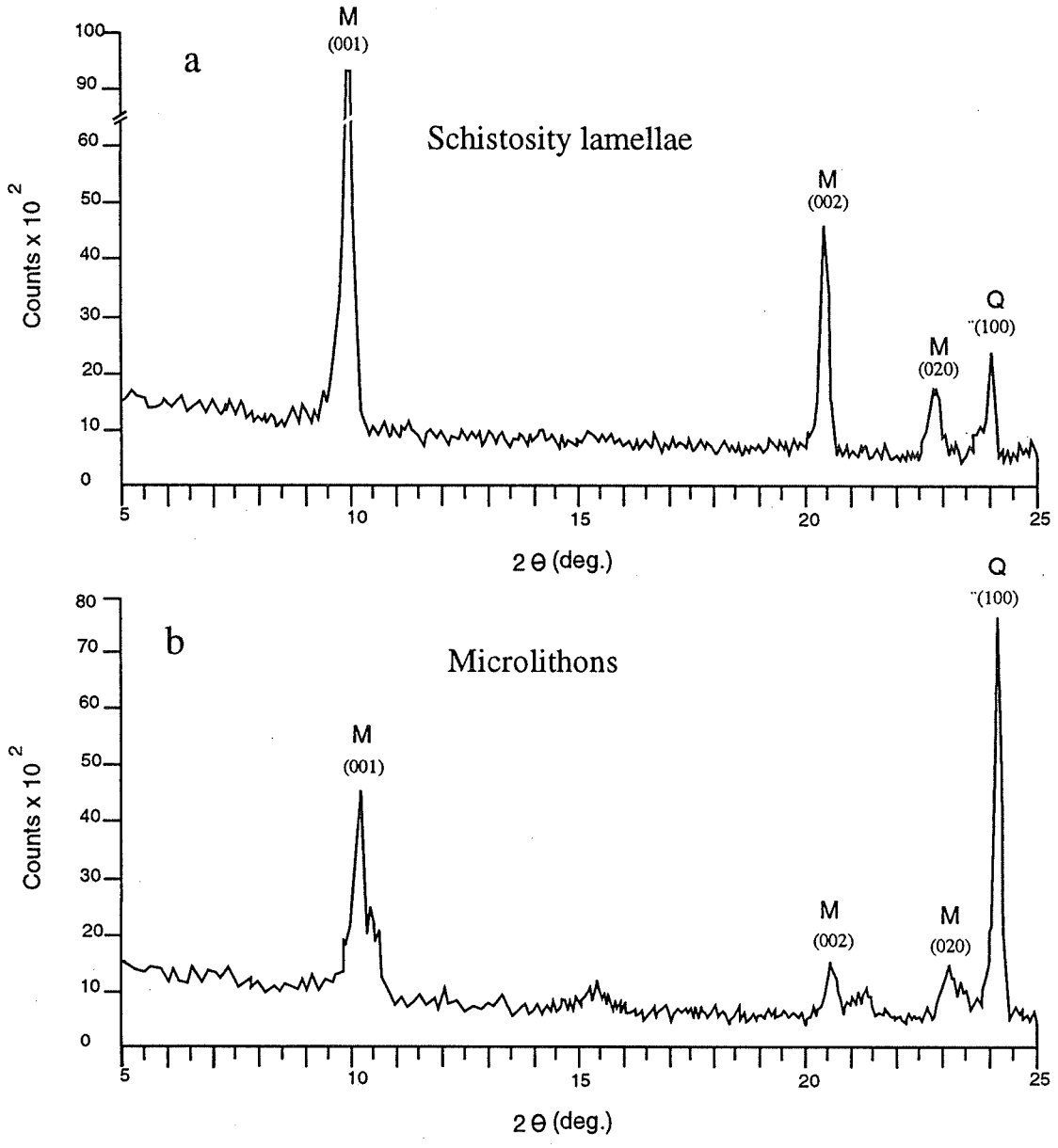

Fig. 3.20 X-ray diffractometer traces showing the mineralogical differences between **(a)** schistosity lamellae compositions and **(b)** microlithon compositions. Note higher content of muscovite (M) and lower content of quartz (Q) in schistosity lamellae.

However, the highly schistose domains have a lower proportion of quartz and higher proportions of phyllosilicates than the microlithon portions.

3.3.2 Chemical differentiation

Chemical differentiation involves differences in bulk chemistry between schistosity-lamellae and microlithon portions of the rocks. Such differentiation may reflect differences in mineral proportions or differences in the chemistry of individual mineral grains. In this study, X-ray fluorescence spectrometry and electron microprobe analyses have been used to establish chemical differentiation associated with schistosity and crenulation cleavages.

3.3.2.1 Variations in bulk-chemical compositions

To study whether chemical changes accompanied the formation of schistosity, samples of microlithon material (rock largely free of schistosity) were compared via X-ray fluorescence spectroscopy with highly schistose samples (data are presented in Chapter 4). Variations in compositions between the microlithon and schistosity-lamellae show that bulk chemical changes were associated with the development of schistosity in the deformed rocks. In each case (Table 4.1), SiO_2 is lower and Al_2O_3, MgO, K_2O, TiO_2 and normally Fe_2O_3 are higher in the schistose samples. Other oxides (MnO, CaO, and P_2O_5) remain essentially uniform in all samples. The ternary SiO_2-Al_2O_3-K_2O diagram (Fig. 3.21) shows the

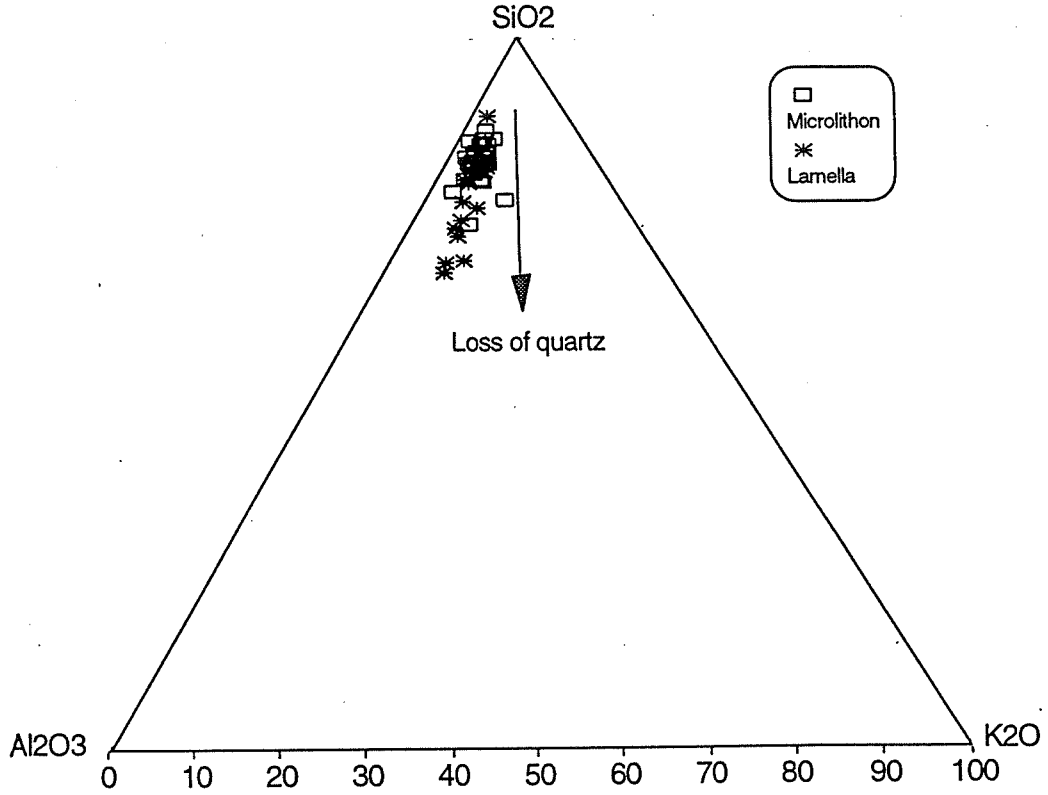

Fig. 3.21 Triangular SiO_2-Al_2O_3-K_2O diagram showing the microlithon and schistosity lamellae chemistry of samples shown in Table 4.1.

variations between the microlithon and schistosity-lamellae chemistry. The results indicate that bulk changes in chemistry associated with the development of the schistosity are proportional to the SiO_2 content (presumably reflecting the abundance of quartz).

3.3.2.2 Variations in mineral chemistry

Microprobe analyses of fine-grain phyllosilicate minerals hosted by schistosity-lamellae show that there is little or no chemical difference between sericite in the original schistosity and those within the microlithon (see Appendix 3.1; note, both groups refer to "dissolution site" minerals). From these analyses, it appears that any changes in phyllosilicate chemistry associated with cleavage development would produce only minor changes in the bulk chemistry. Furthermore, petrographic studies suggest that the major portion of the chemical differentiation discussed above is due to variations in the proportions of minerals rather than differences in mineral compositions.

3.4 CHEMISTRY OF CLEAVAGES - EVIDENCE FOR THE PREFERENTIAL DISSOLUTION OF MATERIALS

Mineralogical differentiation is a common feature of cleavage fabrics. The differentiation has been explained by the concentration of relatively insoluble

material along developing cleavages during the dissolution of more soluble minerals (Williams, 1972; Gray, 1978). Petrographic studies of crenulation cleavages at Mobrun indicate that cleavages commonly consist of trains of chemically resistant grains such as rutile distributed within dimensionally oriented phyllosilicates (such as sericite and chlorite) which approach parallelism with the cleavage direction.

In crenulated rocks with prominent cleavages, mineralogical differentiation is reflected in different quantities of minerals in the hinges and limbs of the crenulations. The limbs commonly show marked enrichments in phyllosilicates (mica and chlorite) and rutile compared to the hinges and remainder of the rock.

3.4.1 Chemistry of minerals in different structural sites

More than 300 microscopic areas in 40 samples showing clear deformation microstructural features were chosen for detailed microchemical analyses of sericite and chlorite. Observations of micro-textures indicate that sericite and chlorite formed during both synvolcanic hydrothermal alteration and syntectonic metamorphism-deformation events. Hydrothermal sericite and chlorite were produced during hydrothermal alteration of precursor components in the initial volcanic rocks (Fig. 3.1). These minerals were then recrystallized during the formation of the deformed schistose rocks, in which precursor grains undergo rotation towards the planes of schistosity. During metamorphism-deformation,

new sericite and chlorite resulted from the recrystallization of previous silicate grains which were dissolved and transported by fluids and were then reprecipitated in low-strain domains such as pressure shadows and sites of extension (Figs. 3.1, 3.2).

3.4.1.1 Sericite

Sericite, a common whole-rock phase in rocks of the Mobrun region, occurs in pressure shadows and in schistosity lamellae where aggregates of preferred oriented grains are finer in size than those of the former undeformed rock. With increasing strain, schistosity fabrics became longer and thicker, as well as becoming more closely spaced. Their development involved dissolution and removal of material at boundaries between schistosity surfaces, together with and formation of layer silicates at these sites. The abundance of this syndeformational sericite increases toward the Main Lens in both the footwall and hangingwall. In addition to this late syntectonic sericite, there is synvolcanic hydrothermal sericite which also typically replaces plagioclase phenocrysts and the surrounding groundmass grains.

Coarser-grained syntectonic sericite forms elongate grains in pressure shadows next to pyrite and other phenocryst grains. It is generally intergrown with quartz and minor chlorite, and oriented subparallel to the S_1 schistosity of the rock.

Table 3.1 presents the average chemical analyses of sericite from different parts of the footwall and hangingwall. Up to 18 grains were analyzed in each sample (see Appendix 3.1 for individual grain analysis) for sericite both in schistosity-lamellae sites and in pressure-shadow precipitation sites. In general, each sample was found to have a relatively consistent composition, except for minor differences between sericite grains in schistosity and pressure-shadow sites (see below). Variations in the composition of different samples may be due to variable bulk-rock compositions as well as variable intensities of metamorphism-deformation in different parts of the deposit.

The sericite grains in pressure shadow sites have a range in composition clearly different from those located within schistosity lamellae domains (Appendix 3.1).

Pressure shadow sericite in precipitation sites are characterized by distinctly higher amounts of Si, moderately higher K, Fe and Mg, distinctly lower Al, and moderately lower Na and Ti relative to the schistose sericite in the same samples (Fig. 3.22).

Figure 3.23 presents the compositions of sericite in a K-Na-Al diagram. The sericite data show that there are small variations in Na-K substitution. In general, sericite grains contain low percentages of both Na_2O (up to 3.5 wt %) and FeO (up to 4.5 wt.%).

Table 3.1 Microprobe analyses of sericite form Mobrun deposit

Sample no.	315	467	244	146	73	146A	51	265B	267A	216	265A	338	194	92	2	91	20	267	332B	489
No. of analyses	(1)	(2)	(7)	(9)	(2)	(2)	(6)	(4)	(1)	(6)	(1)	(9)	(18)	(3)	(6)	(4)	(6)	(9)	(2)	(2)
SiO2	47.89	46.67	46.43	46.39	49.02	43.91	47.05	46.76	46.99	47.52	44.98	47.85	46.81	44.97	46.94	46.84	47.17	46.73	51.01	47.21
TiO2	0.35	0.31	0.09	0.12	0.05	0.25	0.16	0.12	0.23	0.06	0.08	1.00	0.15	0.04	0.20	0.12	0.21	0.39	0.07	0.23
Al2O3	33.01	31.73	37.30	33.82	35.13	33.82	30.94	34.89	31.44	37.09	34.30	35.64	35.14	34.67	29.79	33.62	32.72	33.23	31.15	32.14
FeO	2.06	3.08	1.15	1.91	0.80	0.38	2.64	0.53	4.36	0.58	1.59	0.47	0.47	0.86	3.81	1.86	1.23	1.75	1.53	2.73
MnO	0.04	0.07	0.01	0.01	0.05	0.00	0.04	0.07	0.04	0.06	0.16	0.01	0.02	0.03	0.03	0.05	0.01	0.02	0.00	0.00
MgO	0.70	1.01	0.18	0.81	1.39	0.79	1.68	0.63	1.00	0.38	1.22	0.13	0.85	0.53	1.31	0.48	1.02	0.89	1.56	1.08
CaO	0.05	0.01	0.01	0.02	0.04	0.10	0.06	0.20	0.04	0.04	0.17	0.04	0.07	0.03	0.24	0.02	0.02	0.08	0.03	0.05
Na2O	0.22	0.27	1.61	0.37	0.48	2.39	0.21	2.12	0.23	0.96	0.54	2.97	0.76	0.82	0.18	0.59	0.22	0.12	0.24	0.20
K2O	11.39	11.20	8.77	10.86	10.94	6.24	10.83	7.68	11.22	10.12	7.77	5.95	10.12	9.69	11.24	10.39	10.76	11.21	10.76	11.27
BaO	0.25	0.17		0.60	0.18	0.23	0.25	0.06	0.33	0.14	0.35	0.12	0.23	0.09	0.13	0.21	0.13	0.23	0.23	
Total	95.96	94.51	95.55	94.91	98.06	88.10	93.86	93.07	95.88	96.93	91.16	94.20	94.62	91.74	93.88	94.18	93.50	94.66	96.56	94.90
Si	6.38	6.36	6.12	6.26	6.32	6.19	6.42	6.27	6.35	6.18	6.19	6.34	6.24	6.19	6.47	6.32	6.40	6.30	6.68	6.37
Ti	0.04	0.03	0.01	0.01	0.00	0.03	0.02	0.01	0.03	0.01	0.01	0.10	0.01	0.00	0.02	0.01	0.02	0.04	0.01	0.03
Al	5.19	5.11	5.76	5.38	5.34	5.62	4.98	5.52	5.01	5.68	5.57	5.51	5.52	5.61	4.84	5.43	5.23	5.28	4.81	5.11
Fe	0.23	0.35	0.13	0.20	0.09	0.05	0.30	0.06	0.49	0.06	0.18	0.05	0.05	0.10	0.44	0.14	0.14	0.20	0.17	0.31
Mn	0.01	0.01	0.00	0.00	0.01	0.00	0.00	0.01	0.01	0.01	0.02	0.00	0.00	0.00	0.00	0.01	0.00	0.00	0.00	0.00
Mg	0.14	0.09	0.04	0.16	0.27	0.17	0.34	0.13	0.20	0.07	0.25	0.03	0.17	0.11	0.27	0.07	0.21	0.18	0.30	0.22
Ca	0.01	0.00	0.00	0.00	0.01	0.01	0.02	0.00	0.02	0.00	0.03	0.00	0.02	0.01	0.01	0.01	0.01	0.01	0.00	0.01
Na	0.06	0.07	0.41	0.10	0.12	0.65	0.01	0.03	0.01	0.24	0.15	0.76	0.20	0.00	0.01	0.00	0.00	0.01	0.06	0.05
K	1.94	1.95	1.47	1.87	1.80	1.12	1.89	1.52	1.94	1.68	1.37	1.00	1.72	1.70	1.98	1.75	1.86	1.93	1.80	1.94
Ba	0.01	0.01	0.00	0.03	0.01	0.01	0.05	0.35	0.06	0.01		0.01	0.01	0.22	0.05	0.18	0.06	0.03	0.01	0.00
Total	13.99	13.97	13.94	14.00	13.96	13.86	14.04	13.89	14.11	13.94	13.75	13.79	13.94	13.95	14.10	13.92	13.92	13.99	13.84	14.04

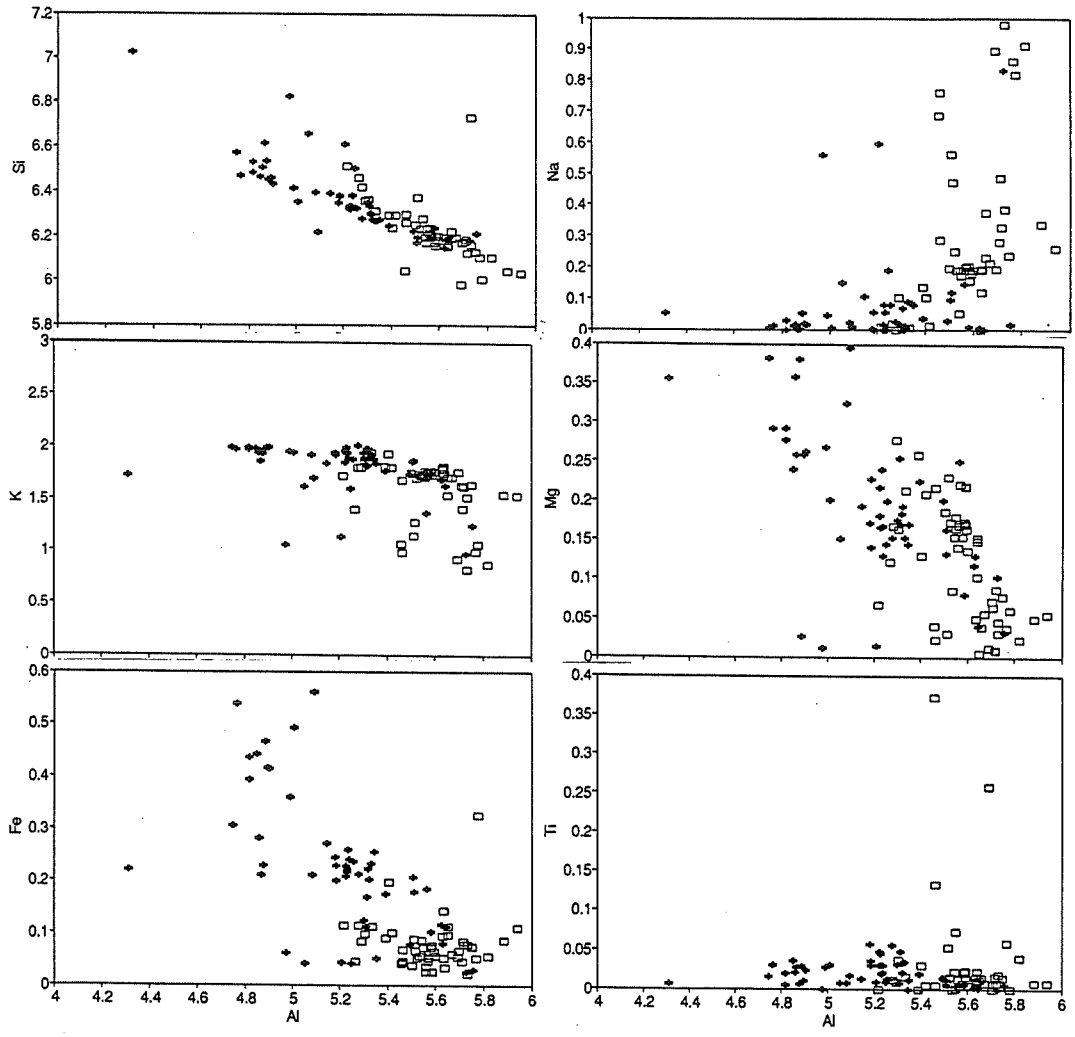

Fig. 3.22 Diagrams illustrating chemical variations in the composition of sericite, analyzed from schistosity lamellae (open boxes) and pressure shadow (crosses) domains. Pressure shadow analyses show higher Si, K, Fe, and Mg relative to schistose sericite in the same samples. Note the analyses of samples are not illustrated separately.

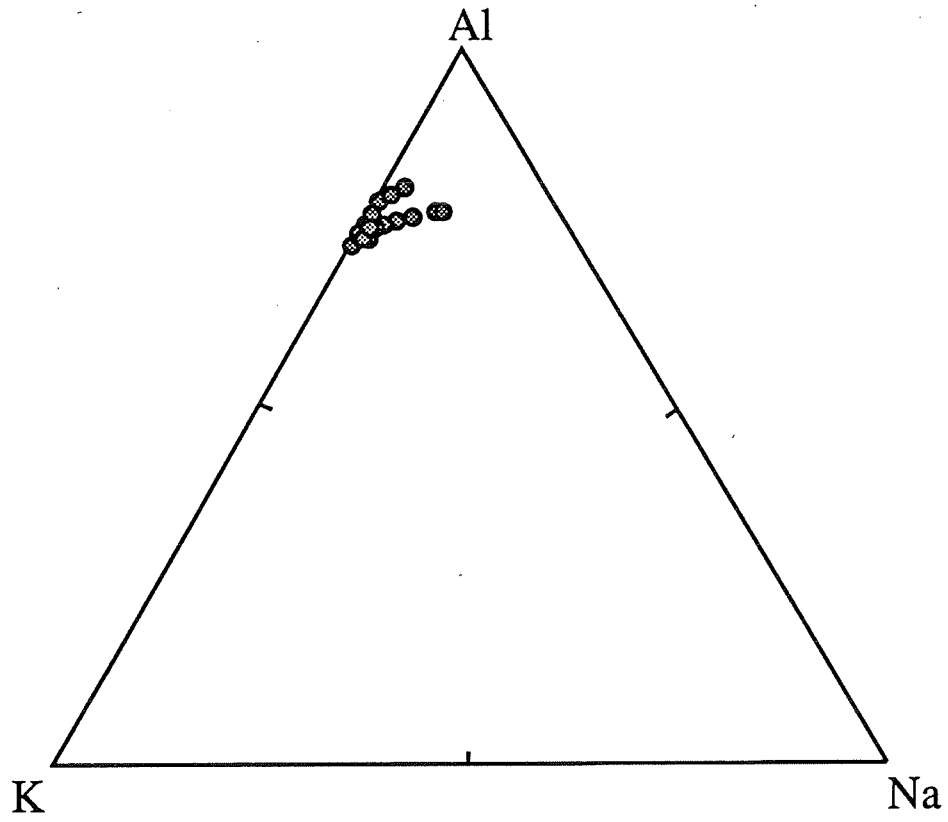

Fig. 3.23 Al-K-Na diagram showing the Na-K solid-solution of sericite at Mobrun.

3.4.1.2 Chlorite

Chlorite is not common in the Mobrun wallrocks; it is mainly present in the central part of the footwall adjacent to the massive orebody of the Main Lens, and in some parts close to the mafic dike. It typically exhibits fine-grained mosaic textures (Fig. 2.10). Coarse-grained chlorite occurs in tension veinlets, as overgrowths on other coarse-grained material (such as pyrite and quartz), and as replacements of plagioclase. Chlorite has a fine-grained appearance where it has replaced glass exhibiting perlitic textures. Chlorite is commonly intergrown with sericite and quartz.

The compositions of chlorite grains analyzed with the electron microprobe are listed in Appendix 3.2, and the average analysis for each sample is presented in Table 3.2. Its composition exhibits a wide range of compositional substitutions between Si-Al and Mg-Fe, but lies consistently within the ripidolite field (Fig. 3.24). All of the chlorites are distinctly Fe-rich, with Fe/Mg ratios ranging up to 6.1.

Analyses of chlorite (Table 3.2) and plots of these data on an Mg-Al-Fe diagram (Fig. 3.25) show a small range of Mg-Fe contents within the chlorite solid-solution field. Compositions range from Mg = 0.4 and Fe = 7.8, to Mg = 4.8 and Fe = 3.7 cation percent. Chlorite is generally Fe-rich and exhibits more chemical variation between samples than do the associated mica grains. However, analyses of overgrowths of chlorite on pyrite show higher Fe/Mg ratios compared to the chlorite located in schistosity lamellae (see Appendix 3.2 for analyses).

Table 3.2 Representive microprobe analyses of chlorites at the Mobrun deposit.

Sample no.	146	467	494	315	232	1	11	267	172A	51	265A	265B
No. of analyses	(2)	(7)	(1)	(3)	(5)	(3)	(8)	(5)	(2)	(4)	(2)	(2)
SiO2	22.99	23.56	23.64	23.20	23.35	23.71	23.91	24.44	24.32	24.72	25.59	26.63
TiO2		0.03	0.00	0.06	0.02	0.07	0.06	0.02	0.06	0.04	0.06	0.02
Al2O3	22.24	22.00	21.00	22.24	22.27	22.03	18.50	22.82	22.93	22.26	23.20	24.23
FeO	38.60	34.94	38.05	40.16	36.38	34.81	42.54	35.34	29.87	32.85	21.57	22.17
MnO	0.10	0.18	0.22	0.20	0.09	0.12	0.08	0.16	0.18	0.19	0.18	0.17
MgO	4.67	6.61	4.62	3.50	5.36	7.58	3.90	7.05	9.73	8.80	14.91	15.38
CaO		0.02	0.00	0.01	0.02	0.01	0.07	0.15	0.49	0.02	0.04	0.00
Na2O	0.16	0.15	0.25	0.19	0.14	0.61	0.23	0.18	0.15	0.16	0.14	0.13
K2O		0.06	0.03	0.04	0.01	0.02	0.02	0.02	0.04	0.03	0.00	0.02
Total	88.76	87.56	87.79	89.60	87.64	88.96	89.31	90.18	87.78	89.06	85.68	88.75
Si	5.16	5.26	5.36	5.24	5.24	5.20	5.47	5.27	5.25	5.33	5.39	5.41
Ti		0.02	0.00	0.01	0.00	0.01	0.01	0.00	0.01	0.01	0.01	0.00
Aliv	2.84	2.74	2.64	2.76	2.76	2.80	2.53	2.73	2.75	2.67	2.61	2.59
Alvi	3.04	3.04	2.97	2.96	3.13	2.90	2.46	3.07	3.09	2.99	3.15	3.21
Fe	7.24	6.52	7.21	7.41	6.83	6.39	8.14	6.37	5.40	5.93	3.80	3.77
Mn	0.02	0.03	0.04	0.04	0.02	0.02	0.01	0.03	0.03	0.03	0.03	0.03
Mg	1.56	2.20	1.56	1.41	1.80	2.48	1.33	2.34	3.13	2.83	4.68	4.66
Ca		0.00	0.00	0.00	0.01	0.00	0.02	0.04	0.12	0.01	0.01	0.00
Na	0.07	0.13	0.11	0.09	0.06	0.26	0.10	0.08	0.06	0.07	0.06	0.05
K		0.02	0.01	0.01	0.00	0.01	0.00	0.01	0.01	0.01	0.00	0.01
Total	19.94	19.97	19.90	19.94	19.84	20.06	20.07	19.94	19.85	19.86	19.75	19.72
Fe/Mg	4.63	2.97	4.63	5.25	3.80	2.58	6.13	2.72	1.72	2.10	0.81	0.81

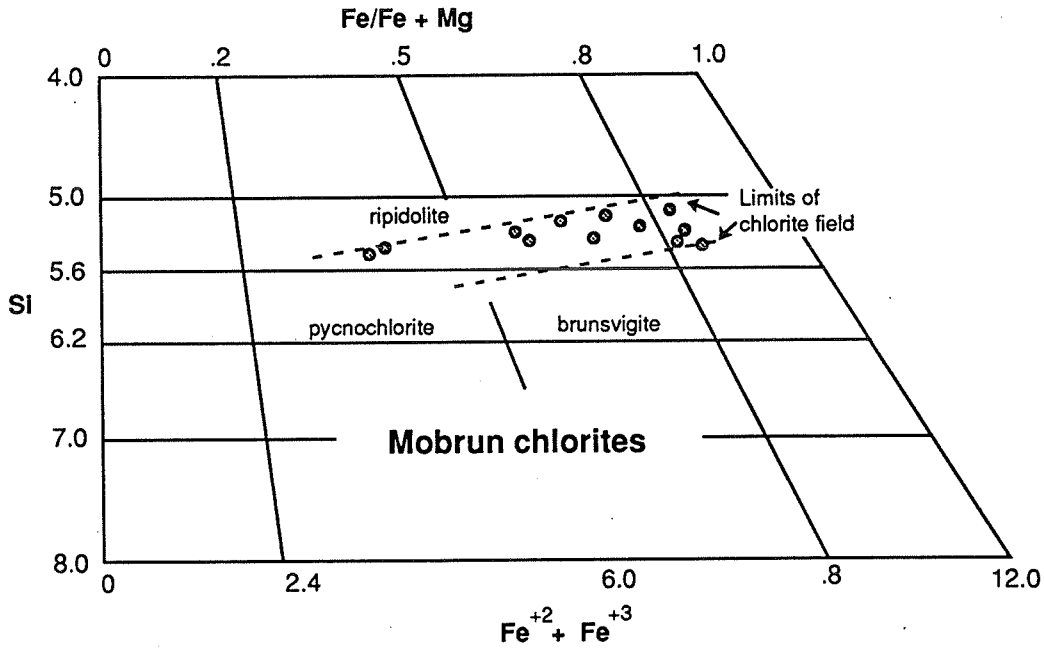

Fig. 3.24 Hey diagram (Hey, 1959) with analyses outlining a solid-solution field for chlorite from the Mobrun deposit.

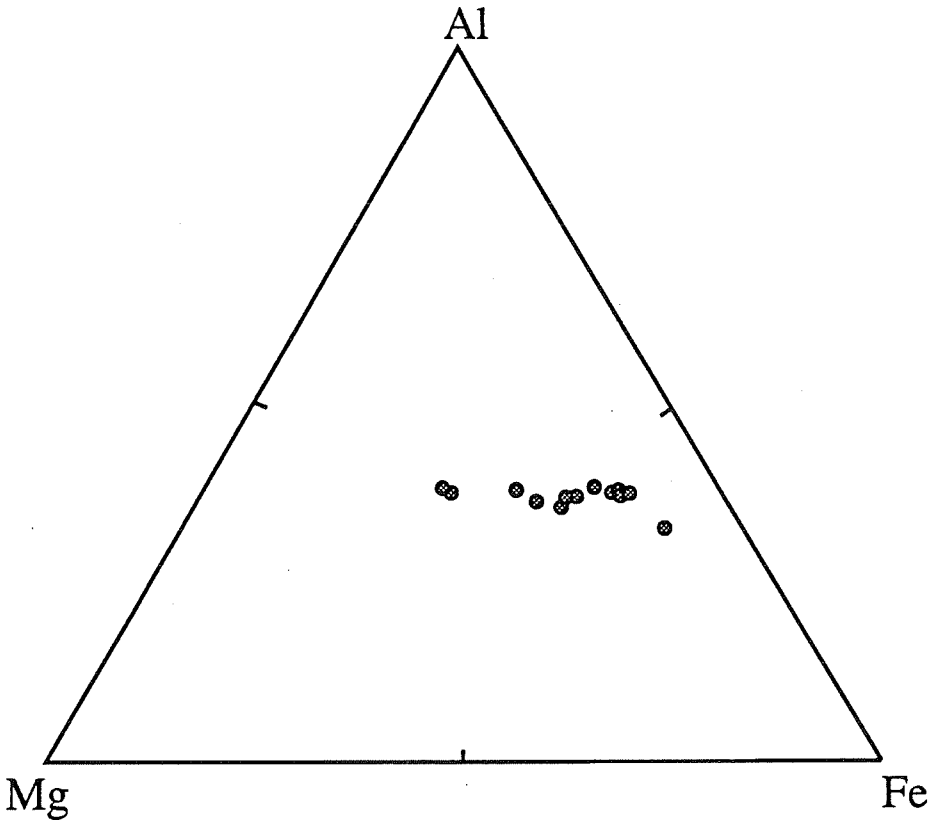

Fig. 3.25 Al-Mg-Fe diagram showing the Fe-Mg solid-solution of chlorite from Mobrun.

3.4.1.3 Carbonate

Carbonate commonly forms widespread aggregates, veins, and disseminated grains in all samples. In detail, it occurs as disseminated grains, as pressure shadows and veinlets (alone or with quartz), and as widespread disseminations within breccia matrices and tuffs. Microprobe analyses have been obtained for the carbonate in all types of microstructural sites. Staining techniques used for the determination of carbonate mineral compositions (Dickson, 1965) also indicated a calcite composition.

3.4.1.4 Feldspar

Feldspar phenocrysts at the Mobrun mine are euhedral albitic plagioclases (Table 3.3). The albite apparently formed mainly from the initial magmatic crystallization and subsequent spilitization of the volcanic host rocks. Mottle (1983) argued that albite may form by removal of Na^+ from seawater at water/rock ratios < 5. They are generally present in least-foliated rocks where the feldspar is partly to wholly replaced by sericite (Fig. 2.7). Albite grains within least-deformed rocks show evidence of brittle and ductile deformation and are partially dissolved under pressure-solution condition.

Structural evidence, including inter-crystal foliation (explained earlier), indicate a syntectonic formation for some albite (Riopel et al., 1992).

Table 3.3 Microprobe analyses of feldspar at the Mobrun deposit

Sample	Na2O	Al2O3	SiO2	K2O	CaO	FeO	Total
426M13	11.66	19.60	68.74	0.00	0.00	0.00	100.0
426M17	11.62	19.57	68.81	0.00	0.00	0.00	100.0
494M2	11.47	19.67	68.86	0.00	0.00	0.00	100.0
332M4	10.57	20.70	67.88	0.61	0.18	0.05	100.0
332M5	11.43	19.90	68.63	0.01	0.03	0.00	100.0
332M8	11.49	19.52	68.99	0.00	0.00	0.00	100.0
332M9	11.18	20.04	68.56	0.21	0.00	0.01	100.0
332M10	11.46	19.56	68.99	0.00	0.00	0.00	100.0
322M14	11.59	19.45	68.93	0.00	0.00	0.03	100.0
332M20	10.85	20.77	67.53	0.66	0.12	0.07	100.0

3.4.1.5 Titanium oxides

Most microprobe analyses of titanium oxides indicate that the material is rutile. However, some leucoxcene grains have been identified (Fig. 3.26). Rutile is fine-grained and is concentrated in highly foliated samples.

3.4.2 Chemistry of the cleavage

Reliable analyses of individual fine-grained pressure-solution cleavage minerals (typically <1 mm in width) within schistose rocks are difficult to obtain. Instead, chemical compositions were investigated by analyses of thin sections at regular spacing (20 μm intervals) across areas showing variable abundances of cleavage lamellae. The traces of three paths of microprobe analyses are shown in Figure 3.27A. The composition for each cleavage area analyzed is given in Table 3.4, and frequency diagrams for Si, Ti and Al are presented in Figures 3.27B.

The analyses of cleavage areas showing an increasing concentration of cleavage planes (Figs. 3.27A.a and 3.27B.a) show that there are variations in compositions related to the intensity of cleavage: for example, Si decreases, Ti and Al increase with increasing deformation. Chemical differentiation is apparently related to increasing deformation.

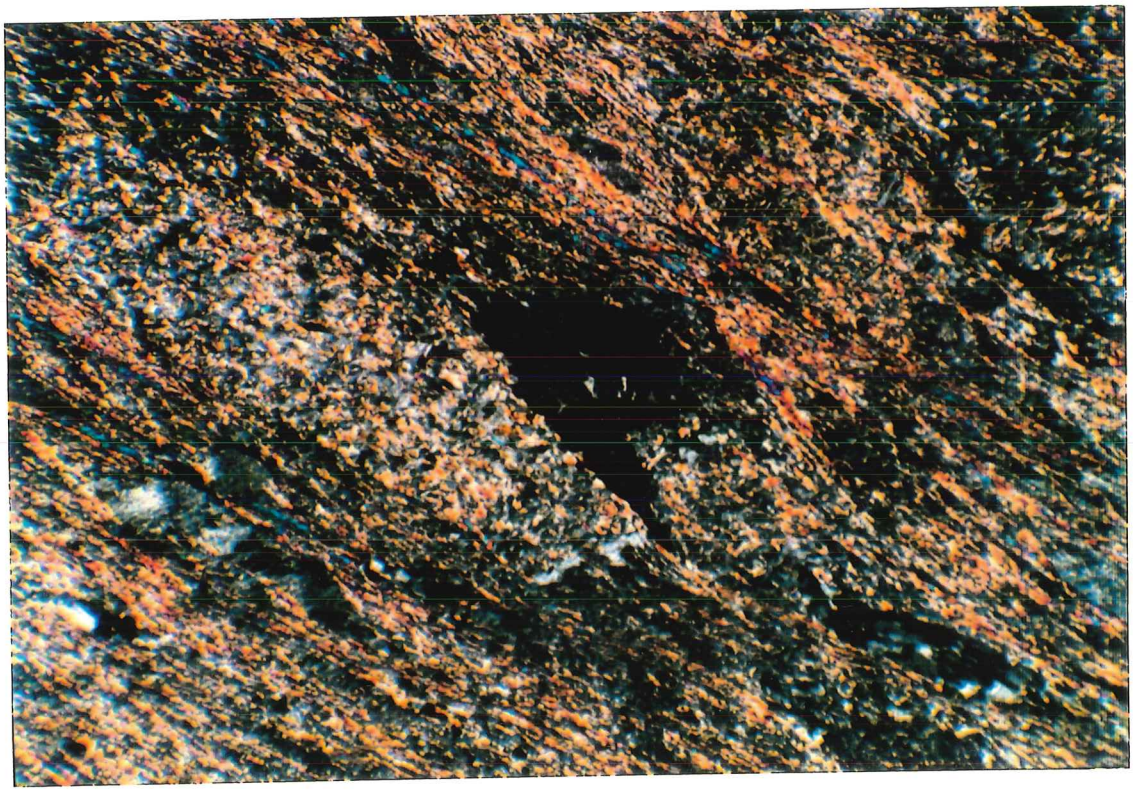

Fig. 3.26 Photomicrograph showing leucoxcene in the matrix of quartz-sericite. Crossed polars, field of view 1 mm across.

Table 3.4a. Analyses of cleavage materials.

Location	7-2-194A	7-2-194A	7-2-194A	7-2-194A	7-2-194A	7-2-194A	7-2-194A	7-2-194A	7-2-194A	7-2-194A	7-2-194A	7-2-194A
Sample #	194M21	194M26	194M22	194M27	194M23	194M28	194M24	194M29	194M25	194M30	194M31	194M32
Analyze #	1	2	3	4	5	6	7	8	9	10	11	12
Si	13.32	17.10	7.53	17.17	14.64	18.85	2.26	7.80	3.74	5.77	16.77	1.94
Ti	7.18	0.06	18.35	0.04	4.61	7.44	28.37	19.98	25.44	23.64	0.05	30.84
Al	12.38	15.53	7.02	15.55	13.67	5.81	2.54	4.90	3.90	3.39	14.92	0.33
Fe	0.16	0.21	0.11	0.18	0.08	0.00	0.04	0.09	0.08	0.05	1.81	0.27
Mn	0.00	0.00	0.04	0.00	0.07	0.00	0.04	0.00	0.04	0.00	0.00	0.05
Mg	0.49	0.61	0.31	0.45	0.45	0.01	0.08	0.06	0.19	0.10	0.61	0.00
Ca	0.02	0.03	0.03	0.05	0.05	0.02	0.00	0.07	0.03	0.09	0.03	0.02
Na	0.44	0.53	0.33	0.50	0.58	3.64	0.24	0.12	0.21	1.23	0.46	0.00
K	3.64	4.79	2.16	4.87	3.86	0.75	0.60	2.54	1.13	0.53	4.41	0.12
Ba	0.05	0.00	0.05	0.05	0.07	0.01	0.10	0.00	0.00	0.09	0.02	0.00
O	62.32	61.14	64.07	61.14	61.92	63.47	65.73	64.44	65.24	65.11	60.92	66.43
Total	100	100	100	100	100	100	100	100	100	100	100	100

Table 3.4b. Analyses of cleavage materials.

Location	82-2-338	82-2-338	82-2-338	82-2-338	82-2-338	82-2-338	82-2-338	82-2-338	82-2-338
Sample #	338M1	338M2	338M7	338M8	338M9	338M10	338M11	338M12	338M14
Analyze #	1	2	3	4	5	6	7	8	9
Si	17.01	17.03	16.69	16.91	27.96	26.56	17.83	17.63	16.60
Ti	0.16	0.11	0.72	1.04	0.00	0.01	0.02	0.37	3.16
Al	16.07	16.24	15.89	15.28	5.38	6.73	15.43	15.30	13.35
Fe	0.15	0.16	0.15	0.12	0.04	0.14	0.25	0.13	0.34
Mn	0.00	0.02	0.00	0.00	0.00	0.00	0.02	0.00	0.00
Mg	0.10	0.06	0.04	0.11	0.06	0.06	0.08	0.06	0.04
Ca	0.02	0.01	0.00	0.01	0.00	0.00	0.01	0.03	0.01
Na	2.39	2.54	2.50	1.92	0.67	0.40	1.57	2.12	1.67
K	2.77	2.44	2.57	2.97	0.98	1.64	3.20	2.74	2.63
Ba	0.01	0.01	0.03	0.07	0.00	0.01	0.00	0.02	0.05
O	61.32	61.38	61.41	61.57	64.91	64.45	61.59	61.60	62.15
Total	100	100	100	100	100	100	100	100	100

Table 3.4c. Analyses of cleavage materials

Location	8-2-73B	8-2-73B	8-2-73B	8-2-73B	8-2-73B	8-2-73B
Sample #	73M1	73M2	73M3	73M4	73M5	73M10
Analyze #	1	2	3	4	5	6
Si	12.59	17.48	17.69	15.95	17.29	14.68
Ti	12.22	0.00	0.03	0.02	0.05	3.57
Al	3.06	14.98	14.73	14.47	15.10	13.16
Fe	8.00	0.25	0.23	2.82	0.64	1.73
Mn	0.00	0.00	0.03	0.03	0.03	0.05
Mg	0.17	0.72	0.77	2.15	1.11	1.17
Ca	0.04	0.02	0.01	0.01	0.03	0.04
Na	0.12	0.38	0.28	0.20	0.49	0.43
K	0.69	5.01	5.00	3.74	3.93	3.78
Ba	0.17	0.02	0.03	0.00	0.00	0.03
O	62.94	61.14	61.20	60.61	61.33	61.36
Total	100	100	100	100	100	100

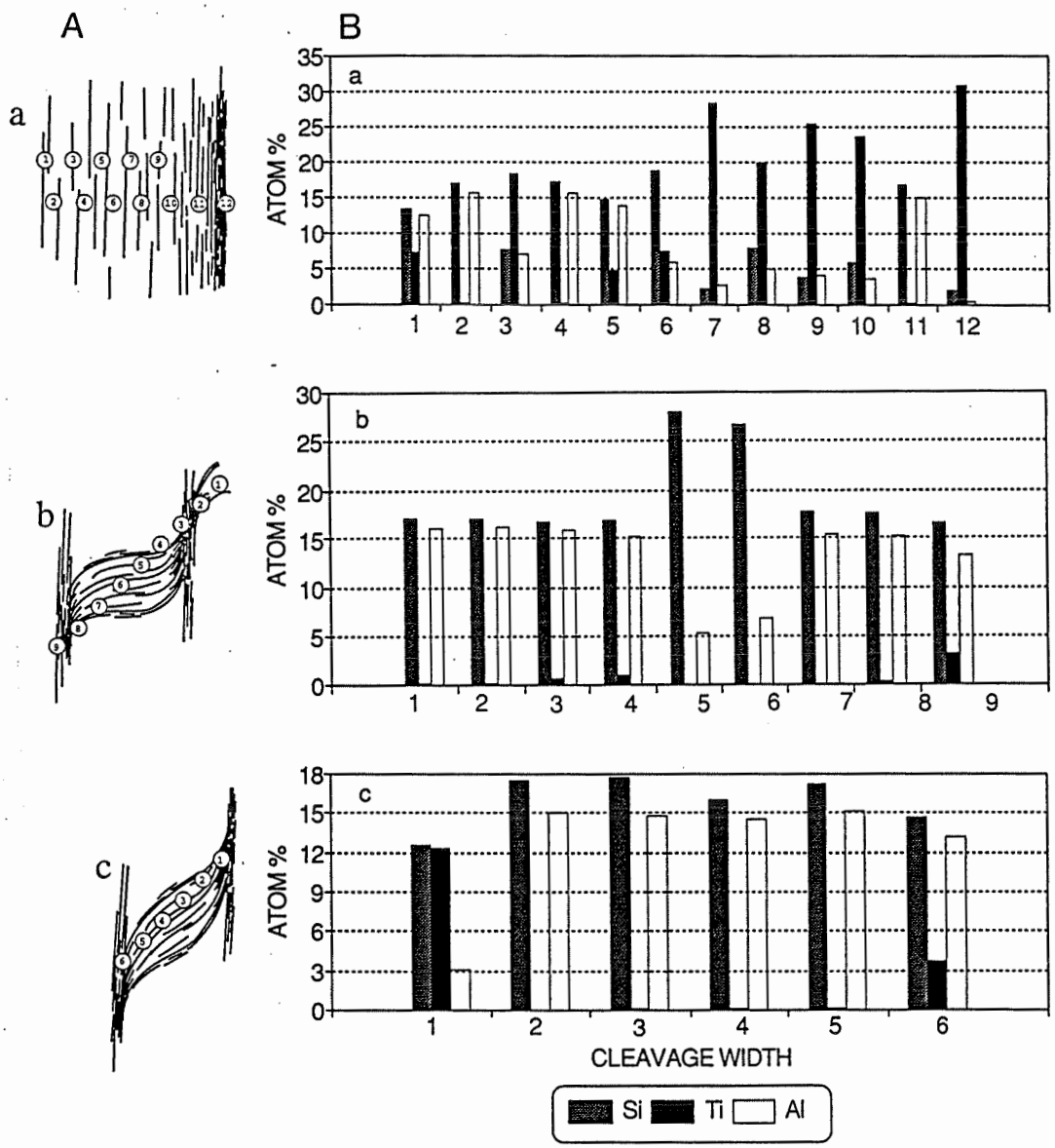

Fig. 3.27 (A) Diagrams showing the traces of three paths of microprobe analyses across cleavages. Circles with numbers represent analyzed points at 20 μm intervals across the cleavages. Photomicrograph of samples are shown in Figs. 3.5 and 3.9.

(B), (a) Chemical analyses of the cleavages and associated microlithon fabrics showing that Si decreases and Al (and commonly Ti) increases within the more cleaved positions of the schist. **(b, c)** chemical differentiation for Si, Ti and Al along two paths of microprobe analyses across crenulated cleavages, reflecting different proportions of mineral constituents between the hinge and limbs of the crenulations.

Chemical differentiation is also reflected by differences in chemical compositions between the hinges and limbs of crenulation cleavages (Gray 1978). Figs. 3.27A.b,c and 3.27B.b,c show relative enrichments in Si in the limb areas and Ti (and K; see Table 3.4b,c) in hinge areas.

These chemical variations are interpreted to reflect mineralogical differentiation associated with the development of cleavage in the fine-grained matrix. Decreases in Si result from the removal of quartz in high-strain domains (e.g., cleavage lamellae) whereas increases in Al and K reflect relative increases in the amounts of sericite. Increases in Ti reflect greater concentrations of rutile along cleavage lamellae.

Scanning electron microprobe analyses across cleavages can also be used to show the distributions of key elements such as Si, Al, K, Fe, Mg, Ti, Na and S within schistosity sites. In Figure 3.28, the schistosity-lamellae are about 100 μm wide and run horizontally across the centre of the image area. Al and K concentrations reflect the distribution of sericite, whereas Na, Ca and Ti concentrations reflect the distributions of albite, carbonate and rutile, respectively. The majority of Fe occurs in pyrite. Mg and a portion of the Fe are related to chlorite.

The results indicate chemical variations along cleavage. Relative to the microlithon area, the cleavage lamellae are enriched in mica (K-Al) and rutile (Ti), and depleted in albite (Na) and quartz (Si). A noticeable decrease in detrital

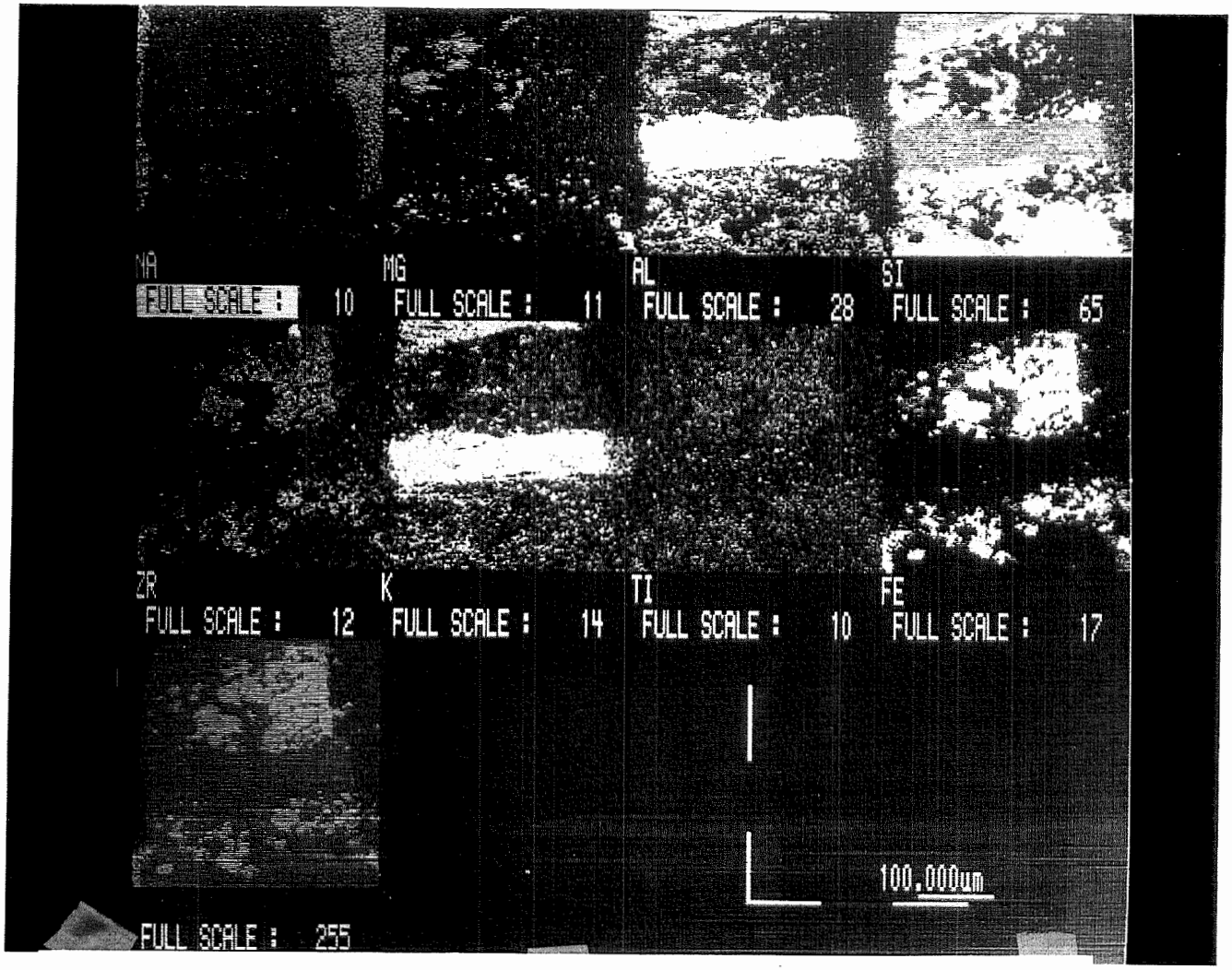

Fig. 3.28 Electron microprobe scans showing the chemical distributions of Si, Al, K, Fe, Mg, Ti, Na and S across the pressure-solution cleavage (identified by high Al, K, and Ti concentrations).

quartz and an increase in sericite are observed in these mineralogically differentiated portions. Consequently, the observed chemical differentiation appears to be largely related to variations in mineral proportions rather than to variations in the chemistry of individual minerals. This conclusion is supported by the petrographic observations discussed in Section 3.2.

3.5 DISCUSSION

The analyses of microstructural features in silicate host rocks at Mobrun indicate the potential for a synmetamorphism-syndeformation mass transfer in modifying the final chemical characteristics of these rocks. The schematic diagram of Figure 3.29 illustrates the sequence of processes involved in the development of microfabrics due to mass transfer during a dissolution-precipitation creep. During metamorphism-deformation, materials are dissolved preferentially from dissolution sites and deposited in precipitation sites. The schistosity-lamellae in schistose rocks and in the limbs of discrete crenulation cleavages indicate the solution and removal of quartz from the high-strain domains, resulting in passive concentrations of residual phyllosilicates. As such, the schistosity or cleavage surfaces are "solution seams" characterized by residual concentrations of insoluble materials such as rutile and zircon. In fact, their enrichments result from selective mass losses of other rock constituents. Therefore, oriented phyllosilicate films containing

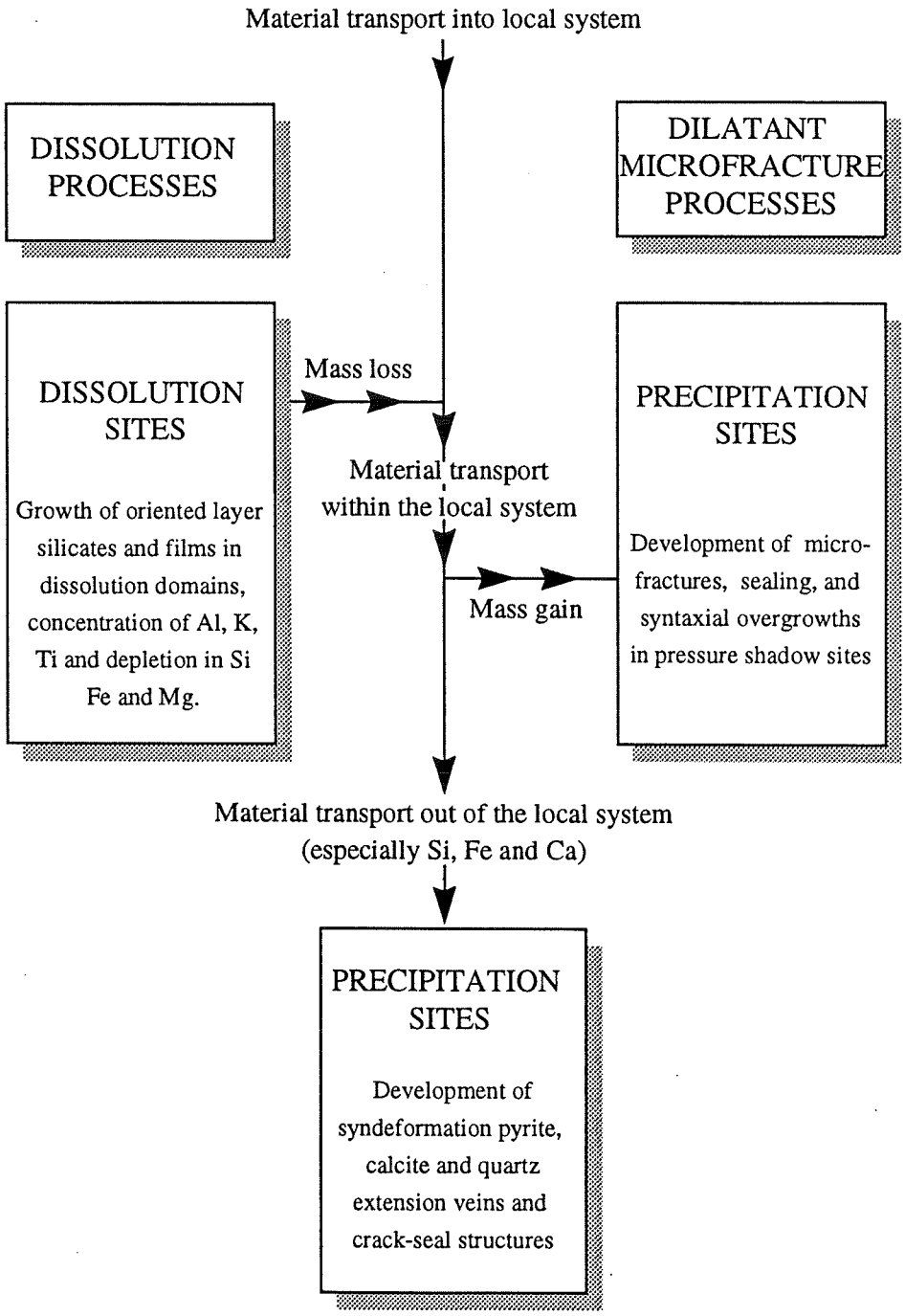

Fig. 3.29 Diagram illustrating the sequence of processes involved in the development of deformation microfabrics during the dissolution-precipitation process.

concentrations of more resistant grains in dissolution sites, together with extensional veins, pressure shadows and the truncation of minerals, indicate pressure-solution characteristics in the deformed rocks at Mobrun.

The relationship between microstructural deformation patterns and the distribution and chemical characteristics of minerals in the altered wallrocks (mainly in the hangingwall of the Main Lens) indicate that solution-precipitation creep played a major role in the mass transfer of remobilized constituents to and from local microstructural sites during the overall metamorphism-deformation event. This mechanism calls for deformation-related mass transfers superimposed on rocks which had previously undergone mass transfers during synvolcanic hydrothermal alteration (Fig. 3.1). Thus, the chemical compositions of Mobrun wallrocks has been modified during both hydrothermal alteration and metamorphism-deformation events.

3.5.1 Mechanism of preferential dissolution of minerals

In the pressure-solution process, dissolution occurs as a result of chemical potential gradients represented mainly by dislocation densities (Bosworth, 1981). In fact, where an individual unstable mineral grain lies in a zone of dissolution, the gradient in dislocation density is formed across the grain boundary (Bell and Cuff, 1989). This change in dislocation density generates a chemical potential that can dissolve the grain rim (Bosworth, 1981).

Fine-grained quartz within the pressure-solution cleavages shows ample evidence of subgrain ellipticalization and dissolution (Fig. 3.6). In contrast, phyllosilicate grains can be deformed without a build up of significant dislocation density gradients across their lattice planes (Hull, 1965). Thus, quartz has undergone dissolution to a much greater extent than the associated phyllosilicates in zones of high strain (dissolution sites).

Therefore, the crystallization of totally new phyllosilicates probably did not take place at schistosity lamellae and the majority of such phyllosilicate are mainly related to ion exchange reactions involving pre-existing grains and the oriented growth of new grains. Nevertheless, phyllosilicate has totally recrystallized in zones of low strain such as pressure shadows containing late sericite.

3.5.2 Distance of mass transfer

The relationship between mineral compositions and microstructural sites in metamorphosed-deformed rocks at Mobrun is clearly reflected in variations in the composition of synmetamorphism-syntectonic sericite. In spite of these compositional variations in sericite, there is a good correlation between the compositions of early and late sericites at the thin-section scale (Appendix 3.1). Concentrations of elements in primary sites are reflected in correspondingly higher or lower concentrations for these same elements in the mineral precipitates formed during metamorphism-deformation. This relationship must surely result from the

migration of mobile elements over only short distances, such that the final mineral products were derived from immediately local dissolution sites.

On the other hand, the ubiquitous presence of syntectonic extension veins and crack-seal structures filled with quartz, calcite and pyrite are obvious manifestations of mass transfer over longer distances (possibly up to metres) than those involved in filling pressure-solution sites. Thus, while Si, Ca and Fe may be associated with long-range migrations (i.e., a chemically open-system), elements remobilized only by the local dissolution and subsequent redeposition of mica in adjacent microsites during metamorphism-deformation did so in an essentially closed-system. In this manner, we identify a syntectonic redistribution of iron, calcium and silica into some syn- to post-tectonic pyrite, carbonate and quartz veins at the Mobrun mine.

Mass transfers during deformation have probably contributed continuously to the fluid budget and to have resulted in a continuous solution/redeposition of many of phases, as evidenced: (1) by crack-seal pyrite-quartz vein microstructures, indicating repeated host-rock failure and vein-filling, (2) by zones of quartz and mica in pressure shadows, indicating mineralogical dissolution in numerous stages, and (3) by the remobilization recognized essentially around aggregates of pyrite and silicate phenocrysts, where further mass transfer led to additions of mass within pyrite pressure-shadows and in tension veins. In the case of successively reopened microcracks, fluids containing similar host-rocks components (Ca^{2+}, CO_3^{2-}

Mg^{2+}, Fe^{2+}, Fe^{3+}, Al^{3+} and Si^{4+}) precipitated similar syntaxial overgrowth grains and fracture-fillings.

3.5.3 Mechanism of chemical variations in composition of minerals

This study argues that the development of pressure-solution cleavages in the Mobrun wallrocks indicates important structural controls over the chemical compositions of syntectonic minerals. Nevertheless, chemical variations in the compositions of minerals in any large-scale metamorphic-deformation-related alteration zone must also be controlled by the water/rock ratio, fO_2, fS_2 and pH, as well as by the temperature, pressure and composition of the associated fluid. None of these parameters should have varied significantly at the microscopic scale of the analyses reported above, some of which represent grains only a few millimetres (or even microns) apart. Therefore, chemical variations in mineral compositions between microstructural sites can be attributed mainly to the compositional evolution of an internal (closed-system) syntectonic fluid as it dissolves material from one microsite and precipitates it at another.

The chemical characteristics of the syntectonic fluid may be evaluated from the behaviour of elements interacting with water during metamorphism-deformation. For example, aluminum, widely considered to be immobile in water/rock interactions (Riverin and Hodgson, 1980; Finlow-Bates and Stumpfl, 1981), probably migrated over only short microstructural distances and

redeposited in immediately adjacent layers, whereas more mobile elements, such as Si, Fe, Ca, and Na, probably migrated to much more variable degrees and over considerable microstructural distances relative to their original dissolution sites.

3.5.4 Physical conditions of fluid

Evidences such as crenulation cleavages and tensional fractures indicate that deformation at Mobrun occurred close to the brittle-ductile transition. Structural displacements created tension cracks which then became channelways for fluids migrating through the rocks, particularly adjacent to the orebodies where the deformation was strongest. According to Etheridge et al., (1983), syntectonic extension veins in low-grade metamorphic rocks indicate that the fluid pressure exceeded the lithostatic rock pressure, at least periodically. Therefore, tension-crack features associated with cleavage development in the volcanic rocks of the Mobrun area illustrates the importance of high fluid pressures in controlling deformation mechanisms.

The networks of syntectonic extension veins filled by quartz, carbonate and pyrite are manifestations of mass transfer over longer distances than those associated with pressure-solution. Pressure-solution sites associated with cleavage development indicate that significant bulk mass and volume changes accompanied the generation of relatively large volumes of syn-tectonic fluids. The advection of large amounts of fluid could be expected to lead to important mass transfers

wherever a circulating fluid is out of equilibrium with the local rock (Etheridge et al., 1984). A disequilibrium in fluid pressure between dissolution and precipitation sites would tend to create such mass transfers. Local disequilibrium in fluid can also be produced by the opening of dilatant sites during deformation (McCaig and Knipe, 1990). All of these factors suggest high pressures and the generation of large volumes of fluid (probably focused) during deformation of the host rocks of the Mobrun mine (for further discussion, see Chapter 5, Sec. 5.5.2).

3.5.5 Remobilization of sulphide ore

Of course, the massive sulphide orebodies at Mobrun were also subject to the same regional tectonic forces as their wallrocks and could also have been affected by pressure-solution processes. It is probable, therefore, that portions of the sulphide ores lenses were remobilized in part during metamorphism-deformation. The amount and distance of remobilization is estimated in Chapter 6. It is proposed here that this remobilization was probably limited and controlled by aqueous fluid transport mechanisms operating in conjunction with the dissolution and precipitation processes discussed above.

One potential result of remobilization is the formation of syntectonic pyritic veinlets. There are two possible mechanisms which may explain the source of pyrite in these veinlets. Firstly, extensional sites may have developed in the domain between cleavages, providing sites for redeposition of pre-existing

sulphides. Secondly, the formation of sulphides in syntectonic veins can be partly attributed to iron remobilized from the initial volcanic rocks during metamorphism-deformation, particularly where iron is seen to be depleted at dissolution sites.

3.6 SUMMARY

Petrographic observations and chemical analyses (via X-ray diffraction, X-ray fluorescence spectrometry and the electron microprobe) have shown that the schistosity and cleavage fabrics at Mobrun represent the development of mineralogically and chemically differentiated domains at the microstructural scale. These analyses indicate that a solution-precipitation mechanism played a major role in controlling deformation and mass-transfer processes during the development of pressure-solution cleavage.

The relationships between mineral compositions and their microstructural sites, and distribution of minerals in different microfabrics have been examined by carefully describing microstructural textures and the compositions and concentration of minerals. These analyses indicate that preferential dissolution of minerals occurred during the metamorphism-deformation event. In dissolution sites (schistosity lamellae), quartz has been dissolved, and sericite and other resistant minerals such as rutile have been passively concentrated by mass losses

of more mobile constituents.

Compared to pressure-shadow grains (precipitation sites), fine-grained sericite in schistosity-lamellae commonly shows compositions low in Si and Fe and high in Al and Ti. The correlation between the compositions of sericite in pressure-solution cleavages and in pressure shadows at the thin-section scale indicate short-range fluid migration for mobile elements. In contrast, synmetamorphic-syntectonic extension veins filled with quartz, calcium and pyrite are an obvious manifestations of mass transfer over longer distances than those associated with microscopic pressure-solution sites.

CHAPTER 4

GEOCHEMISTRY OF VOLCANIC ROCKS

4.1 BULK-ROCK ANALYSES

Sixty-two samples of felsic host rocks of the Main Lens (see Fig. 4.1 for sample locations) have been analyzed chemically. A portion of the samples were collected by the author during a visit to the Mobrun Main Lens in August 1991; others were chosen from Riopel's (1989) collection. Chemical analyses for major elements in glass beads were done by X-ray fluorescence at McGill University; trace elements in pressed powder where analyzed at the Université de Montréal using instrumental neutron activation techniques (Table 4.1a,b).

The host rocks of the Mobrun mine are variably deformed. The wallrocks are highly schistose close to the orebody, and they grade outward from the orebody into relatively undeformed and less altered rhyolite. The 62 samples were separated into two groups based on megascopically and microscopically visible criteria: group 1 is essentially undeformed or least-deformed, with altered compositions resulting only from hydrothermal alteration (sericitization, silicification, weak chloritization); group 2 shows evidence of intense deformation, with altered compositions resulting from both hydrothermal alteration and metamorphism-deformation events (sericitization, silicification and weak

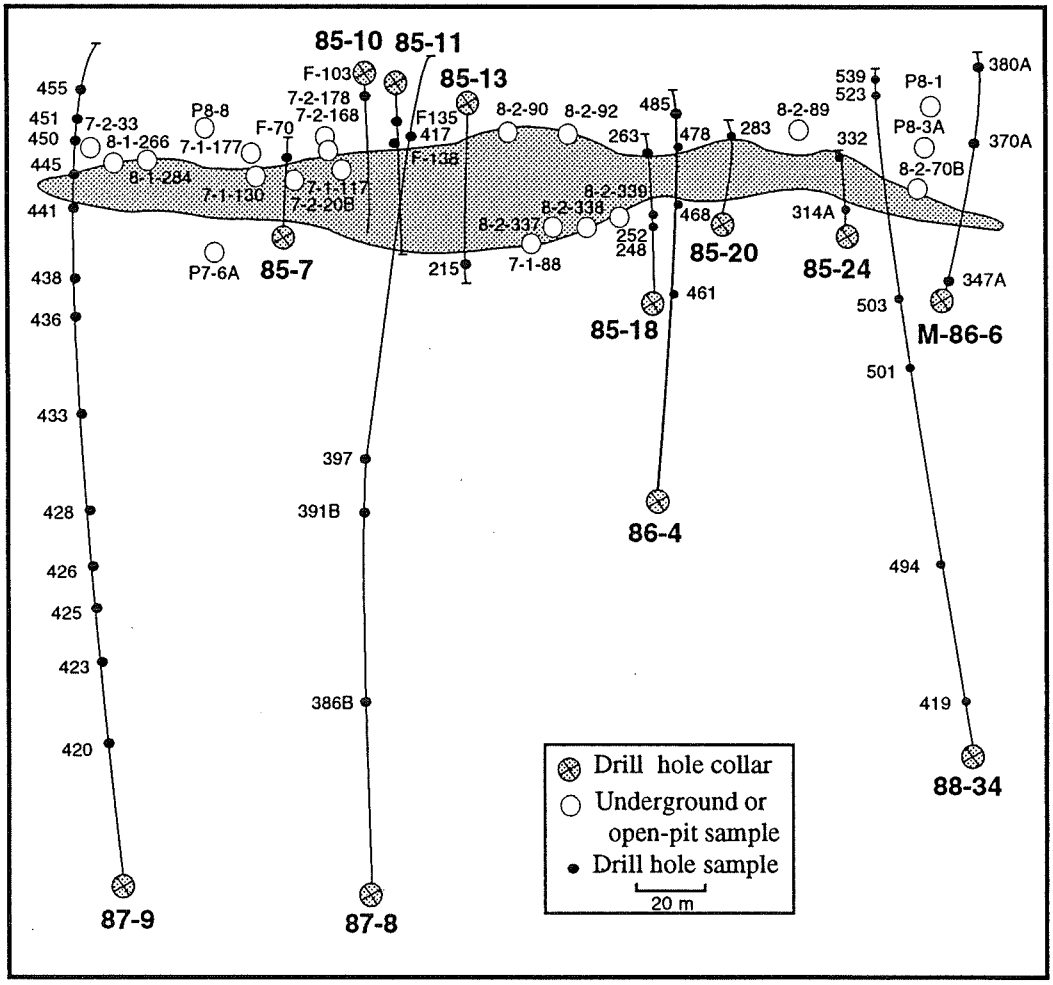

Fig. 4.1 Vertical projection to surface of drill holes and underground samples from Main Lens used in this study.

chloritization associated with foliation).

4.2 IMMOBILE ELEMENTS

A number of studies of volcanogenic massive sulphide deposits in the Noranda and Matagami regions (MacLean and Barrett, 1993; Barrett et al., 1991, 1993; MacLean, 1991; MacLean, 1988; MacLean, 1990; MacLean and Kranidiotis, 1987) have stressed the identification and use of elements that remain immobile during hydrothermal alteration. These investigations show that most major elements (K, Na, Ca, Si, Mg, Mn and P) and many trace elements are mobile during hydrothermal alteration and metamorphism, and cannot be used to identify and classify the precursor compositions. In contrast, Al, Ti, Zr, Y, and HREE are commonly immobile (inert) during alteration and metamorphism, and they are now widely used for precursor and affinity identification. These immobile elements are mainly hosted by chemically resistant minerals such as apatite, zircon and rutile which show little evidence of dissolution or precipitation during alteration and metamorphism (Pearce and Cann, 1973; Winchester, 1975).

Nevertheless, it is important to confirm the immobility of these elements in each study area. A simple and convenient test of element immobility uses binary plots of chemical data from a rock unit that was initially chemically homogeneous

Table 4.1a Composition of representative Mobrun footwall volcanic rocks.

Location	Sample No.	SiO2 (%)	TiO2 (%)	Al2O3 (%)	FeO* (%)	MnO (%)	MgO (%)	CaO (%)	Na2O (%)	K2O (%)	P2O5 (%)	LOI (%)	S (%)	Rb (ppm)	Sr (ppm)	Nb (ppm)	Zr (ppm)	Y (ppm)	Ba (ppm)	Zr/Y	Total
Altered (least deformed) samples:																					
85-13	215	77.80	0.20	10.28	4.84	0.00	0.00	0.02	0.4	2.74	0.03	3.50	0.00	49	18	13	304	36	143	8.4	99.9
85-18	248	75.33	0.25	12.42	4.03	0.00	0.15	0.09	0.76	3.36	0.02	3.55	2.95	52	12	15	351	39	351	8.9	103.0
85-18	252	74.46	0.25	13.89	1.73	0.05	0.29	0.96	3.98	2.12	0.05	2.10	2.71	34	25	15	354	46	369	7.7	102.7
88-6	347-A	73.20	0.24	13.63	1.68	0.01	0.33	0.41	0.45	7.98	0.06	1.44	0.70	88	29	14	354	51	1432	6.9	100.3
87-8	386-B	73.15	0.26	14.28	1.33	0.02	0.62	1.95	4.64	1.66	0.05	2.06	0.33	26	93	16	384	68	327	5.6	100.4
87-9	420	77.49	0.22	12.75	0.47	0.01	0.00	1.12	6.36	0.51	0.06	0.85	0.01	13	60	14	335	52	286	6.4	99.9
87-9	423	74.38	0.25	13.49	3.27	0.04	1.53	1.57	1.59	2.23	0.04	2.11	0.02	62	136	16	374	55	356	6.8	100.6
87-9	425	73.28	0.25	14.05	1.52	0.03	0.54	1.59	5.62	1.09	0.05	1.85	0.00	20	83	16	382	55	222	6.9	99.9
87-9	426	70.49	0.23	12.95	1.34	0.06	0.45	4.06	4.08	1.90	0.05	4.02	0.01	31	70	16	355	53	323	6.7	99.7
87-9	428	72.50	0.24	14.24	0.84	0.03	0.22	2.25	5.06	1.87	0.05	2.45	0.02	30	74	15	371	43	328	8.5	99.9
87-9	433	70.03	0.25	13.71	3.44	0.11	1.81	2.25	0.22	4.21	0.04	4.11	0.01	103	38	15	381	57	371	6.7	100.3
87-9	436	73.42	0.23	13.11	1.46	0.05	0.33	1.63	3.81	2.38	0.05	2.20	0.34	45	47	14	344	37	283	9.3	99.1
87-9	438	66.97	0.24	13.12	6.66	0.15	0.32	2.44	0.4	3.57	0.04	5.60	5.10	51	31	14	334	49	421	6.9	104.7
87-9	441	75.59	0.25	13.08	1.75	0.02	0.62	1.08	3.79	1.88	0.05	1.71	0.01	33	52	15	360	45	365	7.9	99.9
86-4	461	71.17	0.26	13.94	3.45	0.05	0.51	1.51	3.31	2.94	0.05	2.49	0.01	54	37	16	375	54	502	7.0	99.8
88-34	494	72.08	0.24	12.82	2.78	0.11	0.42	2.05	2.49	3.06	0.05	3.12	0.18	50	34	14	350	54	414	6.5	99.5
88-34	501	72.58	0.25	13.56	2.44	0.06	0.37	1.57	3.84	2.40	0.05	2.69	0.00	42	43	16	367	53	454	7.0	99.9
Level-1	7-1-88	78.96	0.23	12.70	1.82	0.00	0.00	0.03	0.45	3.36	0.03	2.45	1.20	51	19	14	330	44	243	7.6	101.3
Level-2	8-2-338	80.15	0.22	12.07	1.84	0.00	0.00	0.03	1.16	1.98	0.01	2.38	1.16	36	64	13	318	32	154	10.0	101.1
Level-2	8-2-339	67.95	0.32	17.27	2.18	0.06	0.08	0.99	5.44	1.82	0.04	2.79	0.07	42	59	23	352	44	286	8.0	99.1
Open-pit	P7-6A	65.92	0.29	18.14	3.59	0.02	2.44	0.03	0.49	5.47	0.03	3.45	0.03	112	8	24	351	72	671	4.9	100.0
Deformed samples:																					
85-24	314-A	70.72	0.29	16.80	2.92	0.00	0.42	0.15	0.26	5.43	0.06	3.24	1.23	77	7	13	303	42	564	7.2	101.6
87-8	391-B	67.44	0.35	19.15	0.95	0.00	0.79	0.80	3.78	4.40	0.06	2.37	0.01	76	43	18	511	80	876	6.3	100.3
87-8	397	58.94	0.36	20.17	6.62	0.01	1.58	0.19	0.74	6.80	0.07	4.14	1.62	132	11	21	532	77	762	6.9	101.4
86-4	468	71.23	0.24	12.79	6.11	0.00	0.15	0.04	0.35	3.67	0.04	4.86	5.20	61	8	13	324	48	261	6.8	104.8
88-34	503	71.39	0.22	12.38	4.07	0.12	0.27	2.14	0.22	3.73	0.04	4.29	2.50	55	19	14	322	47	331	6.9	101.4
Level 2	8-2-337	76.39	0.27	16.78	0.51	0.00	0.01	0.01	1.71	2.36	0.02	2.18	0.13	47	110	15	421	42	2	10.0	100.4
Least altered samples from Barrett et al. (1992), average of 4 samples:																					
		77.48	0.21	11.98	2.17	0.04	0.53	1.79	4.41	1.36	0.04			24	53	13	334	43		7.8	100.1

Table 4.1b Composition of representative Mobrun hangingwall volcanic rocks.

Location	Sample No	SiO2 (%)	TiO2 (%)	Al2O3 (%)	FeO* (%)	MnO (%)	MgO (%)	CaO (%)	Na2O (%)	K2O (%)	P2O5 (%)	LOI (%)	S (%)	Rb (ppm	Sr (ppm	Nb (ppm	Zr (ppm	Y (ppm	Ba (ppm)	Zr/Y	Total
Altered (least deformed) samples:																					
85-24	332	76.10	0.23	13.08	1.19	0.03	0.58	1.44	0.98	3.32	0.04	2.78	0.03	63	34	18	256	44	710	5.9	99.9
88-6	370-A	75.58	0.22	12.56	2.89	0.02	0.39	0.65	1.39	3.32	0.05	2.61	1.48	57	33	17	243	46	739	5.3	101.3
88-6	380-A	73.57	0.14	9.98	1.27	0.13	0.46	4.59	3.38	1.38	0.03	4.66	0.02	36	133	17	219	56	215	3.9	99.7
87-8	417	74.25	0.18	11.66	2.64	0.07	0.00	2.07	4.64	1.61	0.05	2.11	1.46	29	104	19	266	66	286	4.0	100.8
87-9	445	75.51	0.21	13.06	2.23	0.02	1.52	2.01	1.81	1.76	0.04	1.96	0.01	59	167	19	259	70	364	3.7	100.2
87-9	450	78.21	0.19	11.43	2.35	0.01	1.37	0.24	2.73	1.85	0.03	1.60	0.28	43	48	16	227	60	392	3.8	100.4
87-9	455	68.34	0.23	11.85	2.22	0.09	1.57	4.35	1.07	3.22	0.05	6.54	0.10	72	84	14	337	53	494	6.4	99.7
86-4	485	72.32	0.20	12.19	3.82	0.06	2.44	1.72	1.62	1.73	0.05	3.44	0.28	50	60	28	315	316	460	1.0	100.0
88-34	523	76.58	0.17	12.00	2.18	0.03	0.39	1.28	2.32	3.07	0.02	2.04	0.06	74	28	22	294	71	368	4.1	100.2
Level-2	7-2-168	71.73	0.27	15.80	1.84	0.02	1.05	0.41	4.27	2.14	0.04	1.62	0.27	58	86	21	310	58	1098	5.3	99.6
Level-2	7-2-178	71.19	0.16	11.64	3.19	0.15	1.56	3.04	0.65	2.95	0.02	5.23	0.01	94	68	21	275	83	540	3.3	99.9
Level-1	8-1-266	74.86	0.17	12.29	3.48	0.08	1.06	0.91	0.86	3.80	0.02	2.49	0.01	139	26	22	289	73	560	3.9	100.1
Level-1	8-1-284	75.57	0.16	12.18	3.29	0.08	0.92	1.31	1.56	2.26	0.02	2.55	0.01	81	60	22	290	74	480	3.9	100.0
Level-2	8-2-70B	69.58	0.18	13.15	3.64	0.10	2.21	2.83	0.65	3.03	0.02	4.61	0.01	100	64	24	303	97	4	3.1	100.1
Level-2	8-2-90	75.27	0.16	11.87	3.24	0.07	0.84	1.04	1.66	2.77	0.02	2.85	0.00	87	49	23	291	76	515	3.8	99.9
Level-2	8-2-92	74.32	0.16	11.50	2.83	0.10	1.41	1.73	1.00	3.02	0.02	4.00	0.00	99	45	21	272	62	4	4.4	100.1
85-10	F-103	72.28	0.20	14.19	2.73	0.04	0.62	0.79	3.07	4.40	0.03	1.49	0.01	96	59	25	336	72	617	4.6	100.0
85-11	F-135	75.96	0.18	12.60	3.18	0.06	1.05	0.88	0.70	3.08	0.02	2.48	0.01	98	32	23	300	71	618	4.2	100.3
85-7	F-70	74.66	0.16	12.01	4.26	0.04	2.42	0.29	0.34	2.47	0.04	3.07	0.96	71	33	27	306	124	286	2.5	100.8
Open-pit	P8-1	74.62	0.18	12.27	3.01	0.06	1.30	1.26	1.09	3.05	0.02	3.16	0.01	97	41	22	295	73	491	4.1	100.1
Open-pit	P8-3A	77.23	0.13	11.36	3.27	0.05	1.87	0.39	0.29	2.51	0.02	2.64	0.01	78	30	21	265	62	400	4.3	99.9
Deformed samples:																					
85-18	263	66.95	0.29	16.90	4.80	0.03	3.08	0.57	0.79	3.27	0.03	3.55	0.01	98	45	50	620	110	401	5.6	100.4
85-20	283	75.67	0.22	12.50	3.71	0.03	2.44	0.10	0.61	2.07	0.02	2.54	0.00	63	58	41	454	99	224	4.6	100.0
87-9	451	64.07	0.17	10.70	9.65	0.03	1.16	2.15	2.18	2.09	0.02	6.07	7.42	45	57	14	197	54	267	3.6	105.8
86-4	478	82.40	0.16	9.52	2.71	0.01	0.56	0.18	1.21	0.92	0.02	3.83	0.15	22	71	12	187	32	155	5.9	101.7
Level-1	7-1-117	62.79	0.34	19.06	5.53	0.05	2.20	0.69	0.96	4.09	0.03	2.91	0.01	119	47	60	693	142	1093	4.9	98.9
Level-1	7-1-130	64.71	0.28	20.11	4.21	0.04	1.04	0.17	1.25	5.06	0.03	3.61	0.01	149	25	38	485	100	946	4.8	100.7
Level-1	7-1-177	68.46	0.26	15.12	4.62	0.04	3.36	0.87	1.11	2.76	0.04	4.26	0.05	83	42	42	463	90	339	5.1	101.1
Level-2	7-2-33	56.45	0.39	22.78	7.47	0.03	2.49	0.34	0.28	5.50	0.04	3.48	0.28	117	23	71	813	187	2	4.4	99.6
85-11	F-138	72.33	0.18	12.84	4.53	0.05	2.07	1.05	0.34	2.88	0.04	5.58	0.96	86	32	28	272	73	402	3.8	102.9
Open-pit	P8-8	56.68	0.38	21.52	7.63	0.05	2.11	0.07	0.49	5.11	0.06	2.41	2.29	139	54	60	732	166	505	4.4	99.0
Least altered samples:																					
88-34	539	73.85	0.17	12.21	3.40	0.08	0.88	1.49	4.30	0.99	0.02	2.07	0.01	30	101	22	292	85	236	3.4	99.5
Level-2	8-2-89	76.21	0.14	11.30	2.41	0.08	0.44	1.71	4.50	0.79	0.02	2.25	0.01	25	174	20	257	78	205	3.3	99.9
Barrett et al. (n=3)		78.22	0.18	12.26	1.03	0.05	0.21	1.40	4.87	1.79	0.00			41	52	20	291	67		4.3	100.1
Dike samples:																					
88-34	514	53.40	0.90	15.29	7.98	0.16	3.30	6.20	5.00	0.12	0.43	6.36	2.52	4	253	9	174	43	121	4.1	101.7
Level-2	7-2-20B	47.93	0.92	15.59	5.38	0.28	5.21	6.00	5.00	0.03	0.44	4.66	0.03	3	31	8	174	47	103	3.7	91.5

and has been subsequently exposed to alteration or metamorphism. With additions or losses in mobile components, data for immobile element pairs typically form linear trends that pass close to or through the origin (MacLean and Barrett, 1993; MacLean, 1990; MacLean and Kranidiotis, 1987). In our case, pairs of Al_2O_3, TiO_2, Zr, Y and Nb generally exhibit regression correlations near unity, thereby confirming their high degrees of immobility (Figs. 4.3, 4.4, 4.5).

4.3 LITHOLOGICAL IDENTIFICATION

The mineralogical, textural and chemical identities of the Mobrun rocks are obscured by hydrothermal alteration and metamorphism-deformation and their original lithologies cannot be reliably distinguished by petrographic studies or chemical analyses. Therefore, the original rock types, their chemical affinities and the mass changes that accompanied alteration are determined through the use of major and trace elements that have been demonstrated to have been immobile.

4.3.1 Rock types

In order to measure the mass losses and gains in host rocks at Mobrun (Chapter 5), it is important to establish the compositions of the initial parent rocks. The parent rock types for the Mobrun samples are estimated here from the Zr/TiO_2 vs Nb/Y diagram of Floyd and Winchester (1977)(Fig. 4.2).

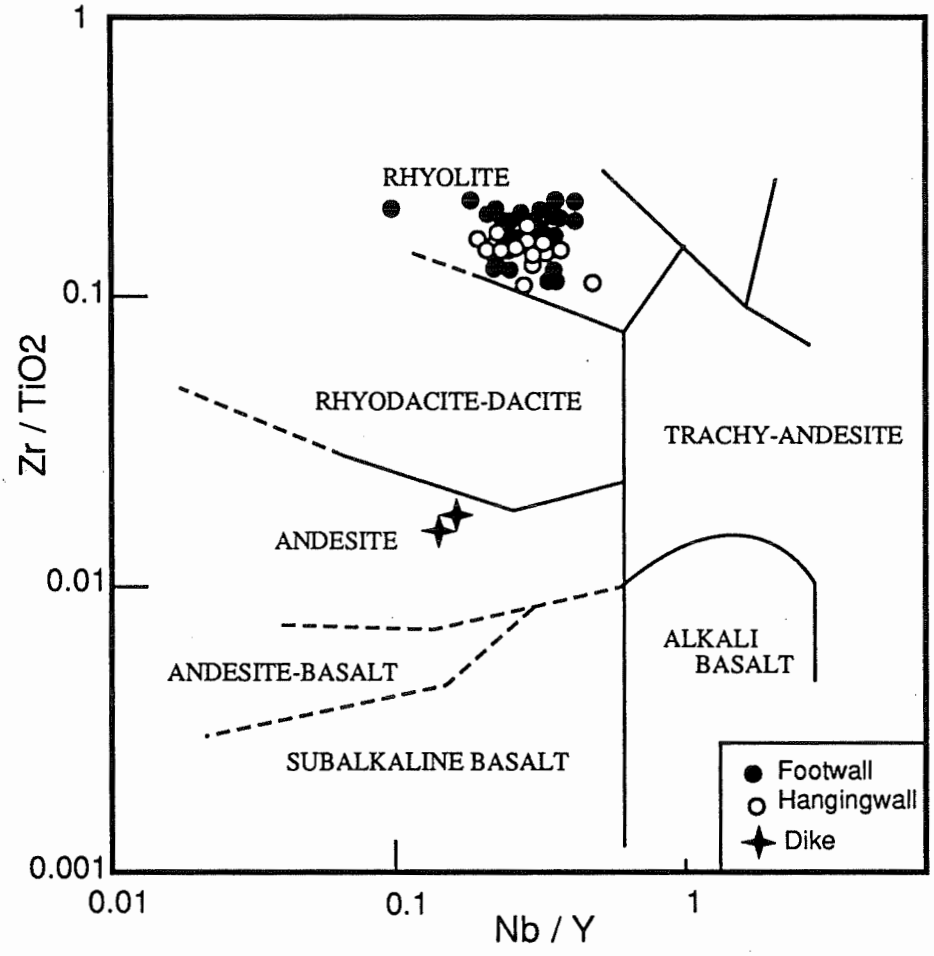

Fig. 4.2 Plot of Zr/TiO_2 against Nb/Y for the Mobrun rocks. Footwall and hangingwall samples fall within the rhyolite field. Two samples from a dike within the sulphide orebody plot in the andesitic field (diagram from Winchester and Floyd, 1977).

All samples from the footwall and hangingwall, except two dike samples, plot within the rhyolite field, confirming the original felsic composition of most Mobrun lithologies. These compositions were subsequently changed mineralogically and chemically by syn-volcanic hydrothermal alteration and overprinted metamorphism-deformation effects.

4.3.2 Host rock affinities

The common presence of highly deformed rocks among the Mobrun rhyolites requires an identification of their initial chemical affinities to determine whether different intensities of deformation had any effect on the distribution of immobile elements. By considering the intensities of deformation (estimated from the extent of foliation), the previously determined affinities of the Mobrun rocks (Caumartin and Caillé, 1990; Barrett et al., 1992) have been tested here using a series of immobile elements (Zr, Y, Nb) (Table 4.1).

A basic step toward identification of the initial character of volcanic rocks is to determine if they belong to a tholeiitic, transitional or calc-alkaline series. A plot of the Zr-Y pair (Fig. 4.3a) indicates that the Mobrun hangingwall rocks have a tholeiitic affinity with Zr/Y ratios of 3.1 to 5.9 (average = 4.5), whereas the footwall rhyolites have a mildly calc-alkaline affinity with Zr/Y ratios of 6.4 to 10.0 (average = 8). These conclusions derive from comparisons with prior analyses of tholeiitic rocks in Abitibi greenstone terrains which have Zr/Y ratios ranging from

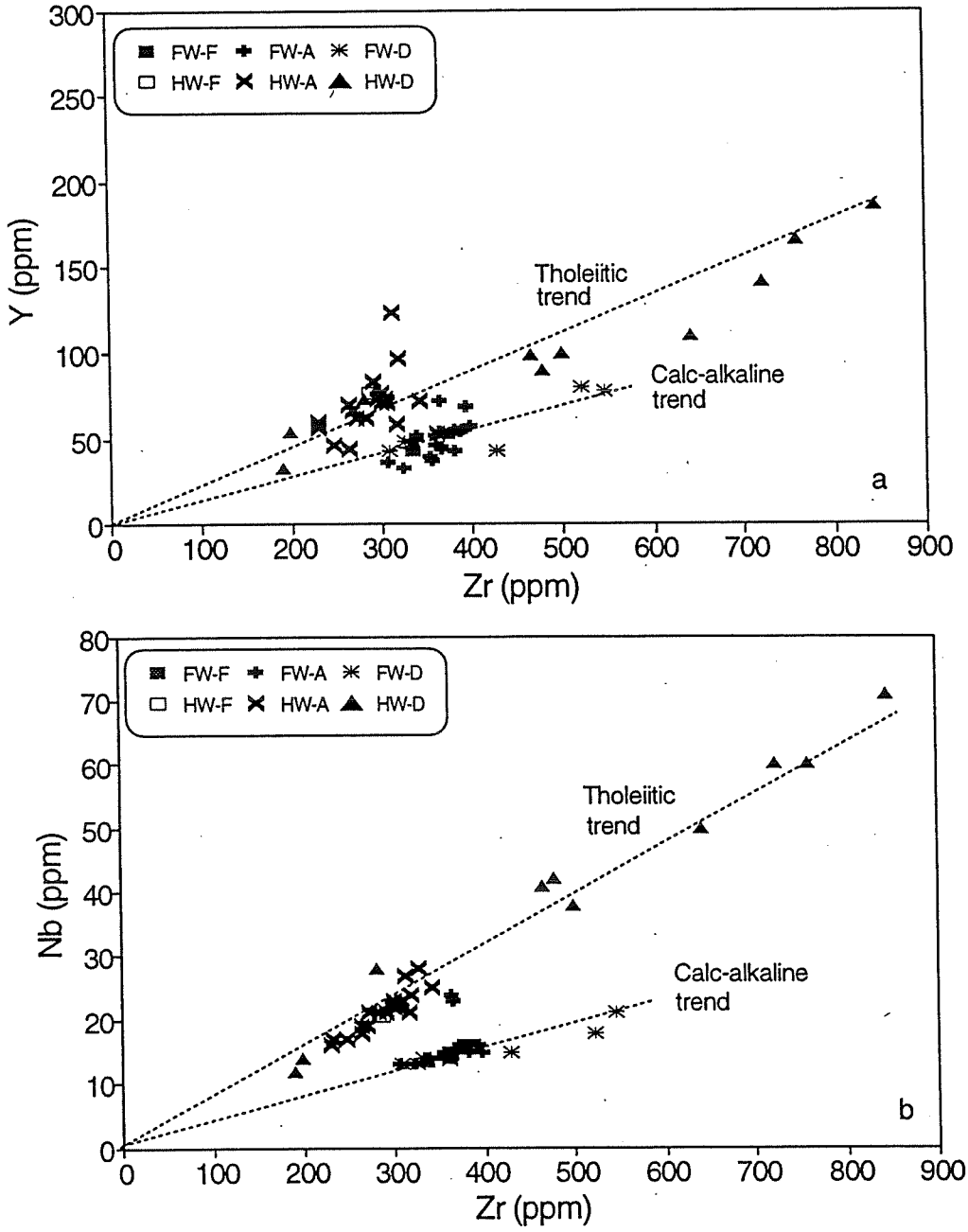

Fig. 4.3 Y-Zr **(a)** and Nb-Zr **(b)** plots for rhyolite of the Main Lens samples identify two distinct units, mildly calc-alkaline and tholeiitic, with the mine stratigraphy. Symbols: FW-F = footwall least-altered, FW-A = footwall altered, FW-D = footwall metamorphosed-deformed, HW-F = hangingwall least-altered, HW-A hangingwall altered and HW-D hangingwall metamorphosed-deformed rocks.

3 to 5, and calc-alkaline rocks which generally have ratios greater than 7 (Pearce and Cann, 1973; Lesher et al., 1986).

A plot of the incompatible and immobile Nb-Zr pair (Fig. 4.3b) again reveals a two-fold separation of volcanic data consistent with these two lithologic types: samples identified as transitional calc-alkaline have a lower Nb-Zr slope than the tholeiitic series. Other studies of Abitibi volcanic rocks show similar ranges for rocks of calc-alkaline and tholeiitic compositions (MacLean and Kranidiotis, 1987; MacLean and Hoy, 1991; Liaghat and MacLean, 1992).

One sample of hangingwall rhyolite immediately above the orebody shows a calc-alkaline affinity. Barrett et al., (1992) determined that the contact between mildly calc-alkaline and tholeiitic rhyolite is about 10 metres above the orebody in the eastern part of the deposit.

In both diagrams (Fig. 4.3a and 4.3b), immobile elements of intensely foliated samples plot within the same fields as their precursors, but their abundances are generally higher or lower compared to those of least-deformed samples. This observation confirms the immobility of so-called immobile elements in highly deformed samples. Significant enrichments or depletions of immobile elements within deformed samples may result from mass transfers associated with both hydrothermal alteration and metamorphism-deformation events.

The concentration of immobile elements in deformed and altered rhyolitic rocks can also be examined through plots of Al_2O_3-TiO_2 (Fig. 4.4) and TiO_2-Zr

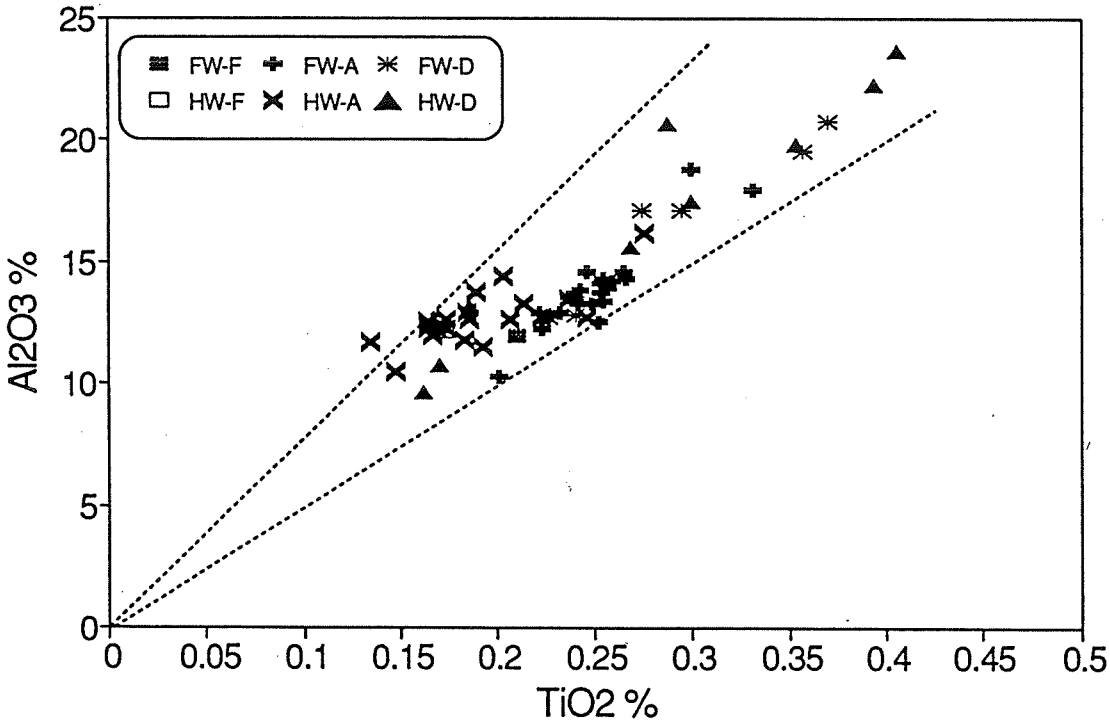

Fig. 4.4 Plot of Al_2O_3 versus TiO_2 of both footwall (mildly calc-alkaline) and hangingwall (tholeiitic) of the Main Lens rhyolite. Immobile element pairs in least-altered, altered and deformed samples plots along the narrow field toward the origin of the diagram. Symbols same as Fig. 4.3.

(Fig. 5.3, Chapter 5). MacLean and Barrett (1993) define linear alteration trends that project to the origin, indicating the immobility of the Ti, Al, Zr group. Although, footwall and hangingwall rhyolites are of different affinities, they plot almost along one fractionation line, probably because major-element compositions tend to have similar values at the end of fractionation in both the tholeiitic and calcalkaline series (Barrett et al., 1993).

4.4 RARE-EARTH ELEMENTS

Rare-earth elements (REEs) are commonly used to distinguish between tholeiitic and calc-alkaline rocks associated with Archean volcanogenic massive sulphide deposits (MacGeehan and MacLean, 1980a,b; Lesher et al., 1986). Chondrite-normalized REE profiles having La_n/Yb_n slopes of less than 2.0 are generally designated as tholeiitic, whereas those with slopes greater than 4.0 are considered to be calc-alkaline (Lesher et al., 1986). However, it is possible that the La_n/Yb_n slopes defined in these prior studies include hidden hydrothermal alteration effects, i.e., that the apparently fresh rocks sampled had in fact been modified and their REE ratios changed during a widespread cryptic hydrothermal alteration event.

Heavy REEs (HREEs: Lu, Yb, Tm) are generally considered to be very immobile during water-rock interaction. On the other hand, the light REEs

(LREEs: La, Ce, Nd) exhibit important mobilities in hydrothermal environments, as in the case of hydrothermally altered rhyolites associated with massive sulphide deposits (Campbell, 1984; MacLean, 1988). The degree of REE mobilization decreases steadily from La to Lu.

REE data for volcanic units of the Main Lens at the Mobrun mine are given in Table 4.2a. The data were obtained by neutron-activation analysis of two highly deformed samples taken immediately above the sulphide orebody and two less-deformed samples taken from the edges of the orebody in hangingwall rocks. REE analyses of three rhyolites from the Main complex footwall rocks (Barrett et al., 1992) are also presented in Table 4.2a. Note that all of the samples have undergone extensive hydrothermal alteration.

REE profiles of altered footwall rhyolites at the Mobrun mine have similar shapes and slopes, with an average La_n/Yb_n ratio of 4.2 (Fig. 4.5b, Table 4.2b). Although the slope expected to vary due to LREE mobility during hydrothermal alteration, all of the slopes are within the normal range of felsic calc-alkaline rocks.

The average slope (La_n/Yb_n) of the two altered least-deformed tholeiitic samples (Zr/Y = 3.8) of the Mobrun hangingwall rocks is 4.2 (Fig. 4.5a, Table 4.2b). This slope is considerably higher than that for volcanic rocks normally designated as tholeiitic (La_n/Yb_n less than or equal to 2; Lesher et al., 1986). Because these rocks are strongly altered, it is possible that certain quantities of

a)	HANGINGWALL				FOOTWALL*		
Location	85-20	88-6	87-9	O.P.	MO18	MO18	MO18A
Sample	283	380A	445	P8-8	52.7	89.9	128
La	50.9	34.6	44.5	33.4	34.0	29.0	32.0
Ce	115.0	69.0	88.0	67.0	79.0	62.0	74.0
Nd	71.0	34.0	40.0	42.0	38.0	29.0	35.0
Sm	19.7	8.8	9.5	13.9	8.2	7.1	7.8
Eu	3.5	1.4	1.3	2.4	1.6	1.4	1.6
Tb	3.1	1.3	1.4	3.7	1.6	1.1	1.4
Ho					2.1	1.6	1.9
Tm	1.4	0.8	0.9	3.1			
Yb	9.8	5.6	7.2	22.0	5.7	3.7	5.3
Lu	1.4	0.9	1.1	3.2	1.0	0.7	1.0

b)	HANGINGWALL				FOOTWALL*			
Sample	283	380A	445	P8-8	52.7	89.9	128	Chondrite
La	207.8	141.2	181.6	136.3	138.8	118.4	130.6	0.25
Ce	180.3	108.2	137.9	105.0	123.8	97.2	116.0	0.64
Nd	149.8	71.7	84.4	88.6	80.2	61.2	73.8	0.47
Sm	127.9	57.1	61.7	90.3	53.2	46.1	50.6	0.15
Eu	60.5	24.7	21.9	40.7	27.6	24.1	27.6	0.06
Tb	82.1	33.4	37.9	96.3	42.1	28.9	36.8	0.04
Ho					36.8	28.1	33.3	0.06
Tm	54.9	31.4	35.3	121.6				0.03
Yb	59.4	33.9	43.6	133.3	34.5	22.4	32.1	0.17
Lu	57.6	34.4	42.4	129.6	39.6	26.0	38.0	0.03
La/Yb	3.50	4.16	4.16	1.02	4.02	5.28	4.07	
Zr/Y	4.60	3.90	3.70	4.40	6.60	7.40	6.30	
Hf	13.2	5.5	7.0	21.5				

* data from Barrett et al. (1992)
** Chondrite data from Evenson et al. (1978)

Table 4.2 (a) REE data for footwall and hangingwall rocks of the Main Lens. Hangingwall samples include two highly deformed samples (283 and P8-8) and two altered samples. (b) Chondrite- normalized data from (a).

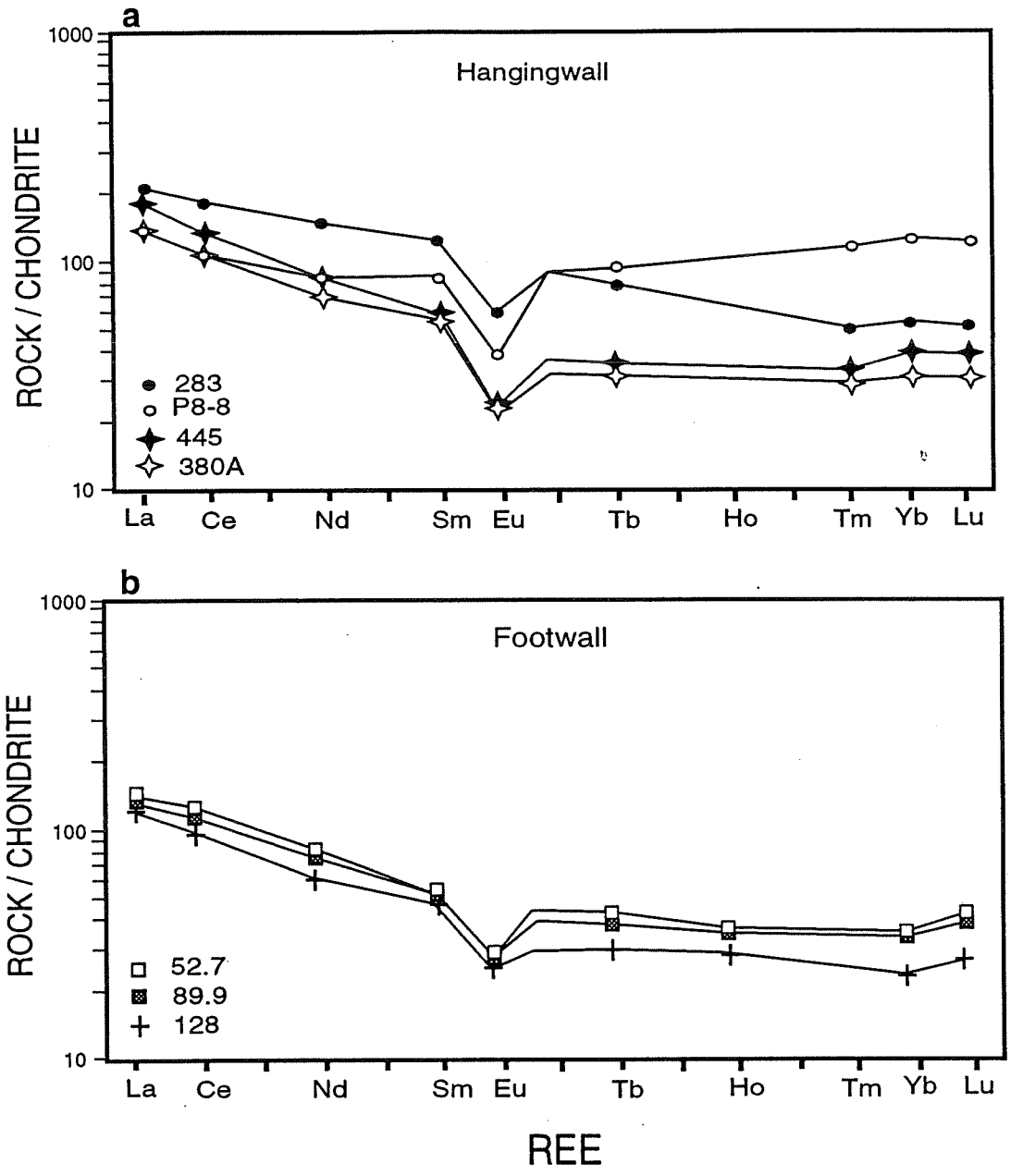

Fig. 4.5 Chondrite-normalized REE profiles for Mobrun rhyolite. **(a)** Hangingwall altered rhyolite (La_n/Yb_n = 4.2); samples # 283 and P8-8 are highly deformed (La_n/Yb_n = 3.5 and 1). **(b)** Footwall rhyolite (La_n/Yb_n = 4.6); data from Barrett et al., (1992).

LREEs were added during hydrothermal alteration, thereby increasing the La_n/Yb_n ratios. The REE profiles of the two deformed hangingwall samples show La_n/Yb_n ratios of 3.5 and 1.0 (Fig. 4.6a, Table 4.2b). Additions and subtractions of LREEs relative to La within the two samples have clearly varied, implying that variable LREE concentrations have resulted from LREE leaching and precipitation during metamorphism-deformation. The main difference between the profiles for least-deformed and deformed rhyolites is the significantly higher HREE concentrations in deformed samples. This difference may result from bulk-mass losses that effectively concentrated immobile REEs during deformation.

All hangingwall samples have strongly negative Eu anomalies. The breakdown of plagioclase, with the accompanying substitution of Eu^{+2} by Ca^{+2}, has apparently liberated Eu^{+2} into solution and led to Eu^{+2} losses which created negative Eu anomalies. The footwall rhyolites also have strongly negative Eu anomalies similar to the hangingwall rhyolites, also indicating Eu^{+2} losses due to Ca^{+2} substitution.

4.4.1 REE mobilities

REE profiles are different between least-deformed and most- deformed samples. For example, the two rock types have distinctly different La_n/Yb_n values. To determine whether the different ratios are related to the degree of mobility of each element, the REEs have been plotted against Hf (Fig. 4.6), an element widely

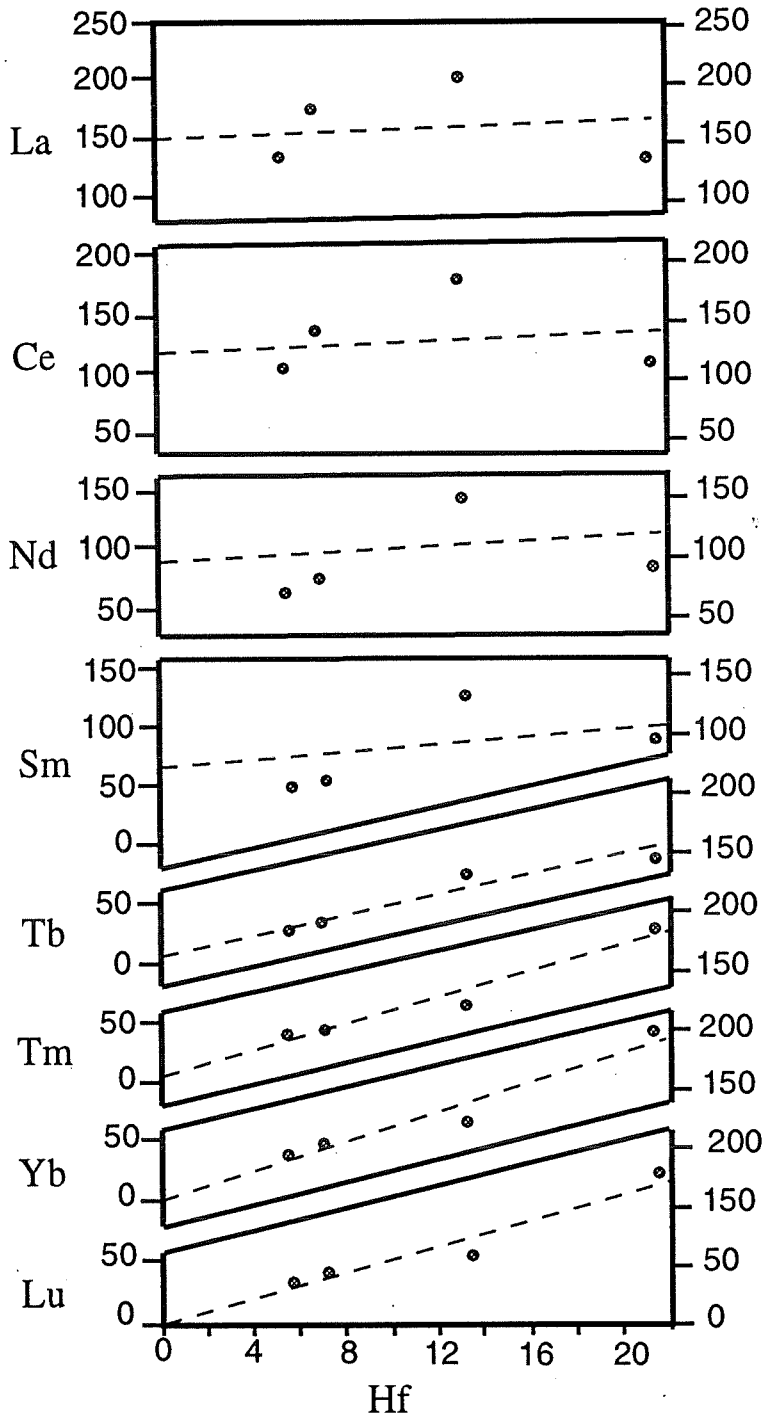

Fig. 4.6 Plot of Hf, a highly incompatible element, against REEs. HREE show a good correlation with Hf as illustrated by the regression lines. LREE are more scattered, indicating mobilization of these elements.

recognized to be incompatible (MacLean and Hoy, 1991). Lu and Yb show good correlations with Hf, indicating that these elements are also highly immobile during metamorphism. For LREEs from La to Sm, there is considerably more scatter in the plots, indicating at least local mobilization of the lighter REEs.

To assess REE mobility during deformation at Mobrun, chondrite-normalized REE values for deformed samples have first been adjusted to the average Lu_n values of the two least-deformed precursors (Table 4.3; Fig. 4.7). This procedure is based on the immobility of Lu as shown by MacLean (1988) and as determined by linear plots with Hf (Fig. 4.6). The normalized patterns reflect additions or depletions in other REEs (relative to Lu) during metamorphism-deformation.

One of the deformed rhyolite samples (Fig. 4.7, sample P8-8) was found to have a REE pattern that is notably depleted in the LREEs and middle REEs (Sm, Eu, Tb). This depletion may have resulted from leaching of mobile elements during deformation. On the other hand, LREE additions in the other deformed sample (#283) may simply reflect a very local transport of mobile REEs to more suitable deformation sites.

c) Sample	283	P8-8	LD
La	138.5	40.39	161.4
Ce	120.2	31.12	123.0
Nd	99.86	26.25	78.06
Sm	85.28	26.74	59.42
Eu	40.34	12.06	23.28
Tb	54.74	28.54	35.66
Tm	36.60	36.02	33.33
Yb	39.60	39.51	38.79
Lu	38.40	38.40	38.40

Table 4.3 Two deformed samples (283 and P8-8) normalized to Lu of least-deformed (LD) samples (see Table 4.2).

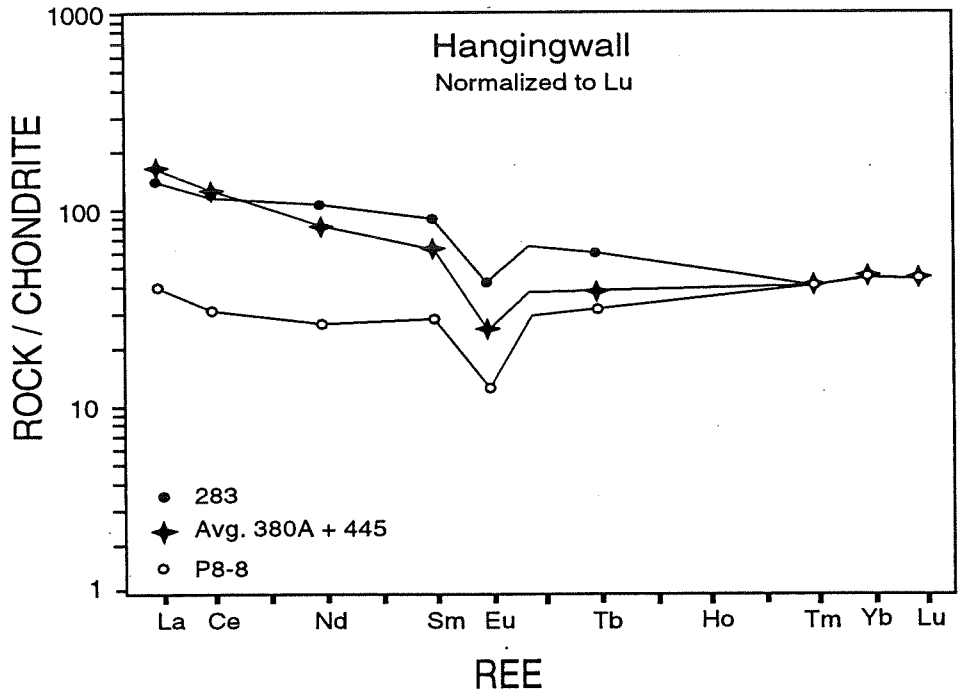

Fig. 4.7 REE data from two deformed rocks (see Figure 4.5) normalized to Lu (the most immobile REE) of the average of two least deformed rocks. The resulting spread of the sample profiles, diverging from Lu to La, are due to REE mobility during metamorphism-deformation.

4.5 NORMATIVE MINERALOGY

Hydrothermal fluids responsible for mineralization at Mobrun have converted fresh host rocks to hydrothermal alteration mineral assemblages. The proportions of these minerals can be estimated from the bulk chemical analyses using standard normative calculations. The normative alteration minerals can be selected from microscopic observations and general occurrences in other deposits in the area. In the Noranda district, the most abundant hydrothermal alteration minerals are quartz, sericite, chlorite, carbonate and minor amounts of albite, epidote, apatite and leucoxene (rutile). Sulphide minerals (pyrite, pyrrhotite, chalcopyrite, and sphalerite) are also present in various amounts in the altered rocks.

Chemical analyses of the altered minerals are used to calculate normative quantities of these minerals. Otherwise, general mineral formulas may be used. The normative minerals were calculated as follows, using a computer spreadsheet program: (1) S is converted to pyrite, the dominant sulphide mineral; (2) Na is converted to albite; (3) K is converted to sericite ($KAl_3Si_3O_{10}(OH)_2$), the only K-bearing mineral formed in the alteration zone; (4) the remaining Al is converted to chlorite (the general formula $(FeMg)_9Al_6Si_5O_{20}(OH)_{16}$ is used here); (5) Ca is converted to epidote and calcite (for simplicity the zoisite end-member $Ca_2Al_3Si_3O_{12}(OH)$ is used); (6) Ti is converted to rutile; (7) P is converted to

apatite; and (8) the remaining Si is converted to quartz.

In Figures 4.8a,b, the arrows show trends from the primary mineral assemblages to altered compositions. In general, the felsic volcanic rocks show a breakdown of albite to quartz + sericite + chlorite, whether they are from the hangingwall or footwall zones.

4.6 DISCUSSION

Geochemical studies (Caumartin and Caillé, 1985; Barrett et al., 1992) have shown that two distinct felsic volcanic series (in general, a calc-alkaline footwall and a tholeiitic hangingwall) occur in the region around the Main Lens orebody. This observation is confirmed by new data presented and interpreted in this study. The close stratigraphic association of the contact between these two rock series with the massive sulphide orebody suggests a genetic relationship between the sulphide orebody and an evolving volcanism. The contrasting lithologies may reflect derivation from slightly different sources of magma.

The Mobrun wallrocks exhibit wide ranges in the concentrations of immobile elements which have been affected by both synvolcanic hydrothermal alteration and post-volcanic metamorphism-deformation processes. Furthermore, there is a detectable correlation between immobile-elements concentrations and the intensity of foliation in the metamorphosed rhyolite. Highly foliated rocks are

clearly enriched or depleted in Ti, Y and Zr compared to slightly foliated rocks. This correlation provides further support for our suggestion that the immobile elements were passively concentrated in dissolution sites or depleted in precipitation sites during the development of a cleavage associated with pressure-solution processes.

Intensely foliated samples also contain relatively higher concentration of REEs than other samples. REEs may be hosted by high field-strength element minerals such as zircon, rutile or apatite, where these minerals typically show good correlations with Zr, Ti and P contents. Or they may, like other large cations such as K and Rb, be incorporated in cation exchange sites in sericite. These REE host minerals are considered to have been resistant and insoluble during metamorphism-deformation at Mobrun (Chapter 3). The enrichment of HREEs within the deformed rocks agrees with previous observations in which immobile elements were found to be enriched within highly deformed samples.

Sericitization is widespread in both the stratigraphic hangingwall and footwall of the Mobrun Main Lens. The severe hydrothermal alteration of wallrocks involved early sericitization of plagioclase, forming an essentially quartz+sericite alteration assemblage. Sericite growth in this hydrothermal phase of alteration is limited by the original aluminum content of the parent rock because this component was immobile. Chloritization followed a similar alteration path, but at a lower intensity.

This initial hydrothermal phase was followed by extensive leaching of quartz during metamorphism-deformation, with the residual sericite forming a sericite schist. Both processes (hydrothermal alteration and deformation-metamorphism) are illustrated on the normative mineralogy diagrams (Figs. 4.8a,b). The reasons for these trends can be partially evaluated using mass changes plots (Chapter 5). The calculations of gains and losses of materials during hydrothermal alteration and metamorphism-deformation correlate with the mineral assemblage formed.

In Chapter 3, it was argued that the development of dissolution precipitation cleavage can be seen as resulting from the partitioning of short-range mass transfers between dissolution and precipitation domains. In the dissolution sites, there were net mass losses, whereas in the precipitation sites, there were net mass gains, which led to approximately equal mass gains and losses overall at the hand-specimen scale. Thus, for short-range mass transfers (on the order of a few centimetres), the metamorphism-deformation effects may be considered to have occurred within a closed system.

However, this argument is not valid for many samples due to the following evidence (see also mass change calculations in Chapter 5). The immobile elements of intensely foliated samples in all binary immobile diagrams plot within the same fields as their precursors (Figs. 4.3, 4.4), but their quantities generally occur in significantly higher or lower proportions compared to the equivalent least-deformed samples. The concentration and depletion of immobile elements are

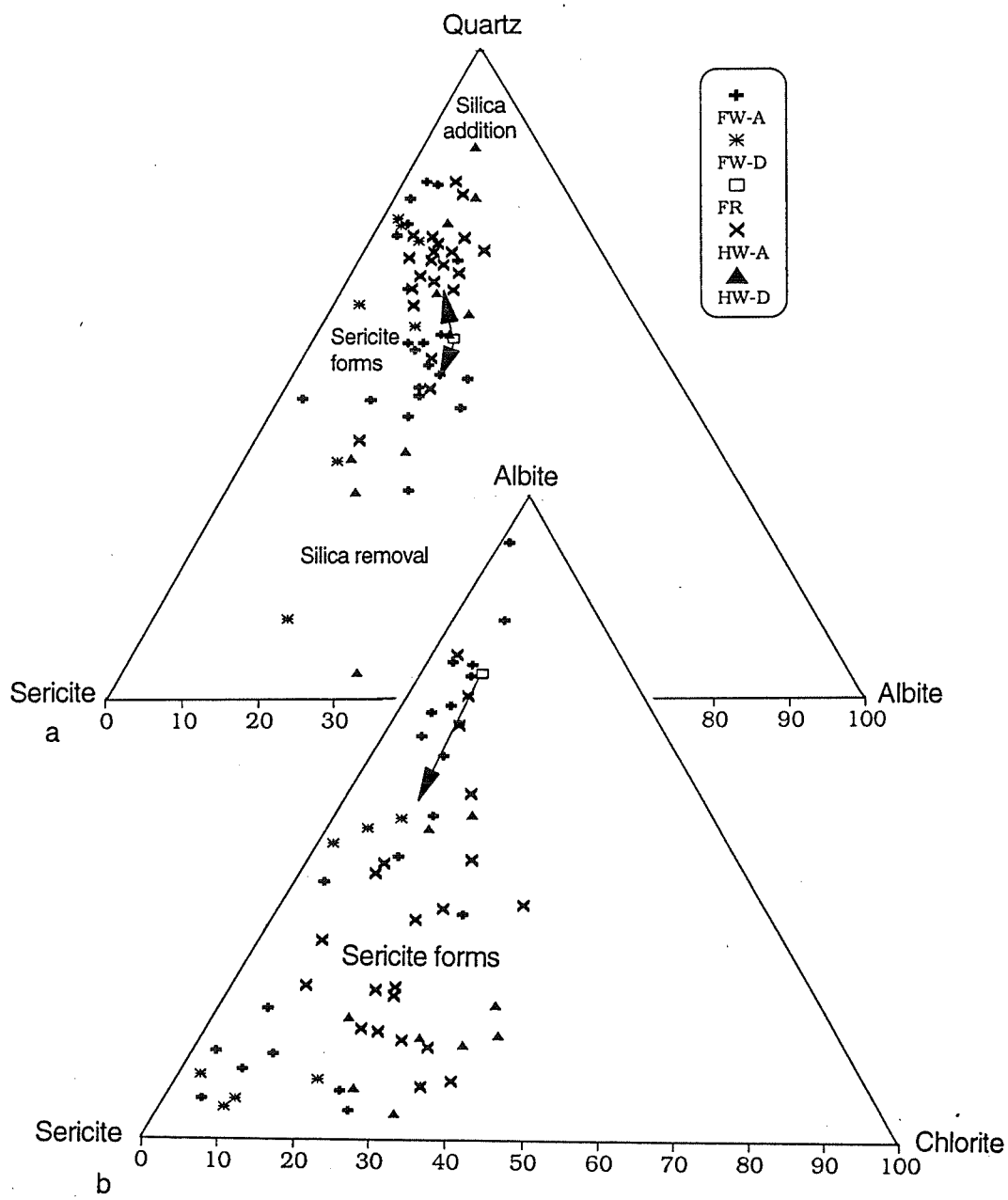

Fig. 4.8 Proportions of minerals in Mobrun rhyolite, estimated from bulk chemical analyses using a normative calculation procedure (see text). **(a)** with breakdown of albite during hydrothermal alteration and metamorphism-deformation, fresh rhyolite shift to a quartz-sericite rock. **(b)** sericitization after albite is the dominate mineralogical change in the Mobrun rhyolite. Only a minor portion of the rocks are moderately chloritized. Symbols same as Fig. 4.3.

related to losses and gains of mass respectively. This major mass change indicates that material was transferred over long-range distances (e.g., an open system) during metamorphism-deformation and caused local mass and volume changes. The amounts of mass and volume changes are calculated in the next chapter.

4.7 SUMMARY

Immobile element plots such as Y-Zr and Nb-Zr show that the rhyolites of the footwall and hangingwall of the Main Lens complex are lithologically different. The hangingwall has tholeiitic Zr/Y ratios (approximately 4.5), whereas the footwall has mildly calc-alkaline Zr/Y ratios (approximately 8.0).

Also, a correlation exists between immobile element concentrations and the intensity of foliation in the rock. Intensely foliated rocks are strongly enriched or depleted in Zr, Y, Ti and HREEs in comparison to rocks showing poor foliations; this difference is attributed to mass transfers during the metamorphism-deformational event.

The variable mineralogy of the wall rock alteration assemblages of the Mobrun mine is typical of the spectrum of alteration assemblage seen in Noranda massive sulphide deposits. Normative quartz, sericite, chlorite and albite are plotted on ternary diagrams in Figure 4.8 to establish the direction of

hydrothermal alteration trends, i.e., toward the sericite-quartz boundary via sericitization and silicification.

CHAPTER 5

MASS AND VOLUME CHANGES ASSOCIATED WITH HYDROTHERMAL ALTERATION AND METAMORPHISM-DEFORMATION

5.1 INTRODUCTION

From prior studies of VMS mineralization in Abitibi, it is generally accepted that the massive sulphide deposits and their wallrocks have been subjected to two major geological events, each of which may have modified the compositions of the deposits and wallrocks from their original compositions. More specifically, the microstructural studies presented in Chapter 3 testify that the wallrocks at the Mobrun mine underwent significant mass transfer during metamorphism-deformation, and recognition of an earlier hydrothermal alteration zone at the Main Lens indicates that mass transfers were also associated with the initial hydrothermal mineralization event. Thus, compositional modifications could have accompanied (1) hydrothermal alteration contemporaneous with the exhalation of ore-forming fluids (essentially synvolcanic in timing), and (2) later metamorphism and deformation overprinted on the hydrothermally altered volcanic rocks (syntectonic in timing).

The mass and volume changes associated with hydrothermal alteration and with subsequent metamorphism-deformation can be estimated by comparison of

the concentrations of immobile mineral constituents (such as rutile and zircon) between (1) relatively undeformed rocks which also show no obvious hydrothermal alteration (called "least-altered rock" in this study), (2) undeformed rocks showing hydrothermal alteration (called "least-deformed rock"), and (3) deformed rocks which had presumably also experienced hydrothermal alteration (called "deformed rock").

Estimates of the gains or losses of mass (or volume) resulting from all major geological events are based on the principle that the relative abundances of immobile elements remain unchanged when other more mobile elements are lost or gained; i.e., among immobile elements, the ratios of their abundances remain unchanged during overall mass gains or losses of mobile elements. Thus, in binary diagrams showing the amounts of immobile elements relative to other immobile elements (e.g., Fig. 5.1), samples of the same precursor composition (e.g., an average rhyolite) which have experienced various degrees of mass gains or losses plot along a straight line (alteration line) passing through the origin (MacLean, 1990). Altered samples deriving from other precursor igneous compositions (e.g., basalts, dacites, etc.) plot along other straight lines, and the sum of all precursor igneous compositions defines a fractionation line generally trending from mafic to felsic compositions (the direction of the trend depends on the immobile elements selected).

Furthermore, among the samples plotting along a given alteration line, those

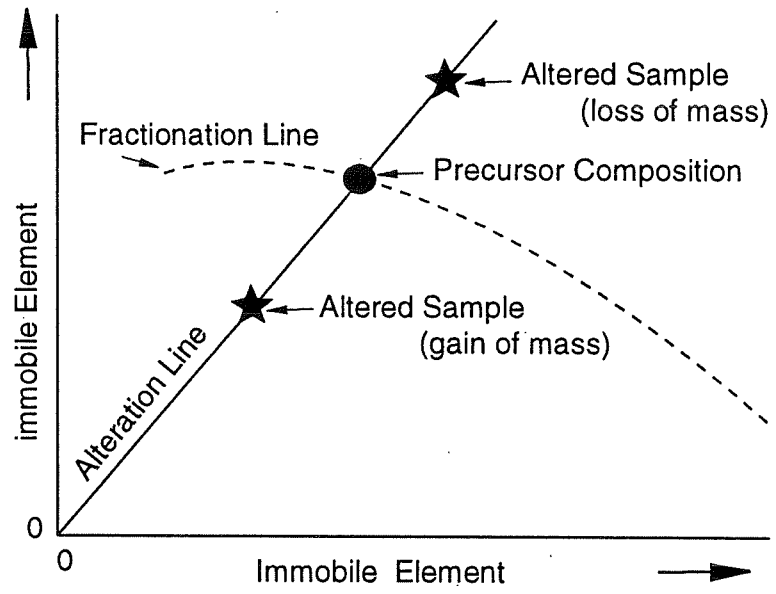

Fig. 5.1 Schematic diagram illustrating fractionation and alteration lines for immobile elements. Alteration line is linear (owing to mass gains and losses) and passes through the origin. The intersection of the alteration and fractionation lines is the precursor composition of altered sample. Note: alteration of a chemically homogeneous rock, such as Mobrun rocks, produces a single precursor system without need to draw a fractionation curve. A plot of an immobile element pair in such a unit forms an alteration line that is linear and passes through the origin and precursor composition. (see also Figure 5.2).

that plot closer to the origin than the parent (precursor) rock have experienced mass gains (their immobile elements have been diluted by the gain of mobile elements), whereas those that plot farther away from the origin than the parent rock have experienced mass losses (their immobile elements have been concentrated by the loss of mobile elements) (Kranidiotis and MacLean, 1987; MacLean, 1990; MacLean and Barrett, 1993). The further the sample plots from the parent composition, the greater the degree of mass gain or loss.

From the above concepts, it is possible to calculate reconstructed (i.e., precursor) compositions for altered samples, and from there to discuss the amount of mass gain or loss that clearly altered rocks may have experienced during various alteration events. This approach may be applied to determine the amounts of mass change that accompanied hydrothermal alteration and metamorphism-deformation in the wallrocks of the Mobrun deposits, and from this information, comments may be made on the possible contributions of each of these two "alteration" events to the present compositions of the Mobrun wallrocks.

5.2 METHODOLOGY

5.2.1 General case for Mobrun

Beginning with a hydrothermally altered sample, and knowing the apparent loss (or gain) of a given immobile element compared to the amount of that element

that would be expected in the parent rock, it is possible to calculate the reconstructed (original) composition for all other elements in the sample. Then the mass change that the sample experienced in passing from its original to altered composition is the difference between the reconstructed and original compositions.

The above calculation requires a reliable estimate of the expected immobile element content in the original parent rock. A reasonable estimate of this value may be drawn from the immobile element content of the average of all least-altered samples analyzed. Then the reconstructed composition can be determined by multiplying the concentrations of all components in an altered rock by the ratio of the estimated immobile monitor element concentration in the precursor and to that element's observed concentration in the altered rocks (MacLean, 1990), i.e.:

Reconstructed composition = % component in altered rock x (% monitor element in precursor / % monitor element in altered rock)

(5.1)

Having determined the reconstructed composition, the mass change is then determined from the difference between the reconstructed composition and the precursor composition (MacLean, 1990):

Mass change = Reconstructed composition - Precursor composition

(5.2)

This method has been used to calculate mass changes during hydrothermal alteration processes associated with numerous massive sulphide deposits, such as the Phelps Dodge (MacLean and Kranidiotis, 1987), the New Insco (Liaghat, 1990), the Horne (MacLean and Hoy, 1991), the Bell Allard (Liaghat and MacLean, 1992); the Norbec (Shriver and MacLean, 1993); Ansil (Barrett et al., 1991); Delbridge, (Barrett et al. 1993) and the Mobrun (Barrett et al., 1993) deposits.

However, in many cases, the hydrothermally altered massive sulphide bodies and their host rocks have been overprinted by metamorphic and deformation effects related to a later tectonic event, and no attempt has been made in these previous studies to evaluate mass changes that may be due to this overprinted metamorphism and deformation. Because the Mobrun deposit occurs in a corridor of intense deformation, it is ideally suited to test for possible mass change effects related to tectonism in addition to the usual synvolcanic hydrothermal effects. The analysis is also aided by the fact that the deposit is hosted by only two lithologies (tholeiitic and calc-alkaline rhyolites), thereby reducing the number of variables to be considered.

In order to make the distinction between initial hydrothermal mass changes and later syntectonic mass changes, it is first necessary to estimate the initial unaltered parent rock composition and then detect the amounts of mass gain or loss that can be attributed to each subsequent event. In an ideal world, we would be able to identify and quantify alterations extending backward from the

presently highly deformed rock at Mobrun, possibly through more than one deformation event, through retrograde and prograde metamorphism, through spatially local synvolcanic hydrothermal alteration pipes, to finally characterize the initial fresh volcanic rock. In this study, we are content to evaluate the cumulative effects of alteration at two stages, (1) mass changes after the hydrothermal alteration associated with emplacement of the VMS mineralization, and (2) mass changes after the widespread metamorphism-deformation generally associated with the Kenoran orogenic event.

In this study, two lithologic suites are recognized: rhyolites of the hangingwall, and rhyolites of the footwall. For each lithologic group, the "fresh" parent composition is estimated by averaging the whole-rock analyses of several least-altered samples selected after careful petrographic study (Fig. 5.2a). We have also selected least-deformed wallrocks as the best representatives of hydrothermally altered, pretectonic rock compositions, and highly deformed rocks as representative of metamorphosed-deformed rock (Fig. 5.2b). The compositional differences between these progressively more altered rocks would indicate the degree of mass change associated first with hydrothermal alteration (Fig. 5.2a) and then with tectonism (Fig. 5.2b).

In Chapter 3, the immobility of elements such as Zr and Ti has been established for both least-deformed and highly deformed samples. Thus, TiO_2-Zr plots (e.g., Fig. 5.3) in which these two elements are considered immobile can

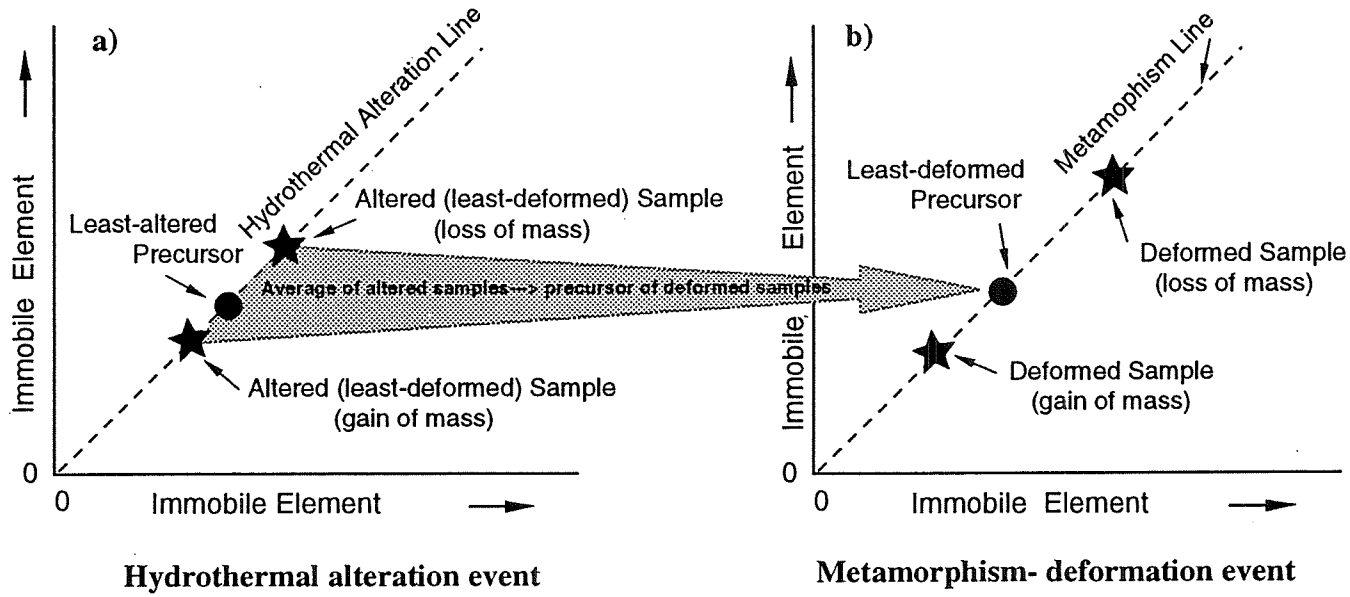

Fig. 5.2 Idealized diagrams illustrating hydrothermal alteration and metamorphism trends for pair of immobile elements at Mobrun. Diagram **(a)** represents the hydrothermal alteration event. A plot of an immobile element pair of hydrothermally altered (least-deformed) samples in such a diagram forms an alteration line that is linear and passes through the least-altered precursor. Diagram **(b)** represent the metamorphism-deformation event. A plot of an immobile element pair of deformed samples forms a metamorphism line. Average of altered (least-deformed) samples is assumed to be the precursor of deformed samples; they are superimposed on the metamorphism line. Mass changes can be calculated from each mobile element based on the dilution or concentration of an immobile component.

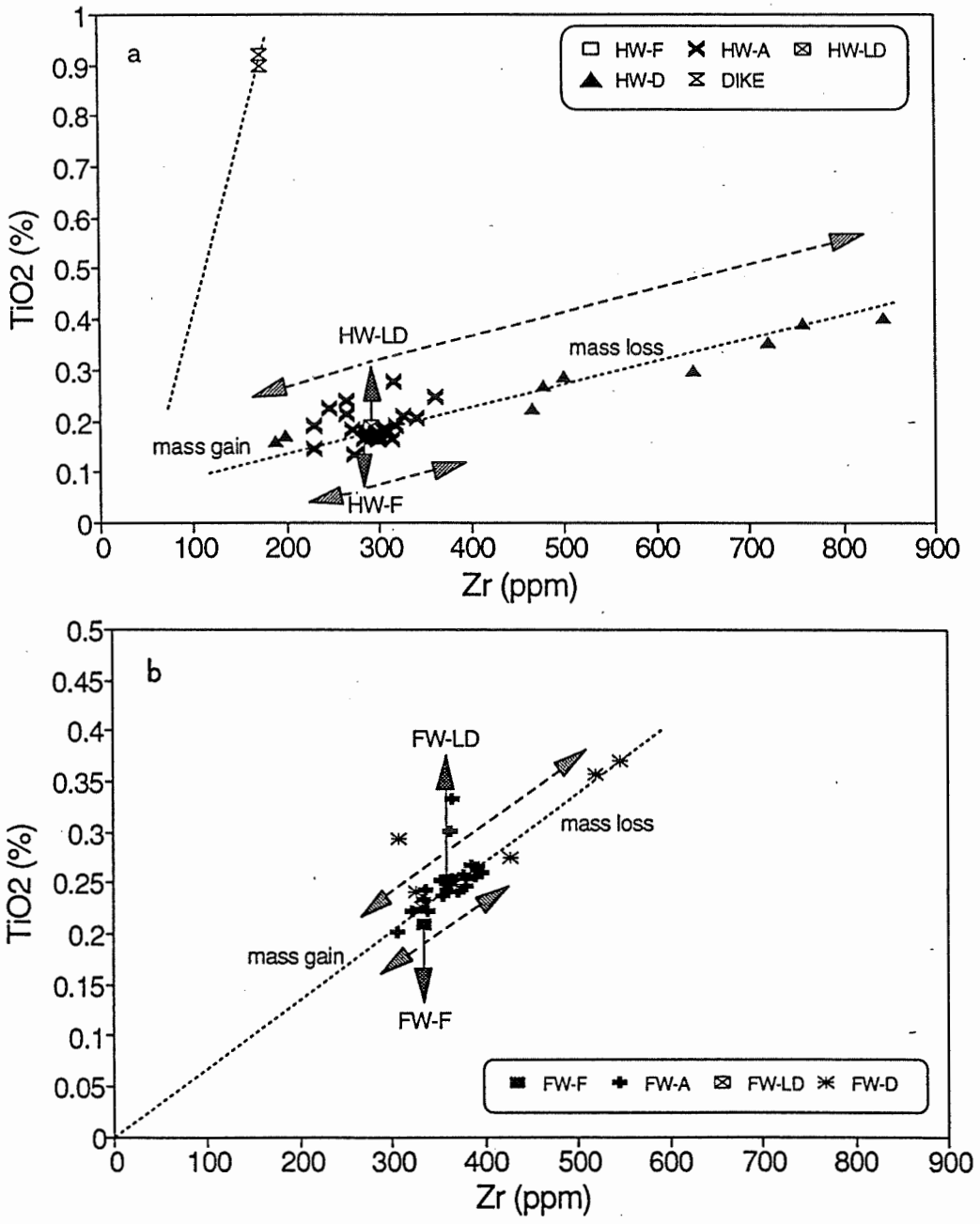

Fig. 5.3 Plot of TiO_2 versus Zr, showing **(a)** the alteration line for tholeiitic volcanic rocks, and **(b)** the alteration line for calc-alkaline volcanic rocks of Mobrun. Mass losses and mass gains during hydrothermal alteration and metamorphism-deformation are indicated by the arrows. Symbols represent: HW-F = hangingwall least-altered, HW-A hangingwall altered, HW-LD = hangingwall least-deformed and HW-D hangingwall deformed rocks.

readily indicate overall mass gains or losses, especially where a sufficiently representative number of samples is involved (MacLean and Kranidiotis, 1987). In theory, a group of samples from a single common parent lithology (e.g., samples from a single tholeiitic flow, Fig. 5.3a) form a recognizable linear array passing through the origin and the parent composition. Also, because titanium is preferentially concentrated in rocks of mafic composition and zircon is concentrated in felsic rocks, mafic sample arrays have steep slopes (e.g., Fig. 5.3a) whereas felsic arrays show low slopes (e.g., Fig. 5.3b). In general, the reconstructed parent compositions of volcanic rocks may be obtained by overlaying a new linear array on the parent volcanic series trend, as established by MacLean (1990).

The following sections present detailed explanations of the calculations required to estimate (1) the compositions of primary unaltered rocks and the mass changes involved in their synvolcanic hydrothermal alteration, and (2) mass changes that may be attributed to syntectonic alteration related to metamorphism and deformation at Mobrun.

5.2.2 Calculation of mass changes associated with hydrothermal alteration alone (theory)

Considering the pervasive overprint of metamorphism and deformation at Mobrun, the best least-altered samples which can be assumed to have experienced

seafloor alteration only (e.g., spilitization) are those which are at the same time least-deformed (least likely to have experienced syntectonic alteration) and most distant from the Main Lens (least likely to have been altered by the hydrothermal fluids which formed the sulphide lenses). They are identified petrographically by their unaltered minerals which typically are plagioclase and by the following bulk chemical features: Na_2O = 3 to 5 %, and low values for K_2O (<2%), FeO (<4%) and MgO (<2%).

For rocks which experienced only hydrothermal alteration, the best estimates of mass changes resulting from that alteration are proportional to the concentration of an immobile element (e.g., Zr) in the least-altered precursor relative to the concentration of this immobile element in obviously hydrothermally altered rock (Fig. 5.2a).

The reconstructed (original) composition of a hydrothermally altered-only sample (RC_{hi}) is given by the following equation which effectively normalizes all changes in mobile components to the Zr concentration of the original volcanic rock:

$$RC_{hi} = \%\ \text{component i in the hydrothermally altered rock} \times (Zr_{\text{least-altered precursor}} / Zr_{\text{hydrothermally altered rocks}}) \quad (5.3)$$

The mass change resulting from this hydrothermal alteration (MC_{hi}) is then calculated from the difference between the least-altered precursor composition

(PC_{hi}) and the reconstructed composition:

$$MC_{hi} = RC_{hi} - PC_{hi} \qquad (5.4)$$

5.2.3 Calculation of mass changes resulting from metamorphism-deformation (theory)

Mass change calculations for rock which have experienced metamorphism-deformation are based on the relative accumulations or dilutions of immobile phases (e.g., Zr) in highly schistose rocks relative to least-deformed rocks (Fig. 5.2b).

Reconstructed compositions (RC_{di}), removing the mass change effects attributable to metamorphism-deformation, are given by:

$$RC_{di} = \%\ \text{component i in deformed rock} \times (Zr_{\text{least-deformed precursor}} / Zr_{\text{deformed rock.}}) \qquad (5.5)$$

Absolute differences in immobile element concentrations between the reconstituted deformed rocks (RC_{di}) and their least-deformed precursors (PC_{di}) are used to calculate mass changes attributable to the metamorphism-deformation event (MC_{di}):

$$MC_{di} = RC_{di} - PC_{di} \qquad (5.6)$$

5.3 APPLICATION OF MASS CHANGE CALCULATIONS TO MOBRUN

Calculations for the effects of synvolcanic hydrothermal alteration on wallrocks of the Mobrun Main Lens have already been made by Barrett et al. (1992). The method was based on the Zr contents of so-called least-altered rocks relative to altered and deformed rocks without distinction between hydrothermal effects and possible metamorphism-deformation-related effects on mass changes. As outlined above, in the present study, the Mobrun samples were separated into two groups based on megascopically and microscopically visible criteria: group 1 samples are least-deformed samples, with altered compositions resulting essentially only from hydrothermal alteration; group 2 samples show intense deformation, with altered compositions resulting from both hydrothermal alteration and metamorphism-deformation events. Using Zr as a monitor of mass change, the gains and losses of chemical components are represented as percentage changes relative to the appropriate parental rocks compositions.

Representative calculated mass changes for the footwall (calc-alkaline) and hangingwall (tholeiitic) altered rhyolites are given in detail in Appendix 5.1 and in summary form in Table 5.1. To improve on the number of representative least-altered samples, our analyses have been combined with data from similar rocks analyzed by Barrett et al. (1992). For mass change calculations, the mean values of data for both the footwall and hangingwall samples are used.

Table 5.1a Representative calculations of mass changes during hydrothermal alteration of rhyolite at the Mobrun deposit.

	SiO2	TiO2	Al2O3	FeO*	MnO	MgO	CaO	Na2O	K2O	P2O5	S	Zr	Total
Hangingwall (HW)													
Precursor (n=5)	77.69	0.17	12.18	1.80	0.06	0.39	1.49	4.73	1.44	0.01	0.00	287	100.0
Altered (n=21)	76.44	0.19	12.69	2.88	0.06	1.23	1.65	1.76	2.78	0.03	0.24	292	100.0
Footwall (FW)													
Precursor (n=4)	77.45	0.21	11.97	2.17	0.04	0.53	1.79	4.41	1.36	0.04	0.00	334	100.0
Altered (n=21)	74.85	0.25	13.92	2.55	0.04	0.54	1.35	2.85	2.85	0.04	0.72	362	100.0
Reconstituted composition: normalized to Zr precursor													
Hangingwall	76.28	0.19	12.57	2.83	0.06	1.20	1.64	1.79	2.73	0.03	0.26	287	99.6
Footwall	69.46	0.23	12.84	2.39	0.04	0.48	1.22	2.59	2.64	0.04	0.71	334	92.7
Net mass changes													
Hangingwall	-1.40	0.00	0.40	1.00	0.00	0.80	0.10	-2.90	1.30	0.00	0.30	0	-0.3
Footwall	-8.00	0.00	0.90	0.20	0.00	0.00	-0.60	-1.80	1.30	0.00	0.70	0	-7.3

Standard Deviation: FW (∓ 6.2), HW (∓ 11.8)
Range of mass changes: FW (-15.8% to 9.1%), HW (-20.5% to 25.1%)

Table 5.1b Representative calculations of mass changes during metamorphism-deformation of rhyolite at the Mobrun deposit.

	SiO2	TiO2	Al2O3	FeO*	MnO	MgO	CaO	Na2O	K2O	P2O5	S	Zr	Total
Hangingwall (HW)													
Precursor (n=21)	76.44	0.19	12.69	2.88	0.06	1.23	1.65	1.76	2.79	0.03	0.24	292	100.0
Deformed (n=10)	68.92	0.28	16.61	5.64	0.04	2.12	0.63	0.94	3.48	0.03	1.26	508	100.0
Footwall (FW)													
Precursor (n=21)	74.85	0.25	13.92	2.55	0.04	0.54	1.35	2.85	2.85	0.04	0.72	362	100.0
Deformed (n=6)	70.70	0.29	16.68	3.60	0.02	0.55	0.57	1.20	4.49	0.05	1.81	410	100.0
Reconstituted composition: normalized to Zr precursor													
Hangingwall	53.32	0.17	10.70	4.16	0.02	1.32	0.60	0.84	2.10	0.02	1.51	292	74.8
Footwall	66.34	0.26	15.01	3.42	0.02	0.44	0.56	0.93	4.09	0.04	1.88	362	93.0
Net mass changes													
Hangingwall	-23.20	0.00	-1.90	1.40	0.00	0.20	-1.00	-1.20	-0.50	0.00	1.30	0	-25.1
Footwall	-8.50	0.00	1.10	0.90	0.00	-0.10	-0.80	-1.90	1.20	0.00	1.20	0	-6.9

Standard Deviation: FW (∓ 20.6), HW (∓ 35.1)
Range of mass changes: FW (-33.8% to 17.5%), HW (-65.4% to 54.9%)

Hydrothermal alteration of rocks (footwall and hangingwall respectively), has resulted in considerable net mass changes in (see Table 5.1a):

SiO_2 (-8% and -1.4%),

Na_2O (-1.8% and -2.9%),

K_2O (1.3% and 1.3%),

and in smaller changes in:

CaO (-0.6 and -0.1%),

MgO (0.0 and 0.8%),

FeO (0.2 and 1.0%),

Al_2O_3 (0.9 and 0.4%).

Similarly, mass changes for deformed rocks (footwall and hangingwall, respectively) display higher changes for (see Table 5.1b):

SiO_2 (-8.5 and -23.2%),

Na_2O (-1.9% and -1.2%),

K_2O (1.2% and -0.5%),

and in smaller changes in:

CaO (-0.8 and -1.0%),

MgO (-0.1 and 0.2%),

FeO (0.9 and 1.4%),

Al_2O_3 (1.1 and -1.9%).

The net changes in mass during hydrothermal alteration and metamorphism-deformation are estimated to have been on the order of: -0.3% and -25.1% for hangingwall rocks, and -7.3% and -6.9% for footwall rocks.

As a result, the most important mass changes are losses in SiO_2 (approx. -8%) for hydrothermal alteration of footwall rocks, and losses in SiO_2 (approx. -23%) for metamorphism-deformation-related alteration of hangingwall rocks. In the hangingwall, many hydrothermally altered samples gained quartz due to silicification, even though the overall average mass change is negative. In general, the hydrothermal alteration event involved additions of quartz and sulphides, whereas mass losses were caused by leaching of silica and alkalis.

During the metamorphism-deformation event, mass gains were reflected by additions of silica (mainly as quartz-filled pressure shadows and extension veins) and locally by deposition of sulphides. Mass losses resulted from the formation of phyllosilicate grains and depletions of quartz.

The formation of sericite during metamorphism-deformation led to enrichments in K_2O in many deformed samples; sericitization was accompanied by increases in K_2O from 1.4 to 2.8%, with corresponding decreases in Na_2O and CaO. Enrichments in Rb along with K_2O (Fig. 5.4) reflect the normal Rb substitution for K in sericite. Near linear plots between K and Rb also occur in the Horne, Aldermac and Ansil deposits (Cattalani et al., 1990a, 1991a; Barrett et al., 1991).

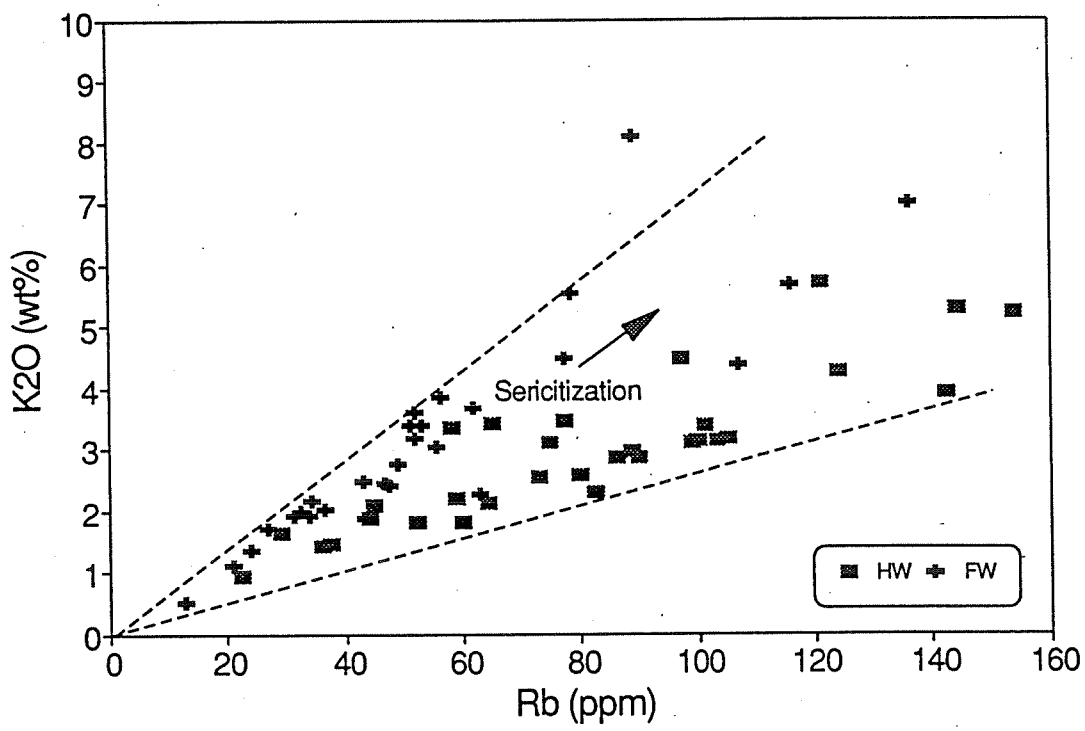

Fig. 5.4 Plots of K against Rb showing a high correlation between K and Rb after sericitization of rocks. HW = hangingwall, FW = footwall rocks.

Elements participating in mass transfers are identified in the binary diagrams of Figure 5.5 in which the horizontal axes show the percent change for given chemical components for given mass changes plotted along the vertical axes. The resulting scatter diagrams reflect variations in the mobilities of elements resulting from both hydrothermal alteration and metamorphism-deformation. The high SiO_2 enrichments and depletions of many highly deformed samples relative to hydrothermally altered-only rocks is clearly a consequence of major SiO_2 transfers during metamorphism-deformation. Even though many of the highly deformed samples plot in areas of high SiO_2 change, some low SiO_2 changes are also observed in these deformed rocks, possibly indicating approximately equal losses and gains of SiO_2 during metamorphism-deformation.

Highly deformed footwall samples show more enrichments and depletions of FeO than hangingwall samples, especially due to pyrite remobilization. Na and Ca were extensively depleted in many samples during both hydrothermal alteration and metamorphism-deformation, probably as a result of both alteration and pressure-solution processes. K_2O and MgO are enriched in many samples due to sericitization and chloritization, but they are depleted in some heavily foliated samples. Many of the hydrothermally altered hangingwall samples which gained Mg because of extensive chloritization compare to footwall rocks.

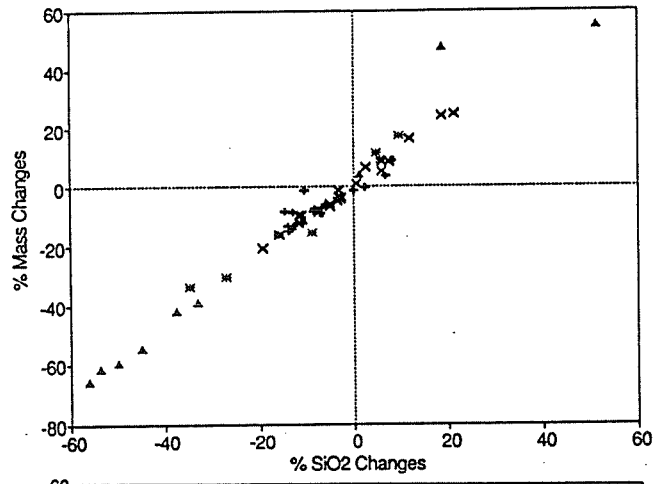

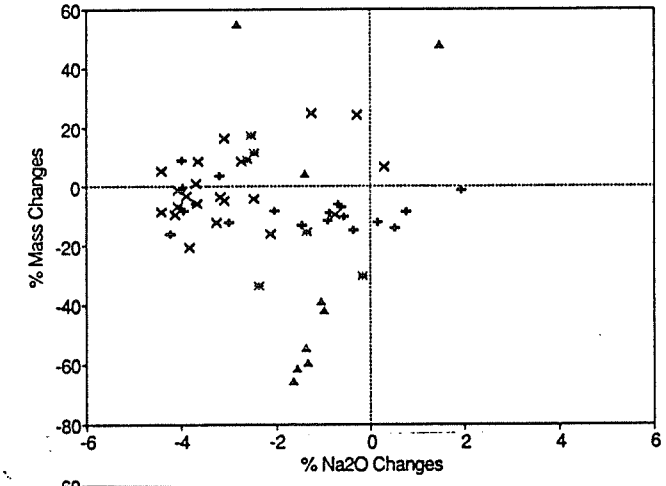

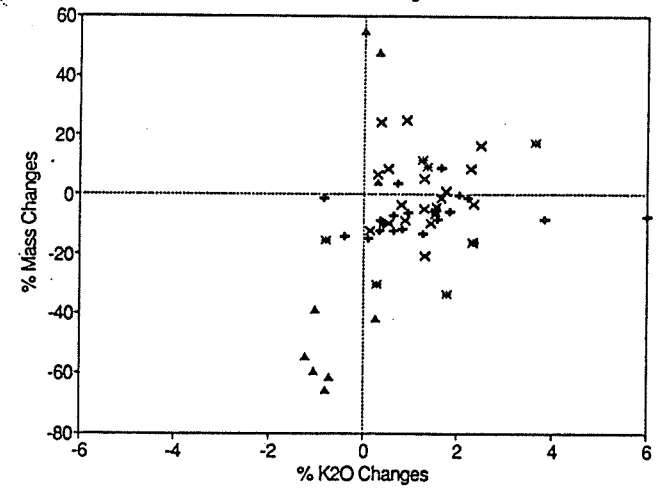

continued (next page)

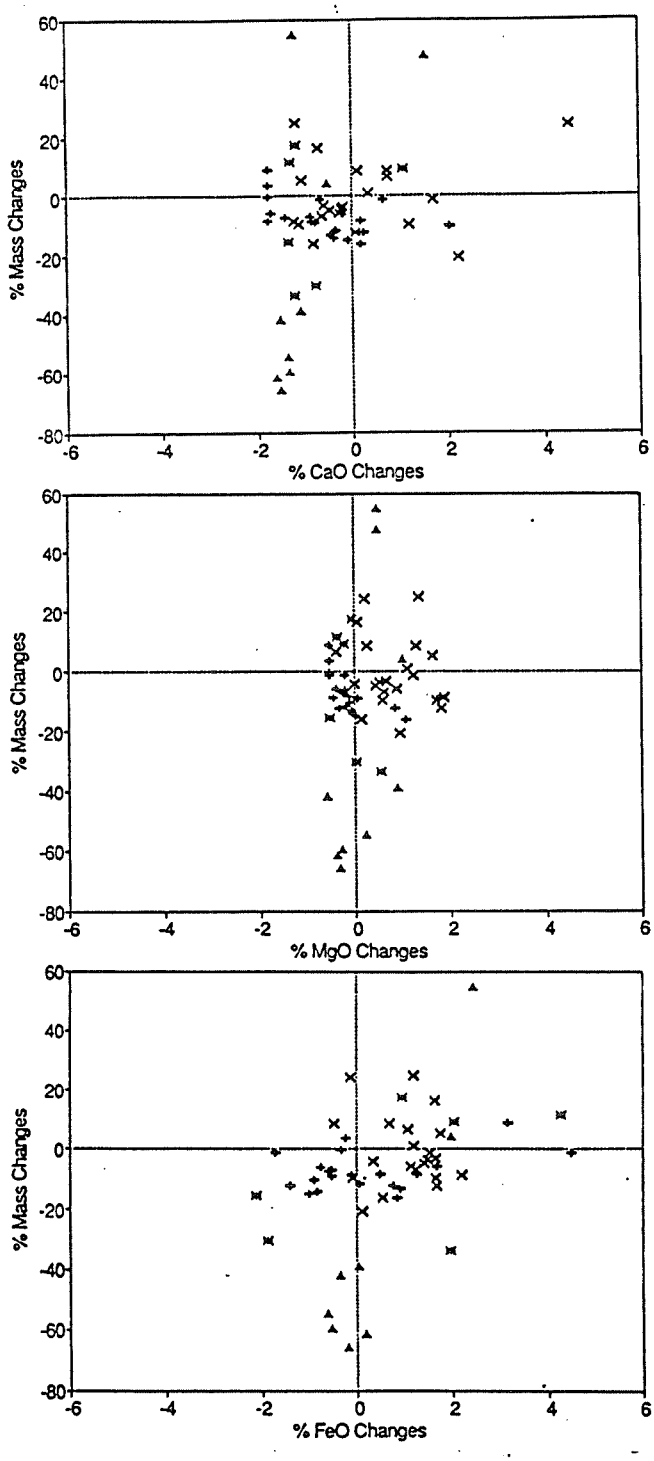

Fig. 5.5 Total mass change from data of Table A5.1 plotted against mass changes for each element. The distribution of elements along the trend is due to mass loss or mass gain. Symbols same as Fig. 5.3.

5.4 VOLUME CHANGE CALCULATIONS

The volume of rock lost or gained (in percent change) can be determined from the bulk compositions using the normative mineralogy and the density of minerals compared to the volume of the estimated precursor rocks.

Tables 5.2a and 5.2b show the step-by-step calculations of volume changes resulting from hydrothermal alteration (Table 5.2a) and from metamorphism-deformation (Table 5.2b) for average footwall and hangingwall samples (see Appendix 5.2 for more complete calculations). Sections I in both tables present the calculated data required to determine the actual volume of precursor compositions of least-altered and least-deformed rocks:

Step [1]: The selection of precursor compositions follows the same procedure as outlined in mass change calculations, i.e.,: the precursor of least-deformed samples (Table 5.2b, step [1]) is obtained from an average composition of altered (least-deformed) samples (Table 5.2a, step [4]).

Step [2]: Cation equivalent proportions are calculated as follow:

Molecular weight of the formula (e.g., SiO_2) $\longrightarrow$
$(Si = 28.09\%) + (O_2 = 15.99\% \times 2) = 60.09$

(5.7)

Table 5.2a Representative calculation of volume changes during hydrothermal alteration of rhyolites at the Mobrun deposit. HW = Hangingwall, FW = Footwall. Numbers in [ ] refer to steps in text.

[1] (I) Least-altered precursor													
	SiO2	TiO2	Al2O3	FeO*	MnO	MgO	CaO	Na2O	K2O	P2O5	S	Zr	Total
HW (n=5)	77.69	0.17	12.18	1.80	0.06	0.39	1.49	4.73	1.44	0.01	0.00	287.0	100.0
FW (n=4)	77.45	0.21	11.97	2.17	0.04	0.53	1.79	4.41	1.36	0.04	0.00	334.0	100.0
[2] Cation equivalent proportion.													
	Si	Ti	Al	Fe	Mn	Mg	Ca	Na	K	P	S		Total
HW	1.29	0.00	0.24	0.02	0.00	0.01	0.03	0.14	0.03	0.00	0.00		1.8
FW	1.29	0.00	0.23	0.03	0.00	0.01	0.03	0.14	0.03	0.00	0.00		1.8
Cation equivalent (normalized to 100%)													
HW	72.69	0.12	13.43	1.41	0.05	0.55	1.42	8.57	1.73	0.01	0.00		100.0
FW	72.84	0.15	13.27	1.54	0.03	0.74	1.71	8.04	1.63	0.03	0.00		100.0
[3] Minerals (cation)													
	Py	Apt	Ab	Ort	Mg-Px	Fe-Px	Ca-Px	An	Qz	Rt			Total
HW	0.00	0.02	42.86	12.09	1.10	2.81	1.29	3.82	36.45	0.12			
FW	0.00	0.10	40.09	8.65	0.71	1.94	1.89	0.00	46.39	0.23			
Minerals (wt.%), (normalized)													
HW	0.00	0.02	40.37	12.08	0.50	1.68	1.99	3.82	39.34	0.17			100.0
FW	0.00	0.10	40.09	8.65	0.71	1.94	1.89	0.00	46.39	0.23			100.0
Volume of minerals in least-altered precursor samples													
HW	0.00	0.01	15.77	4.74	0.16	0.42	0.69	1.38	14.84	0.04			38.1
FW	0.00	0.03	15.66	3.39	0.22	0.49	0.66	0.00	17.51	0.05			38.0

Continued (next page)

[4] (II) Altered (least-deformed samples)

	SiO2	TiO2	Al2O3	FeO*	MnO	MgO	CaO	Na2O	K2O	P2O5	S	Zr	Total
HW (n=21)	76.45	0.19	12.69	2.88	0.06	1.23	1.63	1.77	2.78	0.03	0.24	291.8	100.0
FW (n=21)	74.85	0.25	13.91	2.55	0.04	0.54	1.35	2.85	2.85	0.04	0.72	361.9	100.0
Reconstituted compositions: normalized to Zr least altered precursor													
HW	76.28	0.19	12.57	2.83	0.06	1.20	1.64	1.79	2.73	0.03	0.26	287.0	99.6
FW	69.08	0.23	12.85	2.35	0.04	0.50	1.25	2.63	2.63	0.04	0.66	334.0	92.3

[5] Cation equivalent proportion.

	Si	Ti	Al	Fe	Mn	Mg	Ca	Na	K	P	S	Total
HW	1.27	0.00	0.25	0.04	0.00	0.03	0.03	0.06	0.06	0.00	0.01	1.7
FW	1.16	0.00	0.25	0.03	0.00	0.01	0.02	0.08	0.06	0.00	0.02	1.6
Cation equivalent: normalized to reconstituted compositions												
HW	72.69	0.14	14.11	2.24	0.05	1.71	1.59	3.29	3.33	0.03	0.45	99.6
FW	65.36	0.16	14.23	1.88	0.03	0.68	0.16	4.69	3.19	0.03	1.26	92.7

[6] Minerals (cation)

	Py	Apt	Ab	Ser	Mg-Ch	Fe-Chl	Epi	Cc	Qz	Rt	Total
HW	0.68	0.07	16.43	23.31	3.79	4.48	0.37	1.45	40.55	0.14	
FW	1.90	0.08	23.43	22.34	1.50	2.78	1.02	1.02	30.02	0.16	
Minerals (wt.%): normalized to reconstituted compositions											
HW	0.53	0.08	17.03	22.28	3.39	5.28	0.40	1.46	48.95	0.22	99.6
FW	1.46	0.10	23.97	20.70	1.34	3.23	1.04	1.01	39.58	0.26	92.7
Volume of minerals in altered samples											
HW	0.11	0.03	6.65	8.57	1.30	1.60	0.12	0.54	18.47	0.05	37.4
FW	0.29	0.03	9.36	7.39	0.52	1.01	0.31	0.37	14.93	0.06	34.3

[7] Net volume changes: FW (-3.7), HW (-0.7)
Average percent volume changes: FW (-9.8), HW (-1.7)
Standard Deviation: FW ($\vec{+}$ 5.5), HW ($\vec{+}$ 11.8)
Range of volume changes HW (-21.4% to 24.2%)
Range of volume changes FW (-19.3% to 3.3%)

Table 5.2b Representative calculation of volume changes during metamorphism-deformation at rhyolite of rhyolites at the Mobrun deposit. HW = Hangingwall, FW = Footwall. Numbers in [ ] refer to steps in text.

[1] (A) Least-deformed precursor

	SiO2	TiO2	Al2O3	FeO*	MnO	MgO	CaO	Na2O	K2O	P2O5	S	Zr	Total
HW (n=21)	76.45	0.19	12.69	2.88	0.06	1.23	1.63	1.77	2.78	0.03	0.25	291.8	100.0
FW (n=21)	74.85	0.25	13.92	2.55	0.04	0.54	1.35	2.85	2.85	0.04	0.72	361.9	100.0

[2] Cation equivalent proportion.

	Si	Ti	Al	Fe	Mn	Mg	Ca	Na	K	P	S	Total
HW	1.27	0.00	0.25	0.04	0.00	0.03	0.03	0.06	0.06	0.00	0.01	1.7
FW	1.25	0.00	0.27	0.03	0.00	0.01	0.02	0.09	0.06	0.00	0.02	1.7
Cation equivalent (normalized to 100%)												
HW	72.80	0.14	14.25	2.29	0.05	1.74	1.58	3.27	3.39	0.02	0.44	100.0
FW	70.41	0.18	15.43	2.01	0.03	0.76	1.29	5.19	3.43	0.03	1.26	100.0

[3] Minerals (cation)

	Py	Apt	Ab	Ser	Mg-Ch	Fe-Chl	Epi	Cc	Qz	Rt	Total
HW	0.66	0.07	16.35	23.72	3.88	4.61	0.00	1.54	40.33	0.14	
FW	1.89	0.09	25.97	24.00	1.68	3.06	0.00	1.24	36.48	0.18	
Minerals (wt.%), (normalized)											
HW	0.53	0.08	17.28	22.70	3.41	5.37	0.00	1.55	48.84	0.22	100.0
FW	1.48	0.11	26.71	22.34	1.44	3.47	0.00	1.21	42.98	0.28	100.0
Volume of minerals in least deformed precursor samples											
HW	0.11	0.03	6.75	8.73	1.31	1.63	0.00	0.57	18.43	0.05	37.6
FW	0.30	0.03	10.43	7.98	0.55	1.08	0.00	0.45	16.22	0.07	37.1

Continued (next page)

[4] (B) Deformed samples

	SiO2	TiO2	Al2O3	FeO*	MnO	MgO	CaO	Na2O	K2O	P2O5	S	Zr	Total
HW (n=10)	68.92	0.28	16.61	5.64	0.04	2.12	0.63	0.94	3.48	0.03	1.26	507.5	100.0
FW (n=6)	70.70	0.29	16.68	3.60	0.02	0.55	0.57	1.20	4.49	0.05	1.80	410.3	100.0
Reconstituted compositions: normalized to Zr least altered precursor													
IIW	53.28	0.17	10.69	4.15	0.02	1.32	0.60	0.84	2.10	0.02	1.51	291.8	74.7
FW	62.38	0.26	14.71	3.18	0.02	0.49	0.50	1.06	3.96	0.04	1.60	362.0	88.2

[5] Cation equivalent proportion.

	Si	Ti	Al	Fe	Mn	Mg	Ca	Na	K	P	S	Total
IIW	0.89	0.00	0.21	0.06	0.00	0.03	0.01	0.03	0.04	0.00	0.04	1.3
FW	1.10	0.00	0.29	0.05	0.00	0.01	0.00	0.03	0.09	0.00	0.06	1.6
Cation equivalent: normalized to reconstituted compositions												
IIW	50.38	0.12	11.89	3.23	0.02	1.87	0.57	1.53	2.53	0.02	2.61	74.8
FW	62.42	0.19	16.62	2.69	0.02	0.61	0.53	1.69	4.92	0.03	3.32	93.0

[6] Minerals (cation)

	Py	Apt	Ab	Ser	Mg-Ch	Fe-Chl	Epi	Cc	Qz	Rt	Total
IIW	3.91	0.05	7.62	17.71	4.14	4.27	1.86	0.51	25.95	0.12	
FW	4.98	0.09	8.45	34.41	1.35	2.28	2.63	0.48	35.58	0.19	
Minerals (wt.%): normalized to reconstituted compositions											
IIW	3.18	0.06	8.35	18.98	4.05	5.60	1.90	0.54	31.88	0.22	74.8
FW	3.90	0.11	8.49	32.53	1.23	2.75	2.52	0.47	40.73	0.29	93.0
Volume of minerals in deformed samples											
IIW	0.64	0.02	3.26	7.30	1.56	1.70	0.56	0.20	12.03	0.05	27.3
FW	0.79	0.04	3.32	11.62	0.47	0.86	0.75	0.17	15.37	0.07	33.5

[7] Net volume changes: FW (-3.7), IIW (-10.3)
Average percent volume changes: FW (-9.6), IIW (-27)
Standard Deviation: FW (∓ 19.7), IIW (∓ 32.8)
Range of volume changes IIW (-65.7% to 49.4%)
Range of volume changes FW (-36.6% to 14.1%)

Average weight per cation ——————→ 60.09 : 1 (number of cations in formula) = 60.09

(5.8)

Cation equivalent proportions ——————→ 77.69 (wt% of SiO_2) : 60.09 = 1.29

(5.9)

The data for all the cations are then calculated and normalized to 100%:

1.29 ——————^{normalized}——————→ 72.69

(5.10)

Step [3]: Least-altered rocks consist mainly of quartz (Qz), albite (Ab), orthoclase (Or), Mg-pyroxene (Mg-Px), Fe-pyroxene (Fe-Px), Ca-pyroxene (Ca-Px), anorthite (An), apatite (Apt), rutile (Rt) and pyrite (Py). Because there are no significant mineralogical changes during metamorphism-deformation, only the abundances of minerals are changed significantly, and the normative mineralogy of least-deformed precursor rocks (Table 5.2b, step [3]) can be calculated in the same manner as altered rocks (Table 5.2a, step [6]).

The normative mineralogy is used for major components of minerals and only the end-member compositions are included in the norms. The dominant control over Si contents is quartz (SiO_2), whereas Na is mainly accommodated by albite ($NaAlSi_3O_8$). Potassium is contained mainly in muscovite ($KAl_3Si_3O_{12}$), and chlorite ($(Fe,Mg)_9\ Si_5Al_6O_{20}$) accounts for most of the Fe and Mg. For the least-altered precursor mineralogies, K and Fe-Mg are accommodated mainly in orthoclase ($KAlSi_3O_8$) and pyroxene $Mg_2Si_2O_6$-$Fe_2Si_2O_6$), respectively. For least-

deformed hydrothermally altered samples, the main host of Ca is calcite ($CaCO_3$), epidote ($Ca_2Al_3Si_3O_{12}$) and apatite ($Ca_5P_3O_{12}$), and for least-altered compositions, Ca is found chiefly in calcic-pyroxene ($Ca_2Si_2O_6$). Rutile (TiO_2) is the dominant host for Ti. Sulphur and corresponding amounts of Fe are accounted for by pyrite (FeS_2).

Mineral cation norms are converted to wt.% norms and then normalized to 100%: e.g.:

Quartz (cation) $\longrightarrow$ 36.45

Quartz (wt.%) $\longrightarrow$ [(Si = 28.09) + (O_2 = 15.99 x 2)] / 1 x 36.45 = 2190.35

(5.11)

The data for all the minerals are then calculated and normalized to 100%:

2190.35 $\xrightarrow{\text{normalized}}$ 39.34

(5.12)

Finally, the volume of each mineral is calculated from the wt.%/density ratio. The densities (D) of minerals have been taken from Deer et al. (1980): Qz = 2.65, Ab = 2.56, Or = 2.55, Mg-Px = 3.21, Fe-Px = 3.96, Ca-Px = 2.87, An = 2.76, Apt = 3.1, Rt = 4.23, Py = 4.95, Mg-Chl = 2.7, Fe-Chl = 3.3, Cc = 2.72, Ep = 3.; e.g.,:

Quartz volume = wt.% / D ——————→ 39.34 / 2.65 = 14.84 (5.13)

Sections II of Tables 2a and 2b present the three-stage calculations needed to determine the actual volumes of hydrothermally altered and metamorphosed-deformed rocks.

Step [4]: The selection of precursor compositions and the calculation of reconstructed compositions of the hydrothermally altered and metamorphosed-deformed rocks follow the same procedure as outlined in mass change calculations described above. For example, the precursor of metamorphosed-deformed samples (Table 5.2b, step [4]) is obtained from the average composition of least metamorphosed/deformed samples (Table 5.2a, step [4]).

Step [5]: Procedures similar to those described in Step [2] are followed here to obtain cation contents, with the exception that data are normalized to the reconstituted total value (e.g. 99.7, see Table 5.2a, step [4]).

Step [6]: The minerals of the hydrothermally altered least-deformed rocks (i.e., precursors of metamorphosed-deformed rocks) consist of quartz (Qz), sericite (Ser), albite (Ab), Mg-chlorite (Mg-Chl), Fe-chlorite (Fe-Chl), calcite (Cc), apatite (Ap), epidote (Ep), rutile (Ru) and pyrite (Py). These minerals are normalized to their reconstructed compositions and converted to volume values based on their densities, as outlined in Step [3] above.

Step [7]: The absolute differences between the volumes of altered and metamorphosed-deformed rocks (see Step [6]) and their corresponding precursor

compositions (see Step [3]) have been used to identify volume changes during hydrothermal alteration and metamorphism-deformation events.

As a result, bulk chemical analyses from hydrothermally altered and metamorphosed-deformed samples of the Mobrun host rocks show substantial volume changes. Hangingwall rocks are characterized by overall volume changes of -21.4 to +24.2% (with a mean of -1.3%) during hydrothermal alteration, and changes of -65.7 to +49.4% (mean = -26.7) during metamorphism-deformation. Corresponding volume changes for footwall rocks have values of -19.3 to +3.3% (mean = -9.3%) and -36.6 to 14.1% (mean = -9.2%), respectively.

5.5 DISCUSSION

The Mobrun wallrocks exhibit wide ranges in concentration of immobile elements, which have been affected by both synvolcanism alteration and metamorphism-deformation processes. The latter is confirmed by the distinct correlation between immobile element concentrations and the intensity of schistosity in the metamorphosed rocks, e.g., highly deformed rocks are clearly enriched or depleted in Zr and Ti in comparison to weakly deformed rocks. These correlations were already observed in Chapters 3 and 4 in which it is shown that immobile elements were passively concentrated into dissolution sites or depleted in precipitation sites during the development of cleavage under pressure-solution

processes. In this chapter, the overall relative concentrations of these immobile elements is attributed quantitatively to mass and volume changes that arose during metamorphism. Modifications of the rock volume are then attributed directly to mass transfers, as shown by the good correlations between mass and volume changes in Figure 5.6.

5.5.1 Volume change calculations

Volume change computations shows that bulk-rock volume may be calculated using the normative mineralogies and densities of each mineral for precursor and reconstructed compositions. The basic observation in this approach is documentation of substantial changes (dilutions or enrichments) of inert phases in altered rocks and along the cleavage surfaces of deformed rocks as measured in bulk-rock compositions.

Similar enrichments of immobile elements have been used for volume change calculations by Waldron and Sandiford (1988) and Stephens et al. (1979). Their studies applied to the immobility and concentration of Ti in phyllosilicate layers due to the removal of mobile constituents. In other methods (Shriver and MacLean, 1993), the changes in volume of the host volcanic rocks of the Norbec mine were determined using the known amounts of immobile Zr in the alteration pipe, and the calculated densities of the precursor rocks. In other cases, enrichments of Zr, Ti, Y in mylonitic rocks from ductile shear zones have been

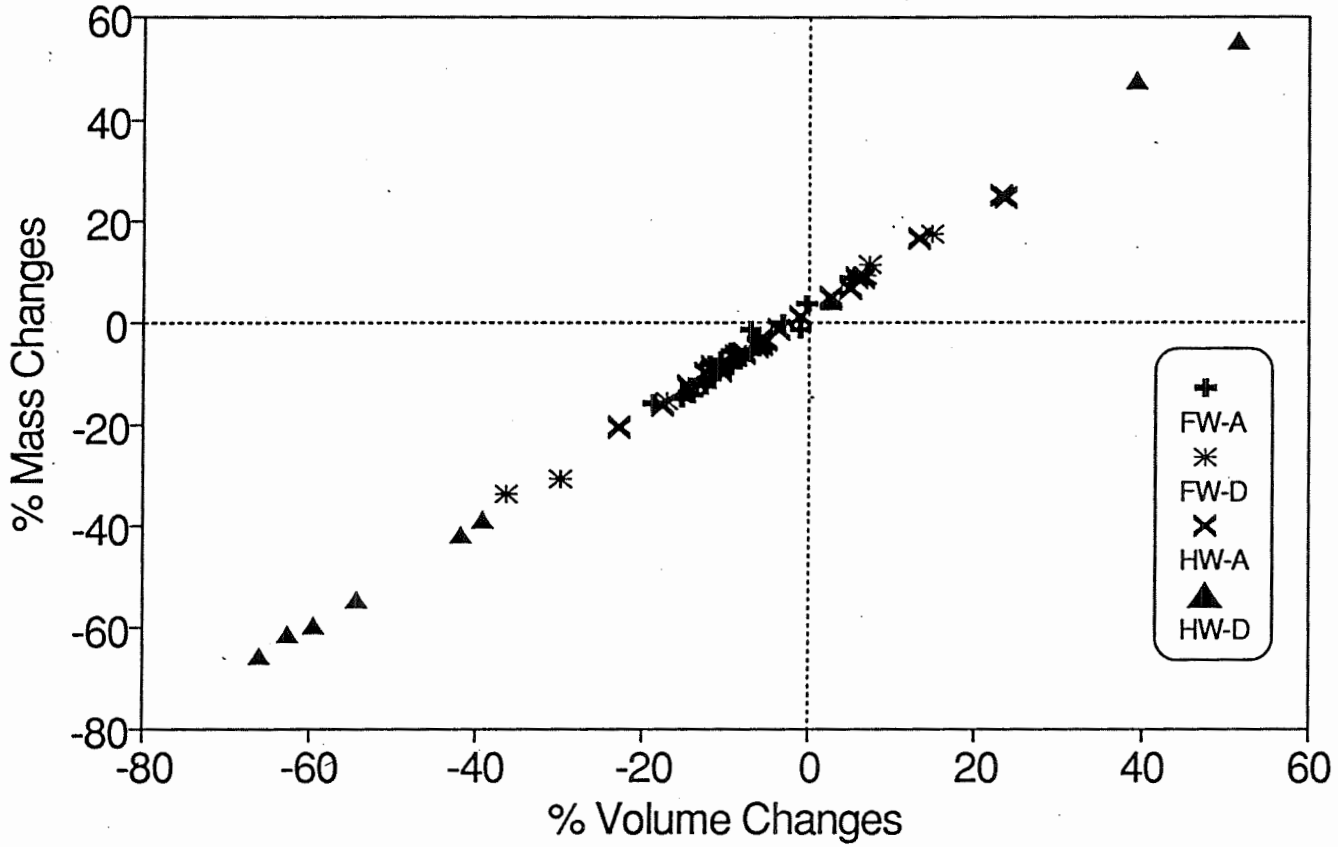

Fig. 5.6 Mass change-volume change diagram showing a good correlation between mass and volume changes at Mobrun. Symbols same as Fig. 5.3.

interpreted as evidence of trace-element mobility caused by the flux of large volumes of fluid (Winchester and Max, 1984; Vokes et al., 1987; Wayne and Sinha, 1988). In other studies, volume changes have been calculated for deformed rocks regardless of their immobile element geochemistry; for example, Schwerdtner (1982) calculated volume changes incurred during the development of infinite shear zones, knowing the principal directions and principal ratios of total strain within the structures. Also, using host-rock specific gravities, Kerrich et al. (1977) calculated the volume changes of rocks within the shear zones of the Laghetti and Yellowknife deposits by considering the transport of chemical species by diffusion under conditions of differential stress .

At Mobrun, volume losses in the strongly deformed hangingwall rhyolite are as much as -66%, with a mean of -27%. This compares closely with the volume loss in chloritized rhyolite at the Phelps Dodge VMS deposit, calculated to have been as high as 60% (MacLean and Kranidiotis, 1987). By contrast, a 10% volume increase was estimated for bulk silicification in the alteration zone of the Horne mine (MacLean and Hoy, 1992). The highest value for volume gain in rhyolite at Mobrun is 50%.

5.5.2 Distance of mass transfers

Mass-balance calculations for the Mobrun deposit show that the metamorphism-deformation event has mobilized considerable amounts of rock

components at the deposit scale. This local effect could result in part from the focusing of fluid flow through small rock volumes, particularly in dilatant sites which are particularly abundant in the vicinity of ductile sulphide bodies.

Major variations in mass and volume changes are dependent in part on whether quartz migrates into immediately adjacent precipitation layers or migrates over greater distances (MacLean, 1990). However, as our calculations of mass and volume changes demonstrate, quartz must have migrated over long distances (deposit-scale) during deformation in order to produce the large-scale mass and volume changes observed at Mobrun. In addition, the existence of syntectonic quartz vein networks within the deformed wallrock terrains points to local solution transfer paths on a scale significantly larger than dissolution and precipitation alone.

Variations in volume change across the mine area are best represented graphically on the Mobrun plan map (Figure 5.7). In this diagram, variations in volume are portrayed as a function of metamorphism-deformation. Microstructural observations indicate that many samples adjacent to the orebody are more deformed and have evidence of extensive mass transfers. However, some samples may represent rock that underwent early syndeformation mass changes and accompanying silica leaching, followed by later additions of sulphide and silica. Therefore, in spite of intense deformation, the net mass and volume changes for those samples can be rather low.

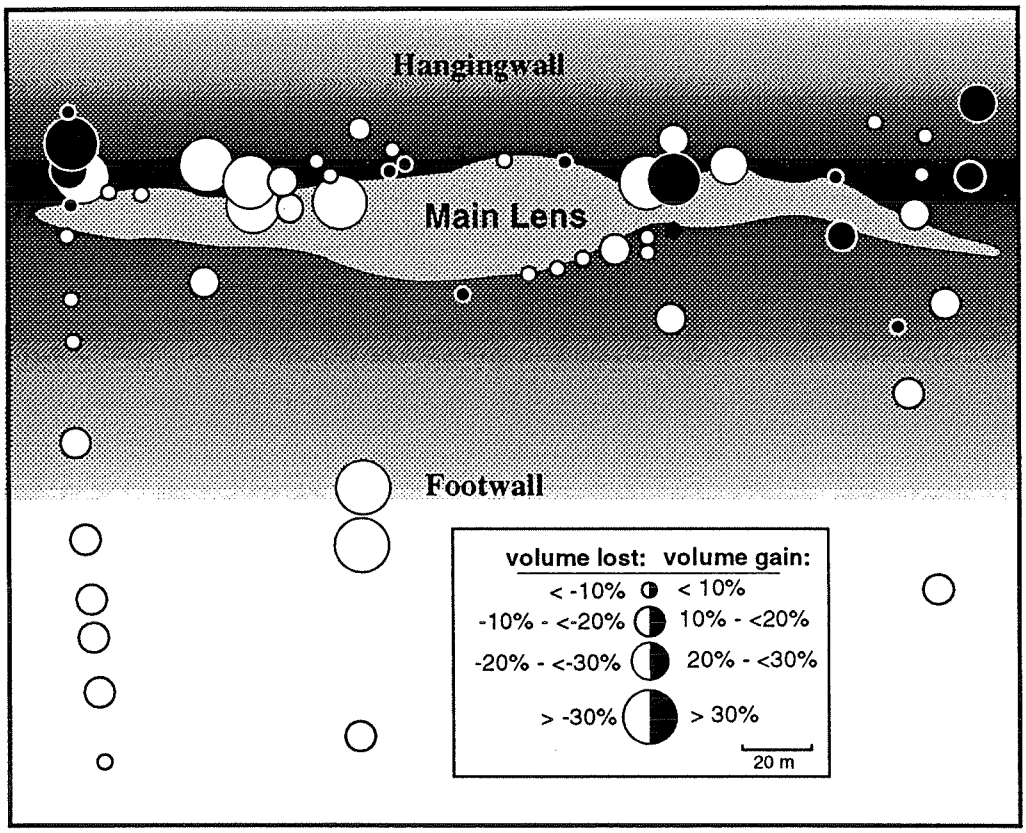

Fig. 5.7 Volume changes on a plan map of the Mobrun mine. The size of the circles represents volume changes of samples projected onto sample location shown in Figure 4.1. The shading is a general representation of the degree of deformation increasing toward the massive sulphide zones.

Although mass transfers due to metamorphism-deformation at Mobrun probably occurred in a closed system (at the deposit-scale) and the mass gained at sites of deposition may be related to mass losses at other nearby sites, substantial mass loss (on the scale of the deposit) (Table 5.1b) may reflect transfers of mass (especially silica) elsewhere within the deposit. Microscopic studies of the massive sulphide ore zones show that they contain considerable amounts of quartz as pressure shadows and filling fractures.

5.5.3 Fluid-rock ratio in metamorphism-deformation event

Mobile fluids probably played a major role in metamorphic reactions, mass transport and deformation processes in the Mobrun deposits. Due to the large amount of mass transported by fluid flow and the limitation in solubility of species in hydrous solutions, significant volumes of fluid are needed to remove this material from cleavage zones formed during metamorphism-deformation. Using a value of 6×10^{-4} g SiO_2/g H_2O for the saturation of SiO_2 in aqueous fluids (temperature ~300°C)(Cobble et al., 1982) and up to 60% dissolution of quartz, a fluid-rock ratio of the order of 10^3 results.

Although the sources of fluids are uncertain, the physical and chemical dewatering of rocks during metamorphism-deformation may have provided some portions of the fluid (i.e., metahydrothermal mineralizing fluids; Fyfe et al., 1978). Other fluids may have been derived via an accumulation of discrete fluid phases

in the regional metamorphic environment, e.g., fluids hosted in microcracks, in cavities or in tubules at the edges and corners of mineral grains (Etheridge et al., 1983). The volume of fluid expelled from these sources is relatively large, especially if some channelling of fluids takes place along macroscopic fracture systems.

Such considerations have demonstrated a need for other permeability paths, such as crack-seal and single-stage vein systems to provide for the focusing of fluids and high fluid-rock ratios. For example, deformation results in a significant increase in interconnected veinlet porosity and hence a generally enhanced rock permeability. Furthermore, the formation of such porosity (e.g., extension crack) during deformation may lead to the convection of fluids due to the instability of the metamorphic fluid under high pressures.

In space between the grains (e.g., pressure-solution domains) high volumes of fluid are not available, and the channelling of fluid is not possible for more than microscopic distances. In this condition the diffusion mechanism may be responsible for dissolution-transfer-precipitation of materials.

Therefore, fluid transport at Mobrun may also have involved a combination of diffusion in grain-scale and focused fluid flow through interconnecting fractures. The rates of diffusion in an aqueous medium, particulary along phyllosilicate domains formed during the active development of cleavage planes, are orders of magnitude greater than the rates for solid-state diffusion (Bell and Cuff, 1989).

However, diffusion in an stationary aqueous phase could account for the recorded short-range (i.e., microscopic-scale) transport of large amounts of material without calling upon unrealistically high amounts of fluid flow.

5.6 SUMMARY

Absolute differences in the Zr contents for the reconstituted compositions of altered and deformed rocks and their corresponding precursors have been used to detect mass changes attributable to hydrothermal alteration and metamorphism-deformation of the Mobrun wallrocks. Computations show that volume changes can be calculated from the normative mineralogies and densities of minerals found in reconstructed precursor compositions. The basic technique involves documentation of inert phases within the altered rocks, such as occurrences of Ti- and Zr-oxide minerals along the cleavage surfaces of deformed rocks.

Mass and volume changes indicate that the host rocks of the Mobrun mine are characterized by a wide range of gains and losses of chemical components, particulary silica. In addition to the previously recognized metasomatism related to synvolcanic hydrothermal alteration, major mass transfers occurred during the metamorphism-deformation of hangingwall rocks. Mass transfer during metamorphism-deformation is assumed to have occurred mainly by convection of metamorphic fluids along local permeability paths within the deformed rocks.

CHAPTER 6

FABRICS IN SULPHIDE ORES

6.1 INTRODUCTION

This chapter is concerned with textural and microstructural features formed in massive sulphide bodies at Mobrun during syngenetic hydrothermal activity and subsequent metamorphism-deformation. Particular attention is given to the effects of diagenesis during initial hydrothermal emplacement of the sulphide bodies and to post-ore metamorphism-deformation effects.

The fabric of massive sulphide ores, as in the associated wallrocks (see Chapter 3), is significantly modified during both deformation and metamorphism. These events play an important role in the evaluation of structural, mineralogic and textural features of the orebodies, and in turn, the interpretations of those aspects may provide valuable information about the geologic history of the mineralization. Previous studies on this topic include Lianxing and McClay (1992), Grenne and Vokes (1990), Gilligan and Marshall, (1993); Marshall and Gilligan (1993), Brill (1989), Cox (1987), McDonald (1976), Vokes (1969, 1971), Mookherjee (1976) and Humphreys (1986). Many of these studies focus on microstructural textures and mass transfers.

6.2 ORE PETROGRAPHY

The mineralogy of the Main Lens complex is dominated by pyrite, with which are associated lesser amounts of chalcopyrite and sphalerite and smaller quantities of galena and pyrrhotite. Minor amounts of digenite, tetrahedrite and magnetite also have been observed. Gold and electrum are present in trace quantities. The dominant gangue minerals are quartz, sericite, chlorite, carbonate, and graphite.

The Main Lens at Mobrun displays a metal zonation typical of Noranda-type volcanic-hosted massive sulphide deposits (LaRocque and Hodgson, 1993; Barrett et al., 1992)(Fig. 6.1). Lower portions of the sulphide body contain high concentrations of chalcopyrite which are overlain by sphalerite-rich ore.

6.2.1 Sulphide minerals

Pyrite, the main mineral (90%) of the sulphide ores, is also a dominant sulphide mineral in the felsic host rocks where it occurs as disseminated grains and vein-fillings.

Textures exhibited by pyrite vary across the deposit depending upon the intensity of deformation and recrystallization that has taken place. In some places, the pyrite occurs as well-formed, extremely fine-grained, allotrimorphic grains (Fig. 6.2), and in other cases, it is found as colloform-banded masses intimately

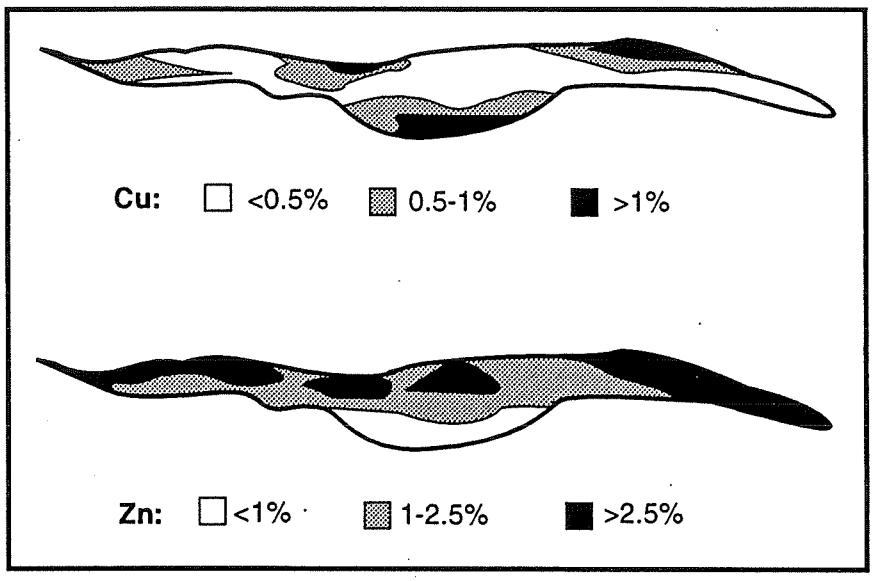

Fig. 6.1 Horizontal section 65 m below surface showing the distribution of the dominant ore metals through the core of the Main Lens. After LaRocque and Hodgson, 1993.

intergrown with varying proportions of other sulphides (sphalerite and chalcopyrite) and microcrystalline gangue material (Fig. 6.3). In less sulphide-rich portions, fine-grained and coarse-grained pyrite appear as disseminated euhedral to subhedral crystals or as aggregates disseminated throughout the chlorite-sericite-quartz groundmass (Fig. 6.4). In some areas, pyrite is accompanied by massive chalcopyrite or sphalerite. Microprobe analyses of pyrite indicate to very low content of arsenic, up to 0.25 atom %.

Sphalerite, the second most abundant sulphide, is most common toward the central hangingwall portions of the Main Lens, as well as in the eastern and western flanks of this sulphide lens where it is found as widespread interlaminated bands of pyrite and sphalerite. At the microscopic scale, sphalerite may form tiny, rounded inclusions in pyrite (Fig. 6.5). Sphalerite commonly contains disseminated grains of chalcopyrite in textures referred to as "chalcopyrite disease" (Fig. 6.6). This texture, previously interpreted as an exsolution feature (e.g., Betekhtin, 1958), is now believed to result from the replacement of iron-bearing sphalerite (Bortnikov et al., 1991; Barton and Bethke, 1987). According to this interpretation, the chalcopyrite formed by the reaction of iron in sphalerite with copper transported in a hydrothermal solution.

Two types of sphalerite are recognized at Mobrun: (1) primary sphalerite, which is associated with colloform pyrite (see below) and formed during hydrothermal activities on the sea-floor, and (2) secondary sphalerite, which is

Fig. 6.2 Photomicrograph showing the very fine-grained primary texture of pyrite between coarser grains of pyrite (euhedral grains), quartz (black) and sericite (black). Field of view 1 mm across. Reflected light.

Fig. 6.3 Very fine-grained colloform pyrite (py) showing growth zoning with intergrown sphalerite (sph) and quartz (qz). Late pyrite veinlet cuts through the earlier colloform pyrite. Field of view 0.5 mm across. Specimen etched with H_2SO_4. Reflected light.

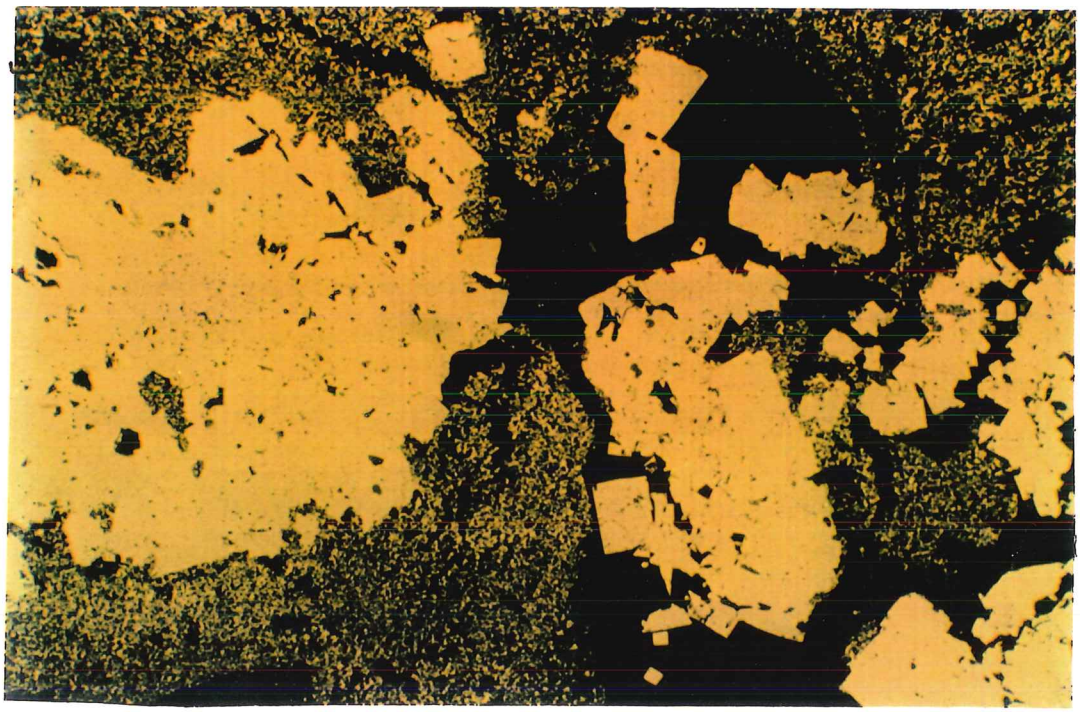

Fig. 6.2

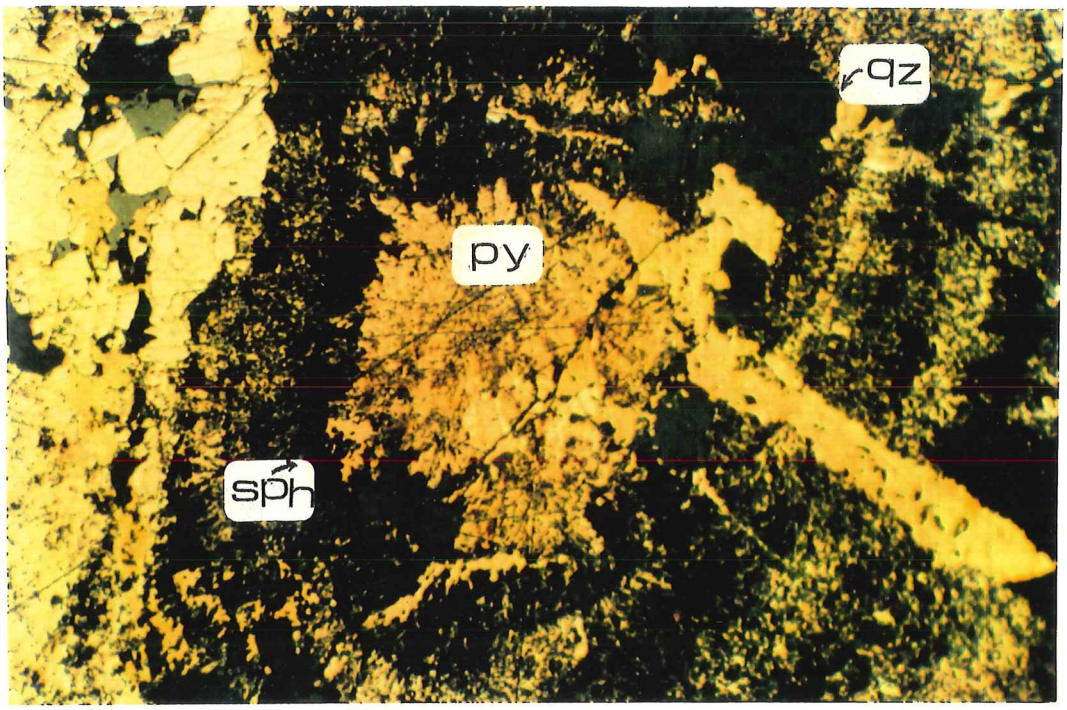

Fig. 6.3

Fig. 6.4 Photomicrograph showing disseminated fine-grained subhedral to euhedral pyrite in a quartz-sericite-carbonate matrix. Field of view 2 mm across. Reflected light.

Fig. 6.5 Photomicrograph showing rounded sphalerite grains located within coarse-grained pyrite. Field of view 0.5 mm across. Reflected light.

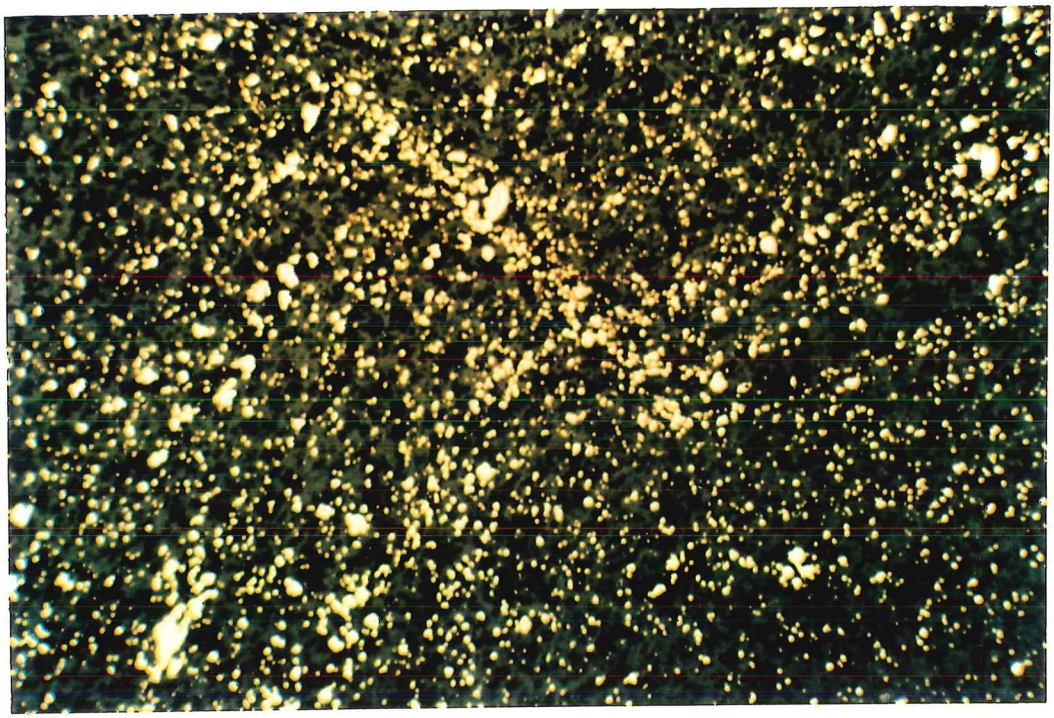

Fig. 6.4

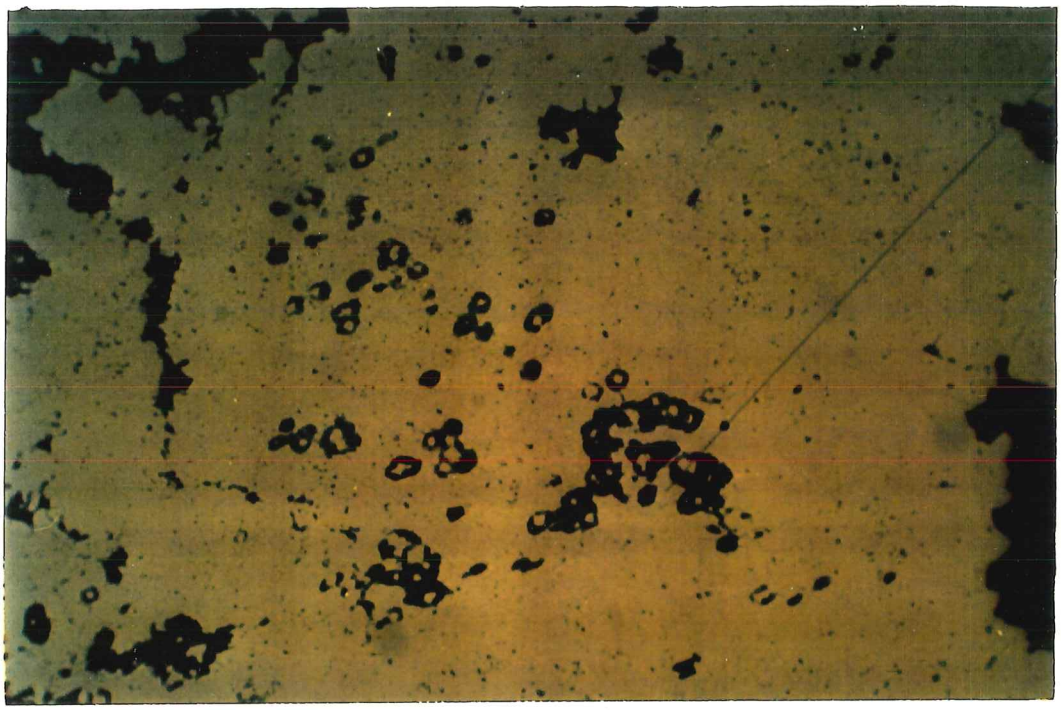

Fig. 6. 5

primary sphalerite that recrystallized during metamorphism-deformation. Microprobe analyses of primary and secondary sphalerite do not show any significant compositional differences. The iron content of sphalerite in both types does not exceed 3 atom %.

Chalcopyrite is almost as abundant as sphalerite in the samples studied. The richest copper ores are located toward the central-footwall part of the orebody.

Chalcopyrite commonly fills fractures in pyrite and forms inclusions within pyrite and sphalerite (Fig. 6.7). Locally, it is present as large masses or patches of a fine-grained pyrite-chalcopyrite assemblage.

Digenite and tetrahedrite occur as trace components replacing chalcopyrite (Fig. 6.8). Galena is relatively uncommon in the sections studied. Where present, it is commonly present in late veins (Fig. 6.9) and at the borders of pyrite grains. Pyrrhotite is present as fine-grained inclusions in pyrite grains (Fig. 6.10). This texture may formed by conversion of pre-existing massive pyrrhotite to pyrite by a sulphidation process. Massive pyrrhotite, such as that observed within the 1100 Lens (LaRocque and Hodgson 1993), has not been observed within the Main Lens complex.

Gold and silver have been investigated by LaRocque and Hodgson (1993). They propose that gold was introduced during initial syngenetic mineralization and was subsequently remobilized during regional metamorphism and tectonic

Fig. 6.6 "Chalcopyrite disease", consisting of fine grains of chalcopyrite oriented within sphalerite. The texture results from replacement (Barton and Bethke, 1987). Field of view 1 mm across. Reflected light.

Fig. 6.7 Photomicrograph showing chalcopyrite (cpy) filling fractures in pyrite metacrysts. Field of view 1 mm across. Reflected light.

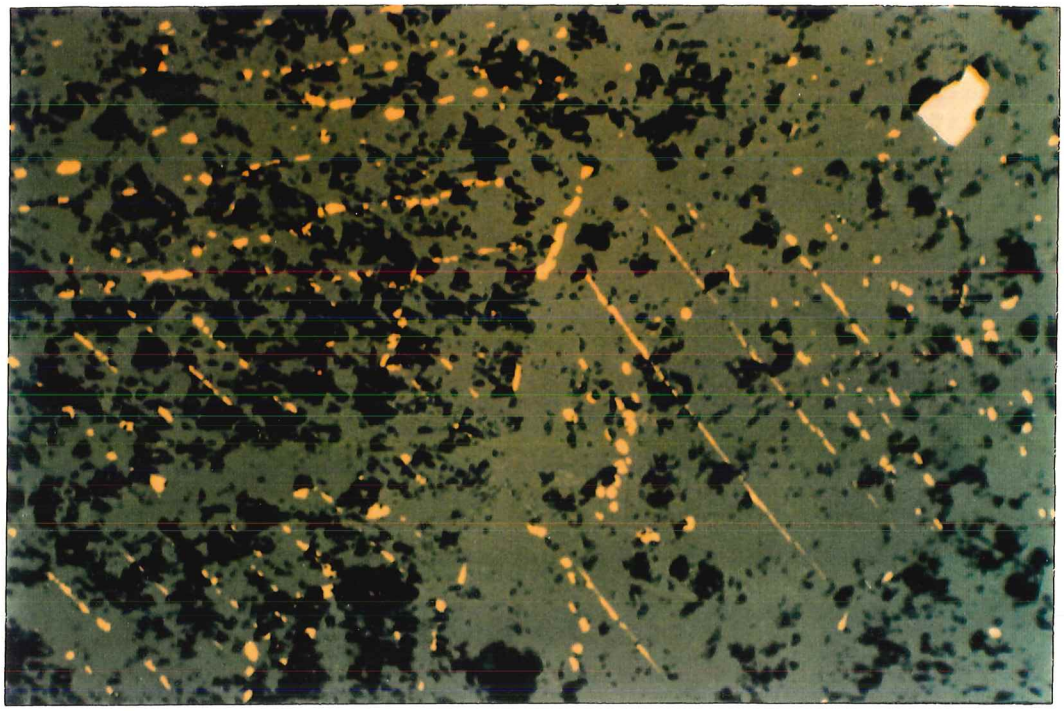

Fig. 6.6

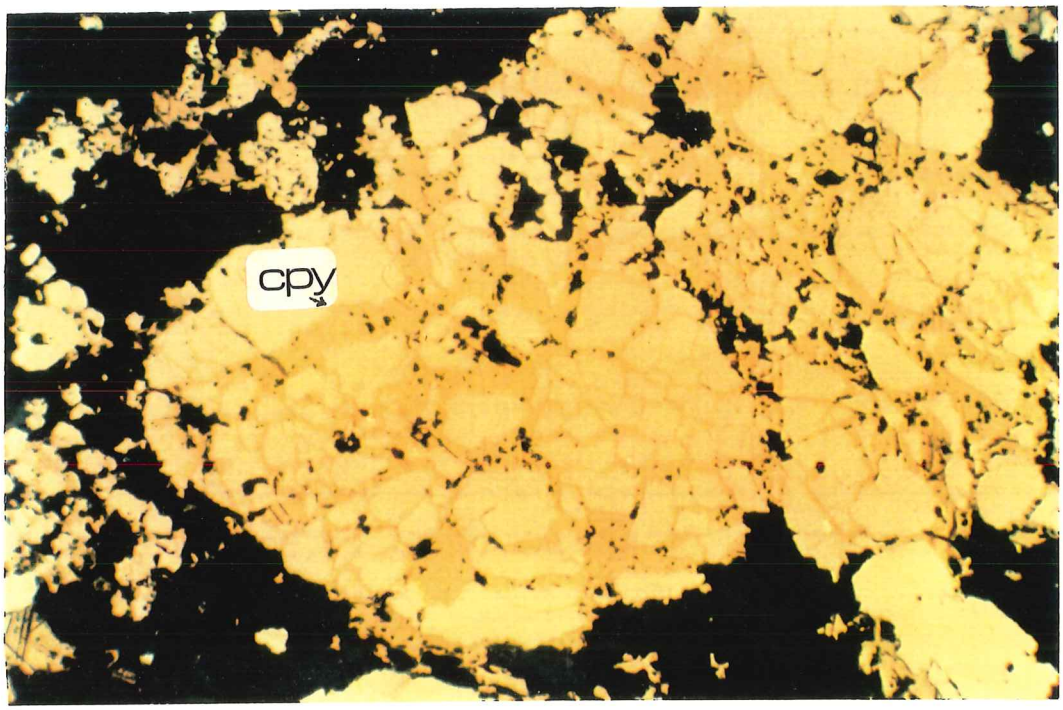

Fig. 6.7

Fig. 6.8 Photomicrograph showing border of chalcopyrite grains replaced by digenite (dig). Field of view 0.5 mm across. Reflected light.

Fig. 6.9 Photomicrograph showing a fracture in pyrite filled with galena. Field of view 0.5 mm across. Reflected light.

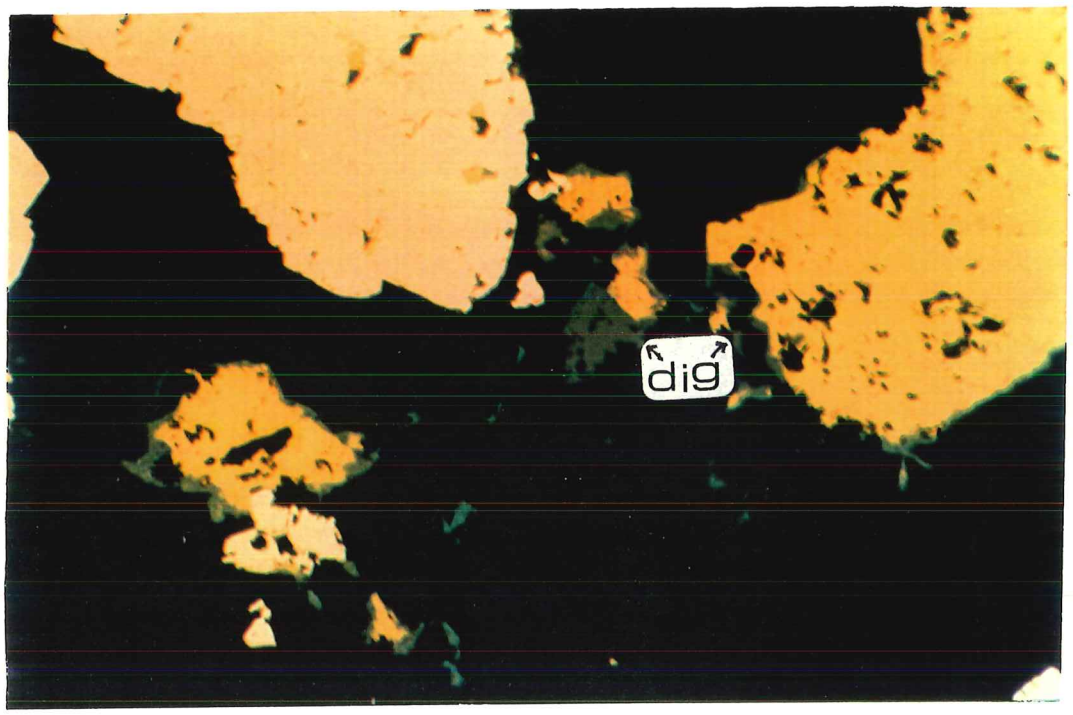

Fig. 6.8

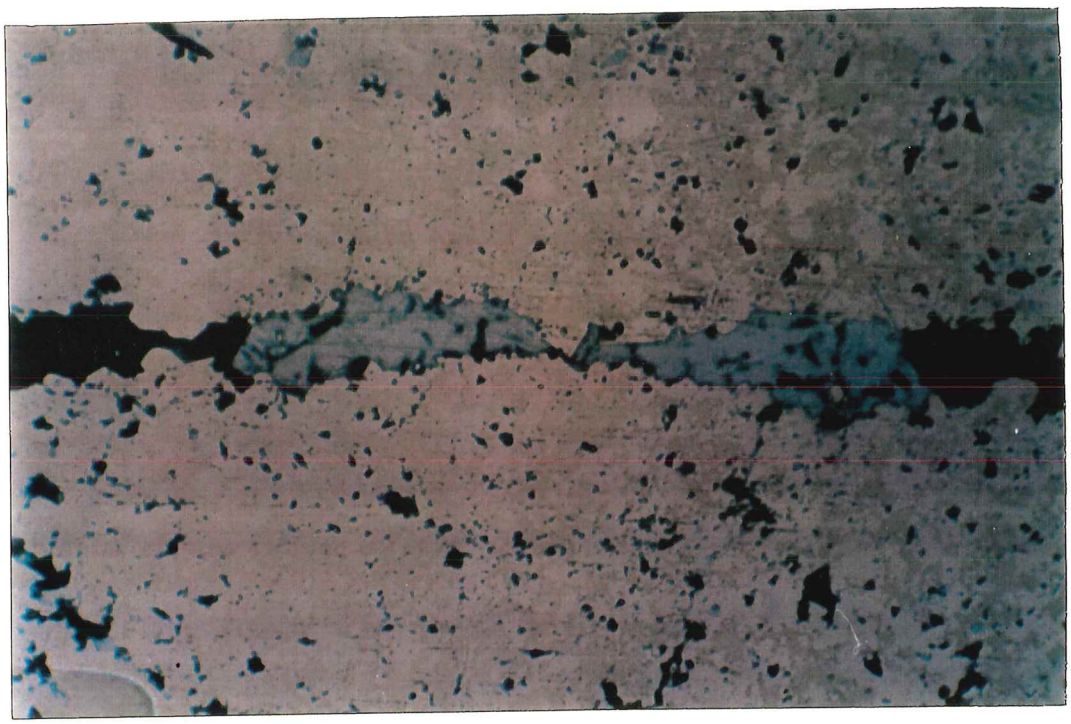

Fig. 6.9

deformation. In some areas, massive undeformed pyrite exhibits concentrations of gold in the range of tens of ppm. In other areas, where pyrite has been recrystallized, gold has been remobilized into different-scale veins containing quartz, calcite, chalcopyrite, sphalerite, galena and/or electrum (Ag-Au).

6.2.2 Sulphide veins

From a geometric point of view, three different types of sulphide veins developed within the Mobrun altered wallrocks; they commonly exist in the same sample. These veins include:

(1) finely disseminated micrometre- to millimetre-size pyrite grains, generally idiomorphic, or irregular and anastomosing, in configuration, and in many cases re-oriented parallel to the host rock schistosity (Fig. 6.11): quartz and calcite commonly fill pressure shadows adjacent to competent grains. This type of veinlet is present in both the footwall and hangingwall and is most concentrated in the stockwork zone. Such veins are generally related to infiltration of rocks during the initial syngenetic hydrothermal activity.

(2) tabular masses of pyrite in veins up to a few millimetres in thickness (Fig. 6.12): this pyrite has a tendency to form coarse-grained idiomorphic aggregates intergrown within other ore and gangue minerals; in some case, the massive pyrite occurs without other sulphides. The geometry of these veins changed under extensional stresses and displacements which took place across the

Fig. 6.10 Photomicrograph showing inclusions of fine-grained pyrrhotite (po) in coarse-grained pyrite. Field of view 0.5 mm across. Reflected light.

Fig. 6.11 Photomicrograph showing band of fine-grained pyrite lying parallel to the foliation. Field of view 3 mm across. transmitted light.

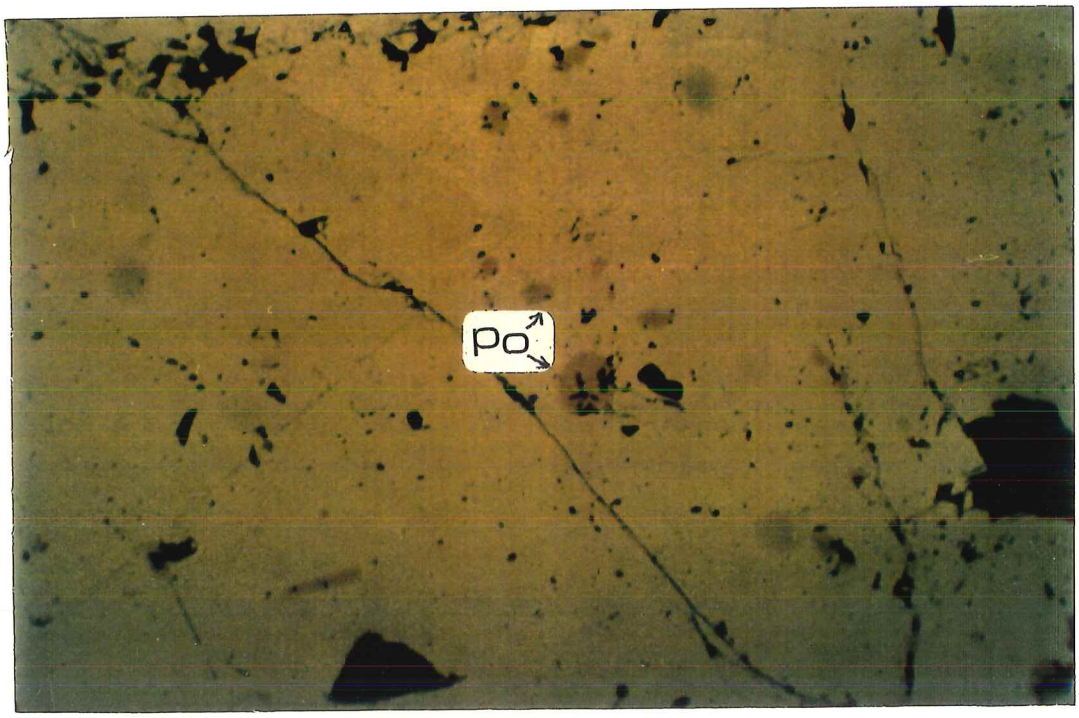

Fig. 6.10

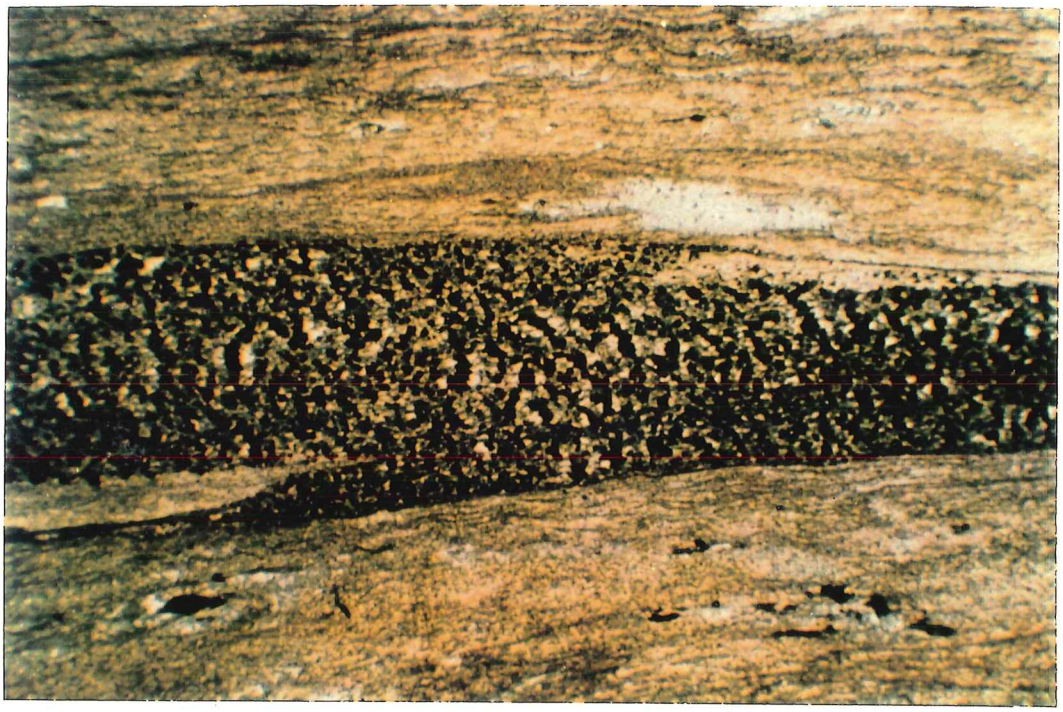

Fig. 6.11

fractures. During deformation, some of these grains were deformed or physically broken into microclasts and re-oriented parallel to the schistosity as a result of extensional stress. The genesis of this type of veins may be related to ore-forming hydrothermal activity, with the mineralization reoriented parallel to schistosity during deformation.

(3) Pyritic crack-seal veins in both the footwall and hangingwall, particularly in the brecciated rhyolite of the footwall stringer zone: this pyrite occurs in veins that are parallel to or crosscut foliation and show a symmetrical internal metal zonation, commonly exhibiting pull apart and boudinage textures (Fig. 6.13). Crack-seal veins are evidence of syntectonic mass transfer involving introductions of matter along the vein structure.

6.2.3 Disseminated pyrite

Disseminated pyrite grains and aggregates of grains occur throughout the mine area, together with quartz, sericite, chlorite and carbonate in pressure shadows. Locally higher concentrations of pyrite are found in the immediate vicinity of the orebodies.

Pyrite grains generally truncate the foliation with pressure shadow of quartz which have grown parallel to schistosity. Individual pyrite grains are also characterized by euhedral shapes and commonly exhibit pull-apart and boudinage textures (Fig. 6.14). Pyrite was commonly well-developed during cataclastic

Fig. 6.12 Tabular pyrite vein displaying mosaic texture. Cataclastic pyrite fragment are initially displaced as a result of deformation, and the extension cracks are filled with quartz and carbonate. Field of view 3 mm across. Transmitted light.

Fig. 6.13 Syntectonic crack-seal pyrite vein at Mobrun. Vein filling developed by repeated increments of micro-crack openings followed by deposition of pyrite from a syntectonic solution. Progressive stages of deformation caused further dilation and addition of quartz in pressure shadows in tension veins. Field of view is 3 mm across. Transmitted light.

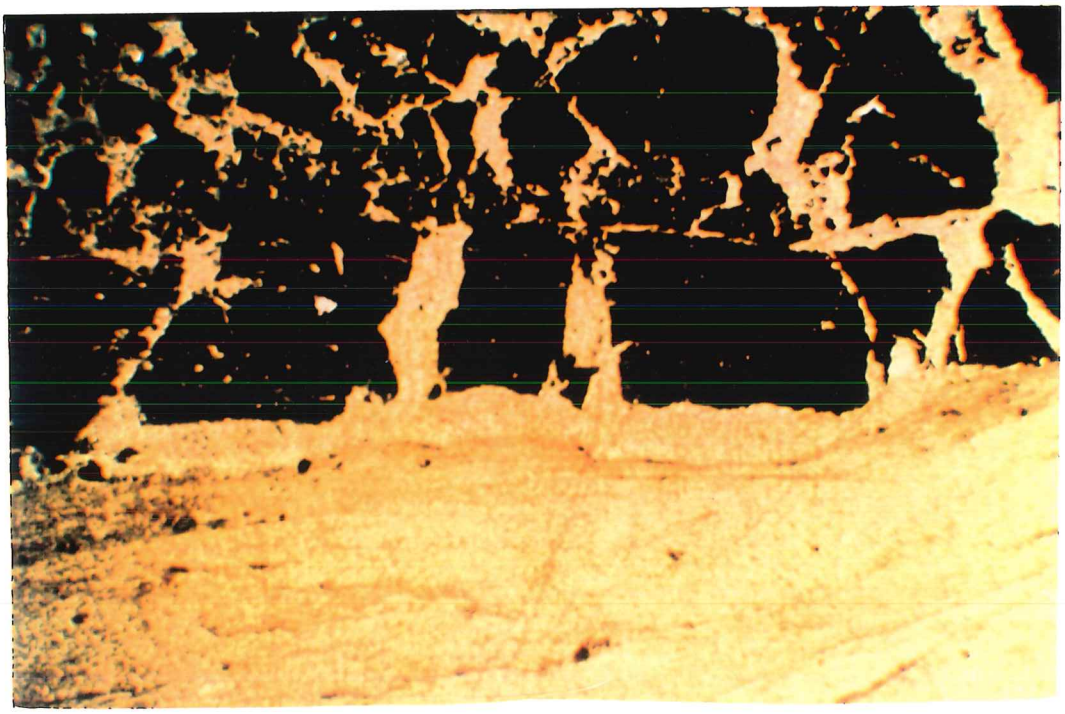

Fig. 6.12

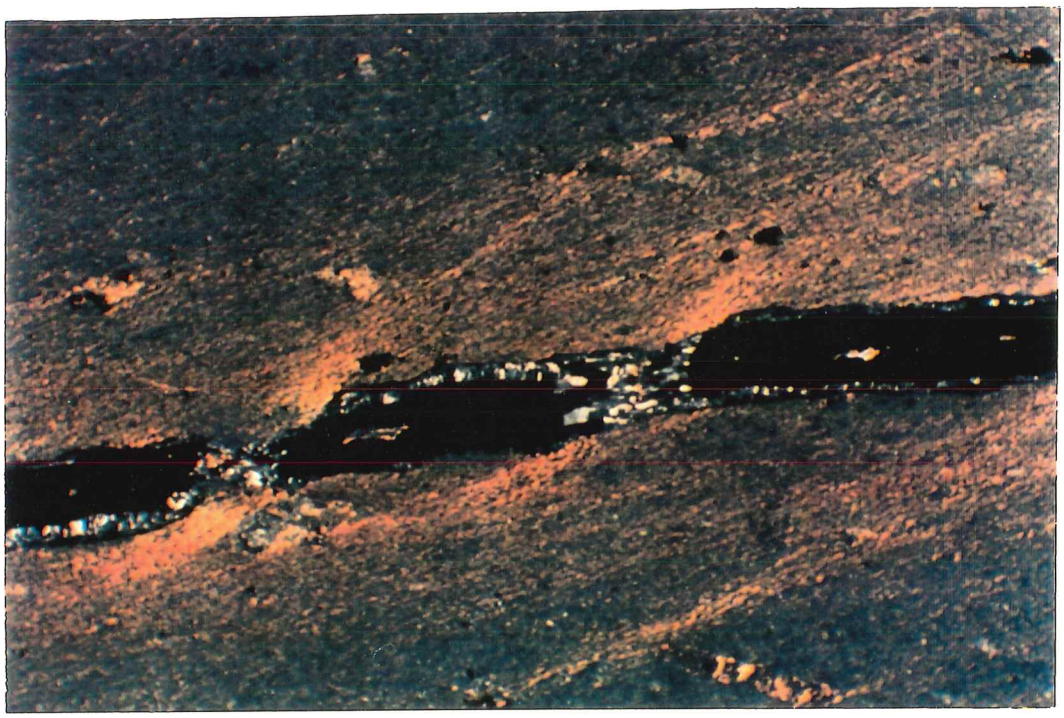

Fig. 6.13

deformation and disseminations of pyrite were re-orientated parallel to schistosity.

High concentrations of tiny pyrite euhedra occur along foliation planes, locally aggregating into very thin continuous seams of pyrite and dimensionally grains orientation (see Section 6.3.2.2). Sulphide-bearing (sphalerite and/or chalcopyrite) pressure shadows are also developed around pyrite crystals.

6.3 ORE TEXTURES AND MICROSTRUCTURES

6.3.1 Methodology

In order to describe the microstructural features of sulphide minerals some of the polished thin-sections are etched with acid, and few thick slices of rocks are prepared for X-ray goniometry.

6.3.1.1 Etching

Numerous polished sections, mainly from the Riopel (1992) collection, were prepared to determine the deformation mechanisms that occurred at the microscopic scale. Representative polished sections of pyrite-rich samples were carefully etched with acids in order that growth and deformation features could be assessed and various pyrite phases recognized, as described by Craig and Vaughan (1981) and Yamada et al. (1979). Details of the etching methods employed are given in Appendix 6.1.

6.3.1.2 X-ray goniometry

The determination of preferred grain orientations in sulphide ores is an important aspect in the analysis of the metamorphism and deformation in ore deposits (Ken and McClay, 1983). X-ray texture analyses were performed with a pole-figure goniometer (Appendix 6.2) used to determine possibly preferred orientations of sulphide ores (pyrite and sphalerite) and of associated gangue minerals (quartz and chlorite) in the Main Lens orebody. The procedure follows the technique of Schulz (1949) for reflection mode, and involved the determination of partial-reflection pole figures in all positions in 3-dimensional space.

Pole-figure analyses done by X-ray texture goniometry may be hampered by a number of factors, such as interfering diffraction peaks from various minerals and reflectance anisotropy caused by coarse-grained or mixed heterogeneous minerals. To obtain the best measurements of pole figures, more than twenty slabs were analyzed with particular attention to the selection of monomineralic, homogeneous and fine-grained specimens. In spite of these precautions, satisfactory analyses were limited to only a few samples.

6.3.2 Textures and microstructures of sulphide ores

The microstructures of ore minerals from the Mobrun mine have been studied in detail in order to determine the deformation mechanisms that operated during metamorphism-deformation of the orebody. Brittle and ductile

deformation, together with metamorphic recrystallization of the sulphide ores (see below) has modified the primary depositional features of the mineralization to a greater or lesser degree; in some cases, primary features were completely obliterated.

6.3.2.1 Primary depositional textures

Primary textures were formed by ascending solutions that exhaled onto the sea floor during essentially synvolcanic hydrothermal activity. This hypothesis agrees with the finding of similar textures in modern deposits (Lianxing and McClay, 1992; Grenne and Vokes, 1990; Graham et al., 1988 and Paradis et al., 1988). Relicts of primary depositional-diagenetic features at Mobrun are generally well preserved in the centre-footwall side of the Main Lens. They are more commonly preserved in pyrite than in other sulphides, and they are also best observed where the ore has been little affected by later metamorphism and deformation. Such textures include: microcrystallites, equidimensional overgrowths, colloform growths, and framboidal-spheroidal textures (Lianxing and McClay, 1992).

In general, the primary textures are modified by deformation and recrystallization, and they have undergone progressive grain growth and replacement to form euhedral or granular grains. Some primary textures were partially destroyed during brittle deformation.

Primary features recognized at Mobrun include the following microstructural textures:

(1) Colloform growths:

The preservation of some colloform textures (Fig. 6.3) from destruction by cataclasis and recrystallization is evident in the many polished sections taken from central parts of the orebody and extends out into flanks. Colloform textures are also observed in some syntectonic veins of pyrite (Fig. 6.15). Rapid mixing of the fluid led to open-space deposition of colloform sulphides, mainly pyrite and sphalerite (Grenne and Vokes, 1990).

(2) Framboidal-spheroidal textures:

Spherulitic intergrowths of pyrite and sphalerite have been found in the central lower part of the orebody as well as in both flanks. Spheroids of micrometres to millimetres in diameter are composed mainly of framboidal cores of pyrite microcrystallites (Fig. 6.16). Sphalerite or chalcopyrite grains can commonly be found at the centres of spheroids and within interlayers. Chalcopyrite layers within spherulites are interpreted by LaRocque et al. (1993) as syngenetic replacements of primary pyrite and sphalerite, based on similar textures which have been documented in seafloor massive sulphide bodies (see, for example, Peter and Scott, 1988).

Microstructural features indicate deformation of some pyrite from approximately spheroidal shapes into ellipsoids (Fig. 6.17).

Fig. 6.14 Photomicrograph showing extension microfractures in a single pyrite grain filled with fibrous quartz. Field of view 0.5 mm across. Transmitted light.

Fig. 6.15 Colloform-banded and zoned growths of pyrite in a fracture filling indicating open-space filling at low temperatures. Right-hand part of sample etched with HNO_3. Field of view 1 mm across. Reflected light.

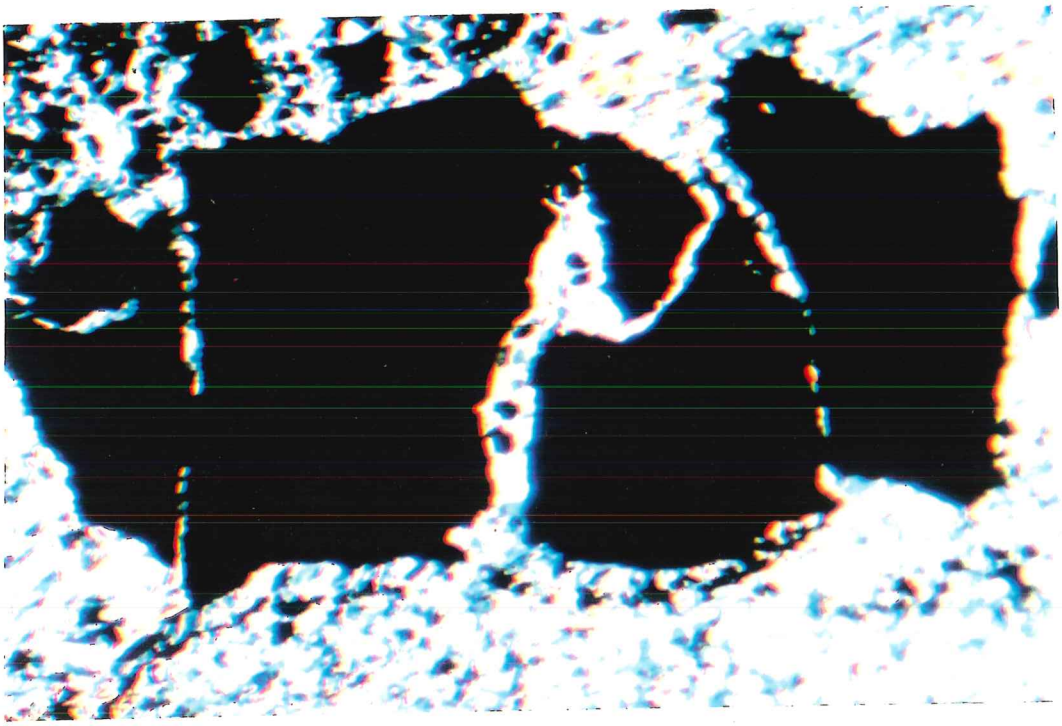

Fig. 6.14

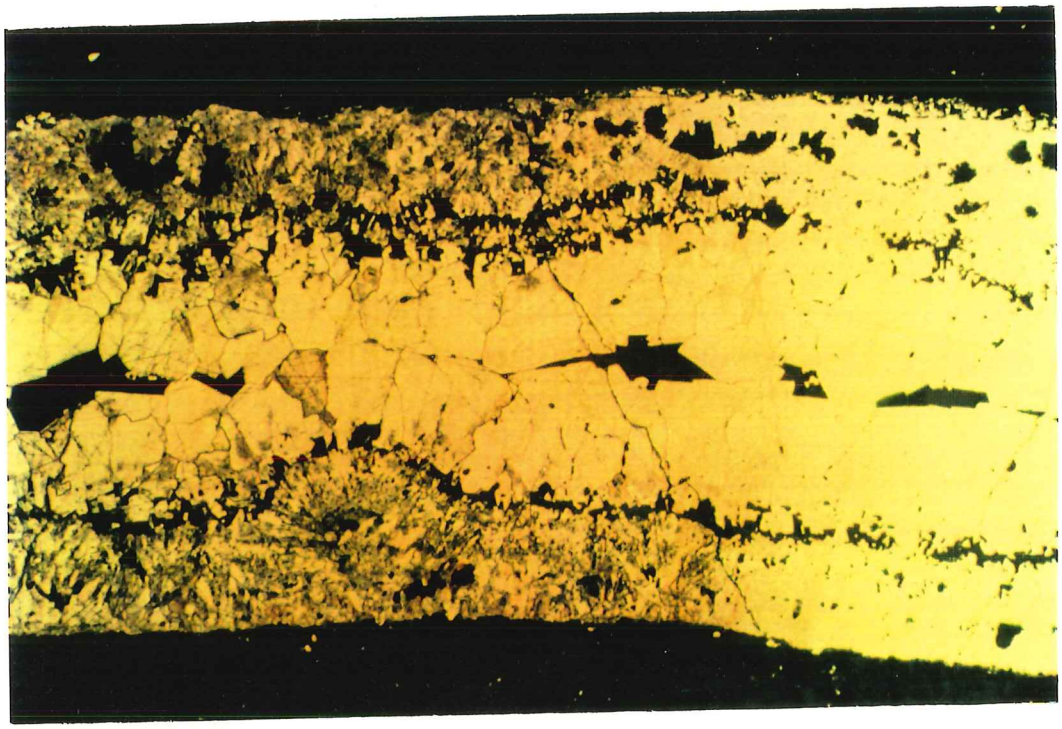

Fig. 6.15

Fig. 6.16 Photomicrograph of spheroidal pyrite surrounded by radial fibrous rim. Field of view 0.5 mm across. Specimen etched with HNO_3. Reflected light.

Fig. 6.17 Photomicrograph showing a deformed pyrite framboid. The oblate pyrite framboid occurs within massive sulphide ore. Field of view 0.5 mm across. Specimen etched with H_2SO_4 + $KMnO_4$. Reflected light.

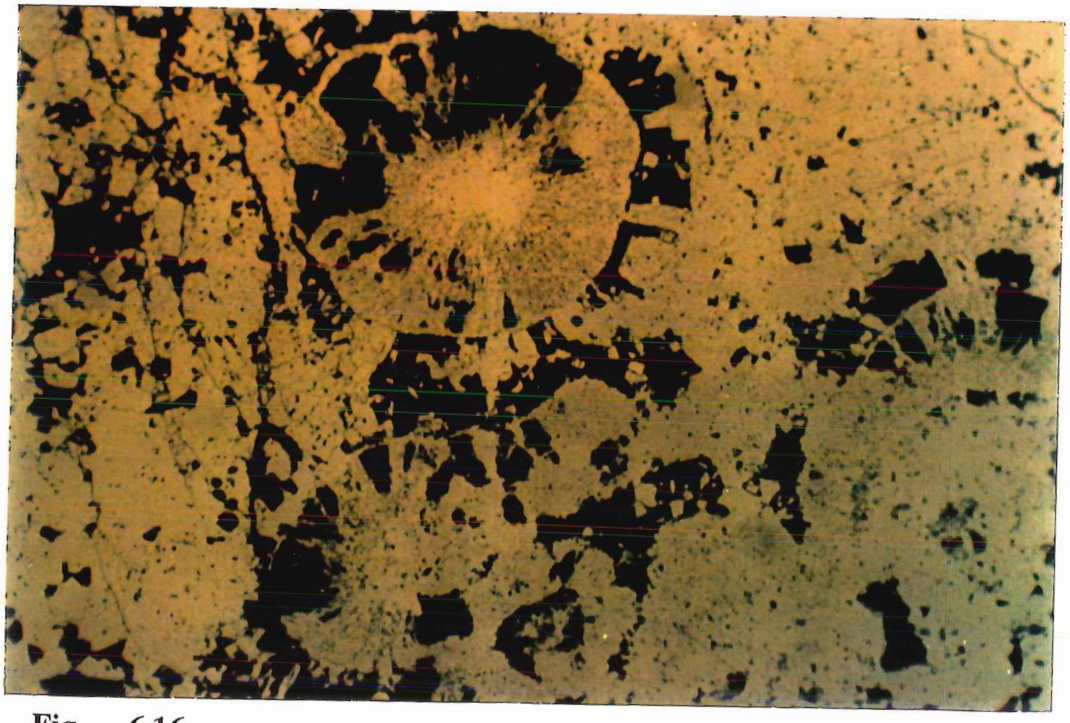

Fig. 6.16

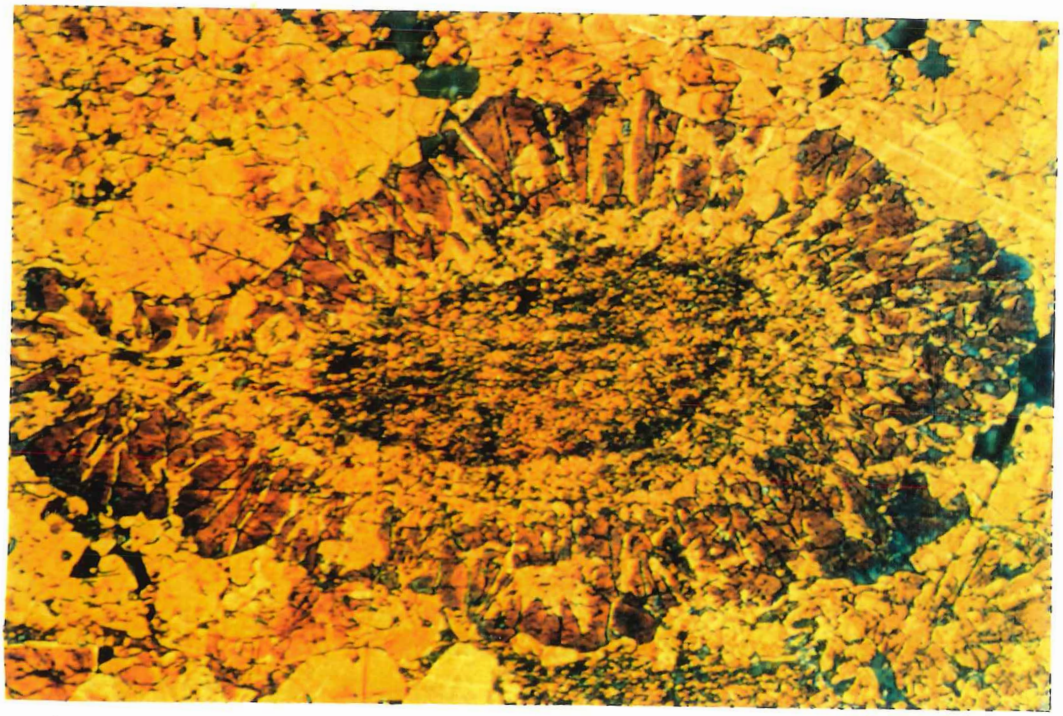

Fig. 6.17

This deformation is produced by boundary sliding of the internal micrograins which ultimately become desegregated with further deformation (Lianxing and McClay, 1992).

(3) Microcrystallites:

Pyrite microcrystallites are very fine-grained, with almost equal grain-size (<10 μm), and are mostly subhedral to euhedral, and etch resistant (Fig. 6.2). In some cases, these microcrystallites are associated with minor quantities of sphalerite forming colloform textures.

This massive fine-grained pyrite is commonly present in the central part of the orebody. Similar extremely fine-grained pyrite is reported by Honnorez et al. (1973) in present-day base-metal precipitates on the sea-floor in zone of hydrothermal activity.

(4) Diagenetic overgrowths:

These overgrowths are commonly seen in many samples. They contain a central pyrite micro-grain with secondary overgrowth phases. Each overgrowth is readily distinguished from others by different degrees of tarnish after etching (Fig. 6.18a). Pyritic overgrowths are usually etch-resistant. Pyrite grains of similar well-zoned equidimensional habit and notably lacking in dimensional preferred orientations are suggested by McClay (1991), and Lianxing and McClay (1992) to be early diagenetic in origin, as indicated by the slow formation of the overgrowths at relatively low temperatures.

In some cases, overgrowths of younger pyrite, mainly euhedral forms, envelop the spheroidal pyrite which exhibits circular growth zones (Fig. 6.18b).

(5) Syngenetic structures:

Banded disseminated pyrite-sphalerite mineralization (Fig. 6.19) is abundant in both the eastern and western flanks. The fine equidimensional size of sphalerite and pyrite grains and the absence of deformational features are interpreted as primary features. Graded bedding of pyrite grains is also observed in some parts, and this is also interpreted as a primary depositional feature formed under sea-floor conditions.

The pyrite grains show very variable degrees of idiomorphism. Typically they show embayment faces (Fig. 6.20), and contain abundant included grains of matrix sulphides and gangue minerals. The embayed crystal of pyrite may be considered to have resulted from syngenetic dissolution of early euhedral crystal. In fact, this process is different from what we see in some grains which occasionally show rounding of their subhedral to euhedral shapes due to chemical dissolution by pressure solution creep or mechanical effects (e.g., cataclasis) caused by deformation.

6.3.2.2 Deformational and metamorphic features of pyrite

Various microstructural deformation features have been recognized in sulphide ores under different metamorphic grades (McClay, 1991; Brown and

Fig. 6.18a Pyrite with well-developed growth zoning. Pyrite grains which appear homogeneous commonly reveal well-deformed growth zoning after etching with acid. Field of view 0.5 mm across. Specimen etched with H_2SO_4 + $KMnO_4$. Reflected light.

Fig. 6.18b Photomicrograph of zoned euhedral overgrowth of pyrite with cores of framboidal relics. Field of view 0.5 mm across. Specimen etched with H_2SO_4 + $KMnO_4$. Reflected light.

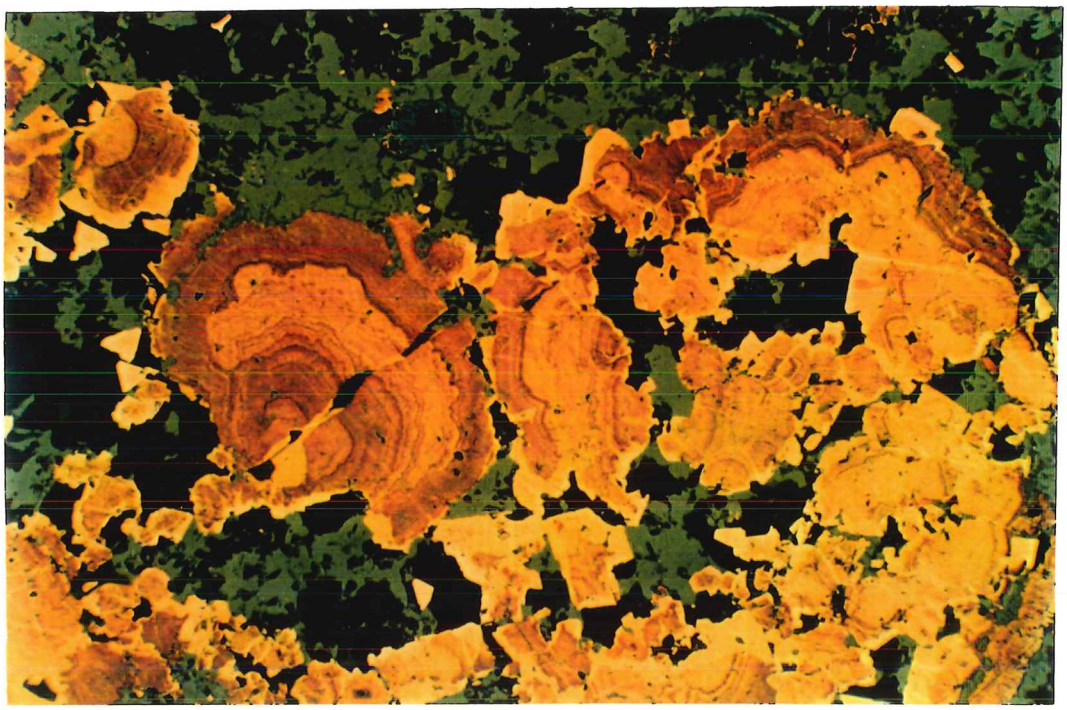

Fig. 6.18a

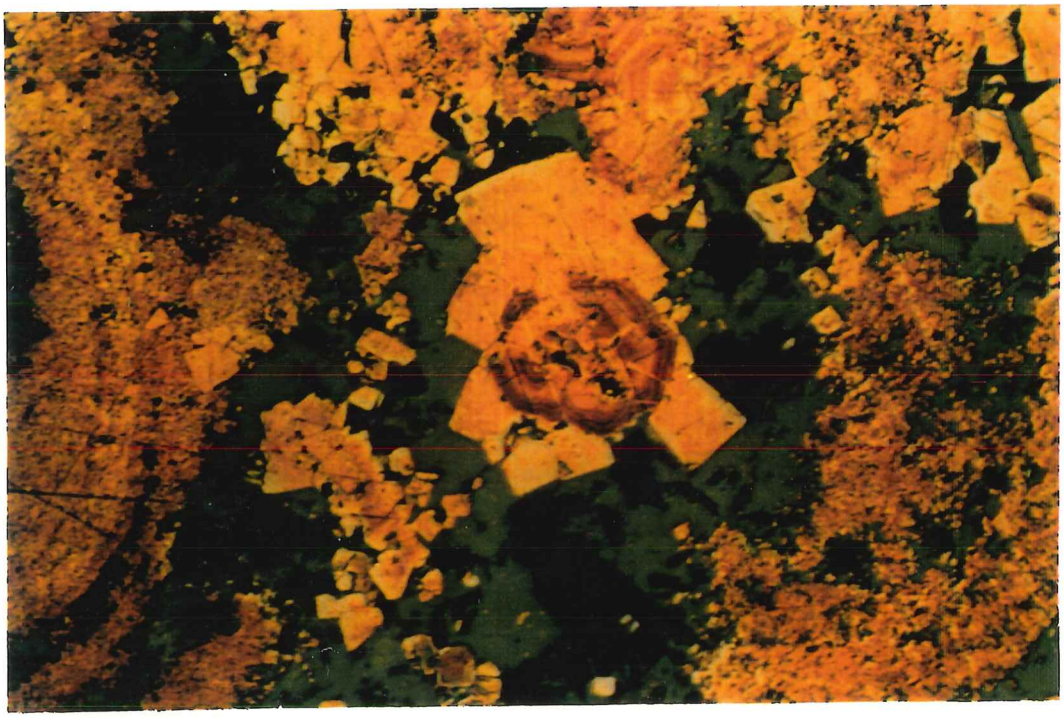

Fig. 6.18b

Fig. 6.19 Photo of banded fine-grained pyrite-sphalerite.

Fig. 6.20 Pyrite crystal showing embayments and inclusions of matrix minerals and gangue minerals. Field of view 1 mm across. Reflected light.

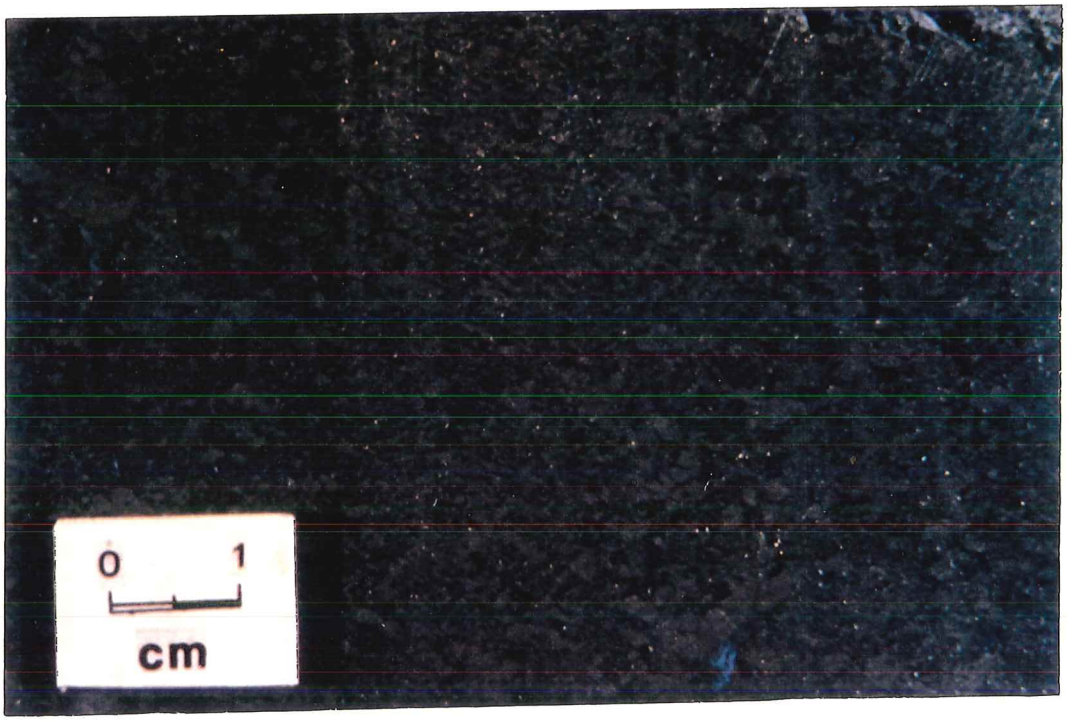

Fig. 6.19

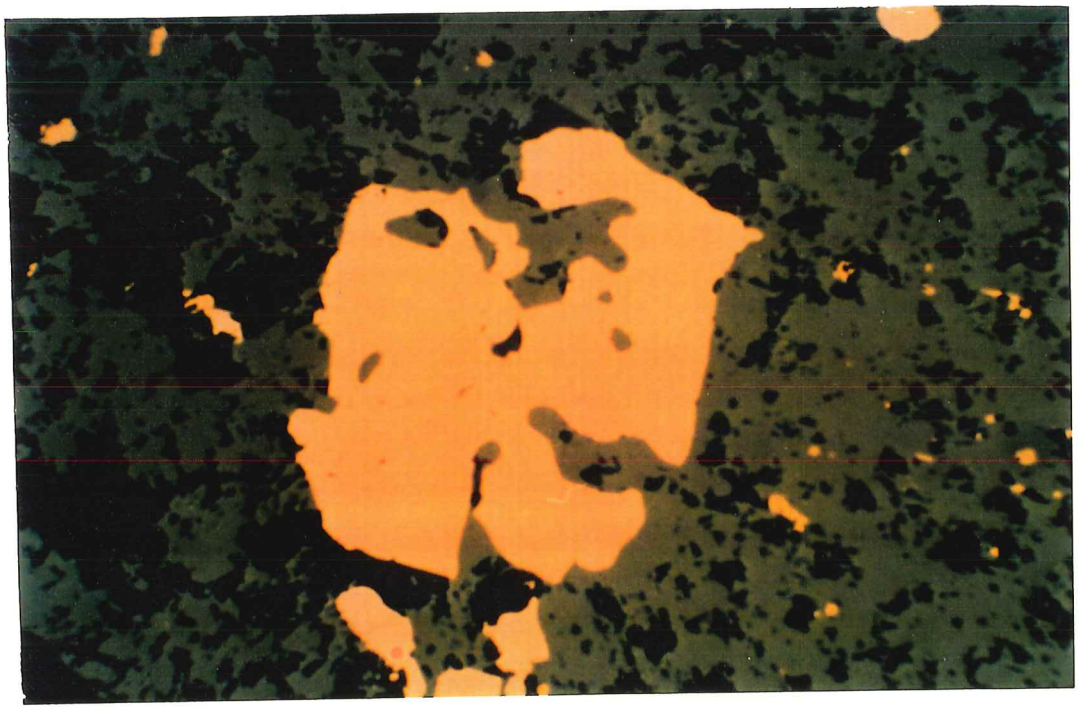

Fig. 6.20

McClay, 1993; McClay and Ellis, 1993, Craig and Vokes, 1992, 1993). The deformation of pyrite under such conditions is illustrated by means of a deformation mechanism map (Frost and Ashby, 1982)(Fig. 6.21) which displays the relationship between flow stress, strain rate, temperature and grain size. The major deformational mechanisms observed at the Mobrun orebodies are restricted to those occurring within low-grade metamorphic environments, including cataclasis, pressure solution, and moderately intense dislocation glide and annealing. These texture are described below:

(1) Cataclastic textures:

Brittle failure has been described as an important deformation mechanism affecting pyritic sulphide bodies (Cox, 1987; Craig, 1983; Mookherjee, 1971). The resulting cataclastic texture occurs at all metamorphic grades and is favoured by low temperatures and low effective confining pressures (Cox, 1987; McClay and Ellis, 1983). The most spectacular effects are produced within relatively brittle sulphides such as pyrite which may be broken into angular fragments of all sizes.

Cataclastic pyrite is widespread at Mobrun and has been found in most samples studied, particularly in coarse-grained specimens. In polycrystalline aggregates of finely crushed pyrite, angular fragments are commonly sealed by quartz, carbonate and mica. Such fracturing is more intense toward the orebody margins and oriented at right angles to the metamorphic foliation (Fig. 6.22). Fractures in pyrite may be filled by remobilized phases such as galena,

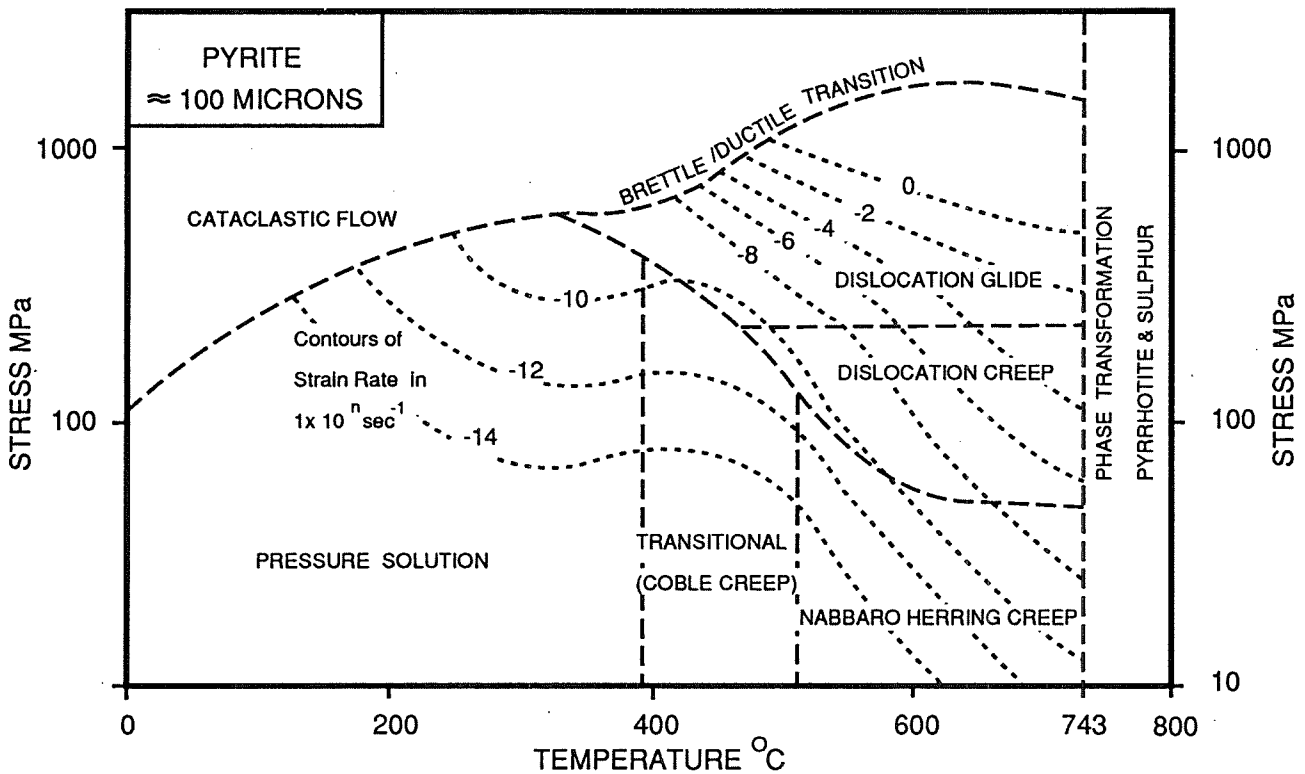

Fig. 6.21 The deformation behaviour of pyrite in a hypothetical deformation mechanism map (McClay and Ellis, 1983). At low metamorphic grades and for reasonable geological strain rates, the dominant deformation mechanisms of pyrite are cataclasis and pressure solution.

Fig. 6.22 Photomicrograph showing extension fracture in pyrite grains which are commonly oriented at right angles to the foliation. Fibrous quartz filled fracture. Field of view 2 mm across. Transmitted light.

Fig. 6.23 Repetitive cataclasis deformation associated with hydrothermal influx. Earlier pyrite (Py 1) fragments are overgrown and fractures filled by later pyrite (Py 2). Field of view 1 mm across. Specimen etched with H_2SO_4. Reflected light.

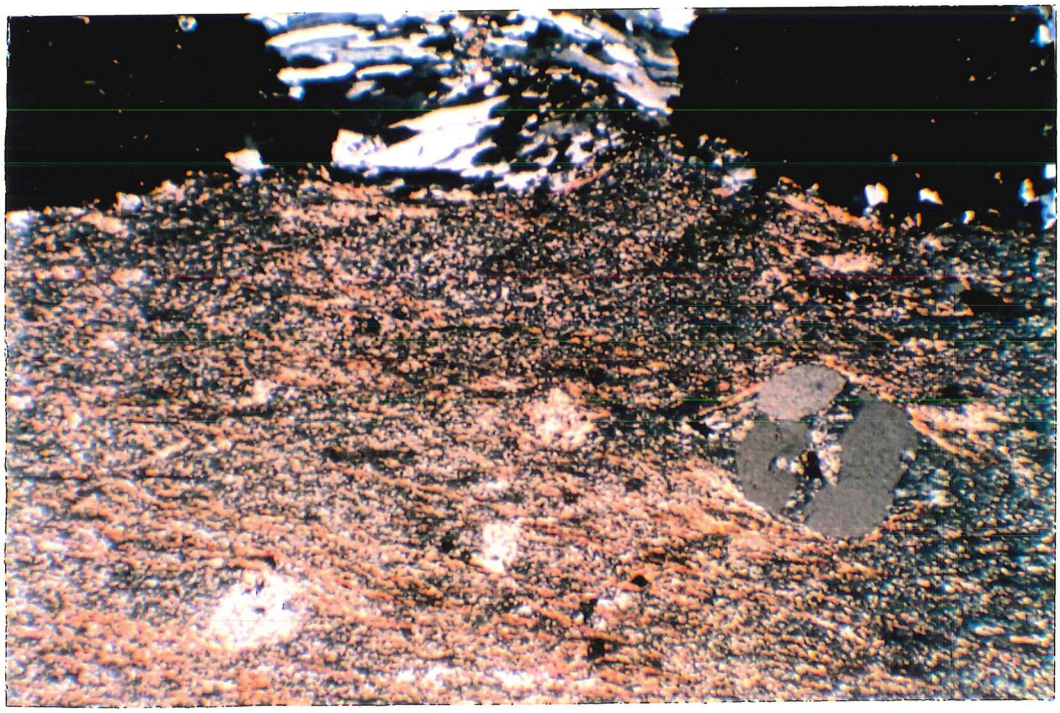

Fig. 6.22

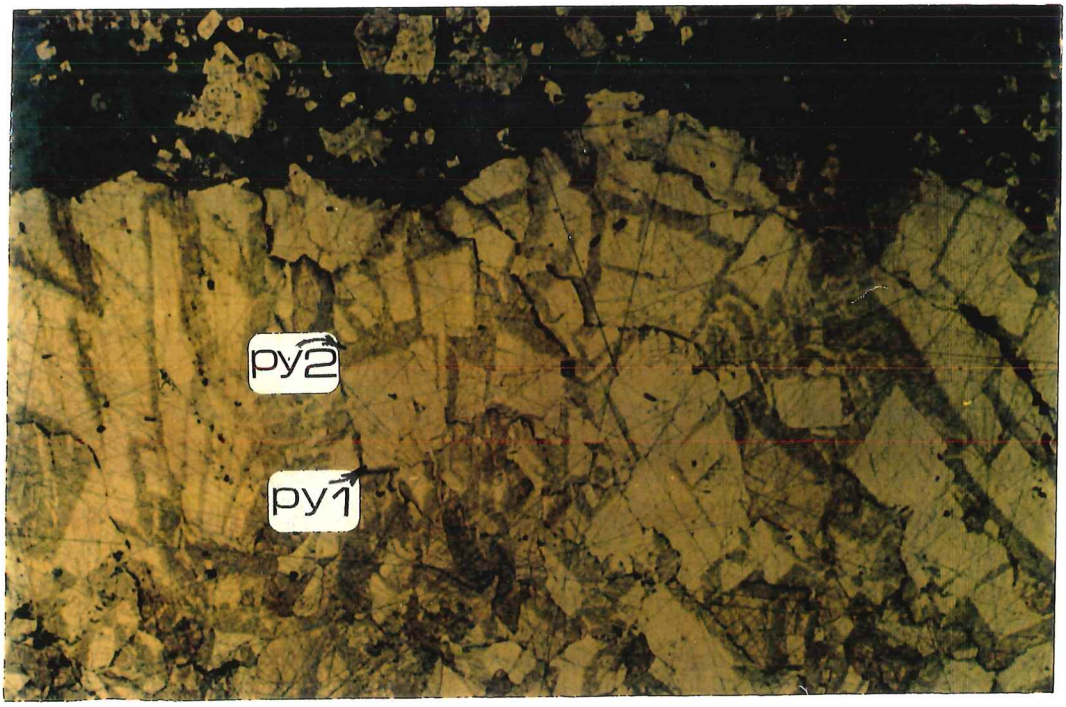

Fig. 6.23

chalcopyrite, sphalerite, carbonate and quartz. Individual pyrite grains show signs of brittle deformation in the form of boudinaged grains and pull-apart textures that have developed from intragranular to intergranular extension microfractures.

Some massive pyrite crystals appear homogeneous in polished sections, but when etched chemically, they display evidence of earlier formed cataclastic pyrite crystals overgrown and fractures annealed by later pyrite (Fig. 6.23). Both types of pyrite (pyrite 1 and 2 in Fig. 6.23) were affected by later episodes of generally brittle deformation and well-defined fracturing which appear to have developed during tectonism. The final episode of ore deformation is characterized by intense fracturing, with fractures filled by remobilized chalcopyrite, or in some instances by remobilized quartz and carbonates. The observed textures can be interpreted as resulting from repeated cataclastic deformation associated with hydrothermal activity.

Microstructural observations also provide evidence of cataclasis throughout the deposit, but mainly along microshears in the footwall and along the flanks of the massive sulphide bodies (Fig. 6.24). Cataclastic flow, responding to the need to re-establish mechanical stability under directed shear stress (Cox, 1987), involved microscopic movement of grain fragments by sliding and rolling along networks of microfractures.

Fig. 6.24 Cataclastic flow deformation in shear zone of poly-crystalline pyrite. Cataclastic flow involving movement of grain fragments by sliding and rolling along microfractures and along discrete shear zones. Field of view 2 mm across. Specimen etched with H_2SO_4. Reflected light.

Fig. 6.25 Photomicrograph showing a pyrite grain with cleavage in subvertical direction, partly filled with chalcopyrite, sphalerite and quartz. Field of view 1 mm across. Reflected light.

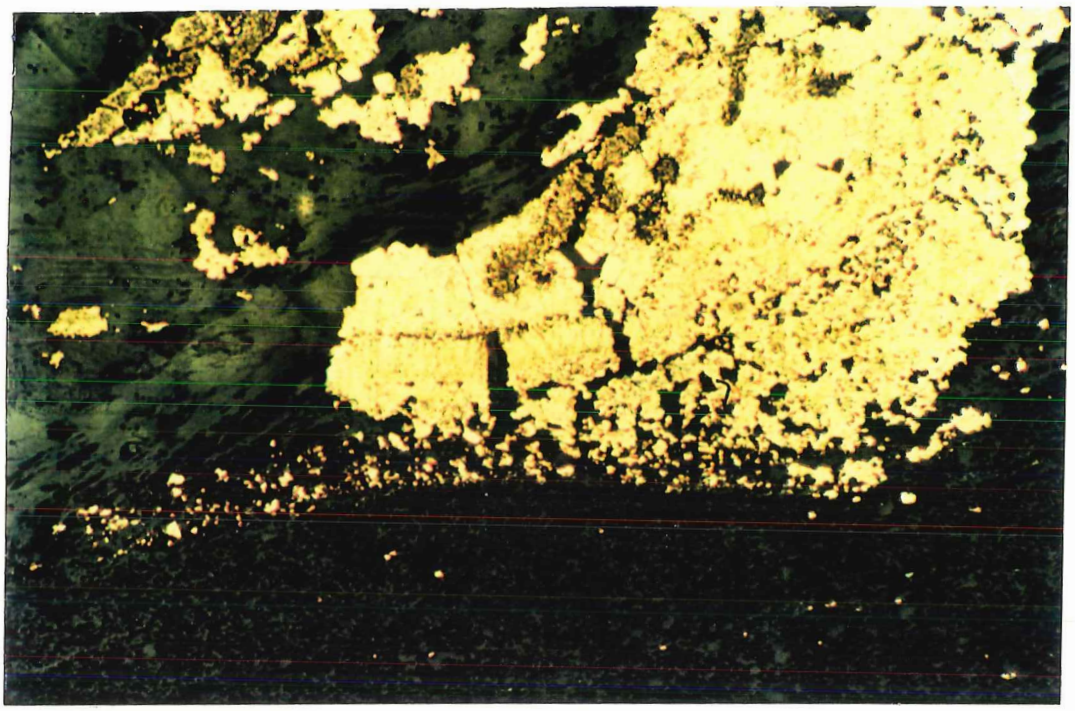

Fig. 6.24

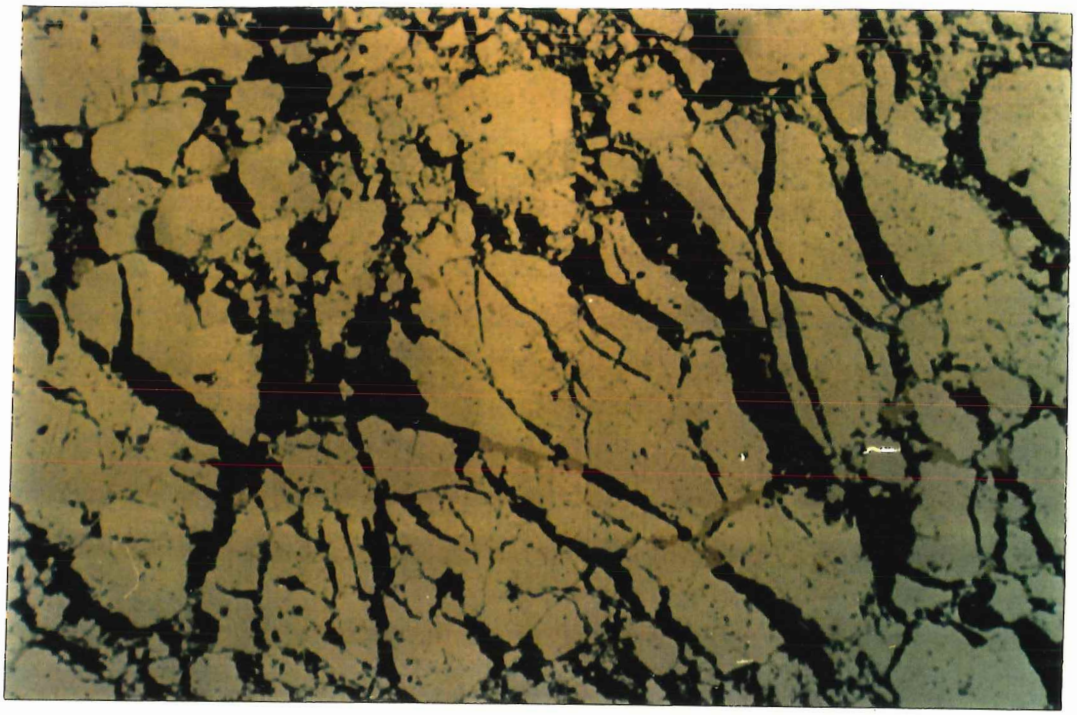

Fig. 6.25

(2) Solution-precipitation creep:

Although the behaviour of pyrite is brittle under most conditions of deformation, several authors (e.g., McClay and Ellis, 1984; Cox, 1987; Marshall and Gilligan, 1987; Cook et al., 1993) have recently pointed out that, in the presence of a pore fluid and under low- to medium-grade metamorphism, pressure solution appears to play a major role in the modification of pyrite textures by dissolution of selective material from high-strain areas; transport is at least on the grain-scale. Many studies indicate that pressure -solution transfer is an important mechanism for the deformation of pyrite in many massive sulphide deposits.

In some cases, deformation textures in the sulphide ores at Mobrun are represented by a foliation of sulphides, typically orientated parallel to the S_1 schistosity of the enclosing metamorphosed host rocks (Fig. 6.25). Pressure-solution within the sulphide ores is characterized by elongation (Fig. 26a), indentation (Fig. 26b) and truncation (Fig. 26c) of pyrite grains. Intense elongation of pyrite grains may produce a preferred orientation fabric. Dissolution of pyrite and other more incompetent sulphides (e.g., chalcopyrite) from dissolution sites results in precipitates at depositional sites, including sulphide overgrowths and in some cases symmetrical pressure shadows (Fig. 6.27) and fillings of dilatant fractures. The following is a description of those features which relate to pressure-solution mass transfer.

Fig. 6.26a Dimensional preferred orientation of pyrite developed by solution precipitation creep. Grains are oriented at high angles to the bulk shortening direction (see arrows). Field of view 0.5 mm across. Specimen etched with HNO_3. Reflected light.

Fig. 6.26b Indented pyrite spheroidal showing dissolution of spheroid overgrowth along an irregular subvertical pressure-solution seam. Field of view 0.5 mm across. Specimen etched with HNO_3. Reflected light.

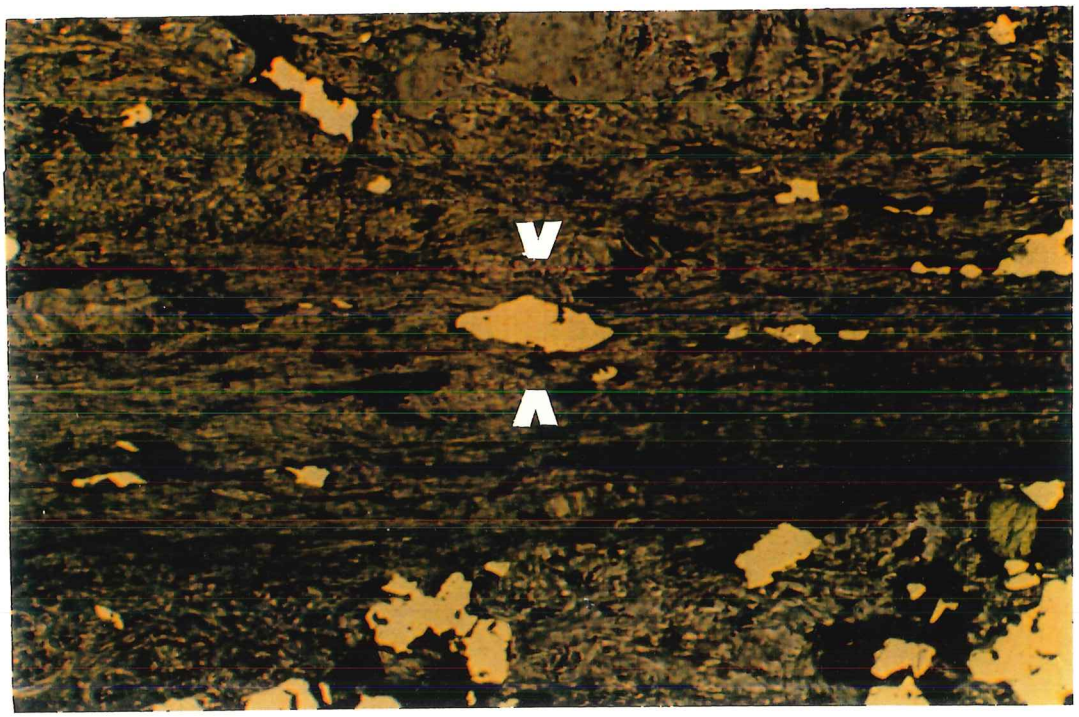

Fig. 6.26a

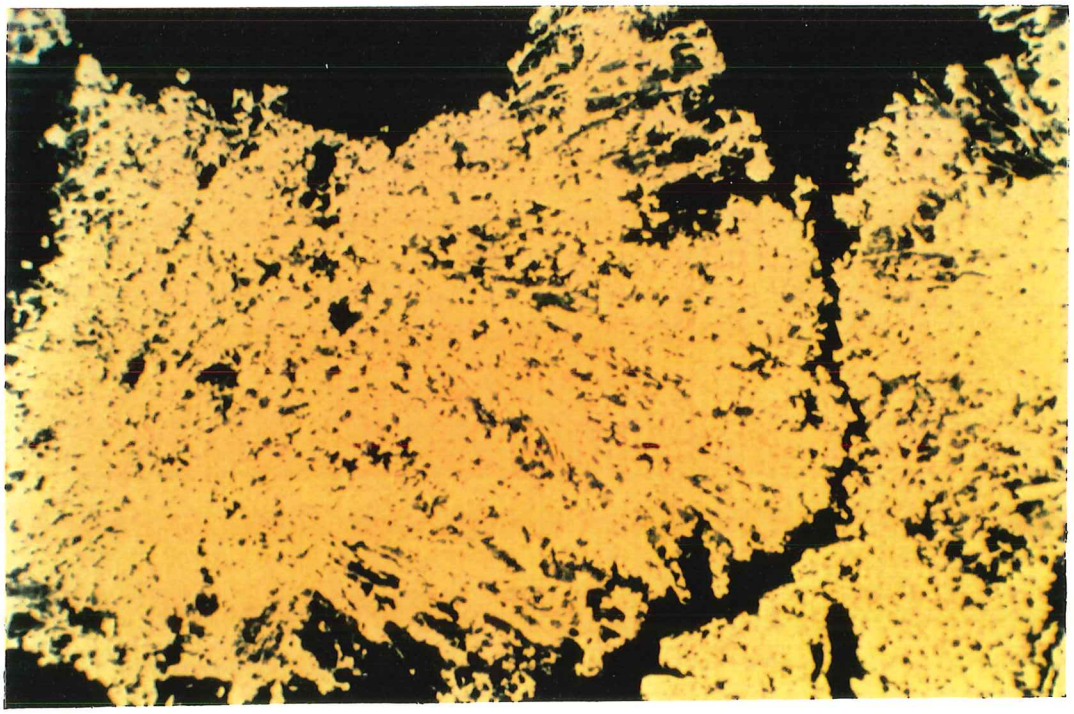

Fig. 6.26b

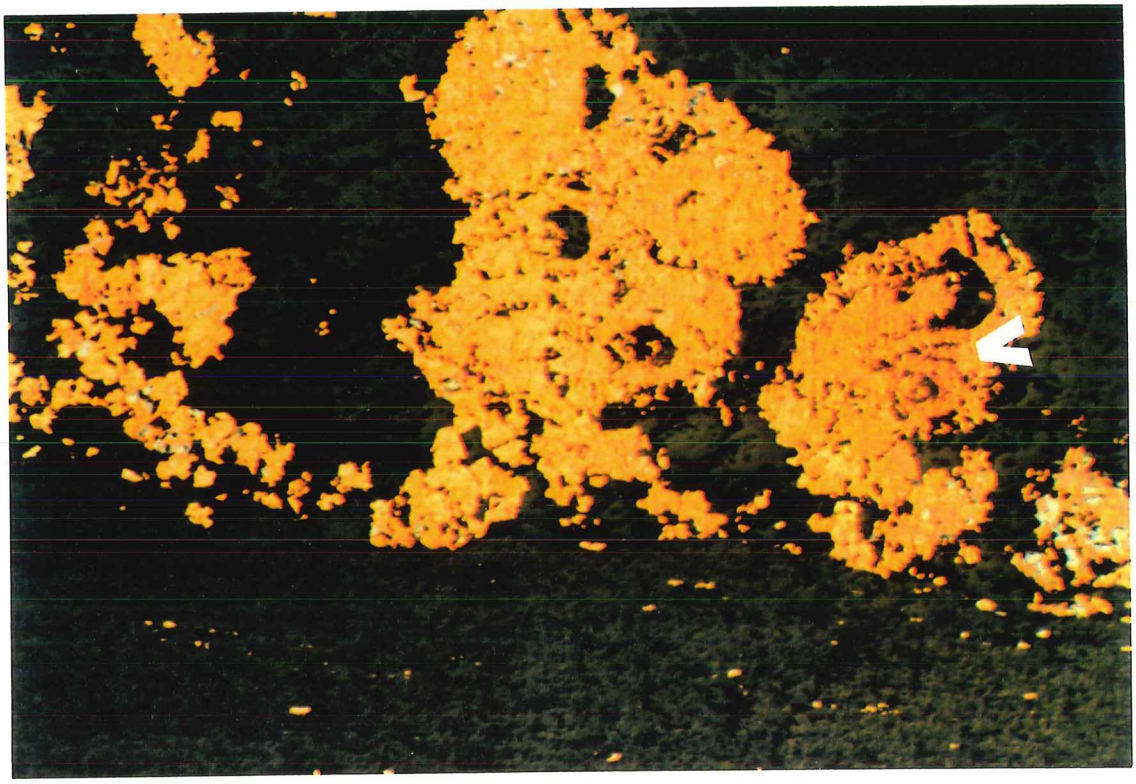

Fig. 6.26c Spheroidal pyrite showing shape elongation and partial dissolution in the high-strain zone (see arrow) of the pressure-solution seam. Lower part of photograph shows very fine grains of pyrite which are elongate due to dissolution of right angles to schistosity. Field of view 1 mm across. Specimen etched with H_2SO_4 + $KMnO_4$. Reflected light.

i) Pyrite grain elongation and preferred orientations:

Deformation may cause dimensional and, in rare cases, lattice preferred orientations in pyrite (e.g., from Mt. Lyell, Tasmania; Siemes et al., 1993). Lattice preferred orientation, defined by Spary (1983), occurs where the crystal structure (lattice), and hence optical axes and other related crystallographic features (faces, cleavage, etc.), are related to lattice orientations. Dimensional preferred orientation refers to inequidimensional units (such as elongated, flaky or prismatic crystals) which have a tendency towards parallelism of one or more morphological axes (Spary, 1983).

a) Dimensional preferred orientation:

In undeformed ores, there is no obvious preferred orientation, and individual mineral grains are more or less equidimensional. Pressure solution is thought to be the likely mechanism responsible for the formation of preferred grain shape fabrics among pyrite grains (Cox, 1987; McClay and Ellis, 1983, 1984; Lianxing and McClay, 1992; Brown and McClay, 1993; McClay, 1991).

Preferred orientations of pyrite grains at Mobrun occur in areas of high bulk strain, and are defined by: (1) elongate, sutured, fine-grained euhedra, and (2) elongate aggregates of intergrown grains. To determine whether the observed dimensional orientation of pyrite is caused by aggregate grains reorganization or by single grain shapes, numerous polished samples were etched with acid (see above) to highlight internal growth textures. What at first appear to be single

Fig. 6.27 Chalcopyrite (cpy) forming pressure shadows at both sides of pyrite grains. Chalcopyrite overgrowths developed on pyrite during pressure-solution creep. Field of view 1 mm across. Reflected light.

Fig. 6.28 Large elongated pyrite aggregate with fracture oriented parallel to the schistosity of the rock. Field of view 2 mm across. Specimen etched with H_2SO_4. Reflected light.

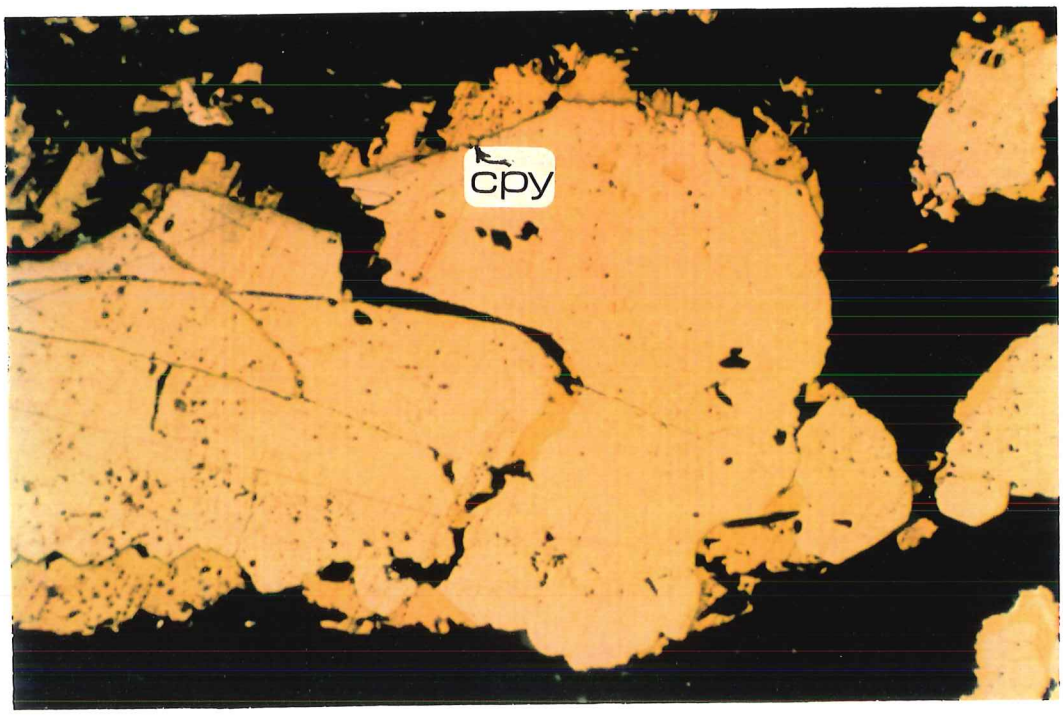

Fig. 6.27

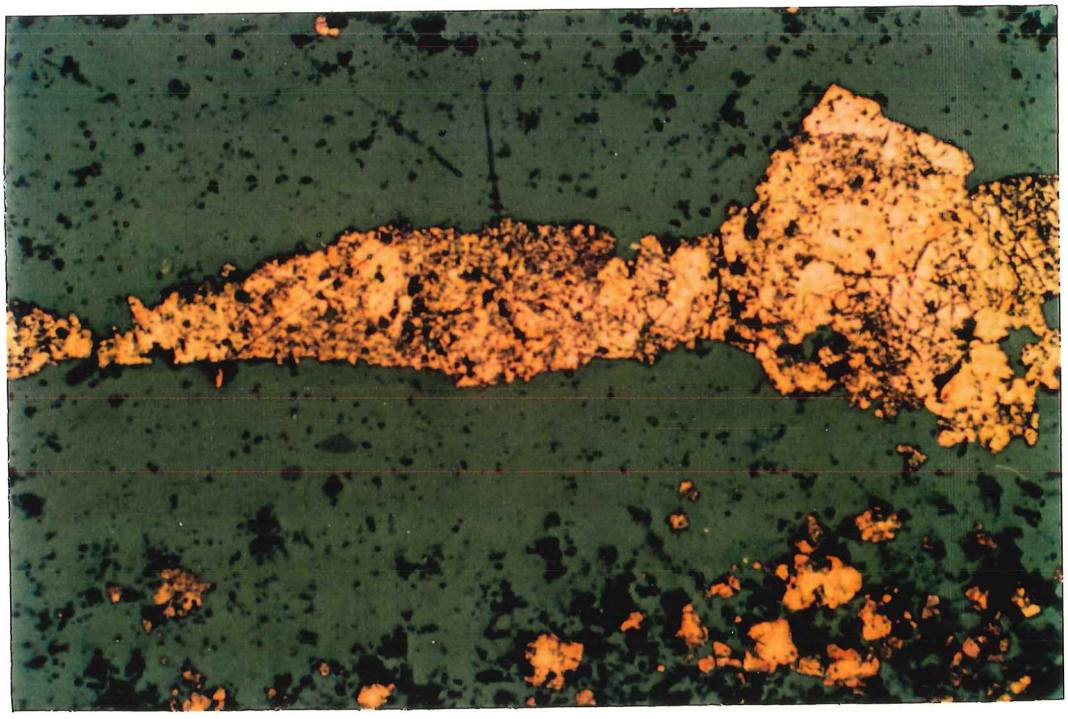

Fig. 6.28

irregular lens-shaped grains are revealed by etching to be granular aggregates composed of many well-nested, more or less equidimensional grains in various dimensional orientations. For example, Figure 6.28 shows a large, elongate pyrite crystal aggregate within a single lens-shaped grain, with long axes parallel to the plane of schistosity.

In contrast, some etched pyrite specimens composed of elongate fine-grained pyrite in the less massive parts of the sulphide ores exhibit pyrite grains oriented subparallel to the foliation (Fig. 6.26a). This fine-grained pyrite is typically elongate, with straight to slightly curved, mildly sutured, and lightly indented grain boundaries.

Pressure-solution overgrowths may give rise to such elongate pyrite grains (Fig. 29a). Sarkar et al. (1980) note that remobilization by pressure-solution is a plausible mechanism for the formation of elongate pyrite grains, by growing of new grains in areas of lower pressure which are located parallel to the schistosity direction (Fig. 6.30). However, Mookherjee (1971) points out that elongation in pyrite grains may be accomplished by plastic deformation, which may be a result of the combination of physical distortion of already formed crystals, probably by internal deformation and gliding. It is assumed that dislocation glide processes may take place during the plastic deformation of pyrite (Cox, 1987).

Thus, transpositions of pyrite at the grain-scale by pressure- solution processes has been identified in many microstructural features, such as in the

Fig. 6.29a Photomicrograph showing elongate fine-grained pyrite due to pressure-solution process. Field of view 3 mm across. Specimen etched with H_2SO_4 + $KMnO_4$. Reflected light.

Fig. 6.29b Photomicrograph showing growth of late pressure-shadow pyrite (py 2) over earlier euhedral pyrite (py 1). Field of view 2 mm across. Reflected light.

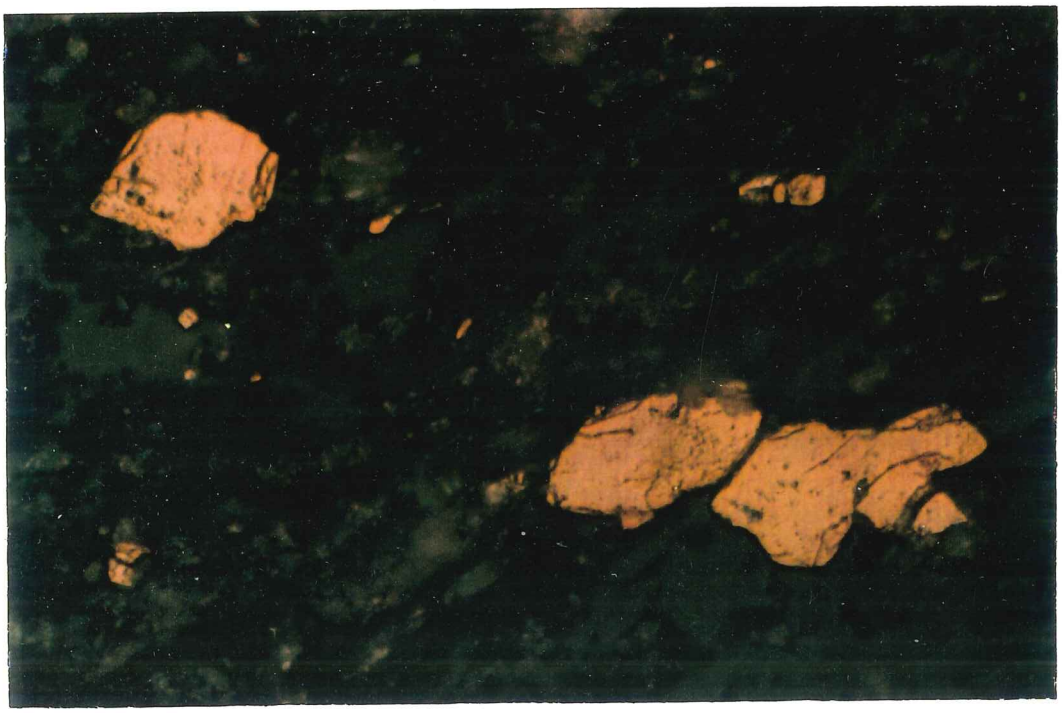

Fig. 6.29a

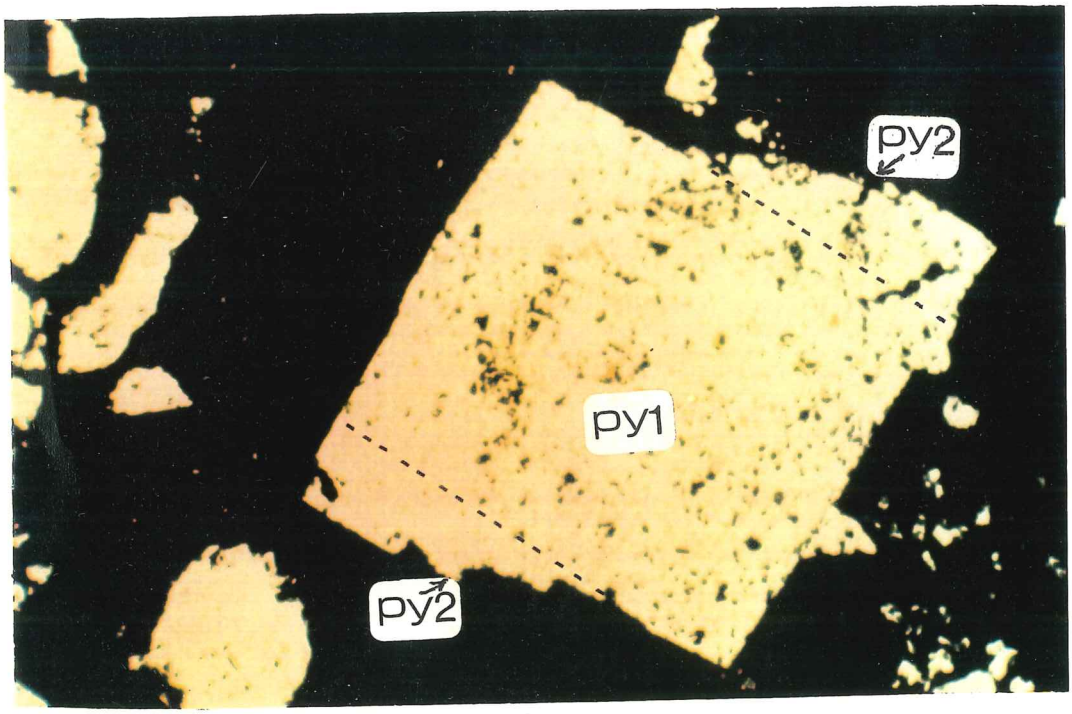

Fig. 6.29b

formation of elongate pyrite grains with overgrowths of secondary pyrite. This mechanism is well exhibited in euhedral pyrite in Figure 6.29b. These features suggest that dissolution and remobilization have occurred, at least at the grain scale. The transposition of pyrite by pressure-solution creep in domains of high strain has produced a dimensional preferred orientation with sutured grain boundaries.

In some cases, pyrite elongation parallel to the schistosity of phyllosilicates has been observed in mineralized schists. Etching by acid did not provide conclusive evidence that a deformational texture (e.g., truncated zoned structures or overgrowth) occurs here. Elongation may have resulted from pyrite growth controlled by a preexisting foliation, as suggested by Graf and Skinner (1970) and Deb (1979).

During pressure-solution of polymetallic ores, sphalerite is relatively insoluble. In fact, sphalerite appears to be relatively refractory during low-grade deformation and is commonly concentrated as remnant and recrystallization grains in the pressure solution seams (McClay, 1991). Such tiny sphalerite lenses are associated with abundant chlorite, sericite and minor amounts of fine-grained elongate grains of pyrite and quartz. Sphalerite grains are generally lozenge-shaped in appearance, with strong dimensional preferred orientations aligned parallel to S_1. Relative enrichment of sphalerite in pressure solution seams is also reported by Lianxing and McClay (1992) and McClay (1991). In the mixed

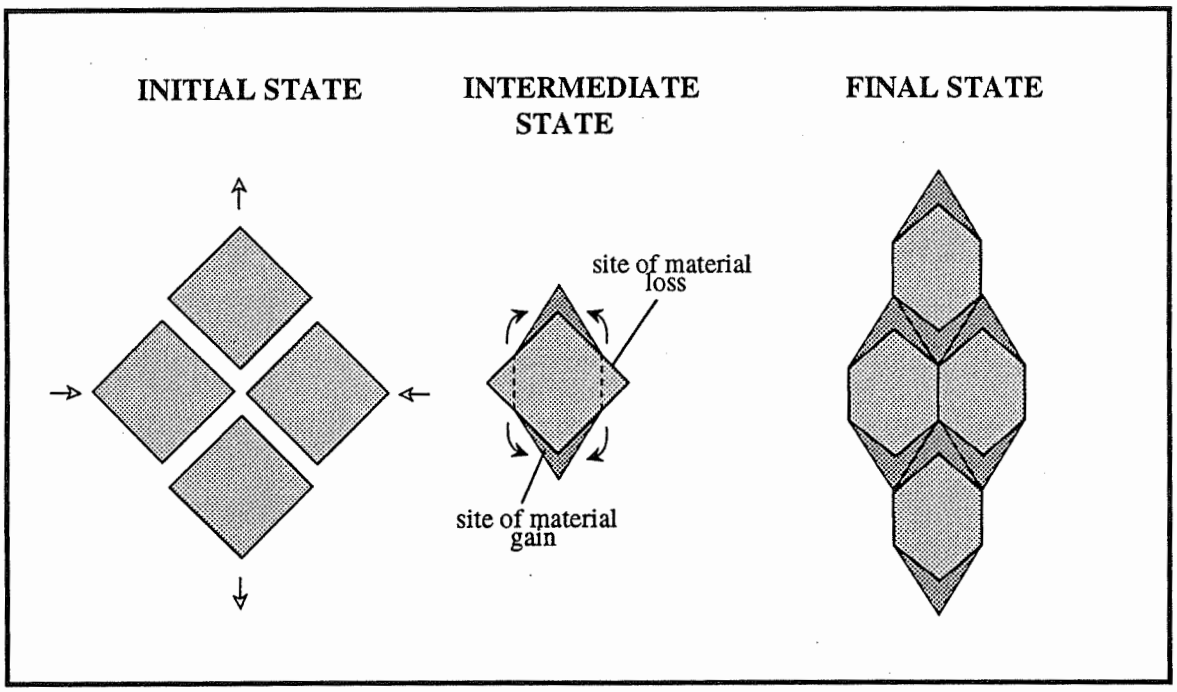

Fig. 6.30 Schematic representation of the formation of elongate pyrite grains by growth of new grains in areas of low pressure resulting from pressure-solution.

sulphide-silicate lithologies of Mobrun (Fig. 6.31), pressure-solution cleavage produced lithons of deformed sulphide and silicate layers in dissolution sites with strong concentration of sphalerite in high-strain zones.

b) Lattice preferred orientation:

The preferred orientations of sulphide grains has been determined via pole figures measured by X-ray diffraction in reflection geometry. The measurement of the {200} lattice of pyrite in 10 slabs of fine-grained pyrite did not reveal any obviously preferred orientation of pyrite grains (Fig. 6.32). This result was expected following the studies of McClay (1983), Cox (1987), Wenk (1985), Zilles et al. (1993), and Ken and McClay, (1983) which indicate that cataclastic as well as pressure-solution mechanisms are unlikely to produce preferred crystallographic orientations in pyrite in low-grade metamorphic environments.

For comparison, quartz and chlorite (two major gangue minerals in the sulphide ore) exhibit strongly preferred crystallographic orientations (Appendix 6.2).

ii) Overgrowths and recrystallization:

Redistribution of pyrite due to pressure solution results in euhedral overgrowths of pyrite which are commonly clear and inclusion-free and found in areas of low mean stress adjacent to truncated spheroids (Fig. 6.33). Less competent sulphide minerals such as chalcopyrite are preferentially located in pressure shadows at the opposite sides of pyrite grains and parallel to the S1

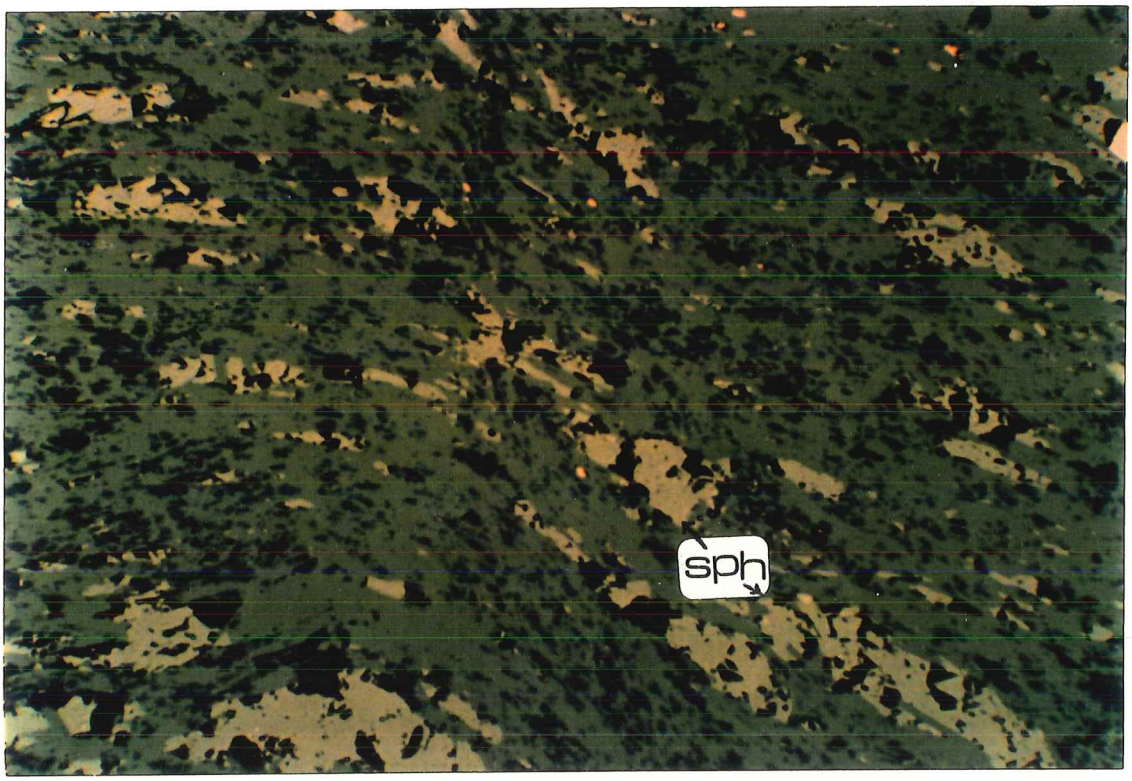

Fig. 6.31 Pressure solution involving pyrite grain-size reduction and concentration of insoluble minerals such as sphalerite ± rutile in dissolution field. Sphalerite (sph) is lens-shaped and elongate parallel to the trace of the foliation. The matrix consists of fine-grained sericite. Field of view 1 mm across. Reflected light.

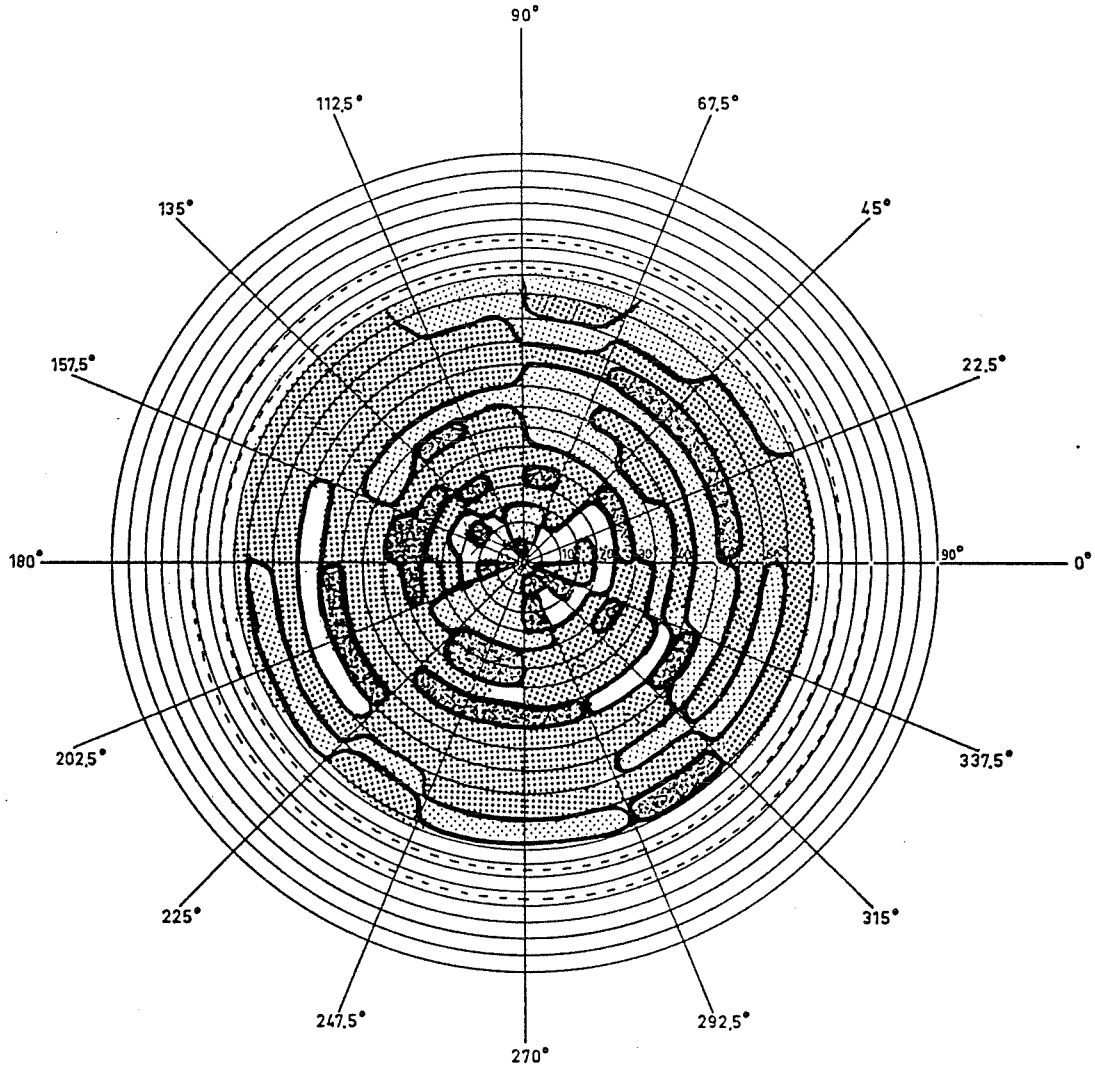

SAMPLE: **337 (pyrite)**
LATTICE PLANE: **200**
d-VALUE: **2.709** AT: **33** °(2θ).
TUBE: Cu ANODE, **40** kV, **20** mA, **Ni**, FILTER.
TIME CONSTANT: **10** SEC.
DISTANCE: **173** mm.
REFLECTION: RING FROM: **0°** TO **70°**.
START TABLE AT: **0°**.
SPECIMENTABLE SPEED: **45°** PER **2** MIN.
RINGSPEED: **5/8.°**
INTEGRATING: **9** mm.

Fig. 6.32 Pole figure of pyrite {200}. Darker areas are higher density. Contour levels are 20% of mean intensity. Schistosity surface is parallel to the plan of projection.

schistosity (Fig. 6.27). This fabric is produced by remobilization of chalcopyrite into sites of low strain during fluid state remobilization of sulphide ores. Pressure-shadow fillings composed of sphalerite also observed in some samples (Fig. 6.34). These overgrowth features can be described as a secondary generation of sulphides formed during metamorphism-deformation.

Microprobe studies of zoned overgrowth pyrite did not detect any compositional differences between the primary and secondary pyrite. The analyses were done with a scanning electron microprobe with a resolution of 3.0 nm (JEOL JXA 8600) at Ecole Polytechnique. However, some trace elements such as gold and silver are not readily measured.

Nevertheless, variations in gold and silver contents have been reported by LaRocque and Hodgson (1993) using a camera ion microprobe. In their study, the primary pyrite contains between 0.4 and 9 ppm "invisible" Au; secondary (recrystallized) pyrite is characterized by Au contents between 1 and 60 percent of those in associated primary pyrite. The microprobe analyses indicate that (Au/Au+Ag) in electrum in secondary faces of mineralization is about 0.5 (LaRocque et al., 1993).

iii) Dilatant veins:

Pyrite associated with sphalerite, chalcopyrite and gangue minerals filling breccia zones and dilatant veinlets are present in both hangingwall and footwall rocks. The dilatant fractures generally overprint the schistosity and show tabular

Fig. 6.33 Photomicrograph showing the development of sphalerite overgrowths on pyrite in areas of low mean stress during solution precipitation creep. Field of view 2 mm across. Reflected light.

Fig. 6.34 Colloform texture in pyrite showing growth zoning with interbanding of pyrite and sphalerite. Coarse-grained pyrite is overgrown on earlier colloform pyrite. Field of view 1 mm across. Specimen etched with H_2SO_4. Reflected light.

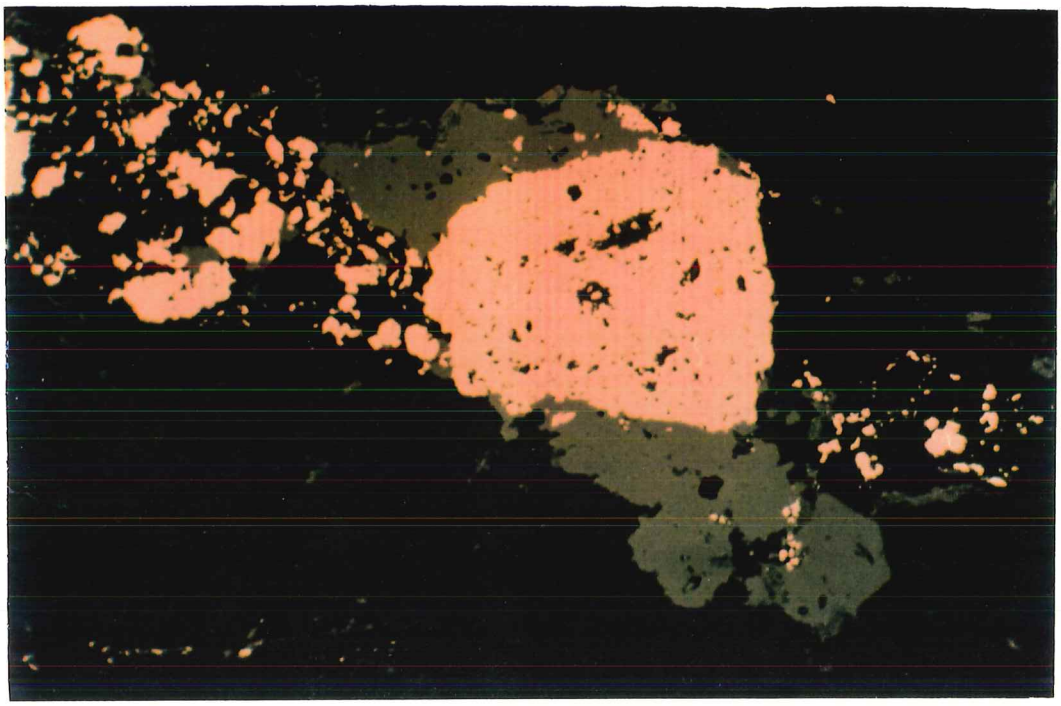

Fig. 6.33

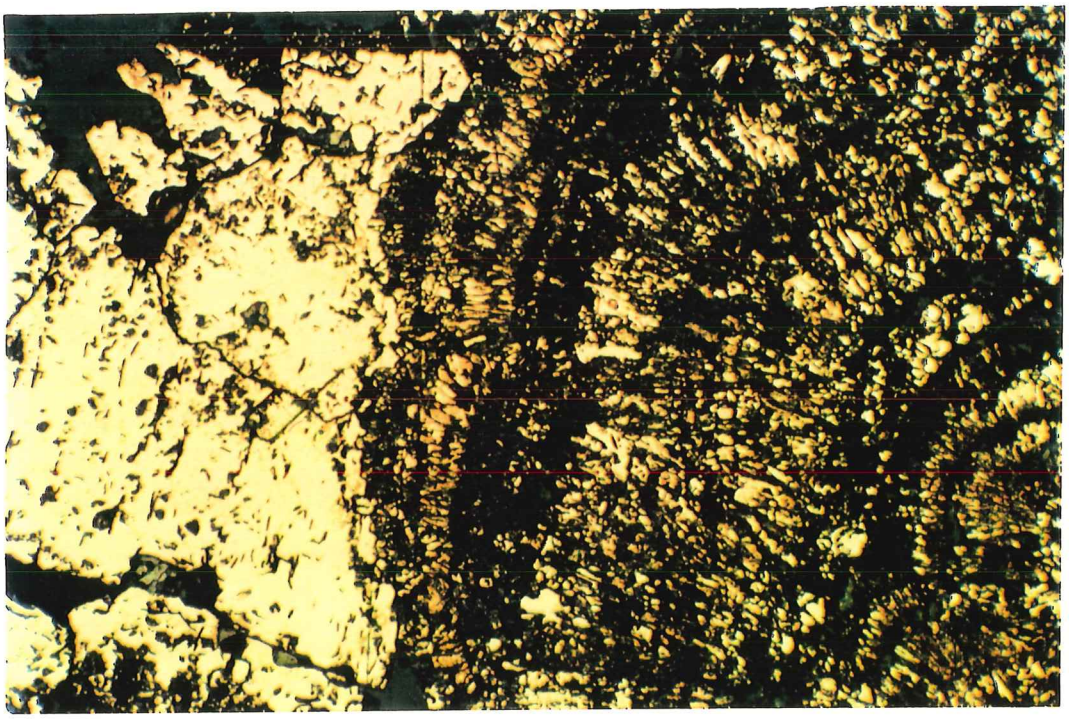

Fig. 6.34

banding in pyrite microstructures due to crack-seal phenomena (Fig. 6.15).

Colloform textures in pyrite were revealed by etching and are indicative of open-space filling. Numerous micrometre- to millimetre-size chalcopyrite-sphalerite veinlets have filled internal fractures and breccia intergranular space in pyrite.

Rhyolite breccia blocks in parts of both the footwall and the hangingwall are cemented with massive pyrite (Fig. 6.35a). The crack-seal features of ore veins indicate that sealing between blocks was produced by the syntectonic remobilization of ore (Fig. 6.35b). Other fractures which cut across blocks were also filled by remobilized pyrite during deformation.

In summary, by far the most significant deformation mechanism observed in the mineralization studied here is that of pressure solution, especially in fine-grained pyrite. In coarse-grained pyrite, deformation was mainly brittle. Evidence for a pressure solution mechanism is found in sulphide-filled pressure shadows around pyrite and in truncation, indentation and overgrowth features on elongate pyrite grains. The relative insolubility and concentration of sphalerite in dissolution seams is a additional evidence of this process.

(3) Dislocation glide:

At the low temperatures and elevated confining pressures that inhibit cataclasis, the brittle failure of pyrite can be suppressed and low-temperature plasticity (ductility) can dominate (Cox, 1987). This process includes deformation

Fig. 6.35 a) Polygonal brecciation rhyolite in the stringer zone underlying the Main Lens. Breccia blocks are aligned along the main shear direction. Pyrite veins (Py1) distributed along breccia block boundaries display an open-space texture overprinted by further dilation and the addition of quartz in tension veins. These pyrite veins were formed from earlier pyrite grains remobilized during deformation. b) The foliation pyrite veins within the breccia blocks (Py2) contain remobilized fine-grained pyrite which may have formed by remobilization during deformation of pyrite initially hosted by breccia blocks.

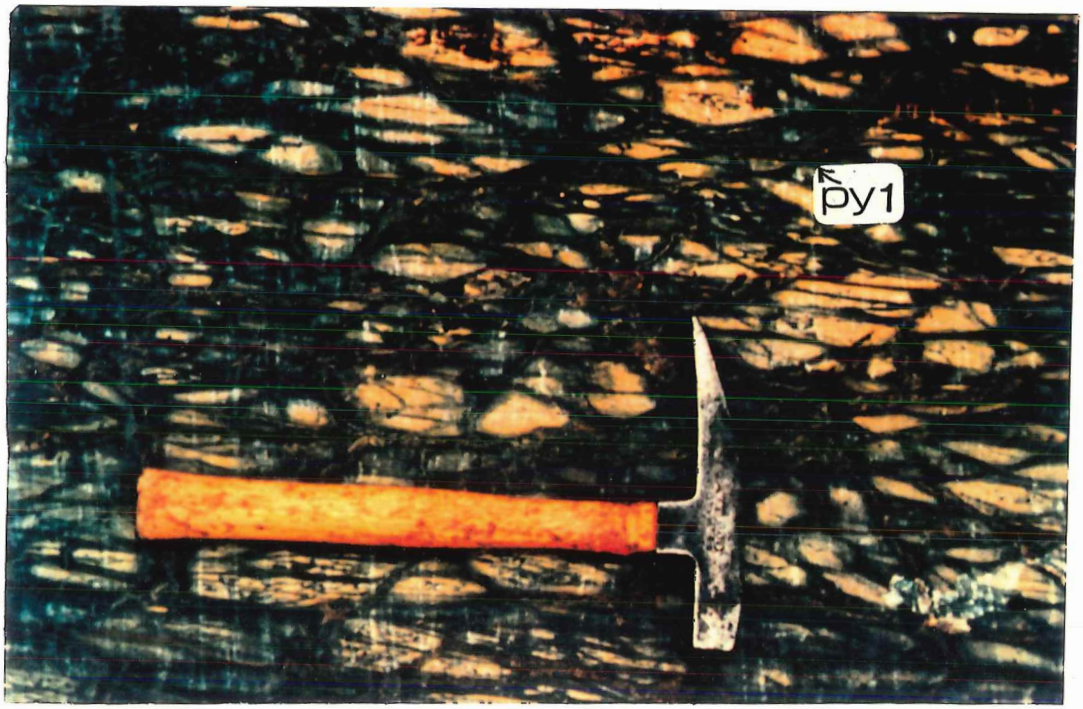

Fig. 6.35a

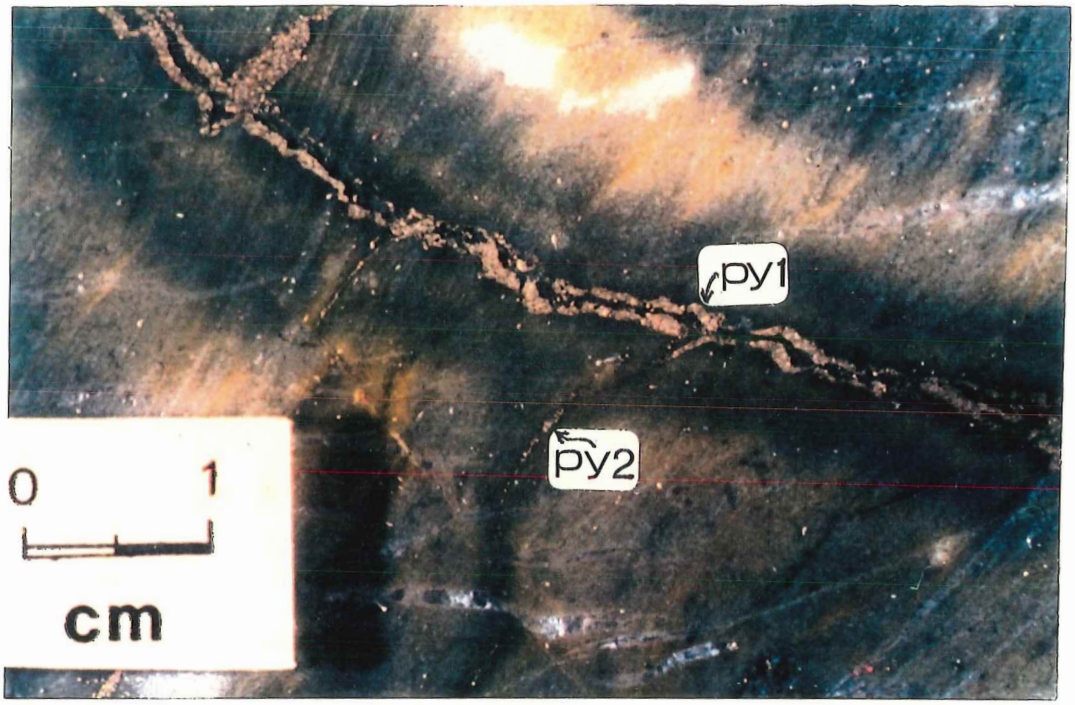

Fig. 6.35b

by dislocation glide which involves only the motion of dislocations through the crystal lattice along glide plans (Cox, 1987). McClay and Ellis, (1983) have described ductile behaviour in naturally deformed pyrite for temperatures greater than 450°C. Furthermore, Cox (1987) provides evidence of ductile deformation of pyrite by pressure- solution in low-grade metamorphic environments. Dislocation glide occurs in pyrite under lower greenschist facies conditions in the form of elongate arrays of etch pits revealed only on careful etching of polished sections (Lianxing and McClay, 1992).

Besides the brittle behaviour of pyrite at Mobrun, there is evidence of a certain amount of ductile behaviour in many samples. Dislocation microstructures in pyrite are characterized by straight and branching dislocation etch pits (Fig. 6.36). Strongly fractured coarse-grained pyrite commonly contains an abundance of dislocation etch pit lines. However, dislocation deformation of Mobrun massive sulphide bodies at elevated temperatures (probably about 300°C; see Chapter 7) appears to be very limited at first glance under the microscope, and it is only observed after acid etching of polished specimens.

With etching, evidence for dislocation glide has been found in many samples. The pits are more common adjacent to fractures within the pyrite grains and they appear to be oriented in one or two direction, indicating plastic deformation by cataclastically preferred slip planes such as those described by Lianxing and McClay (1981), Cox (1987), McClay and Ellis (1984), Marshall and

Fig. 6.36 Slip lines revealed by alignment of dislocation etch pits in pyrite grains, indicating plastic deformation. Such glide involves only the motion of dislocation through the crystal lattice without loss of cohesion. Field of view 0.3 mm across. Specimen etched with H_2SO_4. Oil immersion, reflected light.

Fig. 6.37 Annealing texture showing equant grains with triple junctions and straight grain boundaries. The dihedral angles tend toward 120° junctions. Field of view 1 mm across. Reflected light.

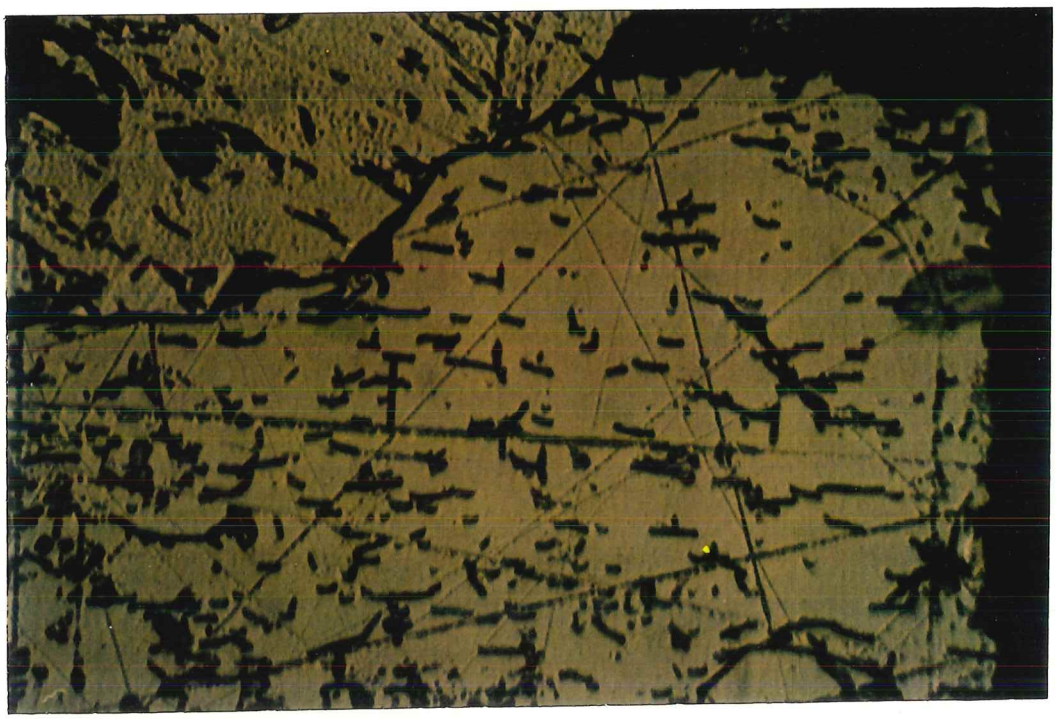

Fig. 6.36

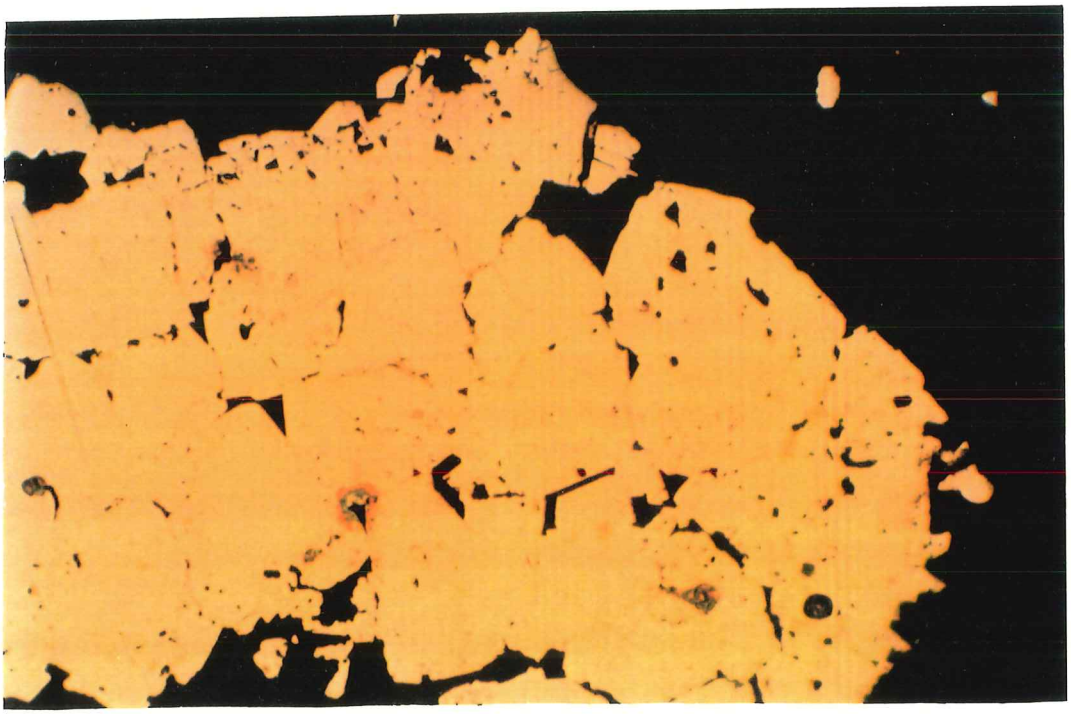

Fig. 6.37

Gilligan (1987), Vokes (1969), and Craig and Vaughan (1981).

(4) Annealing textures

Recrystallization in pyrite to form annealing textures are also observed at Mobrun. However, in coarse-grained massive pyrite, equant grains with straight to slightly curved grain boundaries meet at 120° triple point junctions, indicating annealing and grain growth textures resulting from metamorphism (Fig. 6.37).

6.3.2.3 Deformation textures in other sulphide ores

Pyrite textures indicate a dominant brittle behaviour, but in some cases there is also evidence of cataclastic flow, plastic deformation and recrystallization. In contrast, sphalerite, galena and chalcopyrite exhibit textures indicating that plastic deformation, twinning and recrystallization are important mechanisms. Interpretations of deformation by glide and recrystallization of sphalerite and galena have been derived largely from the works of Richards (1966), Frater (1985), Clark et al. (1977), Clark and McClay (1973) and McClay (1980).

Sphalerite from the Mobrun mine shows textures which indicate deformation by recrystallization, plastic deformation and annealing twins. Twinning is the most characteristic microstructure in sphalerite under low-grade metamorphism (Cox, 1987). Twins in sphalerite at Mobrun exhibit: (a) numerous narrow tapering twins which do not extend completely across the grain, and (b) relatively wide twins within single grains, with clearly parallel sides which again

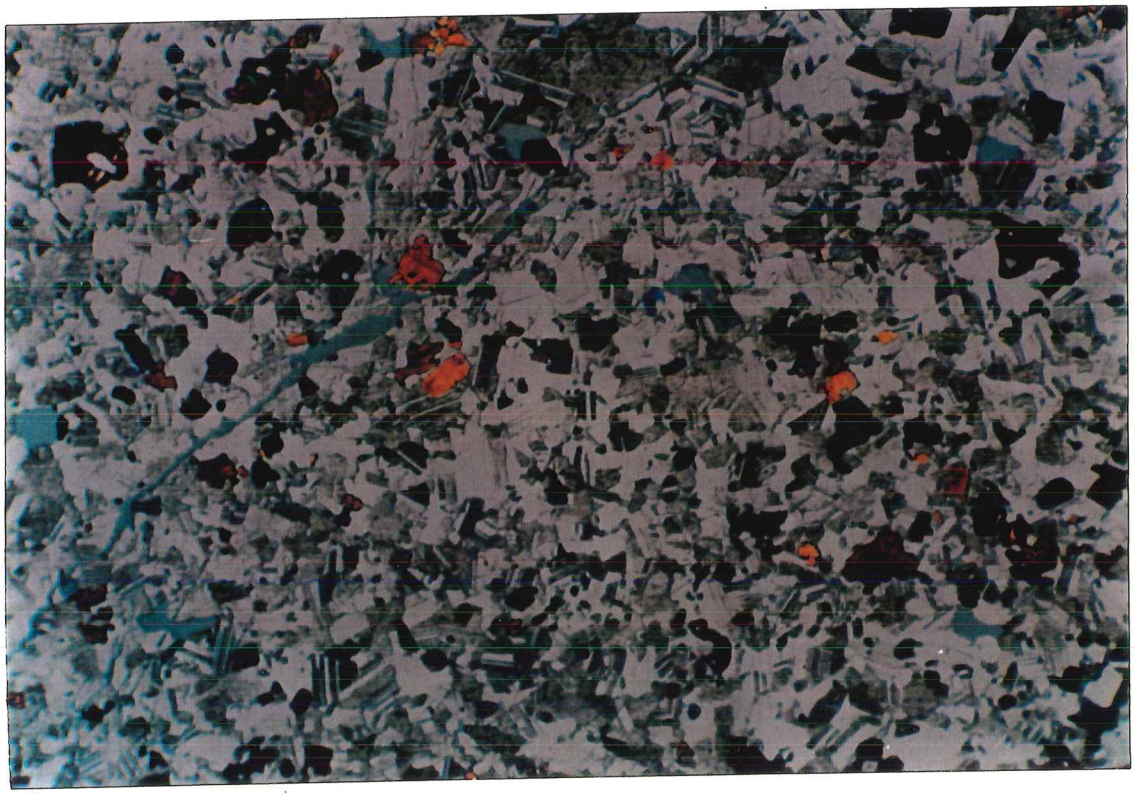

Fig. 6.38 Equant sphalerite grains showing broad annealing twinning or growth twins and deformation twins. Field of view 1 mm across. Specimen etched with H_2SO_4. Reflected light.

extend across the grain (Fig. 6.38). These features are related to (a) deformation and (b) growth or annealing processes, respectively, in agreement with the criteria set forward by authors such as Richards (1966), Stanton (1972), Cox (1987) and Brill (1989). Annealing twins at Mobrun occur locally, and are particularly visible in etched samples.

Deformation twins tend to be orientated at low angles relative to the general trend of ductile flow bands (Pesquera and Velasco, 1993). However in the case of Mobrun, deformation twins are replaced by annealing twins which tend to adopt disoriented orientations. This observation confirms those made by Stanton and Gorman (1968) and Clark and Kelly (1973).

The {111} pole figures of sphalerite has been measured within polished slices of rock. Although, the selected sample was fine-grained and consisted mostly of sphalerite, preferred orientations are not clearly evident because the coarse-grained sphalerite, includes some mineral impurities (especially pyrite) and is inhomogeneously distributed through matrix. However, the pole figures of some sphalerite samples exhibit weak lattice orientations parallel to the general foliation plane (Fig. 6.39). These weak pole figures suggest rotation of the sphalerite lattice with respect to the compression axes.

Chalcopyrite at Mobrun typically displays evidence of ductile deformation including grain flattening, elongation and twinning, although less commonly than sphalerite. Deformation textures in chalcopyrite are commonly revealed by filling

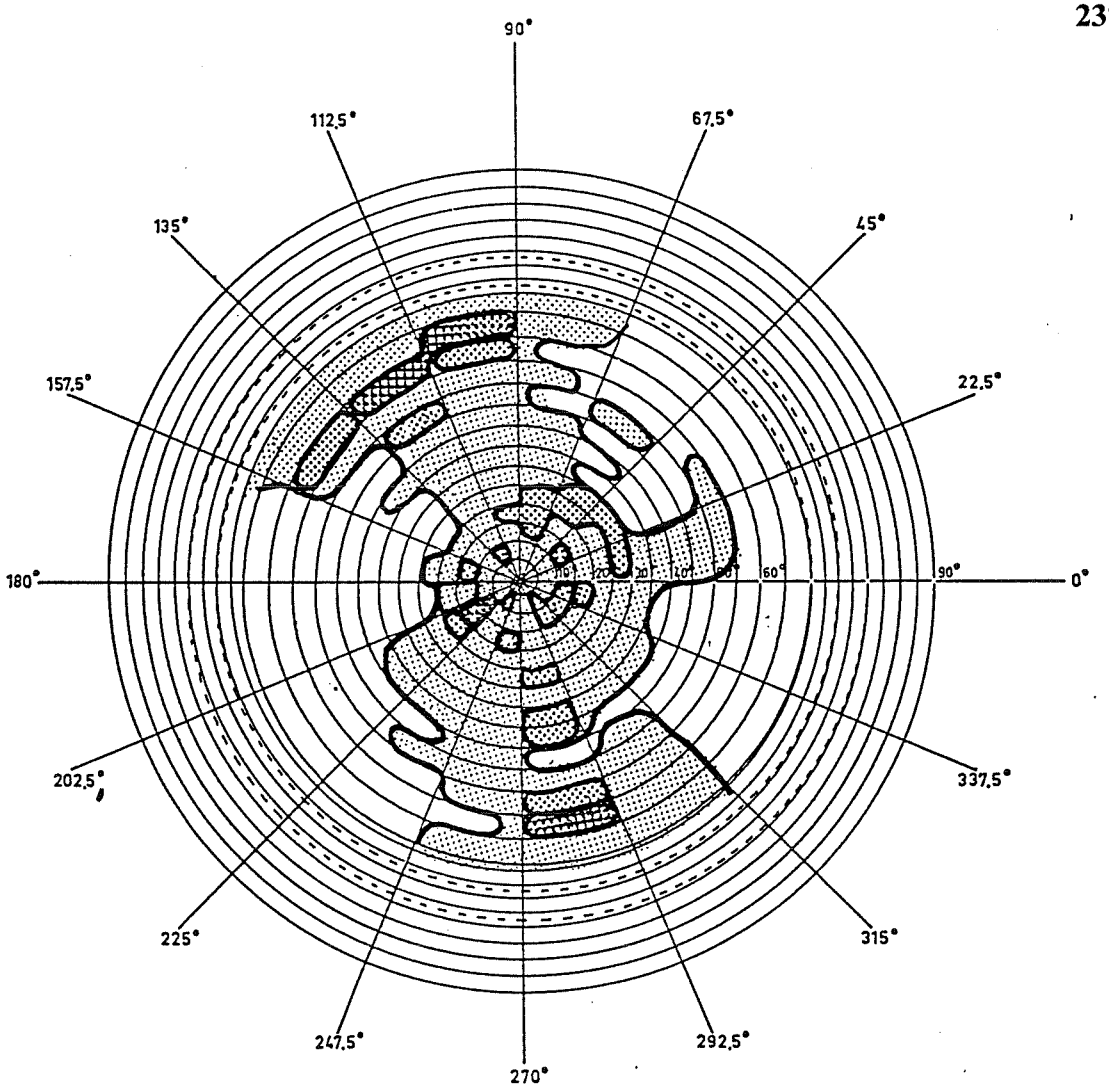

SAMPLE: **(sphalerite)**
LATTICE PLANE: **111**
d-VALUE: **3.123** AT: **28.5** °(2θ).
TUBE: Cu ANODE, **40** kV, **20** mA, **Ni**, FILTER.
TIME CONSTANT: **10** SEC.
DISTANCE: **173** mm.
REFLECTION: RING FROM: **0°** TO **70°**.
START TABLE AT: **0°**.
SPECIMENTABLE SPEED: **45°** PER **2** MIN.
RINGSPEED: **5/8.°**
INTEGRATING: **9** mm.

Fig. 6.39 Pole figure of sphalerite {111} showing the development of moderate lattice preferred orientation of pyrite. Darker areas are higher density. Contour levels are 20% of mean intensity. Schistosity surface is parallel to the plan of projection.

of fractures in pyrite (Fig. 6.7). Chalcopyrite also shows replacement textures which result from a chemical reaction between chalcopyrite and pyrite along fracture surfaces. Replacement tends to produce rounded irregular surfaces (Fig. 6.40), whereas fracture fillings leave the original fractured surfaces intact (Craig and Vaughan, 1981).

Chalcopyrite also shows evidence of "durchbewegung texture" (Vokes, 1969). This texture develops in intensely deformed rocks due to penetrative deformation (Fig. 6.41). Durchbewegung texture formed by increasing degrees of complex cataclasis; both ore and gangue minerals are stretched and rotated under pressure.

6.4 DISCUSSION

Based on the microstructural features described above, it is possible to trace a history of ore textures at Mobrun through two major events: (1) a diagenetic event related to the initial exhalative deposition of the massive sulphide bodies, and (2) a metamorphism-deformation event related to subsequent tectonic overprinting on these deposits. Fig. 6.42 give an overview of the sequence of crystallization and recrystallization of the sulphide and associated gangue minerals. According to the microstructural studies of sulphide minerals in this chapter and silicate minerals in Chapters 3 and 4, the principal chronological events are hydrothermal alteration

Fig. 6.40 Subhedral pyrite replaced along fractures by chalcopyrite in a matrix of silicates. Field of view 1 mm across. Reflected light.

Fig.6.41 Durchbewegung texture developed in intensely deformed chalcopyrite. The black silicate material has been stretched and rotated as the chalcopyrite matrix flowed under pressure. Field of view 1 mm across. Reflected light.

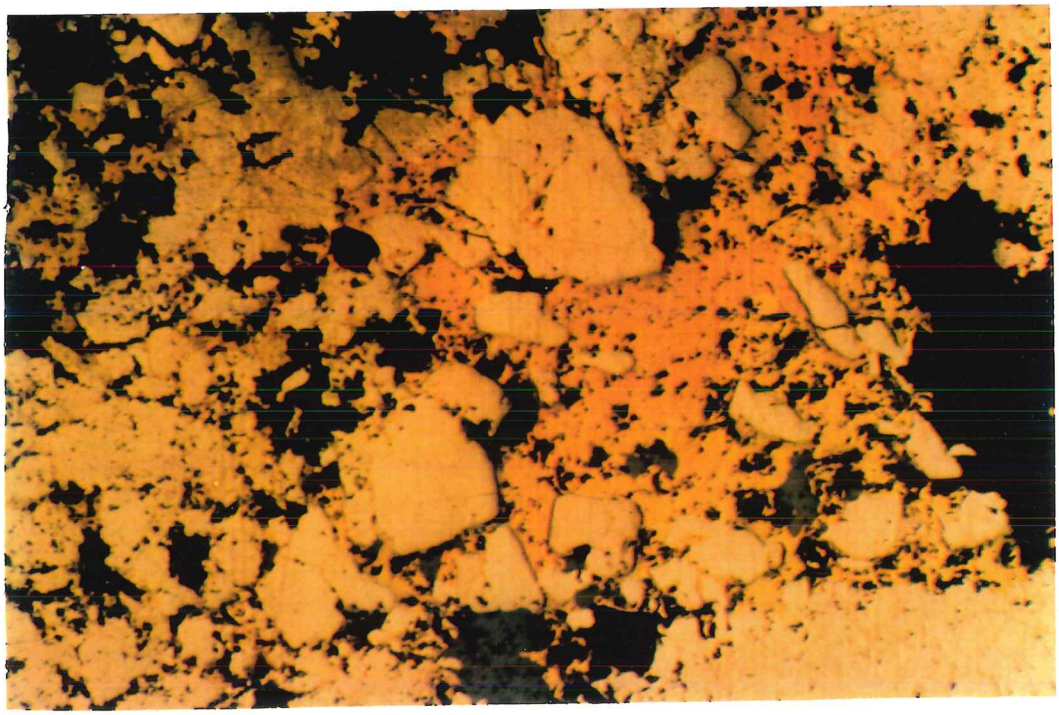

Fig. 6.40

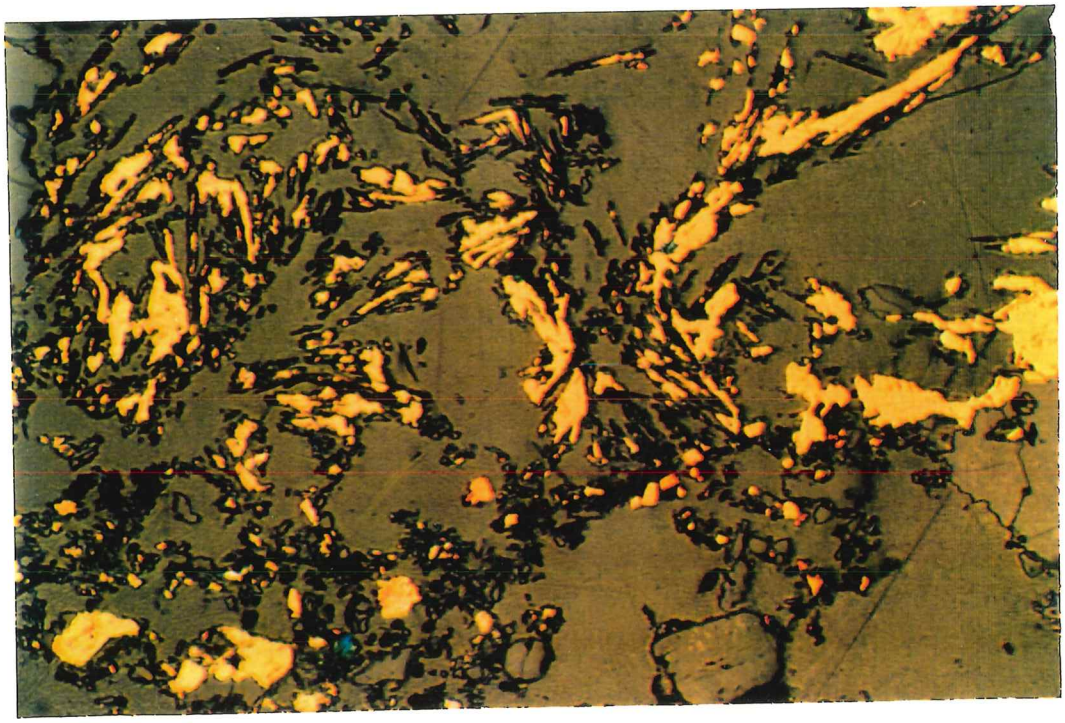

Fig. 6.41

and metamorphism-deformation alteration. Each of these events may subdivided into early and late stages.

6.4.1 Diagenetic event

The first event is believed to be the formation of ore mineralization on the sea-floor from exhalative metalliferous fluids. These hydrothermal fluids discharged onto the sea-floor and precipitated pyrite and sphalerite. Textures such as colloform pyrite and sphalerite are considered to have formed under these early primary conditions by very rapid precipitation, probably by sudden mixing of generally hot hydrothermal fluids with cold sea-water.

As the hydrothermal system developed, hotter fluids with temperatures probably rising through the range of 250 to 300°C introduced significant amounts of copper to the orebodies. Chalcopyrite may have precipitated within the pore spaces of the earlier-formed sulphide mounds and replaced sphalerite at the base of the orebodies. Chalcopyrite commonly exhibits chalcopyrite disease textures, indicating replacement of earlier sphalerite (Barton and Bethke, 1987).

Fine-grained pyrrhotite enclosed within pyrite grains may be syngenetic, formed from the primary iron sulphide-rich hydrothermal fluid. The interpretation of pyrrhotite as a primary phase in massive sulphide (Scott et al., 1977; Finlow-Bates, 1987) is supported by the observation of pyrrhotite as a major phase in modern sea-floor deposits. Tetrahedrite and digenite formed by

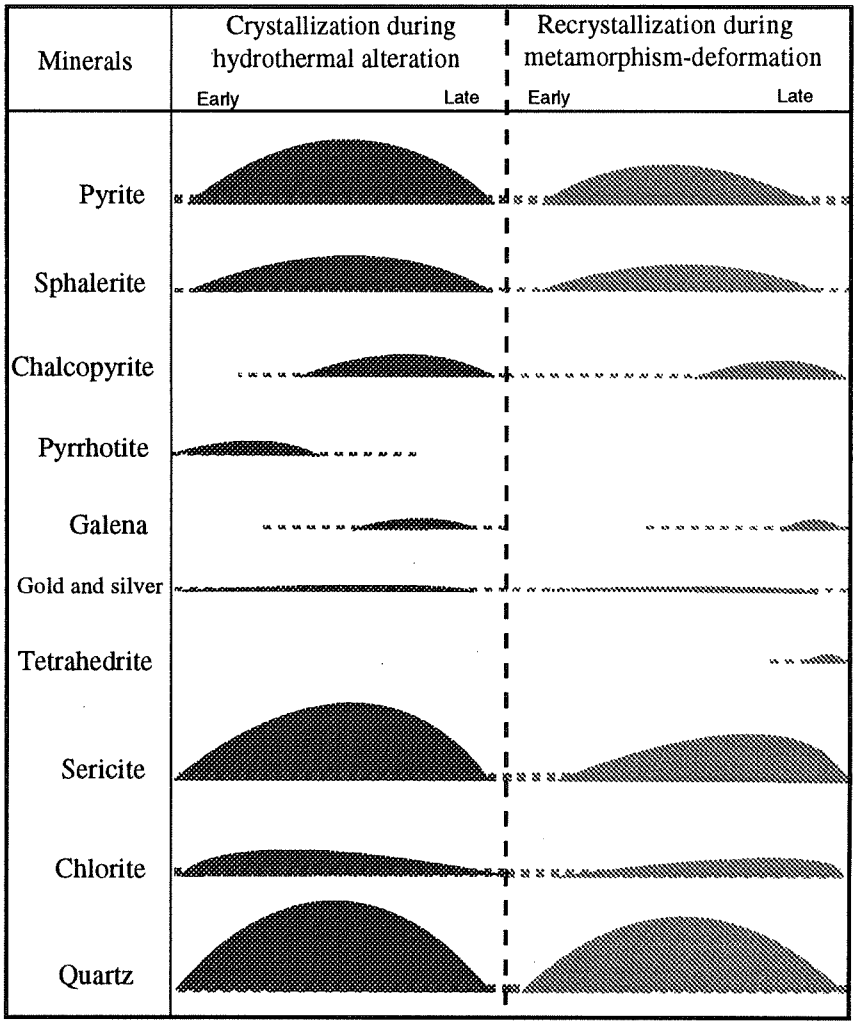

Fig. 6.42 Paragenetic sequence diagram for the crystallization and recrystallization of ores at the Mobrun Main Lens.

replacement of former copper sulphide minerals.

Later ore bearing fluids and/or recrystallization of ore minerals produced well-zoned equidimentional overgrowths around primary grains. In many cases, overgrowths of younger pyrite, mainly with euhedral forms, envelop the early spheroidal pyrite.

6.4.2 Deformation-metamorphism event

During subsequent deformation-metamorphism, another phase of mineralization modifies the primary textures through the formation of extensive re-crystallization and healing textures. This event can be explained in the light of syntectonic remobilization related to the interplay of stress, recrystallization and metamorphic mobilization under pressure-solution conditions. Pressure-solution deformation is considered to be the dominant mechanism for fine-grained pyrite at low metamorphic grades (at temperature of approximately 300 °C), with reasonable geological strain rates (10^{-12} to 10^{-14} sec^{-1}) under low stress (Fig. 6.21)(McClay and Ellis, 1983). Cataclasis is the major mechanism responsible for the development of deformation textures in pyrite at all grades of metamorphism.

The early stages of the deformation-metamorphism event are characterized by the cataclasis of pyrite and by the filling of fractures by remobilized chalcopyrite, sphalerite and pyrite. Late-stage remobilization of ore is represented

by late veins containing pyrite, chalcopyrite sphalerite. Gold and silver were initially deposited from hydrothermal fluid during diagenetic event and were recrystallized during metamorphism-deformation (Fig. 6.42).

Syntectonic mineralization overprinting the primary massive sulphide orebody at Mobrun is commonly formed by local dissolution, by short-range fluid flows, and by re-deposition of ore within the orebody under pressure-solution conditions. Most evidence indicates that essentially short-range mobilization was responsible for overgrowth, pressure shadow and intra-grain fracture features. For example, chalcopyrite has typically migrated from a nearly random or crystallographically aligned distribution within sphalerite and pyrite grains into concentrations along grain boundaries, along the fractures of more brittle minerals (such as pyrite), and into pressure shadows.

Micro-scale syntectonic mineralized veins within the orebody and host rocks may also have resulted from a fluid state remobilization of ore and could be explained by assuming that the mineralization took place by long-range mobilization measured on the scale of a few metres. Although some evidence points to an important long-range mobilization of ore material at Mobrun, there is a serious problem in evaluating the extent of such processes.

Literature dealing with the general subject of the long-range remobilization of ore constituents during metamorphism and deformation of preexisting massive sulphide deposits is extensive (e.g., Vokes 1969, 1971; Mookherjee, 1976; Guha and

Koo, 1974; Brill, 1989; Lianxing and McClay, 1992; Marshall and Gilligan, 1973, 1993; Vokes and Craig, 1993). There have been many discussions of microstructural features resulting from metamorphism and deformation similar to those found at Mobrun, and there appears to be a general agreement on the mechanism of deformation of minerals and the nature of mobile phases (e.g., on how the ore components are taken into solution, transported and redeposited). The main points of contention deal with the possible distance of remobilization; however, most authors appear to agree that the distances are very limited. For example, in describing metamorphic phenomena in lead-zinc deposits of the Canadian Cordillera, Lianxing and McClay (1992) show that there was in situ recrystallization and only short-range transport of ore masses. Even among the more mobile sulphides (e.g., chalcopyrite) which are commonly found in microstructural sites (pressure shadows, tension fractures, fracture cleavage, etc.), major portions of these sulphides remain spatially linked to the original depositional sites within the parent orebodies.

It appears that metamorphic-deformation at Mobrun also involved limited transport distances (on the order of micrometres to metres), rather than the hundreds of metres observed in some Australian massive sulphide deposits. For example, the sulphides, silica and dolomite in syntectonic veins at the Mt. Isa deposit can be attributed to the removal of those minerals from host rocks during intense deformation in the sulphide schist ore (Perkins, 1984; Swager, 1985; Bell

et al., 1988).

During deformation, the sulphide bodies react plastically and their associated phyllosilicate-rich altered rocks easily shear and assume a strong cleavage so that strain is commonly partitioned throughout the ore body and alteration zone (Large, 1992). Under such conditions, the possibility for external mechanical remobilization is consequently very high (Marshall, 1991a). External remobilization is promoted by differences in the mechanical and/or chemical behaviour of the principal minerals in massive sulphide bodies compared with those in their host rocks (Marshall and Gilligan, 1987).

The concept of external remobilization also requires substantial volumes of water for chemical mobilization of the sulphide minerals into the silicate host rocks. Walker and Buchanan (1969) have argued that metals can be extracted and transported out of mineralized rocks by aqueous fluids at relatively low temperatures. Despite the importance of fluids for remobilization at Mobrun they have had limited impact on the external chemical remobilization of sulphide masses, as described by (Marshall and Gilligan, 1987; Marshall 1991a). These limitations include the fact that: (1) sulphides cannot undergo metamorphic de-watering; (2) admixing or interacted silicate assemblages hosting sulphide orebody release insufficient fluid for significant dissolution of sulphide. Although infiltration of a fluid may be possible due to the increased permeability of the sulphide mass resulting from intense cataclasis, the potential for external

mechanical remobilization is probably low.

In summary, our observations on the Mobrun deposits indicate that the distances of migration of sulphide material from their sources were small (generally measurable in micrometres to metres). The mobilized material moved into pressure shadows, into veinlets within nodules and porphyroblasts, and into veinlets (in tension fractures), which terminate within the parent rock. The scale of these mass transfers is demonstrated in schematic form in Figure 6.43 in which metamorphism-deformation is clearly shown to have formed sulphide veins by remobilization of disseminated sulphide grains from the preexisting orebody and/or by remobilization of disseminated sulphide grains from the siliceous host rocks.

6.5 SUMMARY

For the low-grade metamorphosed sulphide rocks of Mobrun, the coarse-grained massive pyrite of the primary orebodies underwent cataclastic deformation, with the development of fractures filled with remobilized chalcopyrite (or to a lesser extent, with remobilized galena and electrum). Pressure-solution creep is found to have been a major deformation mechanism in fine-grained pyrite, as shown by overgrowths, truncated spheroids, indented grains, elongation of grains, and spaced cleavages.

Pressure-solution textures indicate significant remobilization and transport

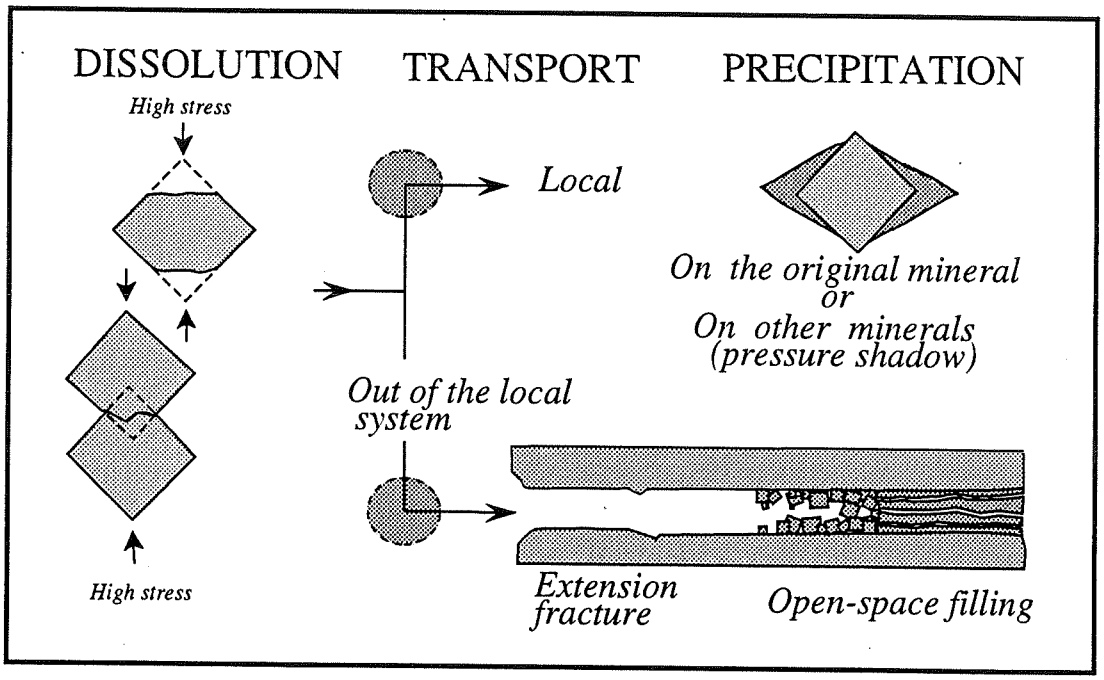

Fig. 6.43 Schematic diagram showing the mechanism of pressure solution at Mobrun. Material diffuses around grain margin, from highly stressed points to less stressed portions of same or adjacent grains or into open-space area.

of sulphide phases over variable distances from their original sites of deposition. Such remobilized material may have been deposited in grain-scale extension sites or in larger veins in the host rocks. Disseminated pyrite in the matrix of silicate host rocks has been deformed by intragranular extension fractures and by pressure-solution creep. These processes involved the development of elongate grain fabrics without crystallographically preferred orientations. Sphalerite and chalcopyrite were probably deformed by pressure solution and deformation twinning processes.

In the light of this microstructural study, there is fairly general consensus that mobilization of ore minerals at Mobrun has been widespread under metamorphism-deformation conditions and that distances of the order of micrometres to metres are involved.

CHAPTER 7

ESTIMATED PRESSURE-TEMPERATURE CONDITIONS DURING METAMORPHISM-DEFORMATION

7.1 INTRODUCTION

Reliable assessments of thermobaric conditions attained during low-grade metamorphism are limited to only a few methods. These include stable isotope measurements, fluid inclusion analyses, and element partitioning among coexisting minerals (e.g., calcite and dolomite, or sphalerite and pyrrhotite, Scolt and Barnes, 1971; Hutchison and Scott, 1981). Pressure and temperature estimates for the metamorphism of sulphide bodies and host rocks at Mobrun are not readily made from minerals phase relationships because of the absence of commonly employed mineral pairs such as dolomite and pyrrhotite, and because of the lack of other useful mineral pairs which might enable us to monitor P-T conditions. In addition, the scarcity of measurable fluid inclusions seriously restricts the application of fluid inclusion analyses; data from a few fluid inclusion measurements are presented in this study.

Oxygen isotope ratios for the host volcanic rocks of the Mobrun deposits have been published by Barrett et al. (1992); Hoy (1993). The results provide some constraints on temperature condition during metamorphism and deformation: $\delta^{18}O$

measurements of quartz for five quartz separates range from 13.0 to 14.6‰, whereas the $\delta^{18}O$ ratios for sericite range from 9 to 10.5‰ (inferred from bulk-rock values and estimated proportions of quartz-feldspar and sericite; cf. MacLean and Hoy, 1991). From the differences in $\delta^{18}O$ values between quartz and sericite (~4‰), and assuming equilibrated quartz-sericite fractionations (O'Neil and Taylor, 1969; Matsuhisa et al., 1979), a temperature of approximately ~250°C is obtained. Barrett et al. (1992) also noted that the relatively low whole-rock $\delta^{18}O$ values of 7 to 9‰ for samples located near the Main Lens complex would result from higher temperatures (~350°C) for a fluid value of ~4‰.

In order to gain more insight into the physical conditions under which minerals formed during metamorphism at the Mobrun deposit, attention is focused here on the molecular compositions of muscovite and chlorite. Even though chlorite and sericite are common minerals over a wide range of hydrothermal and metamorphic conditions, their specific mineral compositions are sensitive to temperature and pressure. The chlorite geothermometer has been described by Cathelineau and Nieva (1985), and the muscovite geobarometer, using the "b_0" method, has been proposed by Sassi (1972) and Sassi and Scolari (1974).

7.2 CHLORITE GEOTHERMOMETRY

Forty-four microprobe analyses of chlorite among 12 samples from different parts of the Mobrun host rocks have been carried out to determine the

temperature attained during metamorphism of the Mobrun host rocks. All of the samples have similar mineral assemblages: mainly quartz and sericite and minor amounts of chlorite, calcite, pyrite and feldspar. Most of the analyses were done on chlorite found in pressure shadows around pyrite and quartz grains.

The chlorite data of the Mobrun mine (Table 7.1) trends toward higher proportions of tetrahedral Al with increasing Fe/(Fe+Mg) ratios (Fig. 7.1). Bailey and Brown (1962) noted that in some, but not all chlorite, increasing octahedral Fe and tetrahedral Al contents seem to correlate with increasing temperatures of formation. Likewise, Cathelineau and Nieva (1985) found that changes in chlorite compositions involving tetrahedral substitution (between Si and Al^{iv}) are temperature dependent in altered andesites from the Los Azufres geothermal area of Mexico. They determined that Al^{iv} and Fe^{vi} in chlorite are positively correlated with temperature, whereas Mg contents are independent of temperature, reflecting instead the bulk compositions of the host rocks.

The correlation between Al^{iv} and temperature is applied in this study to estimate temperatures of metamorphism-deformation using the exchange between Fe and (Mg-Al^{iv}). According to Cathelineau and Nieva (1985), suitable rocks for chlorite geobarometry should be those containing Al-saturated mineral assemblages. As illustrated in a Si-Al-(Fe+Mg) diagram (Fig. 7.2), all chlorite samples from the Mobrun deposit are Al-saturated and associated with Al-rich phases such as sericite, albite, epidote.

Table 7.1 Calculations of temperature based on microprobe analyses of chlorites from Mobrun deposit

Sample no.	146	467	494	315	232	1	11	267	172A	51	265A	265B
No. of analyses	(2)	(7)	(1)	(3)	(5)	(3)	(8)	(5)	(2)	(4)	(2)	(2)
SiO2	22.99	23.56	23.64	23.20	23.35	23.71	23.91	24.44	24.32	24.72	25.59	26.63
TiO2		0.03	0.00	0.06	0.02	0.07	0.06	0.02	0.06	0.04	0.06	0.02
Al2O3	22.24	22.00	21.00	22.24	22.27	22.03	18.50	22.82	22.93	22.26	23.20	24.23
FeO	38.60	34.94	38.05	40.16	36.38	34.81	42.54	35.34	29.87	32.85	21.57	22.17
MnO	0.10	0.18	0.22	0.20	0.09	0.12	0.08	0.16	0.18	0.19	0.18	0.17
MgO	4.67	6.61	4.62	3.50	5.36	7.58	3.90	7.05	9.73	8.80	14.91	15.38
CaO		0.02	0.00	0.01	0.02	0.01	0.07	0.15	0.49	0.02	0.04	0.00
Na2O	0.16	0.15	0.25	0.19	0.14	0.61	0.23	0.18	0.15	0.16	0.14	0.13
K2O		0.06	0.03	0.04	0.01	0.02	0.02	0.02	0.04	0.03	0.00	0.02
Total	88.76	87.56	87.79	89.60	87.64	88.96	89.31	90.18	87.78	89.06	85.68	88.75
Si	5.16	5.26	5.36	5.24	5.24	5.20	5.47	5.27	5.25	5.33	5.39	5.41
Ti		0.02	0.00	0.01	0.00	0.01	0.01	0.00	0.01	0.01	0.01	0.00
Aliv	2.84	2.74	2.64	2.76	2.76	2.80	2.53	2.73	2.75	2.67	2.61	2.59
Alvi	3.04	3.04	2.97	2.96	3.13	2.90	2.46	3.07	3.09	2.99	3.15	3.21
Fe	7.24	6.52	7.21	7.41	6.83	6.39	8.14	6.37	5.40	5.93	3.80	3.77
Mn	0.02	0.03	0.04	0.04	0.02	0.02	0.01	0.03	0.03	0.03	0.03	0.03
Mg	1.56	2.20	1.56	1.41	1.80	2.48	1.33	2.34	3.13	2.83	4.68	4.66
Ca		0.00	0.00	0.00	0.01	0.00	0.02	0.04	0.12	0.01	0.01	0.00
Na	0.07	0.13	0.11	0.09	0.06	0.26	0.10	0.08	0.06	0.07	0.06	0.05
K		0.02	0.01	0.01	0.00	0.01	0.00	0.01	0.01	0.01	0.00	0.01
Total	19.94	19.97	19.90	19.94	19.84	20.06	20.07	19.94	19.85	19.86	19.75	19.72
Aliv (corrected)	2.83	2.73	2.62	2.74	2.75	2.79	2.52	2.72	2.74	2.66	2.60	2.59
Fe/Fe+Mg	0.82	0.75	0.82	0.84	0.79	0.72	0.86	0.73	0.63	0.68	0.45	0.45
Aliv/Aliv+Alvi	0.48	0.47	0.47	0.48	0.47	0.49	0.51	0.47	0.47	0.47	0.45	0.45
Temp. (°C)	318	307	296	309	310	314	285	306	309	300	294	292

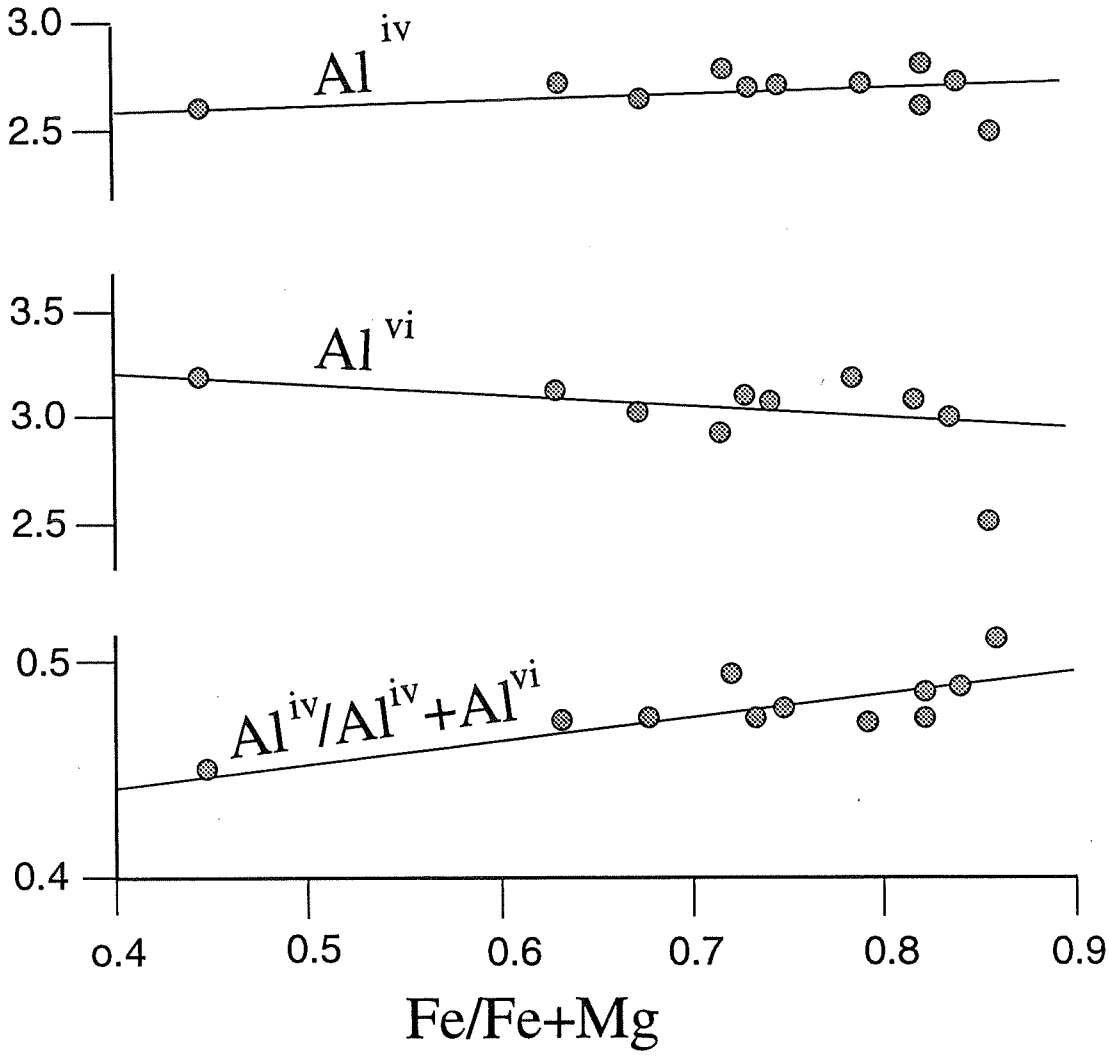

Fig. 7.1 Compositions of chlorites for $Al^{iv}/ Al^{iv} + Al^{vi}$, Al^{iv}, Al^{vi} against Fe/Fe + Mg.

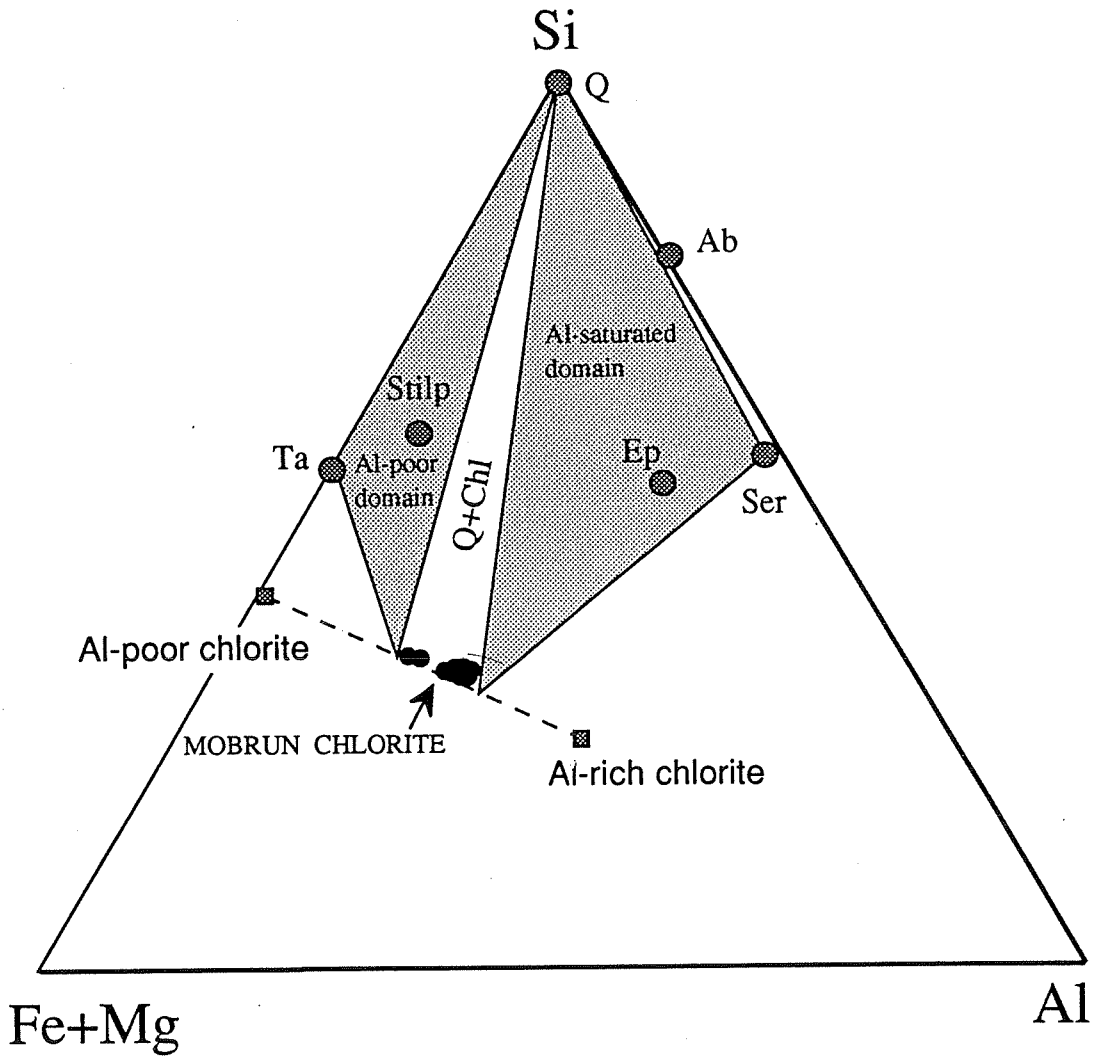

Fig. 7.2 Si-Al-Fe+Mg plot of chlorite data (average compositions) and fields of stable mineral assemblages. Albite (Ab), sericite (Ser) and stilpnomelane (Stilp) fall outside the system. The presence of sericite, albite and epidote at Mobrun fixes chlorite compositions at the end of the Al-Si solid-solution field.

The estimates for temperatures of formation for Mobrun chlorites are given in Table 7.1, using the Cathelineau and Nieva's (1985, Fig. 9) Al^{iv} vs T°C diagram. The regression line of this diagram was solved for T°C and converted to the following formula (Kranidiotis and MacLean, 1987):

$$T°C = 106 \times Al_{corrected}^{iv} + 18, \quad (7.1)$$

where Al^{iv} contents are corrected for their slight Fe-Mg dependency using the formula:

$$Al_{corrected}^{iv} = Al_{sample}^{iv} \pm 0.7\ Fe/(Fe+Mg). \quad (7.2)$$

Analyses of chlorites from the Mobrun mine have been superimposed on the diagram of Cathelineau and Nieva (1985) in Figure 7.3. Our chlorite analyses form a field indicating that temperatures of approximately 300°C were reached at Mobrun during peak metamorphism-deformation.

7.3 MUSCOVITE GEOBAROMETRY

The lateral spacing of the b_0 cell dimension of muscovite has been suggested by Sassi (1972) and Sassi and Scolari (1974) as a reliable method for determining barometric conditions in low-grade metamorphic rocks. They attempted to

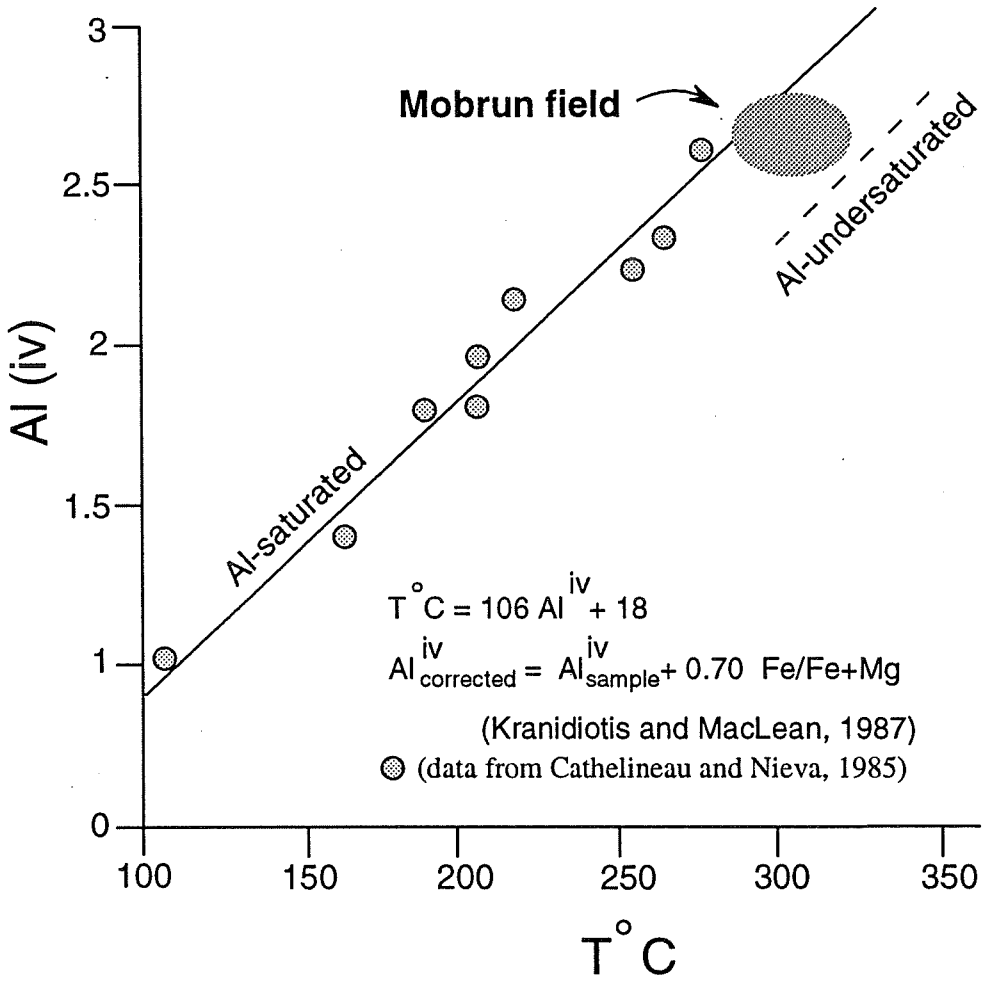

Fig. 7.3 Chlorite geothermometer (after Cathelineau and Nieva, 1985; Kranidiotis and MacLean, 1987) showing Al saturation regression line. Mobrun field is plotted on the basis of chlorite analyses in this study.

calibrate the b_0 cell parameter of muscovite as a geobarometer for greenschist facies metapelites in the Eastern Alps. Later studies have extended the method to other greenschist facies lithologies (Padan et al., 1982; Ritter, 1981). Brill (1988) applied the method to the massive sulphide mineralization of the Cobar district of eastern Australia, to understand physical conditions present during ore formation and subsequent metamorphism. This approach has been examined and extended in many studies such as: Rieder et al. (1992); Guidotti et al. (1992); Ruiz et al. (1980); Guidotti (1973), and Atzori and Sassi, (1973).

Changes in the b_0 value are due to the celadonite content of muscovite, $[KAl^{3+}(Mg^{2+},Fe^{2+})SiO_4O_{10}(OH)_2]$, in the sense of substitution of silicon (Si^{iv}) for aluminium (Al^{iv}) in tetrahedral sites and of magnesium (Mg^{+2}) and iron (Fe^{+2}) for aluminium (Al^{vi}) in octahedral sites. These substitutions cause increases in the b_0 value according to the following relationship:

$$[Al^{vi} \Rightarrow (Mg^{+2},Fe^{+2})^{vi}],\ [Si^{iv} \Rightarrow Al^{iv}] \Longrightarrow b_0\uparrow \qquad (7.3)$$

The positive correlation between the b_0 parameter and the celadonite content suggests that the b_0 value is a good indicator of the celadonite content of K-white mica (Sassi and Scolari, 1974; Guidotti and Sassi, 1976).

According to Sassi and Scolari (1974) and Guidotti an Sassi (1976), there are three principal factors that cause variations in the b_0 values of muscovite (i.e.,

variations in its celadonite content): (1) pressure, (2) temperature, and (3) the bulk-rock chemistry of the rock, or more specifically the Na/Na+K ratio of the muscovite:

Sassi (1976) and Sassi and Scolari (1974) noted that the celadonite content of muscovite, as well as the b_0 parameter in specific mineral assemblages (see below) increase with increasing pressure if temperature is held constant. Similarly, Guidotti et al., (1986) show that temperature varies inversely with the b_0 spacing of muscovite. However, temperature-related effects are important where the calibration involves only rocks of low metamorphic grade.

As for bulk-rock chemistry, Sassi (1972), Sassi and Scolari (1974) and Guidotti and Sassi (1976) provide detailed discussions on mineral assemblages suitable for b_0 measurements. Their suggestions include:

1) hematite and magnetite must be absent, because a rock with hematite or magnetite will probably have a high Fe^{+3}/Fe^{+2} ratio. In such cases, it would be impossible to decide whether a high b_0 value means celadonitic muscovite or ferrimuscovite;

2) paragonite, margarite, K-feldspar must be avoided because in such specimens it has been found that the b_0 values of muscovite are higher;

3) samples with particulary abundant quartz and/or chlorite should be avoided, because the muscovite is found to be enriched in celadonite;

4) carbonate-bearing rocks should be avoided, because in some cases very low b_0 values have been found in the muscovite.

5) muscovite should be abundant.

On the other hand, specimens with abundant muscovite containing mineral assemblages of ilmenite, ilmenite + Fe-sulphides, or graphite + ilmenite + Fe-sulphides, can be used without difficulty. Guidotti et al. (1989) indicate that the effects of Na-K substitution becomes important only where Na/(Na+K) ratio exceeds 15 mole percent; lower Na-K substitution has negligible effects. Therefore, for muscovite having low Na contents and occurring in suitable mineral assemblages (see above), the celadonite content of muscovite formed under low-grade metamorphism depends largely upon pressure only (Cipriani et al., 1971).

7.3.1 Application of b_0 geobarometry at the Mobrun deposit

Several studies, primarily in low-grade pelitic schists, have used the b_0 parameter to estimate metamorphic pressures. However, the pressures obtained by this method are relative only, and are not calibrated to absolute pressures. To investigate the potential use of b_0 as a parameter of metamorphic pressure at Mobrun, the relationships between b_0 and other parameters that might produce similar variations must first be examined.

From 20 samples taken form wallrocks of the Mobrun Main Lens complex, 100 grains of muscovite (mostly overgrowths) were chemically analyzed with the

electron microprobe (Table 7.2). In order to avoid the influence of variable bulk-rock compositions, rocks containing the non-limiting assemblage quartz-plagioclase-muscovite-chlorite were chosen; the geobarometric scale of Sassi and Scolari (1974) is based on rocks of this mineralogical composition. Chlorite, quartz and calcite-rich samples were avoided because the white micas in such samples have been found to be enriched in celadonite (Guidotti and Sassi, 1976). In all cases, the mineral assemblages were similar and the pre-requisites of Guidotti and Sassi (1976) were confirmed.

Most of the sericite at the Mobrun mine has a celadonite (phengite) composition (Table 7.2). The solid-solution of celadonite in muscovite is very small, reaching only 0.4 moles in Fe. However, the solid solution of paragonite in muscovite is more extensive and many samples reach the lower limits defined by Guidotti et al. (1989). Generally, the effects of the Na content of sericite on the b_0 value were found to be negligible.

Therefore, with regard to low-grade metamorphism, suitable mineral assemblages and unvarying temperature, it is reasonable to attribute the celadonite content of sericites at Mobrun to be due mainly to pressure effects. With these prerequisites satisfied, the b_0 values of sericite have been measured using the Guinier camera technique (Table 7.2; Appendix 7.1) and the experimentally derived equation of Guidotti et al., (1976):

Table 7.2 Calculation of "bo" based on microprobe analyses of sericite from Mobrun deposit.

Sample no.	315	467	244	146	73	146A	51	265B	267A	216	265A	338	194	92	2	91	20	267	332B	489
No. of analyses	(1)	(2)	(7)	(9)	(2)	(2)	(6)	(4)	(1)	(6)	(1)	(9)	(18)	(3)	(6)	(4)	(6)	(9)	(2)	(2)
Asso. minerals*	[1]	[1]	[1]	[1]	[1]	[1]	[1]	[1]	[3]	[4]	[4]	[4]	[4]	[4]	[4]	[4]	[4]	[4]	[5]	[5]
SiO2	47.89	46.67	46.43	46.39	49.02	43.91	47.05	46.76	46.99	47.52	44.98	47.85	46.81	44.97	46.94	46.84	47.17	46.73	51.01	47.21
TiO2	0.35	0.31	0.09	0.12	0.05	0.25	0.16	0.12	0.23	0.06	0.08	1.00	0.15	0.04	0.20	0.12	0.21	0.39	0.07	0.23
Al2O3	33.01	31.73	37.30	33.82	35.13	33.82	30.94	34.89	31.44	37.09	34.30	35.64	35.14	34.67	29.79	33.62	32.72	33.23	31.15	32.14
FeO	2.06	3.08	1.15	1.91	0.80	0.38	2.64	0.53	4.36	0.58	1.59	0.47	0.47	0.86	3.81	1.86	1.23	1.75	1.53	2.73
MnO	0.04	0.07	0.01	0.01	0.05	0.00	0.04	0.07	0.04	0.06	0.16	0.01	0.02	0.03	0.03	0.05	0.01	0.02	0.00	0.00
MgO	0.70	1.01	0.18	0.81	1.39	0.79	1.68	0.63	1.00	0.38	1.22	0.13	0.85	0.53	1.31	0.48	1.02	0.89	1.56	1.08
CaO	0.05	0.01	0.01	0.02	0.04	0.10	0.06	0.20	0.04	0.04	0.17	0.04	0.07	0.03	0.24	0.02	0.02	0.08	0.03	0.05
Na2O	0.22	0.27	1.61	0.37	0.48	2.39	0.21	2.12	0.23	0.96	0.54	2.97	0.76	0.82	0.18	0.59	0.22	0.12	0.24	0.20
K2O	11.39	11.20	8.77	10.86	10.94	6.24	10.83	7.68	11.22	10.12	7.77	5.95	10.12	9.69	11.24	10.39	10.76	11.21	10.76	11.27
BaO	0.25	0.17		0.60	0.18	0.23	0.25	0.06	0.33	0.14	0.35	0.12	0.23	0.09	0.13	0.21	0.13	0.23	0.23	
Total	95.96	94.51	95.55	94.91	98.06	88.10	93.86	93.07	95.88	96.93	91.16	94.20	94.62	91.74	93.88	94.18	93.50	94.66	96.56	94.90
Si	6.38	6.36	6.12	6.26	6.32	6.19	6.42	6.27	6.35	6.18	6.19	6.34	6.24	6.19	6.47	6.32	6.40	6.30	6.68	6.37
Ti	0.04	0.03	0.01	0.01	0.00	0.03	0.02	0.01	0.03	0.01	0.01	0.10	0.01	0.00	0.02	0.01	0.02	0.04	0.01	0.03
Aliv	1.62	1.64	1.88	1.74	1.68	1.81	1.58	1.73	1.65	1.82	1.81	1.66	1.76	1.81	1.53	1.68	1.60	1.70	1.32	1.63
Alvi	3.57	3.47	3.88	3.63	3.66	3.82	3.40	3.79	3.36	3.86	3.76	3.85	3.76	3.80	3.31	3.75	3.63	3.59	3.49	3.48
Fe	0.23	0.35	0.13	0.20	0.09	0.05	0.30	0.06	0.49	0.06	0.18	0.05	0.05	0.10	0.44	0.14	0.14	0.20	0.17	0.31
Mn	0.01	0.01	0.00	0.00	0.01	0.00	0.00	0.01	0.01	0.01	0.02	0.00	0.00	0.00	0.00	0.01	0.00	0.00	0.00	0.00
Mg	0.14	0.09	0.04	0.16	0.27	0.17	0.34	0.13	0.20	0.07	0.25	0.03	0.17	0.11	0.27	0.07	0.21	0.18	0.30	0.22
Ca	0.01	0.00	0.00	0.00	0.01	0.01	0.02	0.00	0.02	0.00	0.03	0.00	0.02	0.01	0.01	0.01	0.01	0.01	0.00	0.01
Na	0.06	0.07	0.41	0.10	0.12	0.65	0.01	0.03	0.01	0.24	0.15	0.76	0.20	0.00	0.01	0.00	0.00	0.01	0.06	0.05
K	1.94	1.95	1.47	1.87	1.80	1.12	1.89	1.52	1.94	1.68	1.37	1.00	1.72	1.70	1.98	1.75	1.86	1.93	1.80	1.94
Ba	0.01	0.01	0.00	0.03	0.01	0.01	0.05	0.35	0.06	0.01		0.01	0.01	0.22	0.05	0.18	0.06	0.03	0.01	0.00
Total	13.99	13.97	13.94	14.00	13.96	13.86	14.04	13.89	14.11	13.94	13.75	13.79	13.94	13.95	14.10	13.92	13.92	13.99	13.84	14.04
FeO+MgO**	0.05	0.07	0.02	0.05	0.05	0.02	0.08	0.02	0.09	0.02	0.05	0.01	0.03	0.03	0.09	0.04	0.04	0.05	0.06	0.06
Na/Na+K	0.03	0.03	0.21	0.05	0.06	0.35	0.03	0.29	0.03	0.12	0.03	0.41	0.10	0.11	0.02	0.07	0.03	0.01	0.03	0.02
b0***	9.005	9.012	8.997	9.005	9.005	8.998	9.016	8.998	9.018	8.996	9.007	8.993	8.999	8.998	9.018	9.002	9.004	9.005	9.010	9.011

* Associated minerals:
[1]: quartz, pyrite, sericite, chlorite + calcite.
[2]: quartz, pyrite, chlorite + calcite.
[3]: quartz, sericite, chlorite + calcite.
[4]: quartz, pyrite, sericite + calcite.
[5]: quartz, sericite + calcite, albite.
** mole proportion
*** b0 = 8.99 + 0.327 x (FeO + MgO)

$$b_0 = 8.99 + 0.327 \times (RM) \quad (7.4)$$

where RM = (molar proportion of FeO) + (molar proportion of MgO). The b_0 values calculated by this equation compare favourably with those obtained through direct measurement of b_0 values of muscovite by X-ray diffractometry (Appendix 7.2).

The b_0 values are plotted on an empirical P-T diagram (Guidotti and Sassi, 1986) contoured for muscovite b_0 values (Fig. 7.4). For a temperature of about 300°C (see previous section), the b_0 data plot at a pressure below the Al-silicate triple point (~2 to 3 kbar).

7.4 FLUID INCLUSION STUDIES

The analysis of fluid inclusions in samples from the Mobrun deposit is curtailed by the scarcity of appropriate minerals with inclusions. Fluid inclusions are observed only in a few quartz overgrowths and within dilatant quartz veins. Overgrowth grains and dilatant vein minerals containing fluid inclusions were generally measured in order to determine the conditions of fluid flow during deformation.

In this study, three doubly polished thin sections were prepared for microthermometric analysis in order to obtain at least a preliminary range of inclusion temperatures and salinities. Two samples contained quartz overgrowths

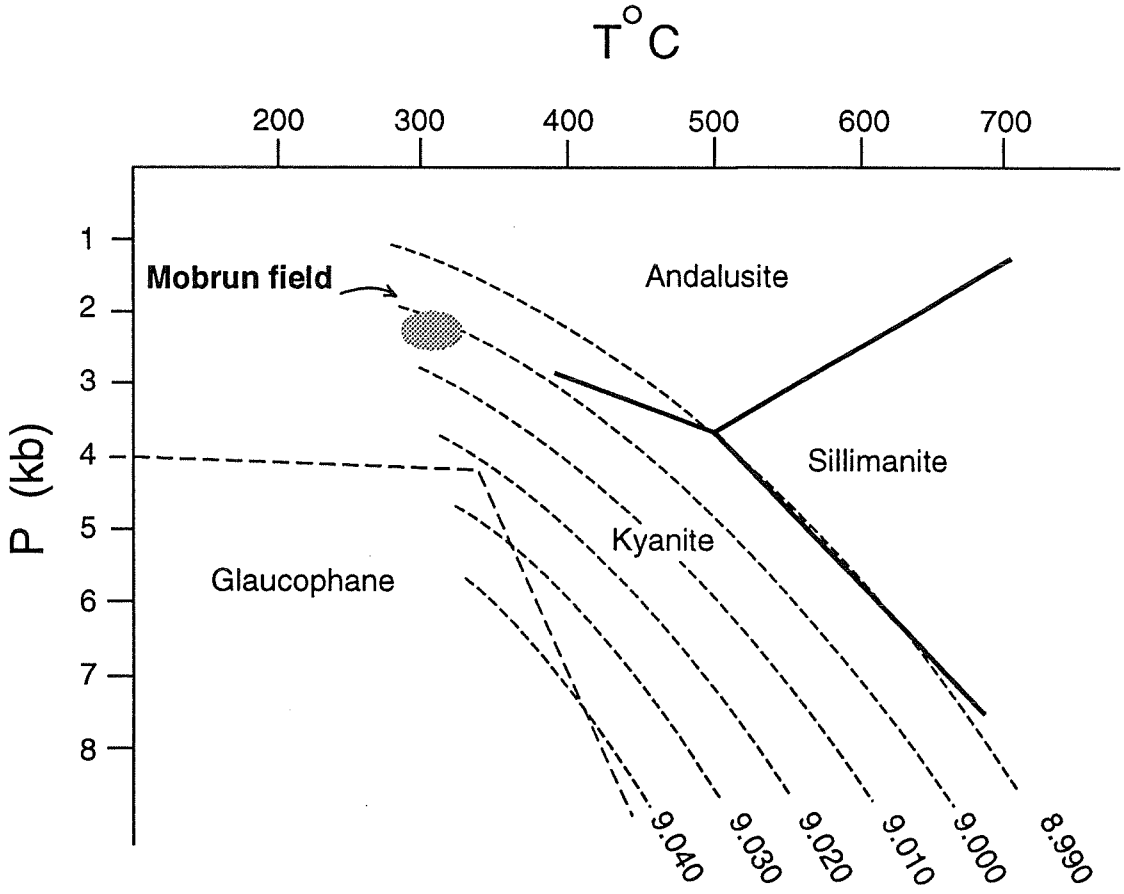

Fig. 7.4 Qualitative plot of muscovite b_0 values (modified after Guidotti and Sassi, 1990). Mobrun field is plotted on the basis of b_0 analyses and a temperature of 300 °C.

on pyrite and the other represented a post-deformational quartz vein. The inclusions were primarily two-phase aqueous inclusions (liquid and vapour, with liquid/vapour ratios of about 10:1) and single-phase inclusions (aqueous liquid, or more rarely invisible vapour bubbles). The inclusions at Mobrun are generally small (~5 μm), irregular in shape, and isolated, clustered, or concentrated along growth planes (Fig. 7.5). No daughter minerals were observed. Most inclusions were classified as primary (contemporaneous with their quartz host minerals) according to the criteria of Roedder (1984).

Homogenization temperatures (Th) were measured during heating runs. This is the temperature at which two phases (aqueous liquid+vapour in our study) initially contained in an inclusion are homogenized into a single phase. Homogenization provides an estimate of the minimum temperature at which the fluid was trapped. The initial (or eutectic) melting temperatures (Te) and final melting temperatures (Tm) were also measured during freezing runs. Initial melting temperatures provide information about the compositions of the fluids in the inclusions, according to the chloride salt systems: KCl (Te = -10.6°C), NaCl (Te = -20.8°C), $MgCl_2$ (Te = -33.6°C) and pure CO_2 (Te = -56.6°C)(data from Crawford 1981).

The final melting temperature, the temperature at which the last ice melts, can be used to determine the salinities from the equation of Potter et al. (1978):

Fig. 7.5 (a) Fluid inclusion within the quartz pressure shadow over pyrite. (b) Fluid inclusion within the syntectonic quartz veins in Mobrun silicate host rocks. Field of view 0.5 mm across each photograph. Transmission light.

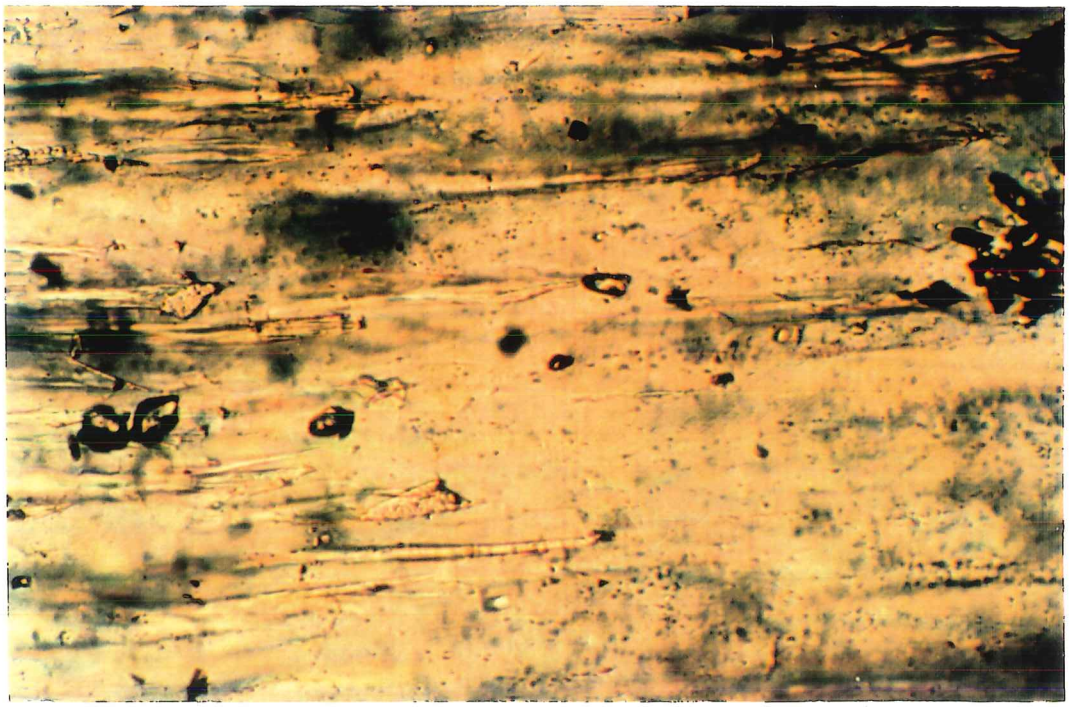

Fig. 7.5a

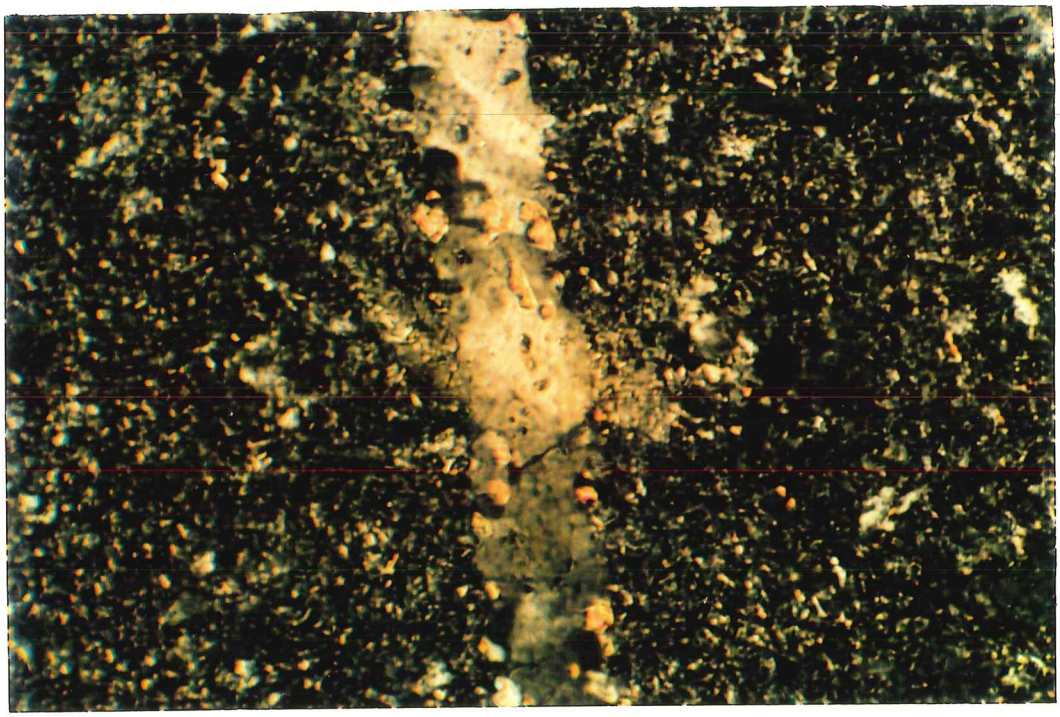

Fig. 7.5b

$$WS = 1.76958 \times D - 4.24 \times 10^{-2} \times D^2 + 5.2778 \times 10^{-4} \times D^3 \quad (7.5)$$

where WS is the equivalent weight percent NaCl, and D is the freezing point depression in °C.

A total of 7 fluid inclusions were analyzed from overgrowth quartz (Appendix 7.3). All of the aqueous inclusions homogenized at temperatures between 110 to 200°C, with a mean temperature of 156°C.

Accurate eutectic temperatures were generally difficult to establish due to the small size of the inclusions, but the inclusions appeared to melt at temperatures between -15 to -30°C, with a mean of -23°C. This range indicates that the fluid inclusions probably contain a multicomponent salt system involving dissolved NaCl, KCl and $MgCl_2$.

The final melting temperatures of Mobrun fluid inclusions were also found to be difficult to determine accurately due to the small size of the inclusions. Those inclusions measured gave final melting temperatures ranging from -5 to -1°C, with a mean of -3°C, corresponding to a salinity of 5.7 wt.% equivalent NaCl. There are insufficient data to establish any correlation between the salinities and the homogenization temperatures.

Three fluid inclusions in vein quartz have eutectic points (-57°C) suggesting a CO_2 component. The estimated homogenization temperatures of these inclusions range from 100 to 122°C. Some inclusions of these inclusions may contain two liquid phases which could have escaped observation during microthermometry

studies.

7.5 DISCUSSION

Although, all precursor conditions required to apply the b_0 method have been carefully employed and the equation relating b_0 to pressure has been tested by Guinier camera techniques, the general application of this method to hydrothermally altered volcanic rocks should still be verified by addition measurements. However, the brief studies described here provide practical preliminary information on the geobarometry and geothermometry of the chlorite and sericite found in the metamorphosed massive sulphide deposits of Mobrun.

According to the geobarometric map of Guidotti and Sassi (1986), the b_0 values for Mobrun indicate low pressure conditions equivalent to about 2 to 3 kbar. This pressure corresponds to a lithostatic load of approximately 8 km (assuming 3.3 km $kbar^{-1}$) during metamorphism-deformation of the Mobrun deposits. Also, a temperature of ~300°C corresponds to a geothermal gradient of ~34°C km^{-1}. This gradient appears to agree with previous estimates of the geothermal gradient for the Abitibi (e.g., 35°C km^{-1}, Powell et al., 1993) and other Archean terrains (e.g., 35°C km^{-1}, Martin 1986; 40°C km^{-1}, Craw and Koons, 1989). At this depth and temperature, the Mobrun host rocks could have undergone both low-grade metamorphism and brittle-ductile deformation.

As for possible errors in the observations and measurements of fluid inclusions at Mobrun (principally due to the small size of the inclusions), it can be assumed that the fluid inclusions within pressure-shadow quartz contain a saline liquid phase, probably a low-chloride metamorphic fluid. This fluid might have been responsible for the dissolution of ore minerals during metamorphism at Mobrun, as outlined in Chapter 6. According to Mookherjee (1976), in view of the extremely limited solubilities of the sulphide minerals in fresh water, the highly charged chlorides of Na, K and Ca are needed to leach and transport metals. Some fluid inclusion data suggest that CO_2 is also an important component; the CO_2 may have been derived from graphite and/or carbonate-bearing mineral assemblages.

Synvolcanic hydrothermal activity probably imposed an isotopic alteration on the volcanic host rocks, followed by isotopic re-equilibration (involving recrystallization and local remobilization) during metamorphism-deformation in a closed system (Riopel et al., 1992). Mineral separates and hand-sample data provided by Riopel et al. (1992) and Barrett et al. (1993) confirm our interpretation that metamorphic fluids equilibrated with wallrocks in a chemically closed system during metamorphism-deformation at Mobrun.

7.6 SUMMARY

The methods presented in this study are based on the molecular compositions of chlorite and sericite in wallrocks of the Mobrun deposit. Microprobe data show that the chlorites exhibit compositional substitution between Si and Al. From the correlation of the Si-Al content of chlorite with temperature (Cathelineau and Nieva 1985), a temperature of about 300°C is estimated for the formation of Mobrun chlorites during metamorphism-deformation.

Many petrographic studies of muscovite indicate a barometric dependency for the celadonite (Fe,Mg) content of muscovite. According to the geobarometric map of Guidotti and Sassi (1986), an absolute pressure about 2-3 kbars is estimated for the peak metamorphic-deformation pressure at Mobrun. Although the general application of b_0 geobarometry to hydrothermal altered volcanic rocks should still be verified, this study attempts to provide new application of this method.

According to the calculation of pressure and temperature, a geothermal gradient of ~34°C km^{-1} is obtained for the metamorphism-deformation (syntectonic) event at Mobrun.

CHAPTER 8

GENERAL DISCUSSION AND CONCLUSIONS

The Mobrun Main Lens occurs in subvertical structures within felsic pyroclastic rocks and lavas. The deposit has many features in common with deposits of the Noranda-type volcanic-associated massive sulphide (VMS) deposits. The geological evidence indicates that massive sulphide ore lenses at Mobrun are essentially stratabound and as such, they form an integral part of the succession of volcanic rocks.

There is evidence of lateral zonation into copper-rich and zinc-rich zones within the orebody. In contrast, there is no evidence of a strong stringer zone in the footwall side, and extensive sericite alteration extends into both the footwall and hangingwall rocks, without an apparent alteration pipe or chloritization zone. During metamorphism-deformation, the Main Lens orebody and its host rocks were affected by chemical and textural modifications. The silicate host rocks were foliated subparallel to the orebody and underwent syntectonic mass and volume changes.

In comparison with other metamorphosed massive sulphide deposits (e.g., the Caledonian deposits of Norway [Vokes and Craig, 1993]; the Cordilleran deposits of Canada [McClay, 1991]; the Tasmania VMS deposits [Large, 1991]), there appears to be a general agreement on the main features of tectonic

remobilization of ores. As regards the distances involved, it appears that there is agreement that remobilization distances are very limited. All studies, including the present research, note that the metamorphic remobilization of the ore minerals (i.e., pyrite) took place within the limits of in situ recrystallization, more precisely within the limits of the orebodies. Even the more mobile sulphides (e.g., sphalerite and chalcopyrite) which commonly occur in tension fractures and pressure shadows, remain within the orebody. In contrast, large-scale mobilization of ore in the banded Mt. Isa (Australia) ores is clearly related to a strong deformation event; the sulphides have moved both laterally towards the troughs and crests of folds and transversely into cross-cutting features within limb positions (McDonald, 1967).

This current study has been undertaken to identify the nature and origin of deformational features and metamorphic effects in both sulphide and silicate rocks. This work was done using detailed petrographic and chemical analyses of the resulting mineralogies and textures. On the basis of these studies, the following conclusions may be drawn:

1) The microstructural studies describe the major metamorphic and microstructural features of host rocks, such as schistosity, pressure-solution cleavage, crenulation cleavage, pressure shadow, crack-seal veins, pull-aparts and boudins. The remarkable geometry of these microstructures provides a key to

understanding of the deformation mechanism and the importance of syntectonic mass and volume transfers in the Mobrun deposit.

2) The specific relationship between microstructural deformation patterns and the distribution and chemical characteristics of minerals has been investigated with the scanning electron microprobe, X-ray diffraction and X-ray fluorescence spectrometry. These analyses show that the schistosity and cleavage fabrics represent the development of narrow mineralogical and chemical differentiated zones. The following specific analyses were done:

i) the chemistry and mineralogy of schistosity lamellae are different from microlithon domains. The schistosity nevertheless shows consistent decreases in SiO_2, due to the deficiency of quartz and increases in Al_2O_3 and K_2O, due to the relative increase in sericite with respect to the microlithon domains. Fine-grained rutile is concentrated in schistosity lamella due to its insolubility.

ii) there are changes in bulk chemical composition between deformed and undeformed rocks. There are decreases in SiO_2 and increases in Al_2O_3, K_2O and immobile elements (Ti, Zr, Y, and Nb) in the deformed rocks.

iii) microprobe analyses of sericite in pressure shadows reveal a range in

compositions different from the sericite within cleavage lamellae. Pressure-shadow sericite is characterized by higher Si, K, Fe and Mg contents and lower Al, Na and Ti contents.

3) Chemical variations associated with cleavage and schistosity fabrics show that the distribution of minerals is due to their preferential dissolution in different microstructural sites. The growth of new phyllosilicate grains was controlled by the behaviour of elements interacting with water during metamorphism.

4) The role of mass transfer in the development of these microstructures indicates that during metamorphism-deformation, pressure-solution creep was a major contributor to mass transport. Element were remobilized by local dissolution from high-strain domains and subsequent redeposition in low-strain domains in adjacent layers. On the other hand, the ubiquitous presence of syntectonic extension veins filled with quartz, calcite and pyrite are obvious manifestation of mass transfer over longer distances than those involved in filling pressure-solution sites.

5) Despite the overprint of alteration and metamorphism-deformation at Mobrun, geochemical analyses using immobile elements (Zr, Y, Nb, HREE and Ti) have been used successfully to identify the chemical affinity and precursor

lithologies of volcanic rocks. Both tholeiitic (Zr/Y = 4.5) and mildly calc-alkaline (Zr/Y = 8) rhyolites are identified, the former in the hangingwall, the latter in the footwall.

6) A correlation is noted between immobile element concentrations and the intensity of foliation in the host rocks. Intensity foliated rocks are strongly enriched or depleted in Zr, Y, Ti and HREEs in comparison to rocks showing weak foliations; this difference is attributed to mass transfers during the metamorphism-deformation event.

7) Mass transfers attributed to hydrothermal alteration and metamorphism-deformation exhibit wide ranges in the concentrations of immobile elements within the wall rocks. Absolute differences in Zr contents for the reconstituted compositions and altered rocks and their corresponding precursors have been used to detect mass changes resulting from hydrothermal alteration and metamorphism-deformation.

8) Volume changes have been calculated from the bulk compositions using the normative mineralogy and density of minerals compared to the volume of the corresponding precursor in both altered and deformed rocks.

9) Mass change calculations demonstrate that mass transport is significant in many hydrothermally altered samples, but still larger scales of mass change are seen in deformed rock. Samples are characterized by overall mass changes of -20% to +25% for hydrothermal alteration effects, whereas deformed rocks show changes of -65% to +55% for metamorphism-deformation effects. Volume changes are similar in range to the observed mass changes.

10) The Mobrun Main Lens fabric contains laminated, massive, and brecciated structures, including fine-grained sulphides that are even colloidal in some cases, along with vein-type mineralization. However the general shape and distribution of the mineralized bodies is due to an exhalative massive sulphide deposition.

11) Deformation and recrystallization of sulphide minerals at Mobrun are the result of metamorphic-deformation. This overprint tends to destroy primary structures formed during synvolcanic exhalations. However, some primary-diagenetic features (such as sphalerite-pyrite banding) are retained, especially in pyrite (framboidal features, colloform textures, etc.).

12) The microstructures developed in sulphides during metamorphism-deformation show that pyrite behaved mainly in a brittle fashion, although there is evidence of a certain ductility. Fine-grained pyrite at Mobrun show evidence of

dislocations, pressure-solution and cataclastic flow.

13) The behaviour of the other sulphides was basically ductile. Deformational and annealing twinning are observed in sphalerite. Likewise in some cases, sphalerite appear to be relatively insoluble in pressure solution seams. Chalcopyrite displays a "chalcopyrite disease" texture, as well as recrystallization within pyrite microfractures. Galena shows recovery and recrystallization features within microstructures.

14) In spite of the primary microstructural features, many sulphide rocks have undergone recrystallization. These effects are shown at microscale to include: dissolution-precipitation creep, annealing, overgrowths, and fillings of fractures. The more ductile phases (such as galena, chalcopyrite and sphalerite) tend to migrate toward the low-pressure area of pressure shadows and microfractures associated with clasts of pyrite. Crack-seal veins of pyrite resulting from metamorphic processes are generally very common at Mobrun. Such textures support the concept of remobilization of ores over longer distances than seen in pressure-solution structures.

15) The temperature of metamorphism-deformation at Mobrun has been determined using the molecular compositions of overgrowth chlorite grains. This

method give a temperature of ~300°C for the formation of metamorphic chlorite.

16) The pressure attained during metamorphism-deformation has been determined from the molecular composition of sericite (Sassi and Scolari, 1974). This geobarometer, based on the celadonite content of muscovite, results from a positive correlation between the b_0 parameter and pressure. According to the geobaric map of Guidotti and Sassi (1986), an absolute pressure about 2 to 3 kbar is estimated for peak pressures at Mobrun.

17) Fluid inclusion studies were done on a few quartz overgrowth grains and within dilatant quartz veins. Fluid inclusions contain a saline liquid phase, probably a low-chloride metamorphic fluid. Some fluid inclusion data suggest that CO_2 is also an important component in the metamorphic fluid.

FINAL STATEMENT

A numbers of studies of massive sulphide deposits in the Abitibi mining district show evidences of metamorphism-deformation (e.g., Matagami Lake mine, Matagami district [Robert, 1975] and Dumagami, Bousquet district [Marquis, 1990]), but the possibility of remobilization of ores and associated silicate rocks has not been previously studied in detail in the Noranda area. In fact, the present

study may be considered the first effort dealing in detail with the general subject of metamorphism in preexisting sulphide deposits in the Noranda area. This study has focused particularly on microstructural remobilization associated with metamorphism-deformation.

The sulphide microstructures at Mobrun are similar to those in the associated silicate-dominated host-rocks. Pressure-solution mass transfer at Mobrun was an important type of deformation in the siliceous host rocks, as well as, in the sulphide ores where pyrite especially shows evidence of pressure-solution. Among the microstructural sites of silicate minerals, short-range (micrometre to hand-specimen scales) dissolution and transfer of materials are recognized. However, more than 50% of the mass and volume changes in the bulk rocks are attributed to mass transfers of material (mainly quartz) at the deposit-scale during metamorphism-deformation.

There is general evidence that remobilization of preexisting sulphide ore at Mobrun was widespread under metamorphic-deformation conditions. Remobilization of ore on short-range scales is a well-developed feature of the ore for distances on the order of micrometres to hand-specimen. Syntectonic long-range (deposit-scale) remobilization of ore has also been recognized in extension veins, particulary in the stringer zone where hydrothermal mineralization is typically associated with a dilatant or replacement vein system.

The analytical methods used in this study, consisting of a combination of

microstructural and geochemical studies, may be employed to generate information about the post-ore history of metamorphosed massive sulphide deposits in general. In addition, the petrographic, geochemical and microstructural criteria described in this study may be used in mineral exploration programs. For example, microstructural and mass changes described may indicate zones of hydrothermal alteration concealed within intensely deformed rock. The hydrothermal alteration could then lead to discoveries of related massive sulphide mineralization.

REFERENCES

AMBROSE, J.W. (1941) Clericy and La Pause map-areas, Québec: Geological Survey of Canada, Memoir 233.

ATZORI, P. and SASSI, F.P. (1973) The barometric significance of the muscovites from the Savoca phyllites (Peloritani, Sicily): Schweizerische Mineralogische und Petrographische Mitteilungen, v. 53, pp. 243-253.

AUDREY RESOURCES INC. (1990) Annual report. Audery Resources Inc., Rouyn-Noranda, Québec, 24 p.

BAILEY, S.W. and BROWN, B.E. (1962) Chlorite polytypism: I Regular and semirandom one-layer structures: American Mineralogist, v. 47, pp. 819-850.

BARAGER, W.R.A. (1968) Major-element geochemistry of the Noranda volcanic belt, Québec-Ontario: Canadian Journal of Earth Sciences. v. 5, pp. 773-790.

BARRETT, T.J., CATTALANI, S., HOY, L., RIOPEL, J. and LAFLEUR, P.-J. (1992) Massive sulphide deposits of the Noranda area, Québec. IV. The Mobrun mine: Canadian Journal of Earth Sciences, v. 29, pp. 1349-1374.

BARRETT, T.J., CATTALANI, S. and MACLEAN, W.H. (1993) Volcanic lithogeochemistry and alteration at the Delbridge massive sulfide deposit, Noranda, Québec: Journal of Geochemical Exploration, v. 48, pp. 135-173.

BARRETT, T.J., MACLEAN, W.H., CATTALANI, S., HOY, L. and RIVERIN, G. (1991) Massive sulphide deposits of the Noranda area, Québec. III. The Ansil mine: Canadian Journal of Earth Sciences, v. 28, pp. 1699-1730.

BARTON, P.B. and BETHKE, P.M. (1987) Chalcopyrite disease in sphalerite: Pathology and epidemiology: American Mineralogist, v. 72, pp. 451-467.

BEAUMIER, M. (1984) Pedogeochimie sur le gisement de Mobrun. Ministère de l'Énergie et des Ressources, Québec, MB 16, 26 p.

BELL, T.H. and CUFF, C., (1989) Dissolution, solution transfer, diffusion versus fluid flow and volume loss during deformation/metamorphism: Journal of Metamorphic Geology, v. 7, pp. 425-447.

BETEKHTIN, A.G., GENKIN, A.D., FILIMONOVA, A.A., and SHADLUN, T.N. (1958) Structures and textures of ores: Moscow, Gosgeoltekhisdat, 435 p. (in Russian; ref. Bortnikov et al. (1991).

BORTNIKOV, K.S., GENKIN, A.D., DOBROVOL'SKAYA, M.G., MURAVITSKAYA, G.N. and FILIMONOVA, A.A. (1991). The nature of chalcopyrite inclusions in sphalerite: exsolution, coprecipitation, or "disease"?: Economic Geology, v. 86, pp. 1070-1082.

BOSWORTH, W. (1981) Strain induced preferential dissolution of halite: Tectonophysics, v. 78, pp. 509-526.

BRILL, B.A. (1988) Illite crystallinity, b_0 and Si content of K-white mica as indicators of metamorphic conditions in low-grade metamorphic rocks at Corbar, New South Wales: Australian Journal of Earth Sciences, v. 35, pp. 295-302.

BRILL, B.A. (1989) Deformation and recrystallization microstructures in deformed ores from the CSA mine, Cobar, N.S.W., Australia: Journal of Structural Geology, v. 11, pp. 591-601.

BROWN D. and McCLAY, K.R. (1993) Deformation textures in pyrite from the Vangorda Pb-Zn-Ag deposit, Yukon, Canada: Mineralogical Magazine, v. 57, pp. 55-66.

CATHELINEAU, M. and NIEVA, D. (1985) A chlorite solid solution

geothermometer: The Los Azufres (Mexico) geothermal system: Contribution to Mineralogy and Petrology, v. 91, pp. 235-244.

CATTALANI, S. and CHARTRAND, F. (1988) Métallogenèse des dépôts de sulfures massifs de métaux de base de la zone Abitibienne, Québec; Dépôts d'Aldermac, d'Ansil et de Mobrun. Rapport preliminaire, Ministère de l'Énergie et des Ressources, Québec, 43 p.

CAMPBELL, I.H., LESHER, C.M., COAD, P., FRANKLIN, J.M., GORTON, M.P. and THURSTON , P.C. (1984) Rare-earth element mobility in alteration pipes below massive Cu-Zn sulfide deposits: Chemical Geology, v. 45, pp. 81-202.

CATTALANI, S., BARRETT, T.J. MACLEAN, W.H., HOY, L., HUBERT, C. and FOX, J.S., (1989) Métallogénie des gisements de métaux de base en Abitibi, Québec: Les mines Horne et Quemont, Noranda. Ministère de l'Énergie et des Ressources du Québec, Rapport ET, 231 p.

CAUMARTIN, C. and CAILLÉ, M.-F. (1990) Volcanic stratigraphy and structure of the Mobrun mine. In: The Northwestern Québec Polymetallic Belt, eds. M. Rive, P. Verpaelst, Y. Gagnon, J.M. Lulin, G. Riverin and A. Simard: Canadian Institute of Mining, Metallurgy and Petroleum, Special Volume 43, pp. 133-142.

CIPRIANI, C., SASSI, F.P. and SCOLARI, A. (1971) Metamorphic white micas: definition of paragenetic fields. Schweizerische Mineralogische und Petrographische Mitteilungen. v. 51, pp. 259-295.

COBBLE J.W., MURRAY, R.C., TURNER, P.J., and CHEN, K., (1982) High-temperature thermodynamic data for species in aqueous solution: Electronic Power Research Institute. Report NP-2400, 179 p.

COOK, N.J., HALLS, C. and BOYLE, A.P. (1993) Deformation and metamorphism of massive sulphides at Sulitjelma, Norway: Mineralogical Magazine, v. 57, pp. 67-81.

COX, S.F. (1987) Flow mechanisms in sulphide minerals: Ore Geology Reviews, v. 2, pp. 133-171.

COX, S.F. and ETHERIDGE, M.A. (1983) Crack-seal fibre growth mechanisms and their significance in the development of oriented layer silicate microstructures: Tectophysics, v. 92, pp. 147-170.

COX, S.F. and ETHERIDGE, M.A. (1889) Coupled grain-scale dilatancy and mass transfer during deformation at high fluid pressures: examples from Mount

Lyell, Tasmania: Journal of Structural Geology, v. 11, no. 1/2, pp. 147-162.

COX, S.F., and ETHERIDGE, M.A. (1983) Crack-seal fibre growth mechanisms and their significance in the development of oriented layer silicate microstructures: Tectophysics, v. 92, pp. 147-170.

CRAIG, J.R. and VAUGHAN, D.J. (1981) Ore Microscopy and Ore Petrography. John Wiley and Sons, U.S.A, 406 p.

CRAIG, J.R. and VOKES, F.M. (1992) Ore mineralogy of the Appalachian-Caledonian stratabound sulfide deposits: Ore Geology Reviews, v. 7, pp. 77-123.

CRAIG, J.R. and VOKES, F.M. (1993) The metamorphism of pyrite and pyritic ores: an overview: Mineralogical Magazine, v. 57, pp. 3-18.

CRAW, D., and KOONS, P.O. (1989) Tectonically induced hydrothermal activity and gold mineralization adjacent to major fault zones. In: The Geology of Gold Deposit: The Perspective in 1988, eds. Keays, R.R., Ramsay, W.R.H. and Groves, D.I.: Economic Geology, Monograph 6, pp. 471-478.

CRAWFORD, M.L. (1981) Phase equilibria in aqueous fluid inclusions:

Mineralogical Association of Canada, Short Course Handbook, v. 6, pp. 75-100.

DEER, W.A., HOWIE, R.A. and ZUSSMAN, J. (1980) An Introduction to the Rock Forming Minerals, Longman, London 528 p.

DEB, M. (1979) Polymetamorphism of ores in Precambrian stratiform massive sulfide deposits at Ambaji-Deri, western India: Mineralium Deposita, v. 14, pp. 21-31.

DE ROO, J.A. (1989) Mass transfer and preferred orientation development during extensional microcracking in slate-belt folds, Elura Mine, Australia: Journal of Metamorphic Geology, v. 7, pp. 311-322.

DICKSON, J.A.D. (1965) A modified staining technique for carbonates in thin section: Nature, no. 4971, p. 587.

DIMROTH, E., IMREH, N., ROCHELEAU, M. and L., GOULET (1982) Evolution of the south-central part of the Archean Abitibi Belt, Québec. Part I: Stratigraphy and paleogeographic model: Canadian Journal of Earth Sciences, v. 19, pp. 1729-1758.

DIMROTH, E., IMREH, L., GOULET, N. and ROCHELEAU, M. (1983) Evolution of the south-central segment of the Archean Abitibi Belt, Québec. Part II: Tectonic evolution and geomechanical model: Canadian Journal of Earth Sciences, v. 20, pp. 1355-1373.

DUQUETTE, A. (1977) Etude pétrographique, pétrochimique et gitologique d'une partie du quart NE du canton de Dufresnoy, Abitibi. Projet de fin d'étude, Département de Génie Géologique, Ecole Polytechnique, Montreal, Québec, 200 p.

EDMOND, J.M., MEASURES, C., MANGUM, B., GRANT, B., SCLATER, F.R., COLLIER, R. and HUDSON, A. (1979) On the formation of metal-rich deposits at ridge crests: Earth and Planetary Sciences; Letters, v. 46, pp. 19-30.

ETHERIDGE, M.A., WALL, V.J. and COX, S.F. (1984) High fluid pressures during regional metamorphism and deformation: implications for mass transport and deformation mechanisms: Journal of Geophysical Research, v. 89, pp. 4344-4358.

ETHERIDGE, M.A., WALL, V.J. and VERNON, R.H. (1983) The role of fluid phase during regional metamorphism and deformation: Journal of Metamorphic Geology, v. 1, 205-226.

FERGUSON, C.C., and HARTE, B. (1975) Textural patterns at porphyroblast margins and their use in determining the time relations of deformation and crystallization: Geological Magazine, v. 112, pp. 467-480.

FINLOW-BATES, T., and STUMPFL, E.F. (1981) The behaviour of so-called immobile elements in hydrothermally altered rocks associated with volcanogenic submarine-exhalative ore deposits: Mineralium Deposita, v. 16, pp. 319-328.

FLEET, M.E. and MACLEAN, P.J. (1988) Oscillatory-zoned As-bearing pyrite from strata-bound and stratiform gold deposits: an indicator of ore fluid evolution. In: The Geology of Gold Deposits: the perspective in 1988, eds: R.R. Keays, W.R.H. Ramsay, D.I. Groves: Economic Geology, Monograph 6. pp. 358-362.

FRANKLIN, J.M., LYDON, J.W. and SANGSTER, D.F. (1981) Volcanic-associated massive sulfide deposits. In: 75th Anniversary Volume, eds. B.J. Skinner. Economic Geology, pp. 485-627.

FLOYD, P.A. and WINCHESTER, J.A. (1977) Identification and discrimination of altered and metamorphosed volcanic rocks using immobile elements: Chemical Geology, v. 21, pp. 291-306.

FYFE, W.S., PRICE, N.J. and THOMPSON, A.B. (1987) Fluid in the Earth's Crust, Elsevier Amsterdam, 383 p.

GÉLINAS, L., BROOKS, C., PERRAULT, G., CARIGNAN, J., TRUDEL, P. and GRASSO, F. (1977) Chemostratigraphic divisions within the Abitibi volcanic belt, Rouyn-Noranda, Quebec; In: Volcanic Regimes in Canada, eds. Baragar, W.R.A., Coleman, L.C. and Hall: Geological Association of Canada, Special Publication no. 16, pp. 265-295.

GÉLINAS, P., TRUDEL, P. and HUBERT, C. (1984) Chemostratigraphic division of the Blake River Group, Rouyn-Noranda area, Abitibi, Quebec: Canadian Journal of Earth Sciences, v. 21, pp. 220-231.

GÉLINAS, L. and LUDDEN, J.N. (1984) Rhyolitic volcanism and the geochemical evolution of an Archaean central ring complex: the Blake River Group volcanics of the southern Abitibi belt, Superior province: Physics of the Earth and Planetary Interiors, v. 35, pp. 77-88.

GILBERT, M. (1985) Géologie de la Propriété Mobrun: Rapport de compliation de Corporation Falconbridge Copper, Rouyn-Noranda, Québec, 42 p.

GILLIGAN, L.B. and MARSHALL, B. (1987) Textural evidence for remobilization in metamorphic environments: Ore Geology Reviews, v. 2, pp. 205-229.

GOODWIN, A.M. and RIDLER, R.H. (1970) The Abitibi orogenic belt. In: Symposium on Basins and Geosynclines of the Canadian Shield, ed. A.J. Baer, Geological Survey of Canada, Paper 70-40, pp. 1-31.

GOODWIN, A.M. (1977) Archean volcanism in Superior Province, Canadian Shield Volcanic Regimes in Canada, eds: W.R., Baragar, L.C., Coleman and J.H. Hall. Geological Association of Canada, Special Paper 16, pp. 265-295.

GRAF, J.L. and SKINNER, B.J. (1970) Strengh and deformation of pyrite and pyrrhotite: Economic Geology, v. 65, pp. 206-215.

GRAY, D.R. (1978) Differentiation associated with discrete crenulation cleavages: Lithos, v. 10, pp. 89-101.

GRENNE, T. and VOKES, F.M. (1990) Sea-floor sulfides at the Hoydal volcanogenic deposit, Central Norwegian Caledonides: Economic Geology, v. 85, pp. 344-359.

GUIDOTTI, C.V. (1973) Compositional variation of muscovite as a function of metamorphic grade and assemblage in metapelites from N.W. Maine: Contributions to Mineralogy and Petrology, v. 42, pp. 33-42.

GUIDOTTI, C.V. (1984) Mica in metamorphic rocks. In: Mica, Reviews in Mineralogy v. 13, ed: S.W. Bailey. Mineralogical Society of America, 584 p.

GUIDOTTI, C.V. and SASSI, F.P. (1976) Muscovite as a petrogenetic indicator mineral in pelitic schists: Neues Jahrbuch Für Mineralogie, Abhandlungen. v. 127, pp. 97-142.

GUIDOTTI, C.V. and SASSI, F.P. (1986) Classification and correlation of metamorphic facies series by means of muscovite b_0 data from low-grade metapelites: Neues Jahrbuch Für Mineralogie, Abhandlungen. v. 153, pp. 363-370.

GUIDOTTI, C.V., SASSI, F.P. and BLENCOE, J.G. (1989) Compositional controls on the a and b cell dimensions of $2M_1$ muscovite: European Journal of Mineralogy, v. 71, pp.71-84.

GUIDOTTI, C.V., MAZZOLI, C., SASSI, F.P. and BLENCOE, J.G. (1992) Compositional controls on the cell dimensions of $2M_1$ muscovite and paragonite:

European Journal of Mineralogy, v. 4, pp. 283-297.

GUHA, J. and KOO, J. (1975) Role of fluid state mobilization during metamorphism of the Henderson ore bodies, Chibougamau, Quebec, Canada: Canadian Journal of Earth Sciences, v. 12, pp. 1516-1523.

HAWLEY, J.E. (1959) Contributed discussion to symposium on the genesis of massive sulphide deposits: Canadian Institute of Mining and Metallurgy, Transcripts, v. 62, 354 p.

HEY, M.H. (1954) A new review of the chlorites: Mineralogical Magazine, v. 30, pp. 277-292.

HONNOREZ, J., HONNOREZ-GUERSTEIN, B., VALETTE, J. and WAUSCHKUHN, A. (1973) Present day formation of an exhalative sulfide deposit at Vulcano (Tyrrhenian Sea), Part II: Active crystallization of Fumarolic sulfides in volcanic sediments of the Baia di Levante. In: Ores in Sediments. Eds. G.C. Amstutz and A.J. Bernard, Springer-Verlag, New York, 350 p.

HOY, L.D. (1993) Regional evolution of hydrothermal fluids in the Noranda district, Quebec: Evidence from $\delta^{18}O$ values from volcanogenic massive sulphide

deposits: Economic Geology, v. 88, pp. 1526-1541.

HULL, D. (1965) An Introduction to Dislocations. Pergamon Press, London, 271 p.

HUBERT, C., TRUDEL, P. and GÉLINAS, L. (1984) Archean wrench fault tectonics and structural evolution of the Blake River Group, Abitibi Belt, Québec: Canadian Journal of Earth Sciences, v. 21, pp. 1024-1032.

HUMPHREYS, H.C. (1986) Metamorphic imprints upon sulphide mineralisation at Boksputs, Northern Caps, South Africa. Mineralium Deposita, v. 21, pp. 271-277.

HUTCHISON, M.N. and SCOOT, S.D. (1981) Sphalerite geobarometry in the Cu-Fe-Zn-S system: Economic Geology, v. 76, pp. 143-153.

JOLLY, W.T. (1978) Metamorphic history of the Abitibi belt. In: Metamorphism in the Canadian Shield. Geological Survey of Canada. Paper 78-10, pp. 63-78.

KERRICH, R., FYFE, W.S., GORMAN, B.E., and ALISON, I. (1977) Local modification of rock chemistry by deformation: Contribution to Mineralogy and

Petrology. v. 65, pp. 183-190.

KNIPE R.J. (1979) Chemical changes during slaty cleavage development: Bulletin of Mineralogy, v. 102, pp. 206-209.

KRANIDIOTIS, P. and MACLEAN, W.H. (1987) Systematics of chlorite alteration at the Phelps Dodge massive sulphide deposits, Matagami, Québec: Economic Geology, v. 89, pp. 1898-1911.

LABELLE, P. (1985) Etude minéragraphique du gisement Mobrun. Collège de l'Abitibi-Temiscaminque, Département de Technologie Minerale, Rouyn-Noranda, 34 p.

LAJOIE, J. and LUDDEN, J. (1985) Petrology of the Archean Pontiac and Kewagama sediments and implications for the stratigraphy of the southern Abitibi belt: Canadian Journal of Earth Sciences, v. 22, pp. 1377-1379.

LARGE, R.R., (1977) Chemical evolution and zonation of massive sulphide deposits in volcanic terrains: Economic Geology, v.72, pp. 549-572.

LAROCQUE A.C.L. and HODGSON, C.J. (1993) Gold distribution in the

Mobrun volcanogenic-associated massive sulfide deposit, Noranda, Quebec: A preliminary evolution of the role of metamorphic remobilization: Economic Geology, v. 88, (in print).

LAROCQUE A.C.L., HODGSON, C.J. and LAFLEUR, P. (1993) Carbonate-rich footwall alteration at the Mobrun mine, a possible Mattabi-type VMS deposit in the Noranda camp: Exploration and Mining Geology, v. 2, pp. 165-169.

LESHER, C.M., GOODWIN, A.M., CAMPBELL, I.H. and GORDON, M.P. (1986) Trace-element geochemistry of ore-associated and barren, felsic metavolcanic rocks in the Superior Province, Canada: Canadian Journal of Earth Sciences. v. 23, pp. 222-237.

LIAGHAT, S. (1990) Use of immobile elements to determine mass changes and origin of hydrothermally altered rocks: Key Tuffite, Matagami, and New Insco mines, Noranda: M.Sc. thesis, McGill University, Montreal, 112 p.

LIAGHAT, S. and MACLEAN, W.H. (1992) The Key Tuffite, Matagami mining district: Origin of the tuff components and mass changes: Exploration Mining and Geology, v. 1, pp. 197-207.

LIAGHAT, S., BROWN, A.C. and HUBERT, C. (1992) Microstructural chemical changes during metamorphism of the Mobrun massive sulphide deposit, Noranda district, Quebec: Geological Association of Canada - Mineralogical Association of Canada, Program with Abstracts, v. 17, p. A66

LIAGHAT, S., BROWN, A.C. and HUBERT, C. (1993) Deformation imprints upon sulphide mineral assemblages at the Mobrun massive sulphide deposit, Noranda district, Quebec: Geological Association of Canada - Mineralogical Association of Canada, Program with Abstracts, v. 18, p. A59.

LIAGHAT, S., BROWN, A.C. and HUBERT, C. (1994) The effect of metamorphism-deformation event in modification of chemical characteristics of massive sulphide deposits: Mobrun mine, Noranda district, Quebec: Geological Association of Canada - Mineralogical Association of Canada, Program with Abstracts, (in print).

LIANXING, G. and McCLAY, K.R. (1992) Pyrite deformation in stratiform lead-zinc deposits of the Canadian Cordillera: Mineralium Deposita. v. 27, pp. 169-181.

LUDDEN, J. and HUBERT, C. (1986) A model for the geological evolution of the late Archean Abitibi greenstone belt of Canada: Geology, v. 14, pp. 707-711.

LUDDEN, J., HUBERT, C. and GARIÉPY, C. (1986) The tectonic evolution of the Abitibi greenstone belt of Canada: Geological Magazine, v. 123, pp. 153-166.

MACGEEHAN, P.J. and MACLEAN, W.H. (1980a) Tholeiitic basalt-rhyolite magmatism and massive sulfide deposits at Matagami, Quebec: Nature, v. 383, pp. 153-157.

MACGEEHAN, P.J. and MACLEAN, W.H. (1980b) An Archean sub-seafloor geothermal system, 'calc-alkali' trends, and massive sulfide genesis: Nature, v. 286, pp. 767-771.

MACLEAN, W.H. (1990) Mass change calculations in altered rock series. Mineralium Deposita, v. 25, pp.44-49.

MACLEAN, W.H. (1988) Rare earth element mobility at constant inter-REE ratios in the alteration zone at the Phelps Dodge massive sulphide deposits, Matagami, Quebec: Mineralium Deposita, v. 23, pp. 231-238.

MACLEAN, W.H., and KRANIDIOTIS, P. (1987) Immobile elements as monitors of mass transfer in hydrothermal alteration: Phelps Dodge massive sulphide deposit, Matagami, Québec: Economic Geology, v. 82, pp. 951-962.

MACLEAN, W.H. and HOY, L.D. (1991) Geochemistry of hydrothermally altered rocks at the Horne mine, Noranda, Quebec: Economic Geology, v. 86, pp. 506-528.

MACLEAN, W.H. and BARRETT, T.J. (1993) Lithogeochemical techniques using immobile elements: Journal of Geochemical Exploration, v. 48, pp. 109-133.

MACROBBIE, P.A. and WATHINSON D.H. (1986) Stratigraphy, hydrothermal alteration and structure of the Mobrun massive sulphide deposit, Rouyn-Noranda. B.Sc. thesis, Carleton University, Ottawa, 46 p.

MARQUIS, P. (1990) Metallogénie des gisements archéens d'Au-Ag-Cu de la mine Donald J. LaRonde (Dumagami), Cadillac, Abitibi, Québec. Ph.D. thesis Département de Géologie, Université de Montréal, 140 p.

MARQUIS, P., BROWN, A.C., HUBERT, C. and RIGG, D.M. (1990) Progressive alteration associated with the auriferous massive sulfide bodies at the Dumagami mine, Abitibi Greenstone Belt, Quebec: Economic Geology, v. 85. pp. 746-764.

MARQUIS, P., HUBERT, C., BROWN, A.C. and RIGG, D.M. (1990) Overprinting of early, redistributed Fe and Pb-Zn mineralization by late-stage Au-Ag-Cu deposition at the Dumagami mine, Bousquet district, Abitibi, Quebec:

Canadian Journal of Earth Sciences, v. 27, pp. 1651-1671.

MARSHALL, B. and GILLIGAN, L.B. (1993) Remobilization, syn-tectonic processes and massive sulphide deposits: Ore Geology Reviews, v. 8, pp. 39-64.

MARTIN, H. (1986) Effects of steeper Archean geothermal gradients on geochemistry of subduction zone magmas: Geology, v. 14, pp. 753-756.

MATSUHISA, Y., GOLDSMITH, J.A.S. and CLAYTON, R.N. (1979) Oxygen isotope fractionation in the system quartz-albite-anorthite-water: Geochimica et Cosmochimica Acta, v. 43, pp. 1131-1140.

McCAIG, A.M. and KNIPE R.J. (1990) Mass transport mechanisms in deforming rocks: Recognition using microstructural and microchemical criteria: Geology, v. 18, pp. 824-827.

McCONNELL, J.W. (1976) Geochemical dispersion in wallrocks of Archean massive sulphide deposits. M.Sc. thesis, Queen's University, Kingstone, 46 p.

McCLAY, K.R. (1991) Deformation of stratiform Zn-Pb (-barite) deposits in the northern Canadian Cordillera: Ore Geology Reviews. v. 6, 435-462.

McCLAY, K.R. (1983) Facies of deformed sulphides: Geologische Rundschau, v. 72, pp. 469-491.

McCLAY, K.R. (1984) Structure of clastic hosted lead-zinc deposits, case histories: Geological Association of Canada, Short Course notes, no. 2, part II, 150 p.

McCLAY, K.R. (1982) Fabric in deformed ores. In: Atlas of Deformational and Metamorphic Rock Fabrics. Eds. G.I., Borradaile; M.B. Bayly; C. MC A. Powell. Springer-Verlag, New York, 551.

McCLAY, K.R. and ELLIS, P.G. (1984) Deformation of pyrite: Economic Geology, v. 79, pp. 400-403.

McCLAY, K.R. and ELLIS, P.G. (1983) Deformation and recrystallization of pyrite: Mineralogical Magazine. v. 47, pp. 527-5.

McDONALD, J.A. (1970) Some effects of deformation on sulphide rich layers in lead-zinc ore bodies, Mount Isa, Queensland: Economic Geology, v. 65, p. 273-298.

MOOKHERJEE, A. (1976) Ore and metamorphism: temporal and genetic relationships. In: Handbook of Strata-bound and Stratiform Ore Deposits. I.

Principles and General Studies. ed. K.H. Wolf, v.: Tectonic and Metamorphism. pp. 203-227.

MORTENSEN, J.K. (1987) Preliminary U-Pb zircon ages for volcanic and plutonic rocks of the Noranda-Lac Abitibi area, Abitibi Subprovince, Québec: Geological Survey of Canada, Part A, Paper 87-1A, pp. 581-590.

MORTON, R.L. and FRANKLIN, J.M. (1987) Two-fold classification of Archean volcanic-associated massive sulphide deposits: Economic Geology, v. 82, pp. 1057-1063.

MOTTL, M.J. (1983) Metabasalts, axial hot springs, and the structure of hydrothermal systems at mid-ocean ridges: Geological Society of America Bulletin, v. 94, pp. 161-180.

O'DOWD, P. (1984) Evaluation de la propriété Mobrun, canton de Dufresnoy, rapport interne de Corporation Falconbridge Copper, Rouyn-Noranda, Québec, 16 p.

O'DOWD, P. (1985) Environement géologique du gisement Mobrun, rapport

préliminaire de Corporation Falconbridge Copper, Rouyn-Noranda, Québec, 19 p.

OFTEDAHL, C. (1958) On exhalative-sedimentary ores. Geol. Foren. Stockholm Forh., v. 80, pp. 1-19.

O'NEIL, J.R. and TAYLOR, H.P., Jr. (1969) Oxygen isotope equilibrium between muscovite and water: Journal of Geophysical Research, v. 74, pp. 6012-6022.

PANDAN, A., KISCH, H.J. and SHAGAM, R. (1982) Use of the lattice parameter b_0 of dioctahedral illite/muscovite for the characterization of P/T gradients of incipient metamorphism: Contributions to Mineralogy and Petrology, v. 79, pp. 85-95.

PEARCE, J.A. and CANN, (1973) Tectonic setting of basic volcanic rocks determined using trace element analyses: Earth and Planetary Sciences Letters, v. 19, pp. 290-300.

PEDERSON, F.D., (1980) Remobilization of the massive sulphide ore of the Black Angel Mine, Central West Greenland: Economic Geology, v. 75, pp. 1022-1041.

PESQUERA, A. and VELASCO (1993) Ore metamorphism in sulfide mineralizations from the Cinco Villas Massif (western Pyrenees, Spain): Economic Geology, v. 88, pp. 266-282.

PETER, J.M. and SCOTT, S.D. (1988) Mineralogy, composition and fluid-inclusion microthermometry of seafloor hydrothermal deposits in the Southern trough of Guaymas basin, Gulf of California, Canadian Mineralogist, v.26, pp. 567-587.

POTTER, II, R.W. and CLYNNE, M.A. (1978) Solubility of highly soluble salts in aqueous media-part 1, NaCl, $CaCl_2$, $NaSO_4$ and K_2SO_4 solubilities to 100°. U.S. Geological Survey, Journal of Research, v. 6, pp. 701-705.

POWELL, W.G., CARMICHAEL, D.M. and HODGSON, C.J. (1993) Thermobarometry in a subgreenschist to greenschist transition in metabasites of the Abitibi greenstone belt, Superior Province, Canada: Journal of Metamorphic Geology, v. 11, pp. 165-178.

POWELL, W.G., HODGSON, C.J., and CARMICHAEL, D.M. (1993) Low-temperature metamorphism and its relationship to the Larder Lake-Cadillac break, Matachewan area, Abitibi belt, Ontario: Canadian Journal of metamorphism Geology, v. 11, pp. 165-178.

RAMSAY, J.G. (1980) The crack-seal mechanism of rock deformation: Nature, v. 284, pp. 135-139.

RIEDER, M., GUDIOTTI, C.V., SASSI, F.P. and WEISS, Z. (1992) Muscovite: d_{060} versus $d_{331,060}$ spacing: its use for geobarometric purposes: European Journal of Mineralogy, v. 4, pp. 843-845.

RIOPEL, J., HUBERT, C., CATTALANI, S. and BARRETT, T.J. (1991) Géologie, structure et géochimie du gisement de sulfures massifs de Mobrun, Noranda, Québec. Ministère de l'Énergie et des Ressources, Projet 82-43G, 150 p.

RIOPEL, J. (1992) Gîtologie et structure du gisement de sulfures massifs de Mobrun, Noranda, Québec. M.Sc thesis, Université de Montréal, 156 p.

RITTER, U. (1981) The baric conditions of mid-and late Proterozoic metamorphic terrains in the lower Orange River region, South Africa: Neues Jahrbuch Für Mineralogie, Monatshefte. v. 3, pp. 133-144.

RIVERIN, G. and HODGSON, C.J. (1980) Wallrock alteration at the Millenbach Cu-Zn mine, Noranda, Québec: Economic Geology, v. 75, pp. 424-444.

ROEDDER, E. (1984) Fluid Inclusions: Mineralogical Society of America, Reviews in Mineralogy, v. 12, 644 p.

RUIZ, J.L., APARICOI, A. and CACHO, L.G. (1980) Chemical variations of muscovites from the Sierra de Guadarrama metamorphic area, Sistema Central, Spain: Geologische Rundschau, Bd, v. 69, pp. 94-106.

RUTTER, E.H. (1983) Pressure solution in nature, theory and experiment: Journal of Geological Society of London, v. 140, pp. 725-740.

SANGSTER, D.F. (1979) Evidence of an exhalative origin for deposits of the Cobar district, New South Wales: BRM Journal of Australian Geology & Geophysics, v. 4, pp. 15-24.

SANGSTER, D.F. (1972) Precambrian volcanogenic massive sulphide deposits in Canada: a review. Geological Survey of Canada, Paper 72-22, pp. 1-44.

SASSI, F.P. (1972) The petrologic and geologic significance of b_0 value of potassium white micas in low-grade metamorphic rocks. An application to the Eastern Alps: Teschermarks Mineralogische und Petrographische Mitteilungen. v. 18, pp.105-113.

SASSI, F.P. and SCOLARI, A. (1974) The b_0 value of the potassic white micas as a barometric indicator in low-grade metamorphism of pelitic schists: Contributions to Mineralogy and Petrology, v. 45, pp. 143-152.

SASSI, F.P., KRAUTNER, H.G. and ZIRPOLI, G. (1976) Recognition of the pressure character in greenschist facies metamorphism: Schweizerische Mineralogische und Petrographische Mitteilungen. v.56, pp. 427-434.

SCHWERDTNER, W.M. (1982) Calculation of volume change in ductile band structures: Journal of Structural Geology, v. 4, pp. 57-62.

SCOTT, S.D. and BARNES, H.L. (1971) Sphalerite geothermometry and geobarometry: Economic Geology, v. 66, pp. 653-669.

SHRIVER, N.A. and MACLEAN, W.H. (1993) Mass, volume and chemical changes in the alteration zone at the Norbec mine, Noranda, Quebec: Mineralium Deposita, v. 28, pp. 157-166.

SPARY, A. (1969) Metamorphic Textures. Pergamon Press, London, 352 p.

SPENCE, C.D. (1967) The Noranda area. Canadian Institute of Mining and Metallurgy, Centennial Field Excursion, Northwestern Quebec-Northern Ontario, pp. 36-39.

SPENCE, C.D. and de ROSEN-SPENCE, A.F. (1975) The place of sulphide mineralization in the volcanic sequence at Noranda, Quebec: Economic Geology, v. 70, pp. 90-101.

STEPHENS, M.B., GLASSON, M.J. and KEAYS, R.R. (1979) Structural and chemical aspects of the metamorphic layering development in metasediments from Clunes, Australia: American Journal of Science, v. 279, pp. 129-160.

STONE, W.E. (1988) Nature and significance of metamorphism in gold concentration. Bousquet township, Abitibi greenstone belt, northwest Quebec. Ph.D. thesis, University of Western Ontario, London, 441 p.

TASSÉ, N., LAJOIE, J. and DIMROTH, E. (1978) The anatomy and interpretation of an Archean volcaniclastic sequence, Noranda region, Quebec: Canadian Journal of Earth Sciences, v. 15, pp. 874-888.

TOURIGNY, G., HUBERT, C., BROWN, A.C. and CREPEAU, R. (1988) Structural geology of the Blake River Group at the Bousquet mine, Abitibi, Quebec: Canadian Journal of Earth Sciences, v. 25, pp. 581-592.

TRUDEL, P. (1979) Le volcanisme archéen et la géologie structurale de la region de Clericy, Abitibi, Québec. Ph.D. thesis, Ecole Polytechnique, Montreal, 307 p.

UJIKE, O. and GOODWIN, A.M. (1987) Geochemistry and origin of Archean felsic metavolcanic rocks central Noranda area, Quebec, Canada: Canadian Journal of Earth Sciences, v. 24, pp. 2551-2567.

VAILLANT, R.I. and HUTCHINSON, R.W. (1982) Stratigraphic distribution and genesis of gold deposits, Bousquet region, north-western Quebec. In: Geology of Canadian Gold Deposits. Eds. R.W. Hodder and W. Petruk: Canadian Institute of Mining and Metallurgy, Special Volume 24, pp. 27-40.

VOKES, F.M. (1969) A review of the metamorphism of sulphide deposits: Earth-Science Reviews, v. 5, pp. 99-143.

VOKES, F.M. (1971) Some aspects of the regional metamorphic mobilization of preexisting sulphide deposits: Mineralium Deposita, v. 6, pp. 122-129.

VOKES, F.M. and CRAIG, J.R. (1993) Post-recrystallization mobilization phenomena in metamorphosed stratabound sulphide ores: Mineralogical Magazine, v. 57, pp. 19-28.

VOKES, R.D., HANSON, G.N. and GRENENFELDER, M. (1987) Rear earth element mobility in the Roffna gneiss, Switzerland: Contribution to Mineralogy and Petrology, v. 95, pp. 145-154.

WALDRON, H.M. and SANDIFORD, M. (1988) Deformation volume and cleavage development in metasedimentary rocks from the Ballarat state belt: Journal of Structural Geology, v. 10, pp. 53-62.

WALKER, A.L. and BUCHANAN, A.S. (1969) Geochemical processes in ore formation, Part. I. The production of hydrothermal fluids from sedimentary sequences: Economic Geology, v. 64, pp. 919-922.

WAYNE, D.M. and SINHA, A.K. (1988) Physical and chemical response of zircons to deformation: Contribution to Mineralogy and Petrology, v. 98, pp. 109-121.

WERRE, Jr., R.W., BODNAR, BETHKE, P.M. and BARTON, P.B. (1979) A novel gas-flow fluid inclusion heating/freezing stage (abstract): Geological Society of America. Programs, v. 11, 539 p.

WENK, H.R. (1985) Preferred Orientation in Deformed Metals and Rocks: An introduction to Modern Texture Analysis. Academic Press, Inc. 610 p.

WESTMAN, S. and MAGNELI, A. (1957) Determination of accurate interplanar spacings and lattice parameters from Guinier powder photographs: Acta Chemica Scandinavica, v. 11, pp. 1587-1593.

WILLIAMS, P.F. (1972) 'Pressure shadow' structures in foliated rocks from Bermagui, New South Wales: Journal of Geological Society of Australia, v. 18, pp. 371-377.

WILLIAMS, P.F. (1972b) Development of metamorphic layering and cleavage in low-grade metamorphic rocks at Bermagui, Australia: American Journal of Science, v. 272, pp. 1-74.

WILSON, M.P. (1972) On syntectonic porphyroblast growth: Tectonophysics, v. 11, pp. 239-260.

WINCHESTER, J.A. and MAX, M.D. (1984) Element mobility associated with syn-metamorphic shear zones near Scatchport, N.W. Mayo, Ireland: Journal of Metamorphic Geology, v. 2, pp.1-11.

YAMADA, S., NANJO, J., NOMURA, S. and HARA, S. (1979) Morphology of iron pyrite crystals: Journal of Crystal Growth, v. 46, pp. 10-14.

APPENDICES

Appendix 3.1a Microprobe analyses of sericite (cation%) from Mobrun deposit

Location	No.	Sample	Positio	Si	Ti	Aliv	Alvi	Fe	Mn	Mg	Ca	Na	K	Ba	Total
DDH	88-14	332BM12	P-S	7.02	0.01	0.98	3.33	0.22	0.00	0.35	0.01	0.05	1.71	0.01	13.70
DDH	88-14	332BM16	P-S	6.34	0.01	1.67	3.64	0.11	0.00	0.25	0.00	0.07	1.88	0.01	13.98
DDH	85-34	489M1	P-S	6.33	0.03	1.67	3.57	0.26	0.00	0.17	0.00	0.06	1.94		14.02
DDH	88-34	489M3	P-S	6.41	0.03	1.59	3.40	0.36	0.00	0.27	0.01	0.05	1.95		14.06
DDH	85-24	315M11	P-S	6.38	0.04	1.62	3.57	0.23	0.01	0.14	0.01	0.06	1.94	0.01	13.99
DDH	86-4	467M2	P-S	6.45	0.03	1.55	3.33	0.47	0.01	0.03	0.00	0.05	1.97	0.01	13.90
DDH	86-4	467M11	P-S	6.27	0.03	1.73	3.60	0.23	0.00	0.15	0.00	0.09	1.93	0.00	14.04
DDH	85-15	244M1	D-S	6.01	0.00	2.00	3.78	0.32	0.00	0.06	0.00	0.82	1.06		14.05
DDH	85-15	244M4	D-S	6.19	0.01	1.81	3.84	0.11	0.00	0.04	0.00	0.23	1.70		13.94
DDH	85-15	244M5	D-S	6.22	0.01	1.78	3.87	0.10	0.00	0.00	0.00	0.37	1.53		13.89
DDH	85-15	244M7	D-S	6.16	0.01	1.84	3.89	0.08	0.00	0.03	0.01	0.38	1.51		13.91
DDH	85-15	244M9	D-S	6.04	0.01	1.96	3.92	0.09	0.00	0.05	0.01	0.34	1.55		13.96
DDH	85-15	244M10	D-S	6.03	0.01	1.97	3.97	0.11	0.00	0.06	0.00	0.26	1.54		13.94
DDH	85-15	244M12	D-S	6.18	0.02	1.82	3.90	0.08	0.00	0.01	0.00	0.49	1.40		13.89
DDH	85-13	216M2	D-S	6.17	0.00	1.83	3.87	0.07	0.00	0.07	0.00	0.19	1.76	0.00	13.96
DDH	85-13	216M5	D-S	6.12	0.01	1.88	3.84	0.08	0.01	0.09	0.02	0.33	1.61	0.00	13.98
DDH	85-13	216M11	D-S	6.18	0.01	1.83	3.88	0.05	0.01	0.06	0.00	0.28	1.62	0.01	13.92
DDH	85-13	216M12	D-S	6.19	0.01	1.81	3.86	0.06	0.01	0.06	0.00	0.21	1.71	0.01	13.93
DDH	85-13	216M13	D-S	6.28	0.00	1.72	3.81	0.06	0.01	0.09	0.01	0.19	1.74	0.02	13.92
DDH	85-13	216M15	D-S	6.13	0.01	1.87	3.88	0.08	0.00	0.08	0.00	0.24	1.64	0.00	13.92
DDH	85-11	146M1	P-S	6.32	0.02	1.68	3.55	0.22	0.00	0.24	0.00	0.08	1.93	0.01	14.05
DDH	85-11	146M2	P-S	6.39	0.01	1.61	3.53	0.27	0.00	0.19	0.00	0.11	1.84	0.05	14.00
DDH	85-11	146M3	P-S	6.17	0.01	1.83	3.68	0.21	0.00	0.16	0.00	0.10	1.86	0.05	14.05
DDH	85-11	146M5	P-S	6.27	0.00	1.73	3.61	0.26	0.01	0.14	0.02	0.09	1.87	0.05	14.04
DDH	85-11	146M6	D-S	6.15	0.01	1.85	3.79	0.14	0.00	0.10	0.00	0.12	1.81	0.02	13.99
DDH	85-11	146M8	P-S	6.33	0.01	1.68	3.58	0.24	0.00	0.20	0.00	0.08	1.88	0.03	14.02
DDH	85-11	146M9	D-S	6.24	0.03	1.76	3.64	0.20	0.00	0.13	0.00	0.10	1.93	0.02	14.04
DDH	85-11	146M11	P-S	6.27	0.01	1.73	3.62	0.05	0.00	0.17	0.00	0.08	1.83	0.05	13.82
DDH	85-11	146M12	P-S	6.19	0.01	1.81	3.70	0.18	0.00	0.13	0.00	0.12	1.87	0.03	14.04
DDH	85-18	265AM9	P-S	6.19	0.01	1.81	3.76	0.18	0.02	0.25	0.03	0.15	1.37		13.75
L-2	8-2-338	338M1	D-S	6.10	0.06	1.90	3.87	0.05	0.00	0.04	0.01	0.86	0.99	0.00	13.88
L-2	8-2-338	338M2	D-S	6.10	0.04	1.90	3.92	0.06	0.01	0.02	0.00	0.91	0.87	0.00	13.84
L-2	8-2-338	338M6	P-S	6.61	0.01	1.39	3.82	0.04	0.00	0.01	0.00	0.60	1.14	0.00	13.62
L-2	8-2-338	338M7	D-S	5.98	0.26	2.02	3.67	0.05	0.00	0.01	0.00	0.90	0.92	0.01	13.82
L-2	8-2-338	338M8	D-S	6.04	0.37	1.96	3.50	0.04	0.00	0.04	0.00	0.69	1.06	0.03	13.73
L-2	8-2-338	338M11	D-S	6.37	0.01	1.63	3.88	0.09	0.01	0.03	0.00	0.56	1.14	0.01	13.72
L-2	8-2-338	338M12	D-S	6.29	0.13	1.71	3.76	0.05	0.00	0.02	0.01	0.76	0.98	0.01	13.71
L-2	8-2-338	338M13	P-S	6.83	0.00	1.18	3.80	0.06	0.00	0.01	0.00	0.56	1.05	0.01	13.49
L-2	8-2-338	338M20	D-S	6.73	0.02	1.27	4.47	0.02	0.00	0.04	0.00	0.98	0.82	0.00	14.34
L-2	7-2-194	194M1	D-S	6.15	0.02	1.85	3.79	0.05	0.00	0.15	0.02	0.19	1.75	0.00	13.98
L-2	7-2-194	194M3	D-S	6.20	0.02	1.80	3.79	0.03	0.00	0.17	0.01	0.16	1.76	0.00	13.93
L-2	7-2-194	194M3A	D-S	6.19	0.01	1.81	3.76	0.05	0.00	0.22	0.00	0.20	1.75	0.01	13.99
L-2	7-2-194	194M4	D-S	6.26	0.01	1.74	3.72	0.07	0.00	0.22	0.01	0.29	1.67	0.01	13.99
L-2	7-2-194	194M5	D-S	6.23	0.01	1.77	3.79	0.03	0.01	0.14	0.01	0.19	1.71	0.01	13.90
L-2	7-2-194	194M7	D-S	6.23	0.02	1.77	3.76	0.05	0.00	0.17	0.01	0.25	1.69	0.02	13.96
L-2	7-2-194	194M8	D-S	6.17	0.07	1.83	3.72	0.06	0.00	0.18	0.00	0.19	1.72	0.01	13.94
L-2	7-2-194	194M10	D-S	6.23	0.00	1.77	3.78	0.07	0.00	0.16	0.02	0.17	1.71	0.02	13.94
L-2	7-2-194	194M11	D-S	6.21	0.01	1.79	3.78	0.04	0.01	0.17	0.02	0.19	1.77	0.02	13.98
L-2	7-2-194	194M14	D-S	6.15	0.01	1.85	3.79	0.03	0.01	0.15	0.02	0.20	1.75	0.01	13.97
L-2	7-2-194	194M15	D-S	6.20	0.01	1.80	3.80	0.06	0.00	0.14	0.01	0.19	1.76	0.02	13.97

L-2	7-2-194	194M16	D-S	6.17	0.02	1.83	3.75	0.07	0.00	0.17	0.01	0.20	1.75	0.01	13.99
L-2	7-2-194	194M17	D-S	6.25	0.01	1.75	3.76	0.04	0.00	0.19	0.01	0.20	1.74	0.02	13.95
L-2	7-2-194	194M18	D-S	6.20	0.01	1.80	3.78	0.05	0.00	0.15	0.02	0.20	1.76	0.02	13.99
L-2	7-2-194	194M19	P-S	6.66	0.01	1.34	3.71	0.04	0.00	0.15	0.10	0.15	1.61	0.01	13.78
L-2	7-2-194	194M20	P-S	6.50	0.01	1.50	3.75	0.04	0.01	0.14	0.00	0.19	1.60	0.01	13.75
L-2	7-2-194	194M26	D-S	6.15	0.02	1.85	3.74	0.08	0.00	0.22	0.01	0.19	1.72	0.00	13.99
L-2	7-2-194	194M27	D-S	6.18	0.01	1.82	3.77	0.06	0.00	0.16	0.02	0.18	1.75	0.02	13.98
L-2	8-2-73B	73M2	D-S	6.29	0.00	1.71	3.68	0.09	0.00	0.26	0.01	0.14	1.80	0.01	13.99
L-2	8-2-73B	73M3	D-S	6.36	0.01	1.64	3.65	0.08	0.01	0.28	0.00	0.10	1.80	0.01	13.94
L-2	8-2-146	146AM1	P-S	6.18	0.00	1.82	3.91	0.03	0.00	0.10	0.01	0.83	0.98	0.01	13.86
L-2	8-2-146	146AM2	D-S	6.21	0.05	1.79	3.73	0.07	0.00	0.23	0.02	0.47	1.27	0.02	13.85
DDH	85-7	92M2	P-S	6.15	0.00	1.85	3.77	0.12	0.01	0.12	0.00	0.01	1.69	0.26	13.71
DDH	85-7	92M7	P-S	6.23	0.01	1.77	3.82	0.10	0.00	0.08	0.01	0.01	1.74	0.15	13.76
DDH	85-7	92M8	P-S	6.18	0.00	1.82	3.82	0.08	0.01	0.13	0.00	0.00	1.68	0.24	13.72
DDH	85-1	2M1	P-S	6.48	0.02	1.52	3.30	0.44	0.00	0.28	0.00	0.03	1.99	0.05	14.05
DDH	85-1	2M2	P-S	6.53	0.01	1.47	3.35	0.39	0.00	0.29	0.01	0.00	1.97	0.05	14.01
DDH	85-1	2M11	P-S	6.46	0.04	1.54	3.32	0.44	0.01	0.24	0.01	0.01	1.98	0.06	14.03
DDH	85-1	2M13	P-S	6.43	0.02	1.57	3.33	0.41	0.02	0.26	0.01	0.01	1.99	0.05	14.06
DDH	85-1	2M14	P-S	6.46	0.01	1.54	3.35	0.42	0.00	0.26	0.01	0.02	1.98	0.04	14.05
DDH	85-1	2M15	P-S	6.47	0.03	1.53	3.23	0.54	0.00	0.29	0.00	0.01	1.96	0.05	14.07
DDH	85-20	267AM1	P-S	6.35	0.03	1.65	3.36	0.49	0.01	0.20	0.02	0.01	1.94	0.06	14.05
DDH	85-7	91M1	P-S	6.38	0.02	1.62	3.62	0.24	0.00	0.13	0.01	0.00	1.89	0.04	13.91
DDH	85-7	91M2	P-S	6.19	0.00	1.81	3.84	0.11	0.00	0.04	0.02	0.00	1.62	0.33	13.63
DDH	85-7	91M3	D-S	6.19	0.02	1.81	3.83	0.09	0.01	0.05	0.00	0.00	1.79	0.18	13.78
DDH	85-7	91M5	D-S	6.51	0.00	1.49	3.73	0.11	0.02	0.07	0.01	0.01	1.72	0.16	13.66
DDH	85-27	20M1	D-S	6.29	0.01	1.71	3.72	0.10	0.00	0.21	0.02	0.01	1.79	0.07	13.85
DDH	85-27	20M3	D-S	6.31	0.02	1.69	3.65	0.11	0.01	0.21	0.01	0.01	1.94	0.07	13.94
DDH	85-27	20M9	D-S	6.42	0.01	1.58	3.70	0.11	0.00	0.17	0.01	0.00	1.80	0.07	13.79
DDH	85-27	20M11	P-S	6.38	0.03	1.63	3.56	0.20	0.00	0.23	0.00	0.00	1.92	0.03	13.94
DDH	85-27	20M13	P-S	6.61	0.03	1.39	3.48	0.21	0.00	0.26	0.00	0.00	1.86	0.02	13.84
DDH	85-27	20M14	D-S	6.36	0.04	1.64	3.67	0.10	0.00	0.16	0.01	0.00	1.87	0.08	13.84
DDH	85-3	51M2	P-S	6.22	0.02	1.78	3.31	0.56	0.01	0.40	0.01	0.01	1.69	0.12	14.00
DDH	85-3	51M3	P-S	6.39	0.01	1.61	3.48	0.21	0.02	0.32	0.02	0.02	1.92	0.05	13.99
DDH	85-3	51M5	P-S	6.51	0.02	1.49	3.37	0.28	0.00	0.36	0.01	0.01	1.94	0.04	13.99
DDH	85-3	51M8	P-S	6.57	0.02	1.43	3.32	0.30	0.00	0.38	0.01	0.01	1.99	0.02	14.03
DDH	85-3	51M10	P-S	6.53	0.01	1.47	3.41	0.23	0.00	0.38	0.02	0.00	1.93	0.02	13.97
DDH	85-3	51M13	P-S	6.33	0.03	1.67	3.55	0.23	0.00	0.22	0.03	0.00	1.85	0.10	13.91
DDH	85-18	265BM5	P-S	6.21	0.00	1.79	3.97	0.03	0.01	0.03	0.00	0.01	1.24	0.46	13.30
DDH	85-18	265BM6	D-S	6.19	0.02	1.81	3.74	0.09	0.00	0.15	0.00	0.05	1.71	0.20	13.77
DDH	85-18	265BM7	P-S	6.22	0.01	1.78	3.71	0.08	0.01	0.20	0.01	0.03	1.74	0.18	13.80
DDH	85-18	265BM12	D-S	6.46	0.01	1.54	3.73	0.05	0.00	0.12	0.00	0.02	1.39	0.55	13.32
DDH	85-20	267M1	P-S	6.35	0.03	1.65	3.65	0.12	0.01	0.18	0.00	0.01	1.94	0.01	13.94
DDH	85-20	267M2	P-S	6.33	0.05	1.68	3.55	0.21	0.00	0.18	0.01	0.02	1.96	0.04	13.98
DDH	85-20	267M3	P-S	6.28	0.06	1.72	3.55	0.21	0.00	0.15	0.02	0.03	2.00	0.01	14.02
DDH	85-20	267M4	P-S	6.24	0.02	1.76	3.63	0.17	0.01	0.23	0.02	0.04	1.76	0.09	13.88
DDH	85-20	267M5	P-S	6.33	0.05	1.67	3.56	0.22	0.00	0.17	0.01	0.00	1.99	0.01	13.99
DDH	85-20	267M6	P-S	6.27	0.02	1.73	3.60	0.20	0.00	0.19	0.01	0.01	1.98	0.05	14.01
DDH	85-20	267M7	P-S	6.35	0.06	1.65	3.53	0.25	0.00	0.17	0.01	0.00	1.94	0.04	13.96
DDH	85-20	267M8	P-S	6.30	0.03	1.70	3.62	0.22	0.00	0.18	0.01	0.01	1.81	0.04	13.89
DDH	85-20	267M9	P-S	6.30	0.05	1.70	3.61	0.17	0.00	0.17	0.01	0.00	1.97	0.01	13.98

DDH = diamond drill hole, L-2 = Level 2, P-S = precipitation site, D-S = dissolution site.

Appendix 3.1b Microprobe analyses of sericite (wt.%) from Mobrun deposit

Location	No.	Sample	Position	SiO2	TiO2	Al2O3	FeO	MnO	MgO	CaO	Na2O	K2O	BaO	Total
DDH	88-14	332BM12	P-S	53.76	0.06	28.00	2.03	0.00	1.82	0.05	0.21	10.28	0.20	96.41
DDH	88-14	332BM16	P-S	48.25	0.08	34.30	1.02	0.00	1.30	0.00	0.26	11.23	0.26	96.70
DDH	85-34	489M1	P-S	47.30	0.23	33.15	2.31	0.00	0.84	0.00	0.22	11.33		95.38
DDH	88-34	489M3	P-S	47.12	0.23	31.12	3.15	0.00	1.31	0.09	0.18	11.21		94.41
DDH	85-24	315M11	P-S	47.89	0.35	33.01	2.06	0.04	0.70	0.05	0.22	11.39	0.25	95.96
DDH	86-4	467M2	P-S	47.13	0.29	30.11	4.07	0.10	1.27	0.02	0.20	11.28	0.25	94.72
DDH	86-4	467M11	P-S	46.20	0.33	33.35	2.08	0.04	0.75	0.00	0.34	11.12	0.08	94.29
DDH	85-15	244M1	D-S	45.41	0.00	37.07	2.93	0.00	0.30	0.00	3.18	6.30		95.19
DDH	85-15	244M4	D-S	46.85	0.14	36.33	1.00	0.02	0.19	0.00	0.89	10.08		95.50
DDH	85-15	244M5	D-S	46.96	0.12	36.21	0.87	0.00	0.02	0.03	1.46	9.07		94.74
DDH	85-15	244M7	D-S	46.31	0.08	36.56	0.70	0.03	0.15	0.05	1.49	8.92		94.29
DDH	85-15	244M9	D-S	46.80	0.07	38.66	0.80	0.00	0.26	0.00	1.35	9.39		97.33
DDH	85-15	244M10	D-S	45.92	0.07	39.57	1.01	0.00	0.29	0.00	1.03	9.32		97.21
DDH	85-15	244M12	D-S	46.76	0.15	36.70	0.76	0.00	0.04	0.00	1.90	8.30		94.61
DDH	85-13	216M2	D-S	46.62	0.00	36.56	0.59	0.00	0.37	0.00	0.76	10.41	0.00	95.31
DDH	85-13	216M5	D-S	47.54	0.08	37.71	0.73	0.09	0.45	0.13	1.32	9.79	0.00	97.84
DDH	85-13	216M11	D-S	47.62	0.06	37.36	0.42	0.06	0.33	0.00	1.12	9.82	0.14	96.93
DDH	85-13	216M12	D-S	47.58	0.08	36.99	0.53	0.09	0.29	0.00	0.85	10.30	0.22	96.93
DDH	85-13	216M13	D-S	47.90	0.00	35.86	0.51	0.09	0.43	0.06	0.74	10.38	0.46	96.43
DDH	85-13	216M15	D-S	47.83	0.15	38.07	0.68	0.00	0.40	0.02	0.95	10.00	0.01	98.11
DDH	85-11	146M1	P-S	47.31	0.19	33.23	2.00	0.00	1.20	0.01	0.30	11.33	0.11	95.68
DDH	85-11	146M2	P-S	46.41	0.13	31.75	2.35	0.00	0.94	0.00	0.39	10.45	0.85	93.27
DDH	85-11	146M3	P-S	46.40	0.06	35.15	1.85	0.00	0.82	0.00	0.37	10.97	0.88	96.50
DDH	85-11	146M5	P-S	46.57	0.00	33.68	2.26	0.07	0.72	0.13	0.33	10.91	0.85	95.52
DDH	85-11	146M6	D-S	46.57	0.11	36.22	1.27	0.00	0.52	0.00	0.47	10.75	0.37	96.28
DDH	85-11	146M8	P-S	46.81	0.12	32.99	2.08	0.01	0.99	0.00	0.30	10.91	0.52	94.73
DDH	85-11	146M9	D-S	45.59	0.29	33.52	1.71	0.00	0.64	0.00	0.39	11.04	0.36	93.54
DDH	85-11	146M11	P-S	46.73	0.11	33.83	2.07	0.01	0.85	0.02	0.30	10.71	0.96	95.59
DDH	85-11	146M12	P-S	45.11	0.11	34.05	1.56	0.00	0.65	0.00	0.46	10.65	0.46	93.05
DDH	85-18	265AM9	P-S	44.98	0.08	34.30	1.59	0.16	1.22	0.17	0.54	7.77	0.35	91.16
L-2	8-2-338	338M1	D-S	46.60	0.56	37.34	0.48	0.00	0.19	0.05	3.38	5.94	0.08	94.62
L-2	8-2-338	338M2	D-S	45.74	0.40	37.00	0.50	0.06	0.11	0.03	3.52	5.13	0.06	92.55
L-2	8-2-338	338M6	P-S	50.25	0.09	33.59	0.40	0.00	0.07	0.19	2.33	6.77	0.00	93.69
L-2	8-2-338	338M7	D-S	45.99	2.65	37.14	0.49	0.00	0.06	0.00	3.55	5.55	0.18	95.61
L-2	8-2-338	338M8	D-S	45.50	3.72	34.89	0.38	0.01	0.20	0.02	2.67	6.26	0.50	94.15
L-2	8-2-338	338M11	D-S	47.02	0.08	34.53	0.78	0.05	0.15	0.02	2.14	6.62	0.03	91.42
L-2	8-2-338	338M12	D-S	47.95	1.35	35.31	0.41	0.00	0.12	0.06	2.98	5.85	0.10	94.13
L-2	8-2-338	338M13	P-S	52.83	0.00	32.68	0.57	0.00	0.07	0.00	2.23	6.36	0.17	94.91
L-2	8-2-338	338M20	D-S	48.81	0.19	38.28	0.19	0.00	0.24	0.00	3.97	5.03	0.00	96.71
L-2	7-2-194	194M1	D-S	45.61	0.22	35.48	0.46	0.03	0.73	0.17	0.73	10.17	0.07	93.67
L-2	7-2-194	194M3	D-S	46.44	0.15	35.53	0.46	0.00	0.85	0.04	0.60	10.35	0.07	94.49
L-2	7-2-194	194M3A	D-S	46.76	0.05	35.69	0.42	0.02	1.12	0.01	0.77	10.35	0.27	95.46
L-2	7-2-194	194M4	D-S	47.92	0.05	35.50	0.61	0.00	1.11	0.07	1.13	10.04	0.21	96.64
L-2	7-2-194	194M5	D-S	46.94	0.13	35.53	0.47	0.07	0.71	0.04	0.74	10.09	0.24	94.96
L-2	7-2-194	194M7	D-S	46.50	0.15	34.99	0.46	0.00	0.86	0.05	0.96	9.90	0.34	94.21
L-2	7-2-194	194M8	D-S	46.11	0.73	35.20	0.50	0.00	0.90	0.00	0.74	10.11	0.11	94.40
L-2	7-2-194	194M10	D-S	46.67	0.01	35.30	0.64	0.01	0.83	0.14	0.67	10.07	0.34	94.68
L-2	7-2-194	194M11	D-S	46.43	0.05	35.28	0.31	0.07	0.84	0.11	0.73	10.35	0.28	94.45
L-2	7-2-194	194M14	D-S	46.07	0.20	35.82	0.30	0.07	0.76	0.14	0.75	10.26	0.18	94.55
L-2	7-2-194	194M15	D-S	46.62	0.05	35.75	0.49	0.03	0.68	0.07	0.73	10.35	0.37	95.14

L-2	7-2-194	194M16	D-S	46.18	0.22	35.46	0.63	0.00	0.86	0.06	0.78	10.28	0.21	94.68
L-2	7-2-194	194M17	D-S	46.07	0.14	34.44	0.33	0.00	0.92	0.04	0.75	10.07	0.30	93.06
L-2	7-2-194	194M18	D-S	44.39	0.07	33.85	0.43	0.00	0.74	0.10	0.75	9.87	0.27	90.47
L-2	7-2-194	194M19	P-S	49.89	0.08	32.12	0.37	0.00	0.76	0.07	0.58	9.46	0.27	93.60
L-2	7-2-194	194M20	P-S	49.80	0.10	34.10	0.34	0.06	0.74	0.00	0.78	9.61	0.21	95.74
L-2	7-2-194	194M26	D-S	47.29	0.24	36.44	0.70	0.00	1.13	0.09	0.75	10.38	0.03	97.05
L-2	7-2-194	194M27	D-S	46.83	0.13	35.99	0.58	0.00	0.83	0.12	0.70	10.41	0.36	95.95
L-2	8-2-73B	73M2	D-S	48.99	0.00	35.61	0.83	0.00	1.35	0.06	0.55	11.01	0.16	98.56
L-2	8-2-73B	73M3	D-S	49.04	0.09	34.64	0.77	0.10	1.43	0.02	0.41	10.86	0.19	97.55
L-2	8-2-146	146AM1	P-S	44.00	0.00	34.60	0.21	0.00	0.49	0.08	3.05	5.44	0.15	88.02
L-2	8-2-146	146AM2	D-S	43.82	0.50	33.04	0.55	0.00	1.09	0.11	1.72	7.04	0.31	88.18
DDH	85-7	92M2	P-S	45.31	0.03	35.35	1.03	0.03	0.58	0.03	1.00	9.75	0.07	93.17
DDH	85-7	92M7	P-S	44.02	0.05	33.45	0.86	0.01	0.38	0.06	0.55	9.60	0.14	89.13
DDH	85-7	92M8	P-S	45.59	0.04	35.22	0.70	0.05	0.64	0.00	0.91	9.72	0.07	92.92
DDH	85-1	2M1	P-S	47.80	0.19	30.13	3.84	0.00	1.37	0.21	0.20	11.49	0.00	95.22
DDH	85-1	2M2	P-S	48.48	0.05	30.34	3.49	0.00	1.45	0.00	0.18	11.43	0.21	95.63
DDH	85-1	2M11	P-S	45.99	0.33	29.29	3.77	0.04	1.14	0.07	0.21	11.03	0.12	91.98
DDH	85-1	2M13	P-S	46.49	0.22	30.09	3.58	0.14	1.27	0.96	0.18	11.28	0.18	94.38
DDH	85-1	2M14	P-S	46.91	0.10	30.15	3.62	0.00	1.26	0.14	0.15	11.29	0.22	93.82
DDH	85-1	2M15	P-S	45.99	0.29	28.74	4.58	0.03	1.39	0.08	0.19	10.94	0.02	92.24
DDH	85-20	267AM1	P-S	46.99	0.23	31.44	4.36	0.04	1.00	0.04	0.23	11.22	0.33	95.88
DDH	85-7	91M1	P-S	47.92	0.21	33.36	2.16	0.00	0.65	0.00	0.15	11.12	0.13	95.70
DDH	85-7	91M2	P-S	46.46	0.01	35.95	0.99	0.00	0.20	0.00	1.27	9.54	0.33	94.75
DDH	85-7	91M3	D-S	45.72	0.15	35.29	0.82	0.08	0.25	0.00	0.69	10.34	0.01	93.34
DDH	85-7	91M5	D-S	47.13	0.00	32.05	0.98	0.13	0.32	0.06	0.59	9.75	0.25	91.24
DDH	85-27	20M1	D-S	47.75	0.12	33.33	1.01	0.00	0.84	0.00	0.27	10.47	0.21	94.00
DDH	85-27	20M3	D-S	47.26	0.31	32.63	1.76	0.01	1.13	0.00	0.10	11.13	0.05	94.38
DDH	85-27	20M9	D-S	49.84	0.27	31.11	1.89	0.00	1.30	0.00	0.09	10.98	0.00	95.48
DDH	85-27	20M11	P-S	46.34	0.36	32.79	0.88	0.00	0.80	0.01	0.29	10.65	0.20	92.31
DDH	85-27	20M13	P-S	44.83	0.05	32.77	0.86	0.02	0.99	0.07	0.27	10.01	0.31	90.17
DDH	85-27	20M14	D-S	47.02	0.15	33.72	0.99	0.04	1.06	0.04	0.28	11.33	0.04	94.66
DDH	85-3	51M2	P-S	44.58	0.16	30.99	4.81	0.08	1.90	0.06	0.43	9.50	0.26	92.76
DDH	85-3	51M3	P-S	46.25	0.07	31.20	1.83	0.13	1.57	0.14	0.17	10.87	0.05	92.28
DDH	85-3	51M5	P-S	48.07	0.21	30.45	2.48	0.00	1.77	0.10	0.14	11.24	0.19	94.64
DDH	85-3	51M8	P-S	48.56	0.15	29.75	2.68	0.01	1.90	0.05	0.06	11.54	0.15	94.83
DDH	85-3	51M10	P-S	47.69	0.06	30.19	2.00	0.00	1.87	0.02	0.07	11.04	0.30	93.23
DDH	85-3	51M13	P-S	47.17	0.30	33.05	2.04	0.03	1.08	0.00	0.37	10.82	0.56	95.41
DDH	85-18	265BM5	P-S	47.59	0.04	37.41	0.27	0.08	0.16	0.10	4.91	2.74	0.00	93.30
DDH	85-18	265BM6	D-S	45.00	0.21	34.19	0.74	0.00	0.75	0.36	0.75	9.76	0.01	91.77
DDH	85-18	265BM7	P-S	45.54	0.14	34.12	0.68	0.21	0.99	0.20	0.68	9.97	0.18	92.70
DDH	85-18	265BM12	D-S	48.92	0.11	33.85	0.41	0.00	0.61	0.14	2.15	8.25	0.06	94.50
DDH	85-20	267M1	P-S	47.49	0.32	33.65	1.11	0.04	0.88	0.10	0.03	11.39	0.05	95.06
DDH	85-20	267M2	P-S	46.79	0.47	32.79	1.84	0.10	0.90	0.11	0.14	11.36	0.26	94.75
DDH	85-20	267M3	P-S	46.11	0.54	32.89	1.86	0.00	0.75	0.18	0.05	11.52	0.40	94.31
DDH	85-20	267M4	P-S	45.79	0.20	33.57	1.52	0.06	1.11	0.24	0.34	10.14	0.37	93.31
DDH	85-20	267M5	P-S	45.93	0.44	32.17	1.89	0.00	0.81	0.00	0.02	11.33	0.15	92.74
DDH	85-20	267M6	P-S	46.21	0.21	33.27	1.78	0.00	0.95	0.04	0.17	11.43	0.21	94.27
DDH	85-20	267M7	P-S	47.71	0.57	33.03	2.20	0.00	0.86	0.00	0.14	11.43	0.26	96.22
DDH	85-20	267M8	P-S	47.90	0.33	34.32	2.03	0.00	0.94	0.07	0.14	10.81	0.28	96.82
DDH	85-20	267M9	P-S	46.68	0.47	33.40	1.49	0.00	0.85	0.00	0.03	11.46	0.11	94.48

DDH = diamond drill hole, L-2 = Level 2, P-S = precipitation site, D-S = dissolution site.

Appendix 3.2a Microprobe analyses of chlorite (cation%) from Mobrun deposit

Location	Analyse	Si	Ti	Aliv	Alvi	Fe	Mn	Mg	Ca	Na	K	Total
85-11	146M4	5.18		2.82	3.06	7.21	0.03	1.54		0.10		19.93
85-11	146M7	5.14		2.86	3.02	7.28	0.01	1.59		0.04		19.94
86-4	467M1	5.19	0.00	2.81	3.04	6.53	0.04	2.23	0.00	0.08	0.00	19.93
86-4	467M3	5.29	0.10	2.71	3.02	6.42	0.03	2.30	0.00	0.08	0.03	19.98
86-4	467M4	5.18	0.01	2.82	3.06	6.47	0.05	2.25	0.00	0.53	0.01	20.38
86-4	467M6	5.30	0.01	2.70	3.03	6.46	0.02	2.23	0.01	0.08	0.02	19.87
86-4	467M8	5.23	0.01	2.77	3.15	6.56	0.02	2.06	0.01	0.01	0.00	19.81
86-4	467M9	5.37	0.00	2.64	2.95	6.73	0.05	2.04	0.00	0.08	0.08	19.92
86-4	467M12	5.25	0.00	2.76	3.03	6.49	0.03	2.26	0.02	0.09	0.00	19.91
88-34	494M5	5.36	0.00	2.64	2.97	7.21	0.04	1.56	0.00	0.11	0.01	19.90
85-24	315M6	5.27	0.02	2.73	3.01	7.28	0.05	1.41	0.01	0.08	0.01	19.88
85-24	315M8	5.24	0.01	2.76	2.96	7.33	0.03	1.51	0.00	0.09	0.00	19.94
85-24	315M10*	5.20	0.00	2.80	2.90	7.63	0.04	1.33	0.00	0.10	0.01	20.00
85-15	244M3*	5.07	0.00	2.93	3.40	7.85	0.03	0.43	0.00	0.08	0.02	19.81
85-15	244M2*	5.43	0.00	2.57	3.62	7.35	0.03	0.45	0.00	0.02	0.00	19.49
85-15	232M1	5.12	0.00	2.88	3.16	6.92	0.00	1.74	0.00	0.07	0.01	19.90
85-15	232M2	5.17	0.01	2.83	3.31	6.84	0.01	1.54	0.01	0.06	0.00	19.78
85-15	232M6	5.44	0.00	2.56	2.99	6.73	0.03	2.00	0.01	0.04	0.00	19.80
85-15	232M10	5.23	0.01	2.77	3.15	6.79	0.02	1.82	0.00	0.04	0.01	19.83
85-15	232M16	5.25	0.01	2.75	3.03	6.86	0.02	1.89	0.01	0.08	0.00	19.89
7-2-7A	1M6	5.25	0.02	2.75	2.94	6.25	0.03	2.56	0.01	0.17	0.00	19.97
7-2-7A	1M7	5.24	0.02	2.76	3.01	6.22	0.00	2.53	0.00	0.12	0.01	19.91
7-2-7A	1M10	5.11	0.00	2.89	2.74	6.69	0.03	2.34	0.00	0.50	0.01	20.32
7-2-11	11M1*	5.52	0.00	2.48	2.50	8.10	0.03	1.32	0.01	0.06	0.00	20.02
7-2-11	11M2*	5.49	0.01	2.51	2.44	8.13	0.00	1.34	0.03	0.10	0.00	20.06
7-2-11	11M3*	5.43	0.01	2.58	2.43	8.26	0.00	1.32	0.01	0.09	0.00	20.11
7-2-11	11M4	5.49	0.02	2.51	2.45	8.03	0.02	1.42	0.01	0.12	0.00	20.06
7-2-11	11M5	5.51	0.01	2.49	2.44	8.16	0.05	1.30	0.00	0.07	0.01	20.05
7-2-11	11M6	5.37	0.02	2.63	2.41	8.25	0.00	1.31	0.02	0.11	0.01	20.13
7-2-11	11M7	5.51	0.02	2.49	2.54	7.89	0.00	1.38	0.04	0.17	0.02	20.05
7-2-11	11M12*	5.45	0.00	2.55	2.45	8.30	0.02	1.23	0.03	0.08	0.00	20.11
85-20	267M2	5.16	0.00	2.84	3.15	6.26	0.01	2.34	0.03	0.10	0.00	19.90
85-20	267M3	5.23	0.00	2.77	3.14	6.22	0.02	2.34	0.05	0.08	0.01	19.86
85-20	267M4	5.22	0.00	2.78	2.92	6.55	0.04	2.33	0.05	0.08	0.00	19.97
85-20	267M10	5.45	0.01	2.55	2.98	6.37	0.05	2.28	0.04	0.08	0.00	19.81
85-20	267M11	5.31	0.00	2.69	3.19	6.47	0.02	2.41	0.00	0.05	0.02	20.15
8-1-172A	172AM5	5.24	0.01	2.77	3.05	5.40	0.04	3.10	0.22	0.05	0.01	19.88
8-1-172A	172AM11	5.27	0.01	2.73	3.13	5.39	0.03	3.16	0.02	0.08	0.01	19.83
85-3	51M4	5.21	0.01	2.79	3.05	5.85	0.00	2.88	0.01	0.05	0.00	19.86
85-3	51M6	5.28	0.01	2.72	2.99	6.06	0.03	2.75	0.00	0.06	0.00	19.89
85-3	51M7	5.54	0.01	2.46	2.95	5.69	0.04	3.00	0.00	0.06	0.02	19.78
85-3	51M15	5.30	0.00	2.70	2.97	6.11	0.04	2.69	0.01	0.08	0.02	19.92
85-18	265M1	5.42	0.00	2.58	3.15	3.71	0.03	4.80	0.00	0.06	0.00	19.74
85-18	265M4	5.37	0.02	2.63	3.16	3.89	0.03	4.57	0.02	0.06	0.00	19.75
85-18	265AM14	5.37	0.00	2.63	3.30	3.83	0.01	4.51	0.00	0.01	0.01	19.68
85-18	265AM15	5.44	0.01	2.56	3.11	3.70	0.05	4.81	0.00	0.09	0.00	19.76

Analyses with * are for overgrowths on pyrite

Appendix 3.2b Microprobe analyses of chlorite (wt.%) from Mobrun deposit

Location	Analyse	SiO2	TiO2	Al2O3	FeO	MnO	MgO	CaO	Na2O	K2O	Total
85-11	146M4	23.24		22.40	38.68	0.14	4.62		0.23		89.31
85-11	146M7	22.74		22.07	38.52	0.06	4.73		0.10		88.21
86-4	467M1	23.59	0.00	22.55	35.50	0.20	6.80	0.01	0.19	0.01	88.85
86-4	467M3	24.18	0.06	22.20	35.07	0.14	7.04	0.00	0.19	0.10	88.99
86-4	467M4	23.54	0.04	22.65	35.15	0.28	6.86	0.00	0.13	0.03	88.67
86-4	467M6	24.13	0.08	22.11	35.14	0.12	6.81	0.05	0.19	0.06	88.69
86-4	467M8	23.71	0.05	22.77	35.53	0.11	6.26	0.02	0.02	0.00	88.46
86-4	467M9	21.81	0.00	19.24	32.72	0.26	5.56	0.00	0.16	0.24	79.99
86-4	467M12	23.99	0.01	22.44	35.48	0.14	6.94	0.07	0.20	0.00	89.26
88-34	494M5	23.64	0.00	21.00	38.05	0.22	4.62	0.00	0.25	0.03	87.79
85-24	315M6	23.99	0.13	22.15	39.62	0.28	4.30	0.04	0.15	0.03	90.69
85-24	315M8	23.55	0.07	21.79	39.39	0.17	4.54	0.00	0.22	0.00	89.73
85-24	315M10	22.85	0.02	21.25	40.07	0.23	3.91	0.00	0.22	0.03	88.56
85-15	244M3	22.42	0.00	23.77	41.54	0.13	1.27	0.00	0.18	0.08	89.40
85-15	244M2	24.91	0.00	24.08	40.28	0.17	1.39	0.02	0.06	0.01	90.90
85-15	232M1	22.91	0.00	22.98	37.05	0.01	5.22	0.00	0.16	0.02	88.35
85-15	232M2	23.43	0.04	23.66	37.09	0.07	4.67	0.05	0.14	0.01	89.14
85-15	232M6	23.81	0.01	20.64	35.21	0.18	5.87	0.04	0.10	0.00	85.85
85-15	232M10	23.13	0.03	22.20	35.91	0.10	5.41	0.00	0.10	0.02	86.90
85-15	232M16	23.45	0.03	21.89	36.63	0.10	5.65	0.04	0.18	0.00	87.96
7-2-7A	1M6	24.24	0.10	22.32	34.52	0.18	7.92	0.03	0.41	0.00	89.70
7-2-7A	1M7	23.99	0.12	22.38	34.05	0.00	7.77	0.00	0.28	0.02	88.60
7-2-7A	1M10	22.91	0.00	21.41	35.86	0.18	7.04	0.00	1.15	0.04	88.59
7-2-11	11M1	24.08	0.00	18.44	42.26	0.13	3.87	0.04	0.14	0.00	88.96
7-2-11	11M2	24.15	0.04	18.52	42.81	0.11	3.97	0.11	0.23	0.00	89.92
7-2-11	11M3	23.50	0.05	18.39	42.77	0.01	3.82	0.04	0.19	0.00	88.76
7-2-11	11M4	24.08	0.11	18.43	42.10	0.09	4.16	0.05	0.28	0.00	89.29
7-2-11	11M5	23.79	0.07	18.10	42.15	0.25	3.78	0.00	0.16	0.04	88.33
7-2-11	11M6	23.37	0.14	18.60	42.89	0.00	3.83	0.07	0.25	0.02	89.17
7-2-11	11M7	24.79	0.10	19.21	42.46	0.00	4.16	0.15	0.39	0.06	91.31
7-2-11	11M12	23.50	0.00	18.34	42.89	0.08	3.58	0.13	0.17	0.00	88.70
85-20	267M2	24.12	0.00	23.76	34.99	0.06	7.33	0.15	0.24	0.01	90.65
85-20	267M3	24.57	0.00	23.53	34.93	0.11	7.37	0.23	0.20	0.04	90.98
85-20	267M4	23.76	0.03	21.98	35.65	0.23	7.11	0.19	0.19	0.00	89.14
85-20	267M10	25.30	0.07	21.75	35.36	0.27	7.11	0.19	0.18	0.00	90.23
85-20	267M11	24.45	0.00	23.06	35.77	0.12	6.33	0.00	0.11	0.05	89.90
8-1-172A	172AM5	23.82	0.05	22.44	29.38	0.22	9.47	0.91	0.11	0.05	86.46
8-1-172A	172AM11	24.81	0.07	23.43	30.37	0.14	10.00	0.07	0.19	0.03	89.10
85-3	51M4	24.23	0.08	23.05	32.52	0.16	8.98	0.05	0.13	0.01	89.20
85-3	51M6	24.17	0.00	22.14	33.14	0.17	8.43	0.00	0.15	0.00	88.19
85-3	51M7	25.84	0.09	21.45	31.76	0.22	9.38	0.00	0.15	0.05	88.94
85-3	51M15	24.65	0.00	22.39	33.99	0.20	8.39	0.04	0.19	0.07	89.91
85-18	265M1	25.95	0.00	23.29	21.24	0.17	15.40	0.00	0.14	0.00	86.19
85-18	265M4	25.24	0.12	23.10	21.90	0.18	14.42	0.08	0.15	0.00	85.17
85-18	265AM14	26.56	0.00	24.87	22.63	0.07	14.96	0.00	0.03	0.03	89.15
85-18	265AM15	26.69	0.04	23.58	21.71	0.28	15.81	0.00	0.23	0.01	88.36

APPENDIX 5.1a Mass change calculations for hangingwall rocks

(i)

Normalized composition of representative hangingwall altered (least-deformed) rocks, Mobrun mine.

	SiO2	TiO2	Al2O3	FeO*	MnO	MgO	CaO	Na2O	K2O	P2O5	S	Zr	Total
Precursor	77.69	0.17	12.18	1.80	0.06	0.39	1.49	4.73	1.44	0.01	0.00	287	100.0
332	78.42	0.24	13.48	1.22	0.03	0.60	1.48	1.01	3.42	0.04	0.03	264	100.0
370-A	76.67	0.22	12.74	2.93	0.02	0.40	0.66	1.41	3.37	0.05	1.50	246	100.0
380-A	77.47	0.15	10.51	1.34	0.14	0.48	4.83	3.56	1.45	0.03	0.02	231	100.0
417	75.26	0.18	11.82	2.67	0.07	0.00	2.10	4.70	1.63	0.05	1.48	269	100.0
445	76.89	0.21	13.30	2.27	0.02	1.55	2.05	1.84	1.79	0.04	0.01	264	100.0
450	79.23	0.19	11.58	2.38	0.01	1.39	0.24	2.77	1.87	0.03	0.28	230	100.0
455	73.38	0.25	12.72	2.39	0.10	1.69	4.67	1.15	3.46	0.05	0.11	361	100.0
485	74.98	0.21	12.64	3.96	0.06	2.53	1.78	1.68	1.79	0.05	0.29	327	100.0
523	78.04	0.17	12.23	2.22	0.03	0.40	1.30	2.36	3.13	0.02	0.06	300	100.0
7-2-168	73.29	0.28	16.14	1.88	0.02	1.07	0.42	4.36	2.19	0.04	0.28	317	100.0
7-2-178	75.26	0.17	12.31	3.38	0.16	1.65	3.21	0.69	3.12	0.02	0.01	290	100.0
8-1-266	76.73	0.17	12.60	3.57	0.08	1.09	0.93	0.88	3.89	0.02	0.01	296	100.0
8-1-284	77.59	0.16	12.51	3.38	0.08	0.94	1.35	1.60	2.32	0.02	0.01	297	100.0
8-2-70B	72.92	0.19	13.78	3.81	0.10	2.32	2.97	0.68	3.18	0.02	0.01	318	100.0
8-2-90	77.62	0.17	12.24	3.34	0.07	0.87	1.07	1.71	2.86	0.02	0.00	300	100.0
8-2-92	77.33	0.17	11.97	2.94	0.10	1.47	1.80	1.04	3.14	0.02	0.00	283	100.0
F-103	73.46	0.20	14.42	2.77	0.04	0.63	0.80	3.12	4.47	0.03	0.01	341	100.0
F-135	77.71	0.18	12.89	3.25	0.06	1.07	0.90	0.72	3.15	0.02	0.01	307	100.0
F-70	76.44	0.16	12.30	4.36	0.04	2.48	0.30	0.35	2.53	0.04	0.98	313	100.0
P8-1	77.01	0.19	12.66	3.10	0.06	1.34	1.30	1.12	3.15	0.02	0.01	305	100.0
P8-3A	79.49	0.13	11.69	3.36	0.05	1.92	0.40	0.30	2.58	0.02	0.01	273	100.0
Avg	76.44	0.19	12.69	2.88	0.06	1.23	1.65	1.76	2.79	0.03	0.24	292	100.0
Least altered (avg n=3)**	78.19	0.18	12.26	1.03	0.05	0.21	1.40	4.87	1.79	0.00	0.00	291	100.0
539	75.80	0.17	12.53	3.49	0.08	0.90	1.53	4.41	1.02	0.02	0.01	299	100.0
8-2-89	78.05	0.14	11.57	2.47	0.08	0.45	1.75	4.61	0.81	0.02	0.01	263	100.0

** Precursor composition from least-altered samples and data from Barrett et al. (1992).

Normalized composition of representative Main Lens hangingwall deformed rocks, Mobrun mine.

	SiO2	TiO2	Al2O3	FeO*	MnO	MgO	CaO	Na2O	K2O	P2O5	S	Zr	Total
Precursor	76.44	0.19	12.69	2.88	0.06	1.23	1.65	1.76	2.79	0.03	0.24	292	100.0
263	69.17	0.30	17.46	4.96	0.03	3.18	0.59	0.82	3.38	0.03	0.01	641	100.0
283	77.68	0.23	12.83	3.81	0.03	2.50	0.10	0.63	2.12	0.02	0.00	466	100.0
451	64.29	0.17	10.74	9.69	0.03	1.16	2.16	2.19	2.10	0.02	7.44	198	100.0
7-1-117	65.43	0.35	19.86	5.77	0.05	2.29	0.72	1.00	4.26	0.03	0.16	722	100.0
7-1-130	66.74	0.29	20.74	4.34	0.04	1.07	0.18	1.29	5.22	0.03	0.01	501	100.0
7-1-177	70.77	0.27	15.63	4.77	0.04	3.47	0.90	1.15	2.85	0.04	0.05	478	100.0
7-2-33	58.72	0.41	23.70	7.77	0.03	2.59	0.35	0.29	5.72	0.04	0.29	846	100.0
F-138	74.34	0.19	13.20	4.65	0.05	2.13	1.08	0.35	2.96	0.04	0.99	280	100.0
P8-8	58.76	0.39	22.31	7.91	0.05	2.19	0.07	0.51	5.30	0.06	2.37	759	100.0
478	83.26	0.16	9.62	2.74	0.01	0.57	0.18	1.22	0.93	0.02	1.27	189	100.0
Avg	68.92	0.28	16.61	5.64	0.04	2.12	0.63	0.94	3.48	0.03	1.26	508	100.0

Note: Precursor composition from altered (least-deformed) samples (average n = 22).

APPENDIX 5.1a
(ii)

Reconstructed compositions of altered samples (HW), normalized to Zr precursor.

	SiO2	TiO2	Al2O3	FeO*	MnO	MgO	CaO	Na2O	K2O	P2O5	S	Zr	Total
332	85.24	0.26	14.65	1.33	0.03	0.65	1.61	1.10	3.72	0.04	0.03	287	108.7
370-A	89.41	0.26	14.86	3.42	0.02	0.46	0.77	1.64	3.93	0.06	1.75	287	116.6
380-A	96.41	0.18	13.08	1.66	0.17	0.60	6.02	4.43	1.81	0.04	0.03	287	124.5
417	80.26	0.19	12.60	2.85	0.08	0.00	2.24	5.02	1.74	0.05	1.58	287	106.6
445	83.69	0.23	14.48	2.47	0.02	1.68	2.23	2.01	1.95	0.04	0.01	287	108.8
450	99.06	0.24	14.48	2.97	0.01	1.74	0.30	3.46	2.34	0.04	0.35	287	125.0
455	58.29	0.20	10.11	1.90	0.08	1.34	3.71	0.91	2.75	0.04	0.09	287	79.4
485	65.81	0.18	11.09	3.47	0.05	2.22	1.57	1.47	1.57	0.05	0.25	287	87.8
523	74.77	0.17	11.72	2.13	0.03	0.38	1.25	2.27	3.00	0.02	0.06	287	95.8
7-2-168	66.42	0.25	14.63	1.71	0.02	0.97	0.38	3.95	1.98	0.04	0.25	287	90.6
7-2-178	74.40	0.17	12.17	3.34	0.16	1.63	3.18	0.68	3.08	0.02	0.01	287	98.9
8-1-266	74.32	0.17	12.20	3.46	0.08	1.05	0.90	0.85	3.77	0.02	0.01	287	96.9
8-1-284	74.91	0.16	12.07	3.26	0.08	0.91	1.30	1.55	2.24	0.02	0.01	287	96.5
8-2-70B	65.88	0.17	12.45	3.44	0.09	2.09	2.68	0.62	2.87	0.02	0.01	287	90.4
8-2-90	74.14	0.16	11.69	3.19	0.07	0.83	1.02	1.63	2.73	0.02	0.00	287	95.5
8-2-92	78.34	0.17	12.12	2.98	0.11	1.49	1.82	1.05	3.18	0.02	0.00	287	101.3
F-103	61.75	0.17	12.12	2.33	0.03	0.53	0.67	2.62	3.76	0.03	0.01	287	84.1
F-135	72.60	0.17	12.04	3.04	0.06	1.00	0.84	0.67	2.94	0.02	0.01	287	93.4
F-70	69.99	0.15	11.26	3.99	0.04	2.27	0.27	0.32	2.32	0.04	0.90	287	91.6
P8-1	72.57	0.18	11.93	2.92	0.06	1.26	1.23	1.06	2.97	0.02	0.01	287	94.2
P8-3A	83.70	0.14	12.31	3.54	0.05	2.03	0.42	0.31	2.72	0.02	0.01	287	105.3
Avg	76.28	0.19	12.57	2.83	0.06	1.20	1.64	1.79	2.73	0.03	0.26	287	99.6

Reconstructed compositions of deformed samples (HW), normalized to Zr precursor.

	SiO2	TiO2	Al2O3	FeO*	MnO	MgO	CaO	Na2O	K2O	P2O5	S	Zr	Total
263	31.51	0.14	7.95	2.26	0.01	1.45	0.27	0.37	1.54	0.01	0.00	292	45.6
283	48.71	0.14	8.05	2.39	0.02	1.57	0.06	0.39	1.33	0.01	0.00	292	62.7
451	94.99	0.25	15.86	14.31	0.04	1.72	3.19	3.23	3.10	0.03	11.00	292	147.8
7-1-117	26.47	0.14	8.04	2.33	0.02	0.93	0.29	0.40	1.72	0.01	0.06	292	40.5
7-1-130	38.92	0.17	12.10	2.53	0.02	0.63	0.10	0.75	3.04	0.02	0.01	292	58.3
7-1-177	43.19	0.16	9.54	2.91	0.03	2.12	0.55	0.70	1.74	0.03	0.03	292	61.0
7-2-33	20.27	0.14	8.18	2.68	0.01	0.89	0.12	0.10	1.98	0.01	0.10	292	34.5
F-138	77.55	0.19	13.77	4.85	0.05	2.22	1.13	0.36	3.09	0.04	1.03	292	104.3
P8-8	22.62	0.15	8.59	3.04	0.02	0.84	0.03	0.20	2.04	0.02	0.91	292	38.5
478	128.97	0.25	14.90	4.24	0.02	0.88	0.28	1.89	1.44	0.03	1.97	292	154.9
Avg	53.32	0.17	10.70	4.16	0.02	1.32	0.60	0.84	2.10	0.02	1.51	292	74.8

APPENDIX 5.1a

(iii)

Representative mass changes in hangingwall altered rhyolite of Mobrun mine.

	SiO2	TiO2	Al2O	FeO*	MnO	MgO	CaO	Na2O	K2O	P2O5	S	Total
332	7.6	0.1	2.5	-0.5	-0.0	0.3	0.1	-3.6	2.3	0.0	0.0	8.7
370-A	18.7	0.0	0.9	-0.1	0.1	0.2	4.5	-0.3	0.4	0.0	0.0	24.5
380-A	18.7	0.0	0.9	-0.1	0.1	0.2	4.5	-0.3	0.4	0.0	0.0	24.5
417	2.6	0.0	0.4	1.1	0.0	-0.4	0.7	0.3	0.3	0.0	1.6	6.7
445	6.0	0.1	2.3	0.7	-0.0	1.3	0.7	-2.7	0.5	0.0	0.0	8.9
450	21.4	0.1	2.3	1.2	-0.0	1.3	-1.2	-1.3	0.9	0.0	0.4	25.1
455	-19.4	0.0	-2.1	0.1	0.0	0.9	2.2	-3.8	1.3	0.0	0.1	-20.5
485	-11.9	0.0	-1.1	1.7	-0.0	1.8	0.1	-3.3	0.1	0.0	0.3	-12.2
523	-2.9	-0.0	-0.5	0.3	-0.0	-0.0	-0.2	-2.5	1.6	0.0	0.1	-4.2
7-2-168	-11.2	0.1	2.5	-0.1	-0.0	0.6	-1.1	-0.8	0.5	0.0	0.2	-9.3
7-2-178	-3.3	-0.0	-0.0	1.5	0.1	1.2	1.7	-4.0	1.6	0.0	0.0	-1.1
8-1-266	-3.3	-0.0	0.0	1.7	0.0	0.7	-0.6	-3.9	2.3	0.0	0.0	-3.1
8-1-284	-2.8	-0.0	-0.1	1.5	0.0	0.5	-0.2	-3.2	0.8	0.0	0.0	-3.4
8-2-70	-11.8	-0.0	0.3	1.6	0.0	1.7	1.2	-4.1	1.4	0.0	0.0	-9.6
8-2-90	-3.5	-0.0	-0.5	1.4	0.0	0.4	-0.5	-3.1	1.3	0.0	-0.0	-4.5
8-2-92	0.7	-0.0	-0.0	1.2	0.0	1.1	0.3	-3.7	1.7	0.0	-0.0	1.3
F-103	-15.9	-0.0	-0.0	0.5	-0.0	0.1	-0.8	-2.1	2.3	0.0	0.0	-15.9
F-135	-5.1	0.0	-0.1	1.2	-0.0	0.6	-0.7	-4.1	1.5	0.0	0.0	-6.5
F-70	-7.7	-0.0	-0.9	2.2	-0.0	1.9	-1.2	-4.4	0.9	0.0	0.9	-8.4
P8-1	-5.1	0.0	-0.2	1.1	-0.0	0.9	-0.3	-3.7	1.5	0.0	0.0	-5.7
P8-3A	6.0	-0.0	0.1	1.7	-0.0	1.6	-1.1	-4.4	1.3	0.0	0.0	5.3
Avg	-1.4	0.0	0.4	1.0	0.0	0.8	0.1	-2.9	1.3	0.0	0.3	-0.3
												11.8

Representative mass changes in hangingwall deformed rhyolite of Mobrun mine.

	SiO2	TiO2	Al2O	FeO*	MnO	MgO	CaO	Na2O	K2O	P2O5	S	Total
263	-44.9	-0.1	-4.7	-0.6	-0.1	0.2	-1.4	-1.4	-1.2	-0.0	-0.2	-54.4
283	-27.7	-0.0	-4.6	-0.5	-0.0	0.3	-1.6	-1.4	-1.5	-0.0	-0.2	-37.2
451	18.6	0.1	3.2	11.4	-0.0	0.5	1.5	1.5	0.3	-0.0	10.8	47.8
7-1-117	-49.9	-0.0	-4.6	-0.5	-0.0	-0.3	-1.4	-1.4	-1.1	-0.0	-0.2	-59.5
7-1-130	-37.5	-0.0	-0.6	-0.3	-0.0	-0.6	-1.5	-1.0	0.3	-0.0	-0.2	-41.6
7-1-177	-33.2	-0.0	-3.1	0.0	-0.0	0.9	-1.1	-1.1	-1.0	-0.0	-0.2	-38.9
7-2-33	-56.1	-0.1	-4.5	-0.2	-0.1	-0.3	-1.5	-1.7	-0.8	-0.0	-0.1	-65.4
F-138	1.2	0.0	1.1	2.0	-0.0	1.0	-0.5	-1.4	0.3	0.0	0.8	4.4
P8-8	-53.8	-0.0	-4.1	0.2	-0.0	-0.4	-1.6	-1.6	-0.7	-0.0	0.7	-61.4
478	51.3	0.1	2.7	2.4	-0.0	0.5	-1.2	-2.8	-0.0	0.0	2.0	54.9
Avg	-23.2	-0.0	-1.9	1.4	-0.0	0.2	-1.0	-1.2	-0.5	-0.0	1.3	-25.1

APPENDIX 5.1b Mass change calculations for footwall rocks

(i)

Normalized composition of representative footwall altered (least-deformed) rocks, Mobrun mine.

	SiO2	TiO2	Al2O3	FeO*	MnO	MgO	CaO	Na2O	K2O	P2O5	S	Zr	Total
Precursor	77.45	0.21	11.97	2.17	0.04	0.53	1.79	4.41	1.36	0.04	0.00	334	100.0
215	78.36	0.20	10.35	4.88	0.00	0.00	0.02	0.40	2.76	0.03	2.97	306	100.0
248	75.97	0.25	12.53	4.07	0.00	0.15	0.09	0.77	3.39	0.02	2.73	354	100.0
252	75.58	0.25	14.10	1.75	0.05	0.29	0.97	4.04	2.15	0.05	0.71	359	100.0
347-A	74.42	0.24	13.86	1.71	0.01	0.34	0.42	0.46	8.11	0.06	0.34	360	100.0
386-B	74.64	0.27	14.57	1.36	0.02	0.63	1.99	4.73	1.69	0.05	0.01	392	100.0
420	78.24	0.22	12.87	0.47	0.01	0.00	1.13	6.42	0.51	0.06	0.02	338	100.0
423	75.57	0.25	13.71	3.32	0.04	1.55	1.60	1.62	2.27	0.04	0.00	380	100.0
425	74.72	0.25	14.33	1.55	0.03	0.55	1.62	5.73	1.11	0.05	0.01	389	100.0
426	73.68	0.24	13.54	1.40	0.06	0.47	4.24	4.26	1.99	0.05	0.02	371	100.0
428	74.48	0.25	14.63	0.86	0.03	0.23	2.31	5.20	1.92	0.05	0.01	381	100.0
433	72.86	0.26	14.26	3.58	0.11	1.88	2.34	0.23	4.38	0.04	0.01	397	100.0
436	75.81	0.24	13.54	1.51	0.05	0.34	1.68	3.93	2.46	0.05	0.35	355	100.0
438	67.62	0.24	13.25	6.72	0.15	0.32	2.46	0.40	3.60	0.04	5.15	338	100.0
441	77.01	0.25	13.33	1.78	0.02	0.63	1.10	3.86	1.92	0.05	0.01	366	100.0
461	73.19	0.27	14.34	3.54	0.05	0.52	1.55	3.40	3.02	0.05	0.01	386	100.0
494	74.84	0.25	13.31	2.89	0.11	0.44	2.13	2.59	3.18	0.05	0.19	363	100.0
501	74.71	0.26	13.96	2.51	0.06	0.38	1.62	3.95	2.47	0.05	0.00	378	100.0
7-1-88	79.91	0.23	12.85	1.84	0.00	0.00	0.03	0.46	3.40	0.03	1.21	334	100.0
8-2-338	81.24	0.22	12.23	1.87	0.00	0.00	0.03	1.18	2.01	0.01	1.18	322	100.0
8-2-339	70.59	0.33	17.94	2.26	0.06	0.08	1.03	5.65	1.89	0.04	0.07	366	100.0
P7-6A	68.32	0.30	18.80	3.72	0.02	2.53	0.03	0.51	5.67	0.03	0.03	364	100.0
Avg	74.85	0.25	13.92	2.55	0.04	0.54	1.35	2.85	2.85	0.04	0.72	362	100.0

Note: Precursor composition from least-altered samples (Barrett et al. 1992, average n = 4).

Normalized composition of representative Main Lens footwall deformed rocks, Mobrun mine.

	SiO2	TiO2	Al2O3	FeO*	MnO	MgO	CaO	Na2O	K2O	P2O5	S	Zr	Total
Precursor	74.85	0.25	13.92	2.55	0.04	0.54	1.35	2.85	2.85	0.04	0.72	362	100.0
314-A	71.93	0.29	17.09	2.97	0.00	0.43	0.15	0.26	5.52	0.06	1.25	308	100.0
391-B	68.97	0.36	19.58	0.98	0.00	0.81	0.82	3.87	4.50	0.06	0.01	522	100.0
397	60.67	0.37	20.76	6.82	0.01	1.63	0.20	0.76	7.00	0.07	1.67	547	100.0
468	71.34	0.24	12.81	6.12	0.00	0.15	0.04	0.35	3.68	0.04	5.21	325	100.0
503	73.52	0.23	12.75	4.19	0.12	0.28	2.20	0.23	3.84	0.04	2.57	331	100.0
8-2-337	77.76	0.27	17.08	0.52	0.00	0.01	0.01	1.74	2.40	0.02	0.13	428	100.0
Avg	70.70	0.29	16.68	3.60	0.02	0.55	0.57	1.20	4.49	0.05	1.81	410	100.0

Note: precursor composition from altered (least-deformed) samples (average n = 21).

APPENDIX 5.1b
(ii)

Reconstructed compositions of altered samples (FW), normalized to Zr precursor.

	SiO2	TiO2	Al2O3	FeO*	MnO	MgO	CaO	Na2O	K2O	P2O5	S	Zr	Total
215	85.46	0.22	11.29	5.32	0.00	0.00	0.02	0.44	3.01	0.03	3.24	334	109.1
248	71.66	0.24	11.82	3.83	0.00	0.14	0.09	0.72	3.20	0.02	2.58	334	94.3
252	70.35	0.24	13.12	1.63	0.05	0.27	0.91	3.76	2.00	0.05	0.66	334	93.1
347-A	69.06	0.23	12.86	1.59	0.01	0.31	0.39	0.42	7.53	0.06	0.31	334	92.8
386-B	63.63	0.23	12.42	1.16	0.02	0.54	1.70	4.04	1.44	0.04	0.01	334	85.2
420	77.28	0.22	12.71	0.47	0.01	0.00	1.12	6.34	0.51	0.06	0.02	334	98.8
423	66.42	0.22	12.05	2.92	0.04	1.37	1.40	1.42	1.99	0.04	0.00	334	87.9
425	64.15	0.22	12.30	1.33	0.03	0.47	1.39	4.92	0.95	0.04	0.01	334	85.9
426	66.25	0.22	12.17	1.26	0.06	0.42	3.82	3.83	1.79	0.05	0.02	334	89.9
428	65.31	0.22	12.83	0.75	0.03	0.20	2.03	4.56	1.68	0.05	0.01	334	87.7
433	61.31	0.22	12.00	3.01	0.10	1.58	1.97	0.19	3.69	0.04	0.01	334	84.2
436	71.29	0.22	12.73	1.42	0.05	0.32	1.58	3.70	2.31	0.05	0.33	334	94.0
438	66.88	0.24	13.10	6.65	0.15	0.32	2.44	0.40	3.57	0.04	5.09	334	98.9
441	70.22	0.23	12.15	1.62	0.02	0.58	1.00	3.52	1.75	0.05	0.01	334	91.2
461	63.38	0.23	12.41	3.07	0.04	0.45	1.34	2.95	2.62	0.04	0.01	334	86.6
494	68.79	0.23	12.24	2.65	0.10	0.40	1.96	2.38	2.92	0.05	0.17	334	91.9
501	66.09	0.23	12.35	2.22	0.05	0.34	1.43	3.50	2.19	0.05	0.00	334	88.5
7-1-88	79.81	0.23	12.84	1.84	0.00	0.00	0.03	0.45	3.40	0.03	1.21	334	99.9
8-2-338	84.17	0.23	12.68	1.94	0.00	0.00	0.03	1.22	2.08	0.01	1.22	334	103.6
8-2-339	64.41	0.30	16.37	2.07	0.06	0.08	0.94	5.16	1.73	0.04	0.07	334	91.2
P7-6A	62.72	0.28	17.26	3.42	0.02	2.32	0.03	0.47	5.20	0.03	0.03	334	91.8
Avg	69.46	0.23	12.84	2.39	0.04	0.48	1.22	2.59	2.64	0.04	0.71	334	92.7

Reconstructed compositions of deformed samples (FW), normalized to Zr precursor.

	SiO2	TiO2	Al2O3	FeO*	MnO	MgO	CaO	Na2O	K2O	P2O5	S	Zr	Total
314-A	84.48	0.35	20.07	3.49	0.00	0.50	0.18	0.31	6.49	0.07	1.47	362	117.4
391-B	47.82	0.25	13.58	0.68	0.00	0.56	0.57	2.68	3.12	0.04	0.01	362	69.3
397	40.14	0.25	13.74	4.51	0.01	1.08	0.13	0.50	4.63	0.05	1.10	362	66.2
468	79.46	0.27	14.27	6.82	0.00	0.17	0.04	0.39	4.09	0.04	5.80	362	111.4
503	80.36	0.25	13.94	4.58	0.14	0.30	2.41	0.25	4.20	0.05	2.81	362	109.3
8-2-337	65.75	0.23	14.44	0.44	0.00	0.01	0.01	1.47	2.03	0.02	0.11	362	84.6
Avg	66.34	0.26	15.01	3.42	0.02	0.44	0.56	0.93	4.09	0.04	1.88	362	93.0

APPENDIX 5.1b
(iii)

Representative mass changes in footwall altered rhyolite of Mobrun mine.

	SiO2	TiO2	Al2O	FeO*	MnO	MgO	CaO	Na2O	K2O	P2O5	S	Total
215	8.0	0.0	-0.7	3.1	-0.0	-0.5	-1.8	-4.0	1.7	-0.0	3.2	9.1
248	-5.8	0.0	-0.2	1.7	-0.0	-0.4	-1.7	-3.7	1.8	-0.0	2.6	-5.7
252	-7.1	0.0	1.1	-0.5	0.0	-0.3	-0.9	-0.6	0.6	0.0	0.7	-6.9
347-A	-8.4	0.0	0.9	-0.6	-0.0	-0.2	-1.4	-4.0	6.2	0.0	0.3	-7.2
386-B	-13.8	0.0	0.4	-1.0	-0.0	0.0	-0.1	-0.4	0.1	0.0	0.0	-14.8
420	-0.2	0.0	0.7	-1.7	-0.0	-0.5	-0.7	1.9	-0.9	0.0	0.0	-1.2
423	-11.0	0.0	0.1	0.7	-0.0	0.8	-0.4	-3.0	0.6	-0.0	0.0	-12.1
425	-13.3	0.0	0.3	-0.8	-0.0	-0.1	-0.4	0.5	-0.4	0.0	0.0	-14.1
426	-11.2	0.0	0.2	-0.9	0.0	-0.1	2.0	-0.6	0.4	0.0	0.0	-10.1
428	-12.1	0.0	0.9	-1.4	-0.0	-0.3	0.2	0.2	0.3	0.0	0.0	-12.3
433	-16.1	0.0	0.0	0.8	0.1	1.1	0.2	-4.2	2.3	-0.0	0.0	-15.8
436	-6.2	0.0	0.8	-0.8	0.0	-0.2	-0.2	-0.7	1.0	0.0	0.3	-6.0
438	-10.6	0.0	1.1	4.5	0.1	-0.2	0.6	-4.0	2.2	-0.0	5.1	-1.1
441	-7.2	0.0	0.2	-0.5	-0.0	0.0	-0.8	-0.9	0.4	0.0	0.0	-8.8
461	-14.1	0.0	0.4	0.9	0.0	-0.1	-0.4	-1.5	1.3	0.0	0.0	-13.4
494	-8.7	0.0	0.3	0.5	0.1	-0.1	0.2	-2.0	1.6	0.0	0.2	-8.1
501	-11.4	0.0	0.4	0.1	0.0	-0.2	-0.4	-0.9	0.8	0.0	0.0	-11.5
7-1-88	2.4	0.0	0.9	-0.3	-0.0	-0.5	-1.8	-4.0	2.0	-0.0	1.2	-0.1
8-2-33	6.7	0.0	0.7	-0.2	-0.0	-0.5	-1.8	-3.2	0.7	-0.0	1.2	3.6
8-2-33	-13.0	0.1	4.4	-0.1	0.0	-0.5	-0.9	0.7	0.4	-0.0	0.1	-8.8
P7-6A	-14.7	0.1	5.3	1.2	-0.0	1.8	-1.8	-3.9	3.8	-0.0	0.0	-8.2
Avg	-8.0	0.0	0.9	0.2	-0.0	-0.0	-0.6	-1.8	1.3	0.0	0.7	-7.3

Representative mass changes in footwall deformed rhyolite of Mobrun mine.

	SiO2	TiO2	Al2O	FeO*	MnO	MgO	CaO	Na2O	K2O	P2O5	S	Total
314-A	9.7	0.1	6.2	0.9	-0.0	-0.0	-1.2	-2.5	3.6	0.0	0.8	17.5
391-B	-27.0	-0.0	-0.3	-1.9	-0.0	0.0	-0.8	-0.2	0.3	-0.0	-0.7	-30.6
397	-34.7	-0.0	-0.2	2.0	-0.0	0.5	-1.2	-2.3	1.8	0.0	0.4	-33.8
468	4.7	0.0	0.4	4.3	-0.0	-0.4	-1.3	-2.5	1.2	0.0	5.1	11.4
503	5.5	-0.0	0.0	2.0	0.1	-0.2	1.1	-2.6	1.3	0.0	2.1	9.4
8-2-33	-9.1	-0.0	0.5	-2.1	-0.0	-0.5	-1.3	-1.4	-0.8	-0.0	-0.6	-15.4
Avg	-8.5	0.0	1.1	0.9	-0.0	-0.1	-0.8	-1.9	1.2	0.0	1.2	-6.9

APPENDIX 5.2a Volume change calculations for hangingwall rocks.

(i)

Normalaized composition of representative hanging wall altered (least deformed) rocks, Mobrun mine.

	SiO2	TiO2	Al2O3	FeO*	MnO	MgO	CaO	Na2O	K2O	P2O5	S	Zr	Total
Precursor	77.69	0.17	12.18	1.80	0.06	0.39	1.49	4.73	1.44	0.01	0.00	287.1	100.0
332	78.42	0.24	13.48	1.22	0.03	0.60	1.48	1.01	3.42	0.04	0.03	264.0	100.0
370-A	76.67	0.22	12.74	2.93	0.02	0.40	0.66	1.41	3.37	0.05	1.50	246.1	100.0
380-A	77.47	0.15	10.51	1.34	0.14	0.48	4.83	3.56	1.45	0.03	0.02	230.6	100.0
417	75.26	0.18	11.82	2.67	0.07	0.00	2.10	4.70	1.63	0.05	1.48	269.1	100.0
445	76.89	0.21	13.30	2.27	0.02	1.55	2.05	1.84	1.79	0.04	0.01	263.7	100.0
450	79.23	0.19	11.58	2.38	0.01	1.39	0.24	2.77	1.87	0.03	0.28	229.6	100.0
455	73.38	0.25	12.72	2.39	0.10	1.69	4.67	1.15	3.46	0.05	0.11	361.3	100.0
485	74.98	0.21	12.64	3.96	0.06	2.53	1.78	1.68	1.79	0.05	0.29	327.0	100.0
523	78.04	0.17	12.23	2.22	0.03	0.40	1.30	2.36	3.13	0.02	0.06	299.6	100.0
7-2-168	73.29	0.28	16.14	1.88	0.02	1.07	0.42	4.36	2.19	0.04	0.28	316.7	100.0
7-2-178	75.26	0.17	12.31	3.38	0.16	1.65	3.21	0.69	3.12	0.02	0.01	290.3	100.0
8-1-266	76.73	0.17	12.60	3.57	0.08	1.09	0.93	0.88	3.89	0.02	0.01	296.3	100.0
8-1-284	77.59	0.16	12.51	3.38	0.08	0.94	1.35	1.60	2.32	0.02	0.01	297.3	100.0
8-2-70B	72.92	0.19	13.78	3.81	0.10	2.32	2.97	0.68	3.18	0.02	0.01	317.7	100.0
8-2-90	77.62	0.17	12.24	3.34	0.07	0.87	1.07	1.71	2.86	0.02	0.00	300.5	100.0
8-2-92	77.33	0.17	11.97	2.94	0.10	1.47	1.80	1.04	3.14	0.02	0.00	283.3	100.0
F-103	73.46	0.20	14.42	2.77	0.04	0.63	0.80	3.12	4.47	0.03	0.01	341.4	100.0
F-135	77.71	0.18	12.89	3.25	0.06	1.07	0.90	0.72	3.15	0.02	0.01	307.2	100.0
F-70	76.44	0.16	12.30	4.36	0.04	2.48	0.30	0.35	2.53	0.04	0.98	313.5	100.0
P8-1	77.01	0.19	12.66	3.10	0.06	1.34	1.30	1.12	3.15	0.02	0.01	304.5	100.0
P8-3A	79.49	0.13	11.69	3.36	0.05	1.92	0.40	0.30	2.58	0.02	0.01	272.6	100.0
Avg	76.44	0.19	12.69	2.88	0.06	1.23	1.65	1.76	2.79	0.03	0.24	292.0	100.0

Note: Precursor composition from least altered samples and data from Barrett et al.(1992).

Normalaized composition of representative hanging wall altered (deformed) rocks, Mobrun mine.

	SiO2	TiO2	Al2O3	FeO*	MnO	MgO	CaO	Na2O	K2O	P2O5	S	Zr	Total
Precursor	76.45	0.19	12.69	2.88	0.06	1.23	1.63	1.77	2.78	0.03	0.25	291.8	100.0
263	69.17	0.30	17.46	4.96	0.03	3.18	0.59	0.82	3.38	0.03	0.01	641.0	100.0
283	77.68	0.23	12.83	3.81	0.03	2.50	0.10	0.63	2.12	0.02	0.00	465.7	100.0
451	64.29	0.17	10.74	9.69	0.03	1.16	2.16	2.19	2.10	0.02	7.44	197.6	100.0
7-1-117	65.43	0.35	19.86	5.77	0.05	2.29	0.72	1.00	4.26	0.03	0.16	721.7	100.0
7-1-130	66.74	0.29	20.74	4.34	0.04	1.07	0.18	1.29	5.22	0.03	0.01	500.7	100.0
7-1-177	70.77	0.27	15.63	4.77	0.04	3.47	0.90	1.15	2.85	0.04	0.05	478.4	100.0
7-2-33	58.72	0.41	23.70	7.77	0.03	2.59	0.35	0.29	5.72	0.04	0.29	845.9	100.0
F-138	74.34	0.19	13.20	4.65	0.05	2.13	1.08	0.35	2.96	0.04	0.99	279.9	100.0
P8-8	58.76	0.39	22.31	7.91	0.05	2.19	0.07	0.51	5.30	0.06	2.37	758.6	100.0
478	83.26	0.16	9.62	2.74	0.01	0.57	0.18	1.22	0.93	0.02	1.27	188.5	100.0
Avg	68.92	0.28	16.61	5.64	0.04	2.12	0.63	0.94	3.48	0.03	1.26	507.8	100.0

Note: Precursor composition from least deformed samples (average n = 21).

APPENDIX 5.2a

(ii)

Reconstructed compositions of altered (least deformed) samples (HW), normalized to Zr precursor.

	SiO2	TiO2	Al2O3	FeO*	MnO	MgO	CaO	Na2O	K2O	P2O5	S	Zr	Total
Precursor	77.67	0.17	12.17	1.80	0.06	0.39	1.49	4.72	1.44	0.01	0.00	287.0	100.0
332	85.24	0.26	14.65	1.33	0.03	0.65	1.61	1.10	3.72	0.04	0.03	287.0	108.7
370-A	89.41	0.26	14.86	3.42	0.02	0.46	0.77	1.64	3.93	0.06	1.75	287.0	116.6
380-A	96.41	0.18	13.08	1.66	0.17	0.60	6.02	4.43	1.81	0.04	0.03	287.0	124.5
417	80.26	0.19	12.60	2.85	0.08	0.00	2.24	5.02	1.74	0.05	1.58	287.0	106.6
445	83.69	0.23	14.48	2.47	0.02	1.68	2.23	2.01	1.95	0.04	0.01	287.0	108.8
450	99.06	0.24	14.48	2.97	0.01	1.74	0.30	3.46	2.34	0.04	0.35	287.0	125.0
455	58.29	0.20	10.11	1.90	0.08	1.34	3.71	0.91	2.75	0.04	0.09	287.0	79.4
485	65.81	0.18	11.09	3.47	0.05	2.22	1.57	1.47	1.57	0.05	0.25	287.0	87.8
523	74.77	0.17	11.72	2.13	0.03	0.38	1.25	2.27	3.00	0.02	0.06	287.0	95.8
7-2-168	66.42	0.25	14.63	1.71	0.02	0.97	0.38	3.95	1.98	0.04	0.25	287.0	90.6
7-2-178	74.40	0.17	12.17	3.34	0.16	1.63	3.18	0.68	3.08	0.02	0.01	287.0	98.9
8-1-266	74.32	0.17	12.20	3.46	0.08	1.05	0.90	0.85	3.77	0.02	0.01	287.0	96.9
8-1-284	74.91	0.16	12.07	3.26	0.08	0.91	1.30	1.55	2.24	0.02	0.01	287.0	96.5
8-2-70B	65.88	0.17	12.45	3.44	0.09	2.09	2.68	0.62	2.87	0.02	0.01	287.0	90.4
8-2-90	74.14	0.16	11.69	3.19	0.07	0.83	1.02	1.63	2.73	0.02	0.00	287.0	95.5
8-2-92	78.34	0.17	12.12	2.98	0.11	1.49	1.82	1.05	3.18	0.02	0.00	287.0	101.3
F-103	61.75	0.17	12.12	2.33	0.03	0.53	0.67	2.62	3.76	0.03	0.01	287.0	84.1
F-135	72.60	0.17	12.04	3.04	0.06	1.00	0.84	0.67	2.94	0.02	0.01	287.0	93.4
F-70	69.99	0.15	11.26	3.99	0.04	2.27	0.27	0.32	2.32	0.04	0.90	287.0	91.6
P8-1	72.57	0.18	11.93	2.92	0.06	1.26	1.23	1.06	2.97	0.02	0.01	287.0	94.2
P8-3A	83.70	0.14	12.31	3.54	0.05	2.03	0.42	0.31	2.72	0.02	0.01	287.0	105.3
Avg	76.28	0.19	12.57	2.83	0.06	1.20	1.64	1.79	2.73	0.03	0.26	287.00	99.62

Reconstructed compositions of deformed samples (HW), normalized to Zr precursor.

	SiO2	TiO2	Al2O3	FeO*	MnO	MgO	CaO	Na2O	K2O	P2O5	S	Zr	Total
Precursor	76.43	0.19	12.69	2.88	0.06	1.23	1.63	1.77	2.78	0.03	0.25	291.8	100.0
263	31.49	0.14	7.95	2.26	0.01	1.45	0.27	0.37	1.54	0.01	0.00	291.8	45.5
283	48.68	0.14	8.04	2.38	0.02	1.57	0.06	0.39	1.33	0.01	0.00	291.8	62.7
451	94.92	0.25	15.85	14.30	0.04	1.72	3.19	3.23	3.10	0.03	10.99	291.8	147.7
7-1-117	26.46	0.14	8.03	2.33	0.02	0.93	0.29	0.40	1.72	0.01	0.06	291.8	40.4
7-1-130	38.90	0.17	12.09	2.53	0.02	0.63	0.10	0.75	3.04	0.02	0.01	291.8	58.3
7-1-177	43.16	0.16	9.53	2.91	0.03	2.12	0.55	0.70	1.74	0.03	0.03	291.8	61.0
7-2-33	20.26	0.14	8.17	2.68	0.01	0.89	0.12	0.10	1.97	0.01	0.10	291.8	34.5
F-138	77.50	0.19	13.76	4.85	0.05	2.22	1.13	0.36	3.09	0.04	1.03	291.8	104.2
P8-8	22.60	0.15	8.58	3.04	0.02	0.84	0.03	0.20	2.04	0.02	0.91	291.8	38.5
478	128.88	0.25	14.89	4.24	0.02	0.88	0.28	1.89	1.44	0.03	1.97	291.8	154.8
avg	53.28	0.17	10.69	4.15	0.02	1.32	0.60	0.84	2.10	0.02	1.51	291.8	74.76

APPENDIX 5.2a

(iii)

Cation equivalent proportion of hanging wall altered (least deformed) samples.

	Si	Ti	Al	Fe	Mn	Mg	Ca	Na	K	P	S	Total
Precursor	1.2928	0.0022	0.2388	0.0250	0.0009	0.0098	0.0253	0.1525	0.0307	0.0001	0.0000	1.7780
332	1.4188	0.0032	0.2874	0.0185	0.0005	0.0161	0.0273	0.0354	0.0791	0.0006	0.0010	1.8881
370-A	1.4882	0.0033	0.2915	0.0476	0.0003	0.0114	0.0130	0.0531	0.0835	0.0008	0.0546	2.0474
380-A	1.6048	0.0023	0.2565	0.0231	0.0024	0.0150	0.1018	0.1429	0.0385	0.0006	0.0008	2.1887
417	1.3359	0.0024	0.2472	0.0397	0.0011	0.0000	0.0379	0.1618	0.0370	0.0008	0.0492	1.9130
445	1.3930	0.0029	0.2839	0.0344	0.0003	0.0418	0.0377	0.0647	0.0415	0.0006	0.0003	1.9013
450	1.6487	0.0030	0.2840	0.0414	0.0002	0.0431	0.0051	0.1116	0.0498	0.0005	0.0111	2.1985
455	0.9702	0.0025	0.1983	0.0264	0.0011	0.0332	0.0628	0.0294	0.0584	0.0006	0.0027	1.3855
485	1.0953	0.0023	0.2176	0.0483	0.0008	0.0551	0.0265	0.0476	0.0335	0.0006	0.0079	1.5355
523	1.2445	0.0021	0.2298	0.0296	0.0004	0.0094	0.0212	0.0731	0.0638	0.0003	0.0018	1.6760
7-2-168	1.1055	0.0031	0.2870	0.0238	0.0003	0.0241	0.0064	0.1276	0.0422	0.0005	0.0078	1.6282
7-2-178	1.2384	0.0021	0.2386	0.0465	0.0022	0.0405	0.0538	0.0219	0.0656	0.0003	0.0003	1.7102
8-1-266	1.2371	0.0021	0.2393	0.0481	0.0011	0.0261	0.0153	0.0276	0.0803	0.0003	0.0003	1.6776
8-1-284	1.2469	0.0020	0.2368	0.0454	0.0011	0.0226	0.0220	0.0499	0.0477	0.0003	0.0003	1.6750
8-2-70B	1.0965	0.0021	0.2442	0.0479	0.0013	0.0519	0.0454	0.0199	0.0610	0.0003	0.0003	1.5709
8-2-90	1.2340	0.0020	0.2293	0.0444	0.0010	0.0205	0.0173	0.0528	0.0580	0.0003	0.0000	1.6596
8-2-92	1.3039	0.0021	0.2378	0.0415	0.0015	0.0369	0.0309	0.0340	0.0677	0.0003	0.0000	1.7566
F-103	1.0279	0.0021	0.2378	0.0324	0.0005	0.0131	0.0114	0.0846	0.0800	0.0004	0.0003	1.4905
F-135	1.2084	0.0022	0.2362	0.0423	0.0008	0.0249	0.0142	0.0216	0.0626	0.0003	0.0003	1.6138
F-70	1.1649	0.0019	0.2208	0.0555	0.0005	0.0563	0.0046	0.0103	0.0493	0.0005	0.0281	1.5927
P8-1	1.2080	0.0022	0.2341	0.0407	0.0008	0.0314	0.0207	0.0342	0.0631	0.0003	0.0003	1.6357
P8-3A	1.3932	0.0018	0.2415	0.0443	0.0008	0.0503	0.0072	0.0101	0.0579	0.0003	0.0003	1.8076
Avg	1.27	0.00	0.25	0.04	0.00	0.03	0.03	0.06	0.06	0.00	0.01	1.74

Cation equivalent proportion of hanging wall deformed samples.

	Si	Ti	Al	Fe	Mn	Mg	Ca	Na	K	P	S	Total
Precursor	1.2722	0.0024	0.2490	0.0401	0.0009	0.0305	0.0276	0.0571	0.0592	0.0004	0.0077	1.7471
263	0.5241	0.0017	0.1559	0.0315	0.0002	0.0359	0.0045	0.0120	0.0327	0.0002	0.0001	0.7989
283	0.8102	0.0018	0.1577	0.0332	0.0003	0.0389	0.0011	0.0127	0.0283	0.0002	0.0000	1.0844
451	1.5799	0.0032	0.3110	0.1991	0.0006	0.0426	0.0539	0.1042	0.0659	0.0004	0.3429	2.7037
7-1-117	0.4404	0.0018	0.1575	0.0325	0.0003	0.0230	0.0049	0.0131	0.0367	0.0002	0.0020	0.7122
7-1-130	0.6474	0.0021	0.2371	0.0352	0.0003	0.0155	0.0017	0.0242	0.0647	0.0003	0.0002	1.0289
7-1-177	0.7185	0.0021	0.1870	0.0405	0.0004	0.0526	0.0093	0.0226	0.0370	0.0004	0.0010	1.0712
7-2-33	0.3372	0.0018	0.1604	0.0373	0.0002	0.0222	0.0021	0.0032	0.0420	0.0002	0.0031	0.6096
F-138	1.2900	0.0024	0.2699	0.0675	0.0008	0.0550	0.0190	0.0118	0.0656	0.0006	0.0321	1.8147
P8-8	0.3762	0.0019	0.1683	0.0381	0.0003	0.0209	0.0005	0.0063	0.0433	0.0003	0.0285	0.6846
478	2.1452	0.0031	0.2921	0.0590	0.0002	0.0217	0.0048	0.0611	0.0306	0.0004	0.0615	2.6797
avg	0.8869	0.0022	0.2097	0.0574	0.0003	0.0328	0.0102	0.0271	0.0447	0.0003	0.0471	1.3188

APPENDIX 5.2a

(iv)

Normalized cation equivalent proportion of hanging wall altered (least deformed) samples.

	Si	Ti	Al	Fe	Mn	Mg	Ca	Na	K	P	S	Total
Precursor	72.69	0.12	13.43	1.41	0.05	0.55	1.42	8.57	1.73	0.01	0.00	100.0
332	81.69	0.19	16.55	1.07	0.03	0.93	1.57	2.04	4.55	0.04	0.06	108.7
370-A	84.77	0.19	16.60	2.71	0.02	0.65	0.74	3.02	4.76	0.05	3.11	116.6
380-A	91.25	0.13	14.59	1.32	0.14	0.85	5.79	8.13	2.19	0.03	0.05	124.5
417	74.47	0.14	13.78	2.21	0.06	0.00	2.11	9.02	2.06	0.04	2.74	106.6
445	79.75	0.17	16.26	1.97	0.02	2.39	2.16	3.71	2.38	0.04	0.02	108.8
450	93.76	0.17	16.15	2.35	0.01	2.45	0.29	6.34	2.83	0.03	0.63	125.0
455	55.62	0.14	11.37	1.51	0.06	1.90	3.60	1.69	3.35	0.03	0.15	79.4
485	62.61	0.13	12.44	2.76	0.04	3.15	1.51	2.72	1.91	0.04	0.45	87.8
523	71.14	0.12	13.14	1.69	0.02	0.54	1.21	4.18	3.65	0.02	0.10	95.8
7-2-168	61.53	0.17	15.97	1.32	0.01	1.34	0.36	7.10	2.35	0.03	0.43	90.6
7-2-178	71.59	0.12	13.80	2.69	0.13	2.34	3.11	1.27	3.79	0.02	0.02	98.9
8-1-266	71.44	0.12	13.82	2.78	0.06	1.51	0.88	1.59	4.63	0.02	0.02	96.9
8-1-284	71.87	0.11	13.65	2.62	0.06	1.30	1.27	2.88	2.75	0.02	0.02	96.5
8-2-70B	63.07	0.12	14.05	2.76	0.08	2.99	2.61	1.14	3.51	0.02	0.02	90.4
8-2-90	71.01	0.11	13.20	2.56	0.06	1.18	1.00	3.04	3.34	0.02	0.00	95.5
8-2-92	75.21	0.12	13.71	2.39	0.09	2.13	1.78	1.96	3.91	0.02	0.00	101.3
F-103	57.97	0.12	13.41	1.83	0.03	0.74	0.64	4.77	4.51	0.02	0.02	84.1
F-135	69.96	0.12	13.68	2.45	0.05	1.44	0.82	1.25	3.63	0.02	0.02	93.4
F-70	66.97	0.11	12.70	3.19	0.03	3.24	0.26	0.59	2.83	0.03	1.61	91.6
P8-1	69.59	0.13	13.49	2.34	0.05	1.81	1.20	1.97	3.64	0.02	0.02	94.2
P8-3A	81.15	0.10	14.07	2.58	0.04	2.93	0.42	0.59	3.37	0.02	0.02	105.3
Avg	72.69	0.14	14.11	2.24	0.05	1.71	1.59	3.29	3.33	0.03	0.45	99.62

Normalized cation equivalent proportion of hanging wall deformed samples.

	Si	Ti	Al	Fe	Mn	Mg	Ca	Na	K	P	S	
Precursor	72.80	0.14	14.25	2.29	0.05	1.74	1.58	3.27	3.39	0.03	0.44	100.0
263	29.86	0.10	8.88	1.79	0.01	2.05	0.26	0.68	1.86	0.01	0.01	45.5
283	46.82	0.10	9.11	1.92	0.02	2.25	0.06	0.73	1.64	0.01	0.00	62.7
451	86.28	0.17	16.98	10.87	0.03	2.33	2.94	5.69	3.60	0.02	18.73	147.7
7-1-117	25.00	0.10	8.94	1.84	0.02	1.31	0.28	0.74	2.08	0.01	0.11	40.4
7-1-130	36.68	0.12	13.43	2.00	0.02	0.88	0.10	1.37	3.67	0.01	0.01	58.3
7-1-177	40.91	0.12	10.65	2.31	0.02	2.99	0.53	1.29	2.11	0.02	0.06	61.0
7-2-33	19.08	0.10	9.08	2.11	0.01	1.25	0.12	0.18	2.38	0.01	0.18	34.5
F-138	74.11	0.14	15.50	3.88	0.04	3.16	1.09	0.68	3.77	0.03	1.84	104.2
P8-8	21.13	0.11	9.46	2.14	0.02	1.17	0.03	0.35	2.44	0.02	1.60	38.5
478	123.92	0.18	16.87	3.41	0.01	1.26	0.28	3.53	1.77	0.03	3.55	154.8
Avg	50.38	0.12	11.89	3.23	0.02	1.87	0.57	1.52	2.53	0.02	2.61	74.8

APPENDIX 5.2a

(v)

Normative mineralogy (mole) of hanging wall altered (least deformed) samples

	Py	Apt	Ab	Ort	Mg-P	Fe-Px	Ca-Px	An	Qz	Rt
Precursor	0.00	0.02	42.86	12.09	1.10	2.81	1.29	3.82	36.45	0.12
	Py	Apt	Ab	Ser	Mg-C	Fe-Ch	Epi	Cc	Qz	Rt
332	0.09	0.10	10.20	31.88	2.06	2.30	0.00	1.51	55.63	0.19
370-A	4.67	0.13	15.11	33.31	1.45	2.57	0.00	0.67	54.64	0.19
380-A	0.07	0.08	40.64	15.31	1.89	2.87	0.00	5.74	52.65	0.13
417	4.12	0.11	45.11	14.45	0.00	1.86	0.00	2.04	36.55	0.14
445	0.03	0.10	18.53	16.63	5.32	4.36	6.72	0.42	46.76	0.17
450	0.94	0.08	31.72	19.84	5.44	4.53	0.00	0.24	53.53	0.17
455	0.23	0.09	8.44	23.44	4.23	3.19	0.00	3.54	31.47	0.14
485	0.68	0.10	13.60	13.40	7.00	5.63	0.50	1.33	32.69	0.13
523	0.16	0.04	20.89	25.52	1.20	3.64	0.00	1.18	38.27	0.12
7-2-168	0.65	0.08	35.51	16.42	2.98	2.46	0.54	0.18	26.10	0.17
7-2-178	0.03	0.05	6.34	26.54	5.20	5.95	0.00	3.08	40.25	0.12
8-1-266	0.03	0.04	7.95	32.44	3.35	6.15	0.00	0.86	36.54	0.12
8-1-284	0.03	0.04	14.38	19.23	2.90	5.80	0.00	1.24	39.77	0.11
8-2-70B	0.03	0.04	5.71	24.57	6.64	6.10	0.00	2.58	32.19	0.12
8-2-90	0.00	0.04	15.18	23.38	2.63	5.68	0.00	0.97	37.03	0.11
8-2-92	0.00	0.05	9.81	27.34	4.73	5.31	0.00	1.75	43.14	0.12
F-103	0.02	0.05	23.87	31.57	1.65	4.05	0.00	0.61	19.59	0.12
F-135	0.03	0.04	6.25	25.38	3.20	5.42	0.00	0.80	40.99	0.12
F-70	2.42	0.08	2.96	19.82	7.19	5.30	0.00	0.22	41.65	0.11
P8-1	0.03	0.04	9.85	25.45	4.02	5.19	0.00	1.17	38.80	0.13
P8-3A	0.03	0.05	2.95	23.60	6.51	5.72	0.00	0.39	53.35	0.10
Avg	0.68	0.07	16.43	23.31	3.79	4.48	0.37	1.45	40.55	0.14

Normative mineralogy (mole) of hanging wall deformed samples

	Py	Apt	Ab	Ser	Mg-C	Fe-Ch	Epi	Cc	Qz	Rt
Precursor	0.66	0.07	16.35	23.72	3.88	4.61	0.00	1.54	40.33	0.14
263	0.01	0.03	3.42	13.05	4.55	3.97	0.14	0.21	11.10	0.10
283	0.00	0.03	3.66	11.46	5.00	4.26	1.85	0.00	27.11	0.10
451	28.09	0.06	28.46	25.18	5.18	3.35	0.00	2.91	48.74	0.17
7-1-117	0.17	0.03	3.71	14.57	2.90	3.97	0.00	0.26	5.88	0.10
7-1-130	0.02	0.04	6.87	25.66	1.95	4.42	0.00	0.07	10.01	0.12
7-1-177	0.08	0.05	6.43	14.75	6.65	5.06	0.00	0.50	16.41	0.12
7-2-33	0.27	0.03	0.92	16.63	2.79	4.49	0.00	0.10	1.00	0.10
F-138	2.76	0.09	3.38	26.40	7.03	6.57	0.00	1.04	42.59	0.14
P8-8	2.40	0.05	1.77	17.05	2.61	2.98	0.32	0.00	4.55	0.11
478	5.33	0.07	17.64	12.38	2.79	3.62	16.31	0.00	92.16	0.18
Avg	3.91	0.05	7.62	17.71	4.14	4.27	1.86	0.51	25.95	0.12

APPENDIX 5.2a

(vi)

Normative mineralogy (wt)of hangingwall altered (least deformed) samples.

	Py	Apt	Ab	Ort	Mg-Px	Fe-Px	Ca-Px	An	Qz	Rt	Total
Precursor	0.00	1.29	2247.85	672.84	27.80	93.33	110.88	212.44	2190.35	9.67	5566.5
	Py	Apt	Ab	Ser	Mg-Chl	Fe-Chl	Epi	Cc	Qz	Rt	Total
332	3.62	5.88	534.80	1513.49	90.04	133.17	0.00	75.75	3343.00	14.87	5714.6
370-A	186.59	7.68	792.57	1581.38	63.26	148.48	0.00	33.30	3283.56	14.86	6111.7
380-A	2.79	5.10	2131.44	726.96	82.52	166.18	0.00	287.22	3163.94	10.46	6576.6
417	164.60	6.87	2365.87	685.76	0.00	107.86	0.00	102.25	2196.26	10.87	5640.3
445	1.19	5.79	971.87	789.44	232.18	252.07	367.35	21.11	2809.90	13.36	5464.2
450	37.73	4.93	1663.87	941.90	237.53	262.21	0.00	12.20	3216.56	13.72	6390.6
455	9.15	5.57	442.71	1112.94	184.79	184.63	0.00	177.41	1890.91	11.27	4019.4
485	27.25	5.93	713.03	636.09	305.52	325.85	27.18	66.63	1964.51	10.43	4082.4
523	6.27	2.54	1095.77	1211.29	52.40	210.75	0.00	59.26	2299.41	9.51	4947.2
7-2-168	26.04	4.70	1862.18	779.62	130.27	142.19	29.26	8.88	1568.18	13.95	4565.3
7-2-178	1.13	2.75	332.32	1259.92	226.89	344.10	0.00	154.22	2418.34	9.69	4749.4
8-1-266	1.07	2.61	417.22	1540.03	146.29	355.82	0.00	42.90	2195.95	9.77	4711.7
8-1-284	1.07	2.60	754.25	912.80	126.54	335.52	0.00	62.11	2390.01	9.16	4594.1
8-2-70B	1.02	2.48	299.54	1166.43	289.72	353.11	0.00	129.32	1934.48	9.83	4185.9
8-2-90	0.00	2.58	796.22	1109.89	114.62	328.52	0.00	48.66	2225.21	9.09	4634.8
8-2-92	0.00	2.77	514.47	1297.91	206.36	307.34	0.00	87.72	2592.33	9.75	5018.7
F-103	0.90	3.29	1251.76	1498.69	71.92	234.08	0.00	30.61	1177.23	9.66	4278.2
F-135	1.04	2.52	327.75	1204.69	139.86	313.34	0.00	40.00	2463.03	9.98	4502.2
F-70	96.80	4.91	155.05	940.93	313.94	306.65	0.00	10.81	2502.71	8.64	4340.4
P8-1	1.05	2.55	516.82	1208.07	175.35	300.17	0.00	58.54	2331.37	10.11	4604.0
P8-3A	1.18	2.88	154.92	1120.12	284.19	330.71	0.00	19.43	3205.65	8.23	5127.3
Avg.	27.17	4.14	861.64	1106.59	165.44	259.18	20.18	72.78	2436.79	10.82	4964.7

Normative mineralogy (wt) of hangingwall deformed samples.

	Py	Apt	Ab	Ser	Mg-Chl	Fe-Chl	Epi	Cc	Qz	Rt	Total
Precursor	26.43	4.16	857.31	1126.25	169.19	266.70	0.00	76.98	2423.71	10.92	4961.7
263	0.50	1.83	179.15	619.45	198.69	229.85	7.43	10.33	666.94	7.79	1922.0
283	0.00	1.69	191.89	543.95	218.35	246.57	101.07	0.00	1629.32	8.20	2941.0
451	1123.27	3.69	1492.57	1195.37	225.94	194.05	0.00	145.53	2928.62	13.79	7322.8
7-1-117	6.71	1.64	194.33	691.61	126.69	229.65	0.00	13.17	353.53	8.15	1625.5
7-1-130	0.64	2.33	360.19	1218.00	85.25	255.88	0.00	3.75	601.72	9.56	2537.3
7-1-177	3.36	3.27	337.21	700.42	290.38	292.90	0.00	24.84	985.84	9.36	2647.6
7-2-33	10.64	1.85	48.12	789.63	121.74	259.99	0.00	4.93	60.09	7.94	1304.9
F-138	110.56	5.61	177.10	1253.17	306.73	380.00	0.00	51.97	2559.12	11.11	4855.4
P8-8	95.99	3.06	92.89	809.24	113.79	172.35	17.68	0.00	273.14	8.53	1586.7
478	213.01	4.12	925.13	587.60	121.80	209.59	891.65	0.00	5537.89	14.49	8505.3
Avg	156.47	2.91	399.86	840.84	180.94	247.08	101.78	25.45	1559.62	9.89	3524.8

APPENDIX 5.2a

(vii)

Minerals of hanging wall altered (least deformed) samples, normalized to wt%.

	Py	Apt	Ab	Ort	Mg-Px	Fe-Px	Ca-Px	An	Qz	Rt	Total
Precursor	0.00	0.02	40.37	12.08	0.50	1.68	1.99	3.82	39.34	0.17	100.0
	Py	Apt	Ab	Ser	Mg-Chl	Fe-Ch	Epi	Cc	Qz	Rt	Total
332	0.07	0.11	10.17	28.79	1.71	2.53	0.00	1.44	63.59	0.28	108.7
370-A	3.56	0.15	15.12	30.17	1.21	2.83	0.00	0.64	62.65	0.28	116.6
380-A	0.05	0.10	40.34	13.76	1.56	3.14	0.00	5.44	59.88	0.20	124.5
417	3.11	0.13	44.73	12.97	0.00	2.04	0.00	1.93	41.52	0.21	106.6
445	0.02	0.12	19.36	15.73	4.63	5.02	7.32	0.42	55.97	0.27	108.8
450	0.74	0.10	32.55	18.43	4.65	5.13	0.00	0.24	62.93	0.27	125.0
455	0.18	0.11	8.75	21.99	3.65	3.65	0.00	3.51	37.37	0.22	79.4
485	0.59	0.13	15.33	13.68	6.57	7.01	0.58	1.43	42.24	0.22	87.8
523	0.12	0.05	21.22	23.46	1.01	4.08	0.00	1.15	44.53	0.18	95.8
7-2-168	0.52	0.09	36.97	15.48	2.59	2.82	0.58	0.18	31.13	0.28	90.6
7-2-178	0.02	0.06	6.92	26.23	4.72	7.16	0.00	3.21	50.34	0.20	98.9
8-1-266	0.02	0.05	8.58	31.66	3.01	7.32	0.00	0.88	45.15	0.20	96.9
8-1-284	0.02	0.05	15.85	19.18	2.66	7.05	0.00	1.31	50.23	0.19	96.5
8-2-70B	0.02	0.05	6.47	25.18	6.25	7.62	0.00	2.79	41.75	0.21	90.4
8-2-90	0.00	0.05	16.41	22.87	2.36	6.77	0.00	1.00	45.85	0.19	95.5
8-2-92	0.00	0.06	10.39	26.20	4.17	6.20	0.00	1.77	52.33	0.20	101.3
F-103	0.02	0.06	24.60	29.45	1.41	4.60	0.00	0.60	23.13	0.19	84.1
F-135	0.02	0.05	6.80	25.00	2.90	6.50	0.00	0.83	51.11	0.21	93.4
F-70	2.04	0.10	3.27	19.85	6.62	6.47	0.00	0.23	52.79	0.18	91.6
P8-1	0.02	0.05	10.58	24.73	3.59	6.14	0.00	1.20	47.72	0.21	94.2
P8-3A	0.02	0.06	3.18	23.00	5.84	6.79	0.00	0.40	65.83	0.17	105.3
Avg	0.53	0.08	17.03	22.28	3.39	5.28	0.40	1.46	48.95	0.22	99.62

Minerals of hanging wall deformed samples, normalized to wt%.

	Py	Apt	Ab	Ser	Mg-Chl	Fe-Ch	Epi	Cc	Qz	Rt	Total
Precursor	0.53	0.08	17.28	22.70	3.41	5.37	0.00	1.55	48.84	0.22	100.0
263	0.01	0.04	4.24	14.67	4.71	5.44	0.18	0.24	15.80	0.18	45.5
283	0.00	0.04	4.09	11.59	4.65	5.25	2.15	0.00	34.72	0.17	62.7
451	22.65	0.07	30.10	24.10	4.56	3.91	0.00	2.93	59.05	0.28	147.7
7-1-117	0.17	0.04	4.83	17.20	3.15	5.71	0.00	0.33	8.79	0.20	40.4
7-1-130	0.01	0.05	8.27	27.98	1.96	5.88	0.00	0.09	13.82	0.22	58.3
7-1-177	0.08	0.08	7.77	16.14	6.69	6.75	0.00	0.57	22.71	0.22	61.0
7-2-33	0.28	0.05	1.27	20.87	3.22	6.87	0.00	0.13	1.59	0.21	34.5
F-138	2.37	0.12	3.80	26.91	6.59	8.16	0.00	1.12	54.95	0.24	104.2
P8-8	2.33	0.07	2.25	19.62	2.76	4.18	0.43	0.00	6.62	0.21	38.5
478	3.88	0.07	16.84	10.69	2.22	3.81	16.23	0.00	100.79	0.26	154.8
Avg	3.18	0.06	8.35	18.98	4.05	5.60	1.90	0.54	31.88	0.22	74.8

APPENDIX 5.2a

(viii)

Volume of minerals contaning hanging wall altered (least deformed) samples.

	Py	Apt	Ab	Ort	Mg-P	Fe-Px	Ca-Px	An	Qz	Rt	Total
Precursor	0.00	0.01	15.77	4.74	0.16	0.42	0.69	1.38	14.84	0.04	38.1
	Py	Apt	Ab	Ser	Mg-C	Fe-C	Epi	Cc	Qz	Rt	Total
332	0.01	0.04	3.97	10.28	0.66	0.77	0.00	0.53	24.00	0.07	40.3
370-A	0.72	0.05	5.91	11.61	0.46	0.86	0.00	0.23	23.64	0.07	43.5
380-A	0.01	0.03	15.76	5.29	0.60	0.95	0.00	2.00	22.59	0.05	47.3
417	0.63	0.04	17.47	4.99	0.00	0.62	0.00	0.71	15.67	0.05	40.2
445	0.00	0.04	7.56	6.05	1.78	1.52	2.17	0.15	21.12	0.06	40.5
450	0.15	0.03	12.72	7.09	1.79	1.55	0.00	0.09	23.75	0.06	47.2
455	0.04	0.04	3.42	8.46	1.40	1.11	0.00	1.29	14.10	0.05	29.9
485	0.12	0.04	5.99	5.26	2.53	2.12	0.17	0.53	15.94	0.05	32.7
523	0.02	0.02	8.29	9.02	0.39	1.24	0.00	0.42	16.80	0.04	36.2
7-2-168	0.10	0.03	14.44	5.95	0.99	0.86	0.17	0.06	11.75	0.07	34.4
7-2-178	0.00	0.02	2.70	10.09	1.82	2.17	0.00	1.18	19.00	0.05	37.0
8-1-266	0.00	0.02	3.35	12.18	1.16	2.22	0.00	0.32	17.04	0.05	36.3
8-1-284	0.00	0.02	6.19	7.38	1.02	2.14	0.00	0.48	18.95	0.05	36.2
8-2-70B	0.00	0.02	2.53	9.68	2.41	2.31	0.00	1.03	15.76	0.05	33.8
8-2-90	0.00	0.02	6.41	8.80	0.91	2.05	0.00	0.37	17.30	0.04	35.9
8-2-92	0.00	0.02	4.06	10.08	1.60	1.88	0.00	0.65	19.75	0.05	38.1
F-103	0.00	0.02	9.61	11.33	0.54	1.39	0.00	0.22	8.73	0.04	31.9
F-135	0.00	0.02	2.66	9.61	1.12	1.97	0.00	0.31	19.29	0.05	35.0
F-70	0.41	0.03	1.28	7.63	2.55	1.96	0.00	0.08	19.92	0.04	33.9
P8-1	0.00	0.02	4.13	9.51	1.38	1.86	0.00	0.44	18.01	0.05	35.4
P8-3A	0.00	0.02	1.24	8.85	2.24	2.06	0.00	0.15	24.84	0.04	39.4
Avg	0.11	0.03	6.65	8.57	1.30	1.60	0.12	0.54	18.47	0.05	37.40

Volume of minerals contaning hanging wall altered (deformed) samples.

	Py	Apt	Ab	Ser	Mg-C	Fe-C	Epi	Cc	Qz	Rt	Total
Precursor	0.11	0.03	6.75	8.73	1.31	1.63	0.00	0.57	18.43	0.05	37.6
263	0.00	0.01	1.66	5.64	1.81	1.65	0.05	0.09	5.96	0.04	16.9
283	0.00	0.01	1.60	4.46	1.79	1.59	0.64	0.00	13.10	0.04	23.2
451	4.58	0.02	11.76	9.27	1.75	1.19	0.00	1.08	22.28	0.07	52.0
7-1-117	0.03	0.01	1.89	6.62	1.21	1.73	0.00	0.12	3.32	0.05	15.0
7-1-130	0.00	0.02	3.23	10.76	0.75	1.78	0.00	0.03	5.22	0.05	21.8
7-1-177	0.02	0.02	3.03	6.21	2.57	2.04	0.00	0.21	8.57	0.05	22.7
7-2-33	0.06	0.02	0.50	8.03	1.24	2.08	0.00	0.05	0.60	0.05	12.6
F-138	0.48	0.04	1.49	10.35	2.53	2.47	0.00	0.41	20.73	0.06	38.6
P8-8	0.47	0.02	0.88	7.54	1.06	1.27	0.13	0.00	2.50	0.05	13.9
478	0.78	0.02	6.58	4.11	0.85	1.16	4.80	0.00	38.03	0.06	56.4
Avg	0.64	0.02	3.26	7.30	1.56	1.70	0.56	0.20	12.03	0.05	27.3

APPENDIX 5.2a

(ix)

Least deformed hanging wall samples

	Net volume changes	%volume changes
332	2.3	6.0
370-A	5.5	14.4
380-A	9.2	24.2
417	2.1	5.6
445	2.4	6.3
450	9.2	24.1
455	-8.2	-21.4
485	-5.3	-13.9
523	-1.8	-4.7
7-2-168	-3.6	-9.5
7-2-178	-1.0	-2.7
8-1-266	-1.7	-4.5
8-1-284	-1.8	-4.8
8-2-70B	-4.3	-11.2
8-2-90	-2.2	-5.7
8-2-92	0.0	0.1
F-103	-6.2	-16.2
F-135	-3.0	-8.0
F-70	-4.1	-10.9
P8-1	-2.7	-7.0
P8-3A	1.4	3.7
Avg	-0.7	-1.7

deformed hanging wall samples

	Net volume changes	%volume changes
263	-20.7	-54.3
283	-14.4	-37.8
451	14.4	37.8
7-1-117	-22.6	-59.4
7-1-130	-15.8	-41.4
7-1-177	-14.9	-39.1
7-2-33	-25.0	-65.7
F-138	1.0	2.5
P8-8	-23.7	-62.2
478	18.8	49.4
Avg	-10.3	-27.0

APPENDIX 5.2b Volume change calculations for footwall rocks.

(i)

Normalized composition of representative footwall altered (least deformed) rocks, Mobrun mine.

	SiO2	TiO2	Al2O	FeO*	MnO	MgO	CaO	Na2O	K2O	P2O5	S	Zr	Total
Precursor	77.45	0.21	11.97	2.17	0.04	0.53	1.79	4.41	1.36	0.04	0.00	334.0	100.0
215	78.36	0.20	10.35	4.87	0.00	0.00	0.02	0.40	2.76	0.03	2.97	306.3	100.0
248	75.97	0.25	12.53	4.06	0.00	0.15	0.09	0.77	3.39	0.02	2.73	354.1	100.0
252	75.60	0.25	14.10	1.75	0.05	0.29	0.97	4.04	2.15	0.05	0.71	358.9	100.0
347-A	74.42	0.24	13.86	1.71	0.01	0.33	0.42	0.46	8.11	0.06	0.33	359.9	100.0
386-B	74.64	0.27	14.57	1.36	0.02	0.63	1.99	4.73	1.69	0.05	0.01	391.8	100.0
420	78.25	0.22	12.88	0.47	0.01	0.00	1.13	6.42	0.51	0.06	0.02	338.2	100.0
423	75.61	0.25	13.71	3.32	0.04	1.55	1.56	1.61	2.26	0.04	0.00	380.2	100.0
425	74.73	0.25	14.33	1.55	0.03	0.55	1.62	5.73	1.11	0.05	0.01	389.1	100.0
426	73.69	0.24	13.54	1.40	0.06	0.47	4.24	4.26	1.99	0.05	0.02	371.5	100.0
428	74.47	0.25	14.62	0.86	0.03	0.23	2.31	5.20	1.92	0.05	0.01	380.8	100.0
433	72.86	0.26	14.27	3.57	0.11	1.88	2.34	0.23	4.38	0.04	0.01	396.9	100.0
436	75.82	0.24	13.54	1.50	0.05	0.34	1.68	3.93	2.46	0.05	0.35	355.2	100.0
438	67.62	0.24	13.25	6.72	0.15	0.32	2.46	0.40	3.60	0.04	5.15	337.7	100.0
441	77.02	0.25	13.33	1.78	0.02	0.63	1.10	3.86	1.91	0.05	0.01	366.4	100.0
461	73.20	0.27	14.34	3.54	0.05	0.52	1.55	3.40	3.02	0.05	0.01	385.8	100.0
494	74.83	0.25	13.31	2.89	0.11	0.44	2.13	2.58	3.18	0.05	0.19	363.4	100.0
501	74.70	0.26	13.96	2.51	0.06	0.38	1.62	3.95	2.47	0.05	0.00	377.5	100.0
7-1-88	79.91	0.23	12.85	1.84	0.00	0.00	0.03	0.46	3.40	0.03	1.21	334.4	100.0
8-2-338	81.23	0.22	12.23	1.87	0.00	0.00	0.03	1.18	2.01	0.01	1.18	322.4	100.0
8-2-339	70.61	0.33	17.94	2.26	0.06	0.08	1.03	5.65	1.89	0.04	0.07	366.1	100.0
P7-6A	68.32	0.30	18.80	3.72	0.02	2.53	0.03	0.51	5.66	0.03	0.03	363.8	100.0
Avg	74.85	0.25	13.92	2.55	0.04	0.54	1.35	2.85	2.85	0.04	0.72	361.9	100.0

Note: Precursor composition from least altered samples (Barrett et al. 1992, average n = 4)

Normalized composition of representative footwall altered (deformed) rocks, Mobrun mine.

	SiO2	TiO2	Al2O	FeO*	MnO	MgO	CaO	Na2	K2O	P2O5	S	Zr	Total
Precursor	74.85	0.25	13.92	2.55	0.04	0.54	1.35	2.85	2.85	0.04	0.72	361.9	100.0
314-A	71.94	0.29	17.09	2.97	0.00	0.43	0.15	0.26	5.52	0.06	1.25	308.2	100.0
391-B	68.97	0.36	19.58	0.97	0.00	0.81	0.82	3.86	4.50	0.06	0.01	522.0	100.0
397	60.67	0.37	20.76	6.82	0.01	1.62	0.20	0.76	7.00	0.07	1.67	547.1	100.0
468	71.34	0.24	12.80	6.12	0.00	0.15	0.04	0.35	3.67	0.04	5.21	325.0	100.0
503	73.51	0.23	12.75	4.19	0.12	0.28	2.20	0.23	3.84	0.04	2.57	331.2	100.0
8-2-337	77.77	0.27	17.08	0.52	0.00	0.01	0.01	1.74	2.40	0.02	0.13	428.2	100.0
Avg	70.70	0.29	16.68	3.60	0.02	0.55	0.57	1.20	4.49	0.05	1.81	410.3	100.0

Note: Precursor composition from least deformed samples (average n=21).

APPENDIX 5.2b

(ii)

Reconstructed compositions of altered (least deformed) samples (FW), normalized to Zr precursor.

	SiO2	TiO2	Al2O3	FeO*	MnO	MgO	CaO	Na2O	K2O	P2O5	S	Zr	Total
Precursor	77.44	0.21	11.97	2.17	0.04	0.53	1.79	4.41	1.36	0.04	0.00	334.0	100.0
215	85.45	0.22	11.29	5.31	0.00	0.00	0.02	0.44	3.01	0.03	3.24	334.0	109.0
248	71.67	0.24	11.82	3.83	0.00	0.14	0.08	0.73	3.20	0.02	2.58	334.0	94.3
252	70.35	0.23	13.12	1.63	0.05	0.27	0.90	3.76	2.00	0.05	0.66	334.0	93.1
347-A	69.07	0.22	12.87	1.59	0.01	0.31	0.39	0.43	7.53	0.06	0.31	334.0	92.8
386-B	63.63	0.23	12.42	1.16	0.02	0.54	1.70	4.03	1.44	0.04	0.01	334.0	85.2
420	77.28	0.22	12.72	0.46	0.01	0.00	1.12	6.34	0.50	0.06	0.02	334.0	98.8
423	66.42	0.22	12.05	2.92	0.04	1.36	1.37	1.42	1.99	0.04	0.00	334.0	87.9
425	64.15	0.21	12.30	1.33	0.03	0.47	1.39	4.92	0.95	0.04	0.01	334.0	85.8
426	66.25	0.22	12.17	1.26	0.05	0.42	3.81	3.83	1.79	0.04	0.02	334.0	89.9
428	65.32	0.22	12.83	0.75	0.03	0.20	2.03	4.56	1.68	0.04	0.01	334.0	87.7
433	61.31	0.22	12.01	3.01	0.09	1.58	1.97	0.19	3.69	0.03	0.01	334.0	84.1
436	71.30	0.23	12.73	1.41	0.05	0.32	1.58	3.70	2.31	0.05	0.33	334.0	94.0
438	66.88	0.24	13.10	6.65	0.15	0.32	2.43	0.40	3.56	0.04	5.10	334.0	98.9
441	70.21	0.23	12.15	1.62	0.02	0.57	1.00	3.52	1.74	0.05	0.01	334.0	91.2
461	63.38	0.23	12.42	3.07	0.04	0.45	1.34	2.95	2.62	0.04	0.01	334.0	86.6
494	68.79	0.23	12.23	2.66	0.10	0.40	1.96	2.37	2.92	0.05	0.17	334.0	91.9
501	66.09	0.23	12.35	2.22	0.05	0.34	1.43	3.50	2.19	0.04	0.00	334.0	88.5
7-1-88	79.82	0.23	12.84	1.84	0.00	0.00	0.03	0.46	3.40	0.03	1.21	334.0	99.9
8-2-338	84.17	0.23	12.67	1.94	0.00	0.00	0.03	1.22	2.08	0.01	1.22	334.0	103.6
8-2-339	64.42	0.30	16.37	2.06	0.05	0.07	0.94	5.16	1.73	0.04	0.06	334.0	91.2
P7-6A	62.73	0.28	17.27	3.42	0.02	2.32	0.03	0.47	5.20	0.03	0.03	334.0	91.8
Avg	69.08	0.23	12.85	2.35	0.04	0.50	1.25	2.63	2.63	0.04	0.66	334.0	92.7

Reconstructed compositions of altered (deformed) samples (FW), normalized to Zr precursor.

	SiO2	TiO2	Al2O3	FeO*	MnO	MgO	CaO	Na2	K2O	P2O5	S	Zr	Total
Precursor	74.87	0.25	13.92	2.55	0.04	0.54	1.35	2.85	2.85	0.04	0.72	362.0	100.0
314-A	84.48	0.34	20.07	3.49	0.00	0.51	0.18	0.31	6.49	0.07	1.47	362.0	117.4
391-B	47.83	0.25	13.58	0.67	0.00	0.56	0.57	2.68	3.12	0.04	0.01	362.0	69.3
397	40.14	0.25	13.74	4.51	0.01	1.07	0.13	0.50	4.63	0.05	1.11	362.0	66.2
468	79.45	0.27	14.26	6.82	0.00	0.17	0.04	0.39	4.09	0.04	5.80	362.0	111.4
503	80.36	0.25	13.93	4.58	0.13	0.31	2.41	0.25	4.20	0.04	2.81	362.0	109.3
8-2-337	65.75	0.23	14.44	0.44	0.00	0.01	0.01	1.47	2.03	0.02	0.11	362.0	84.5
Avg	62.38	0.26	14.71	3.18	0.02	0.49	0.50	1.06	3.96	0.04	1.60	362.0	93.0

APPENDIX 5.2b

(iii)

Cation equivalent proportion of footwall altered (least deformed) samples.

	Si	Ti	Al	Fe	Mn	Mg	Ca	Na	K	P	S	Total
Precursor	1.2889	0.0026	0.2348	0.0272	0.0006	0.0132	0.0303	0.1423	0.0289	0.0006	0.0000	1.7694
215	1.4223	0.0027	0.2215	0.0739	0.0000	0.0000	0.0004	0.0141	0.0640	0.0005	0.1010	1.9004
248	1.1929	0.0030	0.2318	0.0533	0.0000	0.0035	0.0014	0.0234	0.0681	0.0003	0.0804	1.6581
252	1.1709	0.0029	0.2574	0.0227	0.0007	0.0067	0.0153	0.1214	0.0426	0.0007	0.0206	1.6617
375-A	1.1496	0.0028	0.2524	0.0221	0.0001	0.0076	0.0066	0.0138	0.1602	0.0008	0.0096	1.6256
386-B	1.0590	0.0029	0.2436	0.0161	0.0002	0.0133	0.0287	0.1302	0.0307	0.0006	0.0003	1.5257
420	1.2864	0.0027	0.2495	0.0065	0.0001	0.0000	0.0189	0.2047	0.0107	0.0008	0.0006	1.7809
423	1.1056	0.0028	0.2363	0.0406	0.0005	0.0338	0.0232	0.0457	0.0423	0.0005	0.0000	1.5313
425	1.0678	0.0027	0.2412	0.0185	0.0004	0.0117	0.0235	0.1588	0.0203	0.0006	0.0003	1.5459
426	1.1027	0.0027	0.2387	0.0175	0.0008	0.0105	0.0646	0.1237	0.0381	0.0006	0.0006	1.6004
428	1.0872	0.0028	0.2516	0.0105	0.0004	0.0050	0.0343	0.1472	0.0358	0.0006	0.0003	1.5756
433	1.0205	0.0027	0.2355	0.0418	0.0013	0.0393	0.0333	0.0062	0.0784	0.0005	0.0003	1.4599
436	1.1867	0.0028	0.2497	0.0196	0.0007	0.0079	0.0268	0.1193	0.0492	0.0007	0.0103	1.6737
438	1.1132	0.0030	0.2570	0.0926	0.0021	0.0079	0.0412	0.0128	0.0758	0.0006	0.1590	1.7650
441	1.1686	0.0029	0.2383	0.0226	0.0003	0.0143	0.0170	0.1136	0.0371	0.0006	0.0003	1.6155
461	1.0549	0.0029	0.2435	0.0427	0.0006	0.0112	0.0227	0.0951	0.0557	0.0006	0.0003	1.5302
494	1.1449	0.0029	0.2399	0.0370	0.0014	0.0100	0.0332	0.0766	0.0622	0.0006	0.0054	1.6142
501	1.1001	0.0029	0.2422	0.0309	0.0007	0.0083	0.0243	0.1128	0.0465	0.0006	0.0000	1.5694
7-1-88	1.3285	0.0029	0.2518	0.0256	0.0000	0.0000	0.0005	0.0148	0.0723	0.0004	0.0377	1.7346
8-2-338	1.4009	0.0029	0.2486	0.0270	0.0000	0.0000	0.0005	0.0395	0.0443	0.0001	0.0381	1.8020
8-2-339	1.0722	0.0038	0.3210	0.0287	0.0008	0.0018	0.0159	0.1664	0.0367	0.0005	0.0020	1.6499
P7-6A	1.0441	0.0035	0.3387	0.0476	0.0003	0.0577	0.0005	0.0151	0.1106	0.0004	0.0009	1.6192
Avg	1.1561	0.0029	0.2519	0.0332	0.0005	0.0119	0.0206	0.0836	0.0563	0.0006	0.0223	1.6400

Cation equivalent proportion of footwall deformed samples.

	Si	Ti	Al	Fe	Mn	Mg	Ca	Na	K	P	S	Total
Precursor	1.2462	0.0032	0.2731	0.0355	0.0006	0.0134	0.0229	0.0919	0.0607	0.0006	0.0223	1.7703
314-A	1.4062	0.0043	0.3938	0.0486	0.0000	0.0125	0.0030	0.0099	0.1380	0.0010	0.0458	2.0630
391-B	0.7961	0.0031	0.2663	0.0094	0.0000	0.0140	0.0096	0.0865	0.0664	0.0006	0.0002	1.2522
397	0.6681	0.0031	0.2694	0.0628	0.0001	0.0266	0.0022	0.0162	0.0985	0.0007	0.0345	1.1822
468	1.3225	0.0034	0.2797	0.0949	0.0000	0.0041	0.0008	0.0126	0.0870	0.0006	0.1811	1.9866
503	1.3376	0.0032	0.2733	0.0638	0.0018	0.0076	0.0407	0.0081	0.0893	0.0006	0.0877	1.9137
8-2-337	1.0943	0.0029	0.2833	0.0061	0.0000	0.0002	0.0001	0.0475	0.0432	0.0002	0.0034	1.4812
Avg	1.1041	0.0033	0.2943	0.0476	0.0003	0.0108	0.0094	0.0301	0.0871	0.0006	0.0588	1.6465

APPENDIX 5.2b

(iv)

Normalized cation equivalent proportion of footwall altered (least deformed) samples.

	Si	Ti	Al	Fe	Mn	Mg	Ca	Na	K	P	S	Total
Precursor	72.84	0.15	13.27	1.54	0.03	0.74	1.71	8.04	1.63	0.03	0.00	100.0
215	81.61	0.16	12.71	4.24	0.00	0.00	0.02	0.81	3.67	0.03	5.80	109.0
248	67.87	0.17	13.19	3.03	0.00	0.20	0.08	1.33	3.87	0.02	4.57	94.3
252	65.57	0.16	14.41	1.27	0.04	0.38	0.86	6.80	2.38	0.04	1.15	93.1
375-A	65.63	0.16	14.41	1.26	0.01	0.43	0.38	0.79	9.14	0.04	0.55	92.8
386-B	59.17	0.16	13.61	0.90	0.01	0.75	1.61	7.27	1.71	0.03	0.01	85.2
420	71.34	0.15	13.84	0.36	0.01	0.00	1.05	11.35	0.59	0.05	0.03	98.8
423	63.43	0.16	13.56	2.33	0.03	1.94	1.33	2.62	2.43	0.03	0.00	87.9
425	59.30	0.15	13.40	1.03	0.02	0.65	1.31	8.82	1.13	0.03	0.01	85.8
426	61.95	0.15	13.41	0.98	0.04	0.59	3.63	6.95	2.14	0.04	0.03	89.9
428	60.52	0.15	14.00	0.58	0.02	0.28	1.91	8.19	1.99	0.03	0.02	87.7
433	58.82	0.16	13.57	2.41	0.08	2.26	1.92	0.36	4.52	0.03	0.02	84.1
436	66.67	0.16	14.03	1.10	0.04	0.45	1.50	6.70	2.77	0.04	0.58	94.0
438	62.37	0.17	14.40	5.19	0.12	0.44	2.31	0.72	4.25	0.03	8.91	98.9
441	65.94	0.16	13.45	1.28	0.01	0.80	0.96	6.41	2.09	0.04	0.02	91.2
461	59.69	0.17	13.78	2.42	0.03	0.63	1.29	5.38	3.15	0.03	0.02	86.6
494	65.20	0.16	13.66	2.11	0.08	0.57	1.89	4.36	3.54	0.04	0.31	91.9
501	62.02	0.16	13.66	1.74	0.04	0.47	1.37	6.36	2.62	0.04	0.00	88.5
7-1-88	76.50	0.17	14.50	1.47	0.00	0.00	0.03	0.85	4.16	0.02	2.17	99.9
8-2-338	80.55	0.16	14.29	1.55	0.00	0.00	0.03	2.27	2.55	0.01	2.19	103.6
8-2-339	59.29	0.21	17.75	1.59	0.04	0.10	0.88	9.20	2.03	0.03	0.11	91.2
P7-6A	59.21	0.20	19.20	2.70	0.01	3.27	0.03	0.86	6.27	0.02	0.05	91.8
Avg	65.36	0.16	14.23	1.88	0.03	0.68	1.16	4.69	3.19	0.03	1.26	92.7

Normalized cation equivalent proportion of footwall deformed samples.

	Si	Ti	Al	Fe	Mn	Mg	Ca	Na	K	P	S	Total
Precursor	70.41	0.18	15.43	2.01	0.03	0.76	1.29	5.19	3.43	0.03	1.26	100.0
314-A	80.05	0.24	22.42	2.77	0.00	0.71	0.17	0.56	7.86	0.06	2.61	117.4
391-B	44.09	0.17	14.75	0.52	0.00	0.77	0.53	4.79	3.68	0.03	0.01	69.3
397	37.39	0.17	15.08	3.51	0.01	1.49	0.13	0.91	5.51	0.04	1.93	66.2
468	74.14	0.19	15.68	5.32	0.00	0.23	0.04	0.71	4.88	0.04	10.15	111.4
503	76.40	0.18	15.61	3.64	0.11	0.43	2.33	0.46	5.10	0.04	5.01	109.3
8-2-337	62.45	0.16	16.17	0.35	0.00	0.01	0.01	2.71	2.46	0.01	0.20	84.5
Avg	62.42	0.19	16.62	2.69	0.02	0.61	0.53	1.69	4.92	0.03	3.32	93.0

APPENDIX 5.2b

(v)

Normative mineralogy (mole) of footwall altered (least deformed) samples.

	Py	Apt	Ab	Ort	Mg-P	Fe-Px	Ca-Px	An	Qz	Rt
Precursor	0.00	0.08	40.21	8.17	1.49	3.07	3.42	0.00	40.61	0.15
	Py	Apt	Ab	Ser	Mg-C	Fe-Chl	Epi	Cc	Qz	Rt
215	8.70	0.07	4.04	25.72	0.00	2.98	0.00	0.00	60.70	0.16
248	6.86	0.04	6.67	27.10	0.44	1.66	0.00	0.06	47.98	0.17
252	1.73	0.10	33.99	16.69	0.83	1.54	0.00	0.80	33.97	0.16
375-A	0.82	0.12	3.94	64.01	0.97	2.20	0.00	0.31	30.10	0.16
386-B	0.02	0.09	36.37	11.99	1.66	1.99	0.28	1.48	26.72	0.16
420	0.05	0.12	56.77	4.16	0.00	0.76	1.26	0.66	33.13	0.15
423	0.00	0.08	13.11	16.98	4.31	5.18	2.17	0.74	33.44	0.16
425	0.02	0.09	44.09	7.88	1.45	2.27	0.23	1.20	23.34	0.15
426	0.05	0.09	34.73	14.97	1.31	2.15	0.00	3.57	28.98	0.15
428	0.02	0.09	40.97	13.96	0.62	1.28	0.00	1.85	26.59	0.15
433	0.02	0.07	1.80	31.65	5.03	5.34	0.00	1.88	29.56	0.16
436	0.87	0.10	33.52	19.36	0.99	1.81	0.00	1.44	33.49	0.16
438	13.36	0.08	3.58	29.73	0.98	1.63	0.44	2.15	43.01	0.17
441	0.02	0.10	32.05	14.64	1.79	2.82	0.00	0.90	32.95	0.16
461	0.02	0.09	26.89	22.04	1.41	5.35	0.00	1.23	20.38	0.17
494	0.47	0.10	21.80	24.80	1.27	4.34	0.00	1.83	30.33	0.16
501	0.00	0.09	31.80	18.35	1.05	3.87	0.00	1.31	25.12	0.16
7-1-88	3.26	0.06	4.27	29.13	0.00	0.86	2.42	0.00	58.40	0.17
8-2-338	3.29	0.02	11.34	17.83	0.00	1.01	10.88	0.00	59.50	0.16
8-2-339	0.17	0.08	46.01	14.21	0.22	3.41	3.66	0.00	15.65	0.21
P7-6A	0.07	0.06	4.29	43.91	7.27	5.94	0.00	0.00	21.15	0.20
Avg	1.90	0.08	23.43	22.34	1.50	2.78	1.02	1.02	34.02	0.16

Normative mineralogy of footwall deformed samples.

	Py	Apt	Ab	Ser	Mg-C	Fe-Chl	Epi	Cc	Qz	Rt
Precursor	1.89	0.09	25.97	24.00	1.68	3.06	0.00	1.24	36.48	0.18
314-A	3.91	0.15	2.81	54.99	1.59	3.25	0.00	0.08	46.28	0.24
391-B	0.02	0.09	23.94	25.76	1.72	1.14	0.00	0.48	15.40	0.17
397	2.90	0.10	4.54	38.58	3.31	5.66	0.00	0.07	3.15	0.17
468	15.23	0.09	3.53	34.14	0.52	0.54	0.08	0.00	55.87	0.19
503	7.51	0.09	2.32	35.72	0.96	2.53	0.00	2.27	53.13	0.18
8-2-337	0.29	0.04	13.55	17.25	0.03	0.56	15.71	0.00	39.64	0.16
Avg	4.98	0.09	8.45	34.41	1.35	2.28	2.63	0.48	35.58	0.19

APPENDIX 5.2b

(vi)

Normative mineralogy (wt) of footwall altered (least deformed) samples.

	Py	Apt	Ab	Ort	Mg-Px	Fe-Px	Ca-Px	An	Qz	Rt	Total
Precursor	0.00	5.15	2108.96	455.09	37.61	101.94	99.46	0.00	2440.45	11.90	5260.56
	Py	Apt	Ab	Ser	Mg-Chl	Fe-Chl	Epi	Cc	Qz	Rt	Total
215	347.81	4.28	211.86	1221.14	0.00	172.67	0.00	0.00	3647.60	12.55	5617.90
248	274.27	2.45	349.87	1286.74	19.39	96.16	0.00	2.88	2883.40	13.46	4928.61
252	69.27	5.94	1782.57	792.46	36.40	89.04	0.00	39.90	2040.96	13.07	4869.61
375-A	32.77	7.26	206.58	3038.78	42.16	127.26	0.00	15.29	1808.41	12.77	5291.28
386-B	0.89	5.43	1907.49	569.33	72.28	115.01	15.19	74.17	1605.89	12.90	4378.57
420	2.05	7.50	2977.30	197.58	0.00	43.89	68.63	33.04	1990.81	12.09	5332.87
423	0.00	4.60	687.37	806.02	188.25	299.70	118.50	37.28	2009.69	12.64	4164.05
425	0.89	5.44	2312.59	374.23	63.15	131.31	12.40	59.92	1402.78	11.95	4374.66
426	1.89	5.76	1821.65	710.86	57.17	124.55	0.00	178.64	1741.41	12.16	4654.09
428	0.91	5.57	2148.87	662.80	27.04	74.16	0.00	92.80	1597.73	12.24	4622.13
433	0.91	4.42	94.45	1502.46	219.61	308.98	0.00	94.00	1776.33	12.65	4013.80
436	34.62	6.02	1757.88	919.19	43.26	104.77	0.00	72.24	2012.31	12.72	4963.01
438	534.33	5.06	187.70	1411.16	42.72	94.17	23.96	107.57	2584.44	13.34	5004.43
441	0.96	5.87	1681.08	694.88	78.05	162.88	0.00	45.05	1980.15	12.90	4661.83
461	0.92	5.59	1410.43	1046.54	61.37	309.51	0.00	61.60	1224.43	13.27	4133.65
494	18.62	5.97	1143.29	1177.17	55.47	250.83	0.00	91.53	1822.75	13.12	4578.75
501	0.00	5.69	1668.09	871.36	45.65	224.12	0.00	65.67	1509.46	13.01	4403.04
7-1-88	130.25	3.93	223.95	1382.76	0.00	49.83	132.10	0.00	3509.13	13.27	5445.22
8-2-338	131.56	1.36	594.99	846.64	0.00	58.40	594.80	0.00	3575.35	13.14	5816.23
8-2-339	6.61	4.60	2413.32	674.38	9.72	197.02	200.25	0.00	940.40	16.70	4463.00
P7-6A	2.92	3.56	224.86	2084.65	317.33	343.65	0.00	0.00	1270.61	15.67	4263.26
Avg	75.83	5.06	1228.87	1060.53	65.67	160.85	55.52	51.03	2044.48	13.12	4760.95

Normative mineralogy (wt) of footwall deformed samples.

	Py	Apt	Ab	Ser	Mg-Chl	Fe-Chl	Epi	Cc	Qz	Rt	Total
Precursor	75.67	5.52	1361.92	1139.41	73.38	176.90	0.00	61.93	2191.96	14.23	5100.92
314-A	156.48	9.15	147.20	2610.73	69.26	187.86	0.00	3.97	2780.93	19.45	5985.04
391-B	0.72	5.26	1255.67	1222.86	74.96	65.95	0.00	24.10	925.53	13.87	3588.93
397	115.81	5.91	238.37	1831.45	144.55	327.52	0.00	3.35	189.26	13.75	2869.98
468	608.92	5.70	185.01	1620.54	22.56	31.51	4.39	0.00	3357.49	15.03	5851.13
503	300.39	5.70	121.59	1695.75	42.11	146.44	0.00	113.60	3192.86	14.40	5632.83
8-2-337	11.74	2.20	710.57	818.74	1.16	32.32	858.98	0.00	2381.79	13.06	4830.57
Avg	199.01	5.65	443.07	1633.35	59.10	131.93	143.90	24.17	2137.98	14.93	4793.08

APPENDIX 5.2b

(vii)

Minerals of footwall altered (least deformed) samples,normalized to wt%.

	Py	Apt	Ab	Ort	Mg-P	Fe-Px	Ca-Px	An	Qz	Rt	Total
Precursor	0.00	0.10	40.09	8.65	0.71	1.94	1.89	0.00	46.39	0.23	100.0
	Py	Apt	Ab	Ser	Mg-C	Fe-C	Epi	Cc	Qz	Rt	Total
215	6.75	0.08	4.11	23.70	0.00	3.35	0.00	0.00	70.80	0.24	109.0
248	5.25	0.05	6.70	24.63	0.37	1.84	0.00	0.06	55.19	0.26	94.3
252	1.32	0.11	34.06	15.14	0.70	1.70	0.00	0.76	39.00	0.25	93.1
375-A	0.57	0.13	3.62	53.30	0.74	2.23	0.00	0.27	31.72	0.22	92.8
386-B	0.02	0.11	37.14	11.08	1.41	2.24	0.30	1.44	31.27	0.25	85.2
420	0.04	0.14	55.14	3.66	0.00	0.81	1.27	0.61	36.87	0.22	98.8
423	0.00	0.10	14.50	17.01	3.97	6.32	2.50	0.79	42.40	0.27	87.9
425	0.02	0.11	45.38	7.34	1.24	2.58	0.24	1.18	27.53	0.23	85.8
426	0.04	0.11	35.19	13.73	1.10	2.41	0.00	3.45	33.64	0.23	89.9
428	0.02	0.11	40.78	12.58	0.51	1.41	0.00	1.76	30.32	0.23	87.7
433	0.02	0.09	1.98	31.50	4.60	6.48	0.00	1.97	37.24	0.27	84.1
436	0.66	0.11	33.31	17.42	0.82	1.99	0.00	1.37	38.13	0.24	94.0
438	10.56	0.10	3.71	27.89	0.84	1.86	0.47	2.13	51.07	0.26	98.9
441	0.02	0.11	32.87	13.59	1.53	3.18	0.00	0.88	38.72	0.25	91.2
461	0.02	0.12	29.54	21.92	1.29	6.48	0.00	1.29	25.65	0.28	86.6
494	0.37	0.12	22.95	23.63	1.11	5.04	0.00	1.84	36.59	0.26	91.9
501	0.00	0.11	33.52	17.51	0.92	4.50	0.00	1.32	30.33	0.26	88.5
7-1-88	2.39	0.07	4.11	25.36	0.00	0.91	2.42	0.00	64.37	0.24	99.9
8-2-338	2.34	0.02	10.60	15.08	0.00	1.04	10.60	0.00	63.69	0.23	103.6
8-2-339	0.14	0.09	49.33	13.79	0.20	4.03	4.09	0.00	19.22	0.34	91.2
P7-6A	0.06	0.08	4.84	44.90	6.83	7.40	0.00	0.00	27.36	0.34	91.8
Avg	1.46	0.10	23.97	20.70	1.34	3.23	1.04	1.01	39.58	0.26	92.7

Minerals of footwall deformed samples,normalized to wt%.

	Py	Apt	Ab	Ser	Mg-C	Fe-C	Epi	Cc	Qz	Rt	Total
Precursor	1.48	0.11	26.71	22.34	1.44	3.47	0.00	1.21	42.98	0.28	100.0
314-A	3.07	0.18	2.89	51.23	1.36	3.69	0.00	0.08	54.57	0.38	117.4
391-B	0.01	0.10	24.26	23.63	1.45	1.27	0.00	0.47	17.88	0.27	69.3
397	2.67	0.14	5.50	42.22	3.33	7.55	0.00	0.08	4.36	0.32	66.2
468	11.59	0.11	3.52	30.85	0.43	0.60	0.08	0.00	63.91	0.29	111.4
503	5.83	0.11	2.36	32.91	0.82	2.84	0.00	2.20	61.96	0.28	109.3
8-2-337	0.21	0.04	12.44	14.33	0.02	0.57	15.03	0.00	41.68	0.23	84.5
Avg	3.90	0.11	8.49	32.53	1.23	2.75	2.52	0.47	40.73	0.29	93.03

APPENDIX 5.2b

(viii)

Volume of minerals contaning footwall altered (least deformed) samples.

	Py	Apt	Ab	Ort	Mg-P	Fe-Px	Ca-Px	An	Qz	Rt	Total
Precursor	0.00	0.03	15.66	3.39	0.22	0.49	0.66	0.00	17.51	0.05	38.01
	Py	Apt	Ab	Ser	Mg-C	Fe-C	Epi	Cc	Qz	Rt	Total
215	1.36	0.03	1.61	8.47	0.00	1.05	0.00	0.00	26.72	0.06	39.29
248	1.06	0.02	2.62	8.80	0.14	0.58	0.00	0.02	20.83	0.06	34.11
252	0.27	0.04	13.31	5.41	0.27	0.53	0.00	0.28	14.72	0.06	34.87
375-A	0.12	0.04	1.42	19.04	0.28	0.70	0.00	0.10	11.97	0.05	33.71
386-B	0.00	0.03	14.51	3.96	0.54	0.70	0.09	0.53	11.80	0.06	32.22
420	0.01	0.04	21.54	1.31	0.00	0.25	0.38	0.22	13.91	0.05	37.72
423	0.00	0.03	5.66	6.07	1.53	1.98	0.74	0.29	16.00	0.06	32.36
425	0.00	0.03	17.73	2.62	0.48	0.81	0.07	0.43	10.39	0.06	32.62
426	0.01	0.04	13.75	4.90	0.42	0.75	0.00	1.27	12.69	0.06	33.89
428	0.00	0.03	15.93	4.49	0.20	0.44	0.00	0.65	11.44	0.05	33.24
433	0.00	0.03	0.77	11.25	1.77	2.02	0.00	0.72	14.05	0.06	30.69
436	0.13	0.04	13.01	6.22	0.32	0.62	0.00	0.50	14.39	0.06	35.28
438	2.13	0.03	1.45	9.96	0.32	0.58	0.14	0.78	19.27	0.06	34.74
441	0.00	0.04	12.84	4.85	0.59	1.00	0.00	0.32	14.61	0.06	34.31
461	0.00	0.04	11.54	7.83	0.49	2.03	0.00	0.47	9.68	0.07	32.15
494	0.08	0.04	8.97	8.44	0.43	1.57	0.00	0.68	13.81	0.06	34.07
501	0.00	0.04	13.09	6.25	0.35	1.41	0.00	0.49	11.45	0.06	33.14
7-1-88	0.48	0.02	1.60	9.06	0.00	0.29	0.72	0.00	24.29	0.06	36.52
8-2-338	0.47	0.01	4.14	5.39	0.00	0.33	3.13	0.00	24.03	0.06	37.56
8-2-339	0.03	0.03	19.27	4.92	0.08	1.26	1.21	0.00	7.25	0.08	34.13
P7-6A	0.01	0.02	1.89	16.03	2.63	2.31	0.00	0.00	10.33	0.08	33.31
Avg	0.29	0.03	9.36	7.39	0.52	1.01	0.31	0.37	14.93	0.06	34.28

Volume of minerals contaning footwall altered (least deformed) samples.

	Py	Apt	Ab	Ser	Mg-C	Fe-C	Epi	Cc	Qz	Rt	Total
Precursor	0.30	0.03	10.43	7.98	0.55	1.08	0.00	0.45	16.22	0.07	37.12
314-A	0.62	0.06	1.13	18.30	0.52	1.15	0.00	0.03	20.59	0.09	42.49
391-B	0.00	0.03	9.48	8.44	0.56	0.40	0.00	0.17	6.75	0.06	25.89
397	0.54	0.04	2.15	15.08	1.28	2.36	0.00	0.03	1.65	0.07	23.20
468	2.34	0.03	1.38	11.02	0.17	0.19	0.02	0.00	24.12	0.07	39.33
503	1.18	0.04	0.92	11.75	0.31	0.89	0.00	0.81	23.38	0.07	39.35
8-2-337	0.04	0.01	4.86	5.12	0.01	0.18	4.45	0.00	15.73	0.05	30.44
Avg	0.79	0.04	3.32	11.62	0.47	0.86	0.75	0.17	15.37	0.07	33.45

APPENDIX 5.2b

(ix)

Least deformed footwall samples

	Net volum changes	% volume changes
215	1.3	3.3
248	-3.9	-10.3
252	-3.1	-8.3
375-A	-4.3	-11.3
386-B	-5.8	-15.2
420	-0.3	-0.8
423	-5.6	-14.9
425	-5.4	-14.2
426	-4.1	-10.8
428	-4.8	-12.6
433	-7.3	-19.3
436	-2.7	-7.2
438	-3.3	-8.6
441	-3.7	-9.7
461	-5.9	-15.4
494	-3.9	-10.4
501	-4.9	-12.8
7-1-88	-1.5	-3.9
8-2-338	-0.5	-1.2
8-2-339	-3.9	-10.2
P7-6A	-4.7	-12.4
Avg	-3.7	-9.8

deformed footwall samples

	Net volum changes	%volume changes
314-A	5.4	14.1
391-B	-11.2	-29.5
397	-13.9	-36.6
468	2.2	5.8
503	2.2	5.9
8-2-337	-6.7	-17.6
Avg	-3.7	-9.6

ETCHING OF POLISHED SECTIONS

The surfaces of numerous pyrite-rich polished sections have been etched with one of the following solution:

(1) $KMnO_4$ (2.5 g in 100 cm^3 H_2O) and H_2SO_4 in the volume ratio 1:1, at room temperature for 5 to 10 minutes;

(2) HNO_3 (one part to one part H_2O), at room temperature for 5 to 10 minutes;

(3) H_2SO_4 (one part to two parts H_2O), at room temperature for 5 to 10 minutes or at 60°C for 3 minutes, as outlined by Yamada et al. (1979); Craig and Vaughan (1981) and Fleet and MacLean (1988).

The reaction of the specimens with the above solutions reveals minerals zonation, twinning, and grain boundaries for grains in various optical orientations. These effects result from the lower chemical resistance of grain edges and the different sensitivities of mineral grains depending on their crystallographic orientations (Ramdohr, 1980).

The use of HNO_3 and H_2SO_4 is suitable for the development of texture etching. The $KMnO_4$-H_2SO_4 solution produces structure etching and zone staining, but the result are not uniform and they are contaminated by a Mn component precipitate (shaking of samples during etching may help in reducing contamination). In many cases, the time for sufficient reaction between the polished section and the etching agent has been determined by direct observation

under the microscope; in this case, use of an old low-power objective lens is recommended because of the possible corrosion by fumes of the etching reaction.

6.2 X-RAY GONIOMETRY

In order to determine the orientation of a lattice plane (hkl) of Mobrun ore specimens, we placed samples in the X-ray beam (Cu Kα) of a Philips PW 1078 texture goniometer and set the detector at the $2\theta_{hkl}$ angles for pyrite, sphalerite, quartz and chlorite. The specimens consisted of 2-5 mm thick slices cut parallel to the schistosity. The sample was rotated on its own two-dimensional plane and on the three rotational axes in space. These rotations change the orientation of the sample relative to the incident beam. Rotations of these axes in spherical coordinates define the orientations of the diffracting lattice plane (hkl) relative to the goniometer.

A pole figure is scanned on a spherical template by measuring the reflected beam intensity at all positions. The reflected beam intensity is a measure of the amount of preferred orientation of grains on the sample surface, following Braggs Law ($n\lambda = 2d\sin\theta$).

In polycrystalline material, 2θ varies according to the relative number of lattice planes in each orientation. If, on the other hand, the sample has only random orientations as in a powdered sample, an equal number of grains diffract

at all angle settings and the recorded intensity is uniform in all directions. Pole figures for quartz and chlorite are presented in Figure A6.1 and A6.2 respectively.

7.1 b_0 SPACING MEASUREMENTS

The measurement of lateral b_0 spacing values for celadonite have been obtained with a Guinier focusing camera. The camera was designed to provide accurate interplanar spacing and unit cell dimensions.

The main features of the Guinier camera geometry are presented by Westman and Magneli (1957) and Reynolds (1989):

(1) an incident-beam monochromator filtered by the bent quartz crystal, which is a large signal crystal cut and oriented to diffract only those rays which satisfy the Bragg condition ($n\lambda=2d\sin\theta$). This means that, for the Kα wavelength, the reflected rays have a very well-defined direction and can be made to converge in a narrow focal line.

(2) the powder samples are situated on a cylinder defined by the film. The sample is mounted on a piece of thin adhesive tape which is attached to a flat metal ring rotated in a plane tangent to the focusing cylinder. The rays reflected by the bent quartz crystal are diffracted by the specimen. The geometry of the focal line, specimen and circular film strip is such that the diffracted rays converge toward sharp diffraction lines for every deviation angles. Four specimens can be exposed

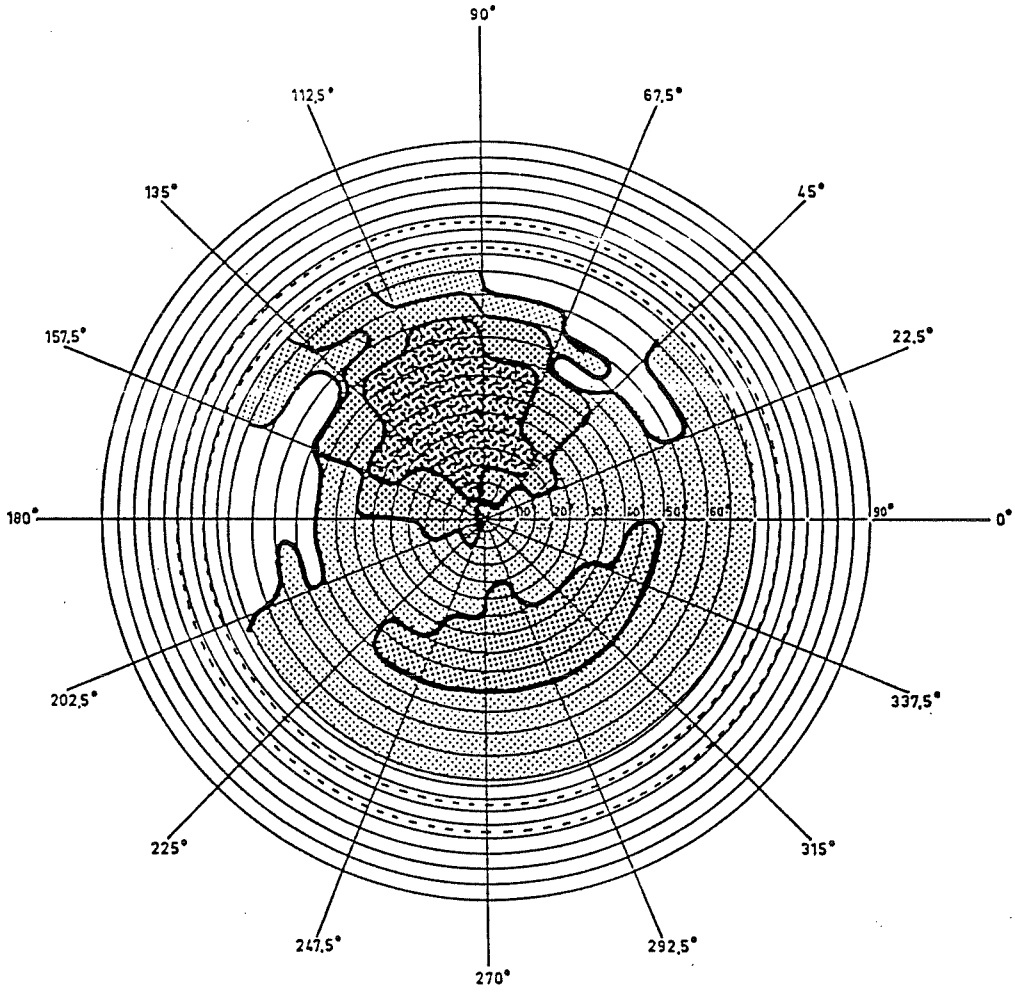

SAMPLE: (quartz)
LATTICE PLANE: 101
d-VALUE: 3.353 AT: 26.6 °(2θ).
TUBE: Cu ANODE, 35 kV, 20 mA, Ni, FILTER.
TIME CONSTANT: 10 SEC.
DISTANCE: 173 mm.
REFLECTION: RING FROM: 0° TO 70°.
START TABLE AT: 0°.
SPECIMENTABLE SPEED: 45° PER 2 MIN.
RINGSPEED: 5/8.°
INTEGRATING: 9 mm.

Fig. A6.1 Quartz, a major constituent of some parts of the deformed orebody, exhibits a strongly preferred orientation. Darker areas are higher density. Contour levels are 20% of mean intensity. Schistosity surface is parallel to the plan of projection.

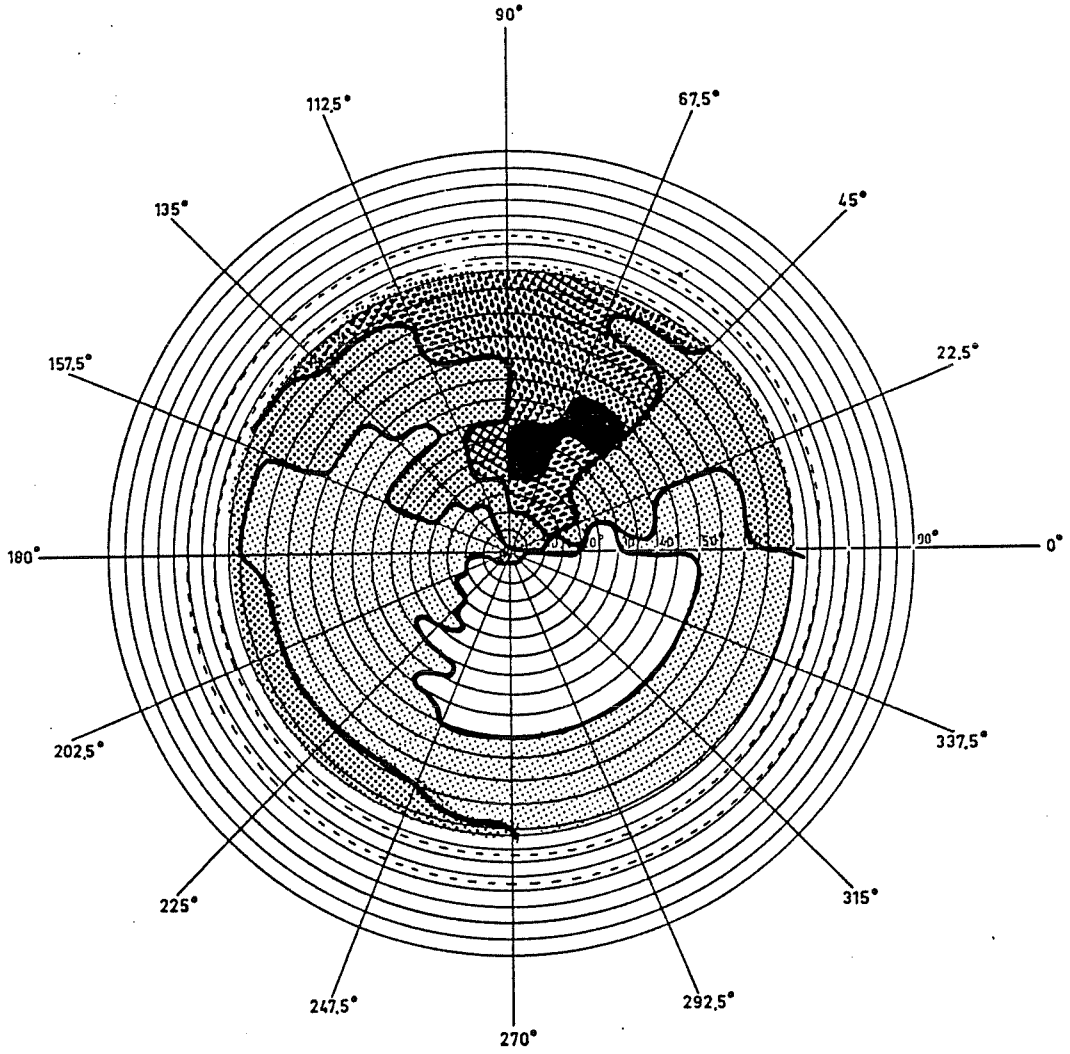

SAMPLE: **167 (chlorite)**
LATTICE PLANE: **002**
d-VALUE: **7.05** AT: **12.7** °(2θ).
TUBE: Cu ANODE, **35** kV, **20** mA, **Ni**, FILTER.
TIME CONSTANT: **10** SEC.
DISTANCE: **173** mm.
REFLECTION: RING FROM: **0°** TO **70°**.
START TABLE AT: **0°**.
SPECIMENTABLE SPEED: **45°** PER **2** MIN.
RINGSPEED: **5/8.°**
INTEGRATING: **9** mm.

Fig. A6.2 Chlorite a silicate constituent of some parts of the deformed ore body, exhibits a strongly preferred orientation. Darker areas are higher density. Contour levels are 20% of mean intensity. Schistosity surface is parallel to the plan of projection.

simultaneously, and the exposure time is about 1 hour. Fig. A7.1 presents analyzed films for 12 specimens.

7.2 SERICITE b_0 DATA

The lateral spacing of the following 13 samples (Table A7.1) were measured, using quartz powder with an accurately known $K\alpha\theta$ value (56.96 Å) to determine the (060) peak (b_0) for each individual muscovite sample.

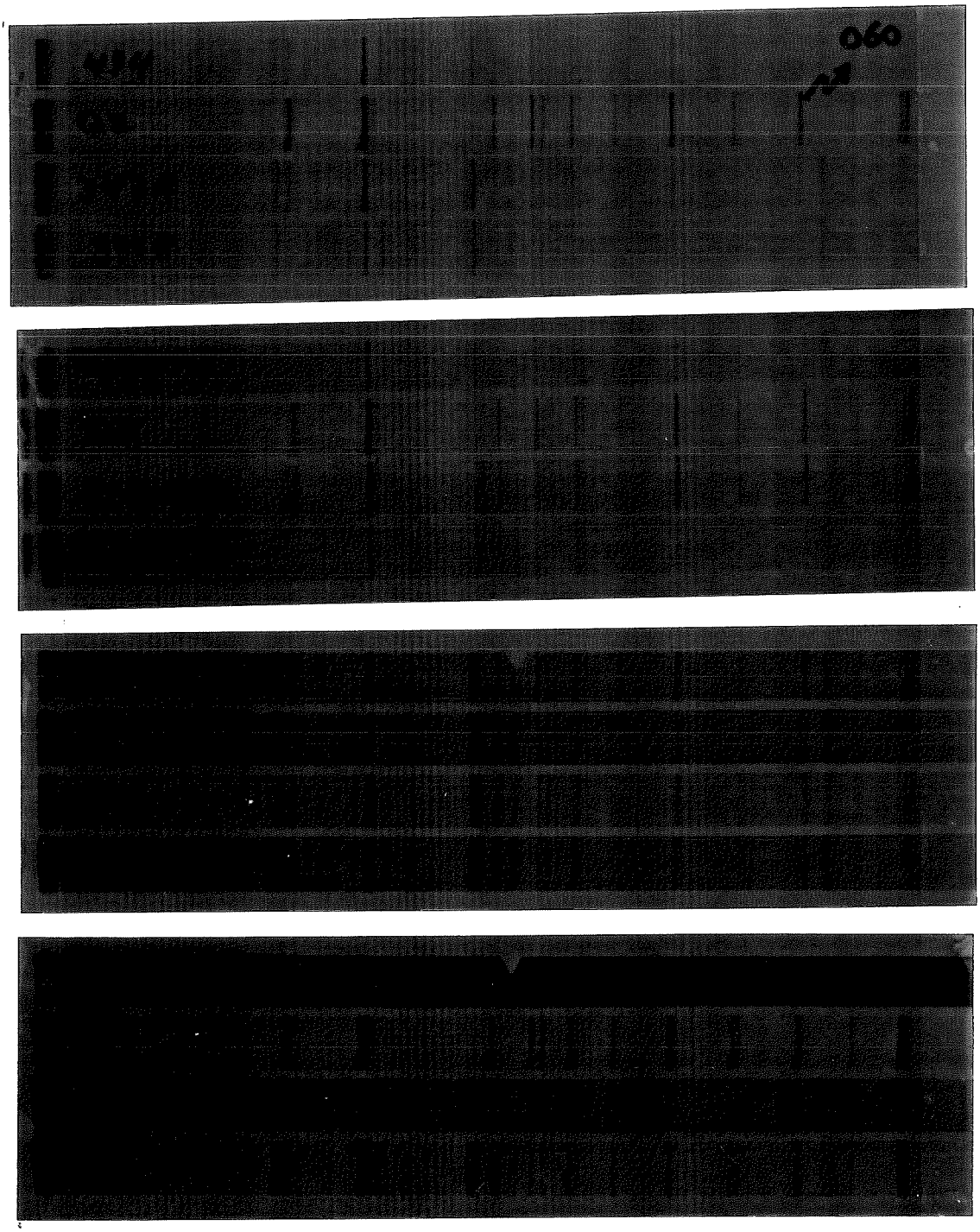

Fig. A7.1 Guinier Camera films of 15 samples from the Mobrun rocks.

Table A7.1 "bo" calculations for sericite minerals from the Mobrun deposit.

Sample	sericite (060)i	quartz (060)ii	2Θ (i - ii)	Θ	+	quartz Θ (59.96)	sericite Θ	Θ (d)	x 6	bo
494	143.260	140.260	3.000	1.500	+	59.96	61.460	1.5076	x 6	9.0456
268	143.470	140.130	3.340	1.670	+	59.96	61.630	1.5036	x 6	9.0216
268	143.430	140.050	3.380	1.690	+	59.96	61.650	1.5032	x 6	9.0192
8-2-337	144.120	140.270	3.850	1.925	+	59.96	61.885	1.4981	x 6	8.9886
8-2-338	144.100	140.210	3.890	1.945	+	59.96	61.905	1.4975	x 6	8.9850
314A	143.780	140.350	3.430	1.715	+	59.96	61.675	1.5027	x 6	9.0162
494	143.420	140.100	3.320	1.660	+	59.96	61.620	1.5038	x 6	9.0228
347A	143.400	140.000	3.400	1.700	+	59.96	61.660	1.5030	x 6	9.0180
391B	143.700	140.220	3.480	1.740	+	59.96	61.700	1.5021	x 6	9.0126
8-2-66	143.050	140.000	3.050	1.525	+	59.96	61.485	1.5068	x 6	9.0408
7-2-33	143.750	140.000	3.750	1.875	+	59.96	61.835	1.4990	x 6	8.9940
P7-6A	143.750	140.370	3.380	1.690	+	59.96	61.650	1.5025	x 6	9.0150
7-1-130	143.860	140.310	3.550	1.775	+	59.96	61.735	1.5014	x 6	9.0084
F-103	143.750	140.000	3.750	1.875	+	59.96	61.835	1.4992	x 6	8.9952
P-88	143.150	140.000	3.150	1.575	+	59.96	61.535	1.5056	x 6	9.0336
7-1-117	143.630	140.000	3.630	1.815	+	59.96	61.775	1.5003	x 6	9.0018
397	143.050	140.000	3.050	1.525	+	59.96	61.485	1.5068	x 6	9.0408

7.3 FLUID INCLUSIONS

Microthermometric analyses of fluid inclusions were performed using an S.E.G. Model III heating-freezing stage based on a USGS design (Werre et al., 1981). Temperatures of the observed phase changes were measured using a chrome-alumel thermocouple and a digital trendicator. The heating rate was maintained below 1°C/min. Fluid inclusion data are presented in Table A7.2.

Table A7.2 Fluid inclusion analyses

a) Quartz pressure shadow:

	Th (°C)	Te (°C)	Tm (°C)
sample #215	160	-30	-5
	155	-29	-2
	190	-30	-1
	110	-24	-3
sample #328	200	-29	-5
	150	-20	-2
	120	-15	-2
Average	156	-23	-3

b) Quartz vein:

	Th (°C)	Te (°C)	Tm (°C)
sample # 494	120	-57	-22
	122	-58	-19
	120	-57	-21
	100	-59	-19
Average	115	-58	-20

Th = homogenization temperature
Te = eutectic temperature
Tm = final melting temperature